CORROSION-FATIGUE TECHNOLOGY

Craig / Crooker / Hoeppner

ASTM STP 642

AMERICAN SOCIETY FOR TESTING AND MATERIALS

CORROSION-FATIGUE TECHNOLOGY

A symposium
presented at
November Committee Week
AMERICAN SOCIETY FOR
TESTING AND MATERIALS
Denver, Colo., 14-19 Nov. 1976

ASTM SPECIAL TECHNICAL PUBLICATION
642
H. L. Craig, Jr., University of Miami,
T. W. Crooker, U.S. Naval Research Laboratory,
and D. W. Hoeppner, University of Missouri,
editors

List price $32.00
04-642000-27

AMERICAN SOCIETY FOR TESTING AND MATERIALS
1916 Race Street, Philadelphia, Pa. 19103

Library of Congress Catalog Card Number: 77-81762

NOTE

Printed in Lutherville-Timonium, Md.
Feb. 1978

Foreword

The symposium on Corrosion Fatigue was presented at the November Committee Week of the American Society for Testing and Materials held in Denver, Colo., 14–19 November 1976. ASTM Committees G-1 on Corrosion of Metals, E-9 on Fatigue, and E-24 on Fracture Testing of Metals sponsored the symposium. H. L. Craig, Jr., University of Miami, T. W. Crooker, U.S. Naval Research Laboratory, D. W. Hoeppner, University of Missouri, and S. R. Novak, U.S. Steel Corporation, presided as symposium chairmen. H. L. Craig, Jr., T. W. Crooker, and D. W. Hoeppner served as editors of this publication.

Related ASTM Publications

Stress Corrosion Cracking of Metals—A State of the Art, STP 518 (1972), $11.75, 04-518000-27

Manual of Industrial Corrosion Standards and Control, STP 534 (1974), $16.75, 04-534000-27

Stress Corrosion—New Approaches, STP 610 (1976), $43.00, 04-610000-27

Use of Computers in the Fatigue Laboratory, STP 613 (1976), $20.00, 04-613000-30

A Note of Appreciation to Reviewers

This publication is made possible by the authors and, also, the unheralded efforts of the reviewers. This body of technical experts whose dedication, sacrifice of time and effort, and collective wisdom in reviewing the papers must be acknowledged. The quality level of ASTM publications is a direct function of their respected opinions. On behalf of ASTM we acknowledge their contribution with appreciation.

ASTM Committee on Publications

Editorial Staff

Jane B. Wheeler, *Managing Editor*
Helen M. Hoersch, *Associate Editor*
Ellen J. McGlinchey, *Senior Assistant Editor*
Sheila G. Pulver, *Assistant Editor*

Contents

Introduction 1

SURVEY AND ANALYSIS

Solution Chemistry Modification within Corrosion-Fatigue Cracks—W. H. HARTT, J. S. TENNANT, AND W. C. HOOPER 5

Corrosion Fatigue of Structural Steels in Seawater and for Offshore Applications—C. E. JASKE, D. BROEK, J. E. SLATER, AND W. E. ANDERSON 19

PHENOMENA

Investigation of Effects of Saltwater on Retardation Behavior of Aluminum Alloys—G. R. CHANANI 51

Influences of Secondary Stress Fluctuations of Small Amplitude on Low-Cycle Corrosion Fatigue—K. ENDO AND K. KOMAI 74

Small Randomly Distributed Cracks in Corrosion Fatigue—H. KITAGAWA, T. FUJITA, AND K. MIYAZAWA 98

MATERIALS CHARACTERIZATION

Corrosion-Fatigue Behavior of Some Special Stainless Steels—C. AMZALLAG, P. RABBE, AND A. DESESTRET 117

Corrosion-Fatigue Behavior of Austenitic-Ferritic Stainless Steels—J. A. MOSKOVITZ AND R. M. PELLOUX 133

Corrosion-Fatigue Behavior of 13Cr Stainless Steel in Sodium Chloride Aqueous Solution and Steam Environment—R. EBARA, T. KAI, AND K. INOUE 155

Influence of Advanced Ingot Thermal-Mechanical Treatments on the Microstructure and Stress Corrosion Properties of Aluminum Alloy Forgings—JOSEPH ZOLA 169

Effects of Flowing Natural Seawater and Electrochemical Potential on Fatigue-Crack Growth in Several High-Strength Marine Alloys—T. W. CROOKER, F. D. BOGAR, AND W. R. CARES 189

Corrosion-Fatigue Properties of Recrystallization Annealed Ti-6A1-4V—J. T. RYDER, W. E. KRUPP, D. E. PETTIT, AND D. W. HOEPPNER 202

Corrosion Fatigue of 5456-H117 Aluminum Alloy in Saltwater—H. P. CHU AND J. G. MACCO 223

HYDROGEN ENVIRONMENTS

Influence of High Pressure Hydrogen on Cyclic Load Crack Growth in Metals—R. P. JEWETT, R. J. WALTER, AND W. T. CHANDLER 243

Effect of Hydrogen Gas on High Strength Steels—B. MUKHERJEE 264

FAILURE ANALYSIS AND DESIGN CONSIDERATIONS

Fatigue of Tantalum in Sulfuric Acid at 150°C—C. C. SEASTROM 289

Corrosion-Fatigue Behavior of Coated 4340 Steel for Blade Retention Bolts of the AH-1 Helicopter—MILTON LEVY AND J. L. MORROSSI 300

SUMMARY

Summary 315

Index 319

Introduction

ASTM Committees G-1 on Corrosion of Metals, E-9 on Fatigue, and E-24 on Fracture Testing of Metals agreed it would be timely to sponsor a symposium on corrosion fatigue. As a result, the Symposium on Corrosion Fatigue was held during ASTM November Committee Week, 1976. The objective of this symposium was to provide a general survey in an exploratory interdisciplinary manner of the broad range of investigation currently being pursued in the technological community.

A diversity of views related to the many aspects of corrosion fatigue was presented at the symposium, but because of the differences in perspective represented by the sponsoring committees, the divergent views did not always converge to points of agreement. Nonetheless, some aspects of the corrosion-fatigue process emerged in a clearer light as a result of the symposium. In addition, some areas in corrosion-fatigue technology that need increased attention surfaced.

The symposium chairmen owe a debt of gratitude to the members of the organizing committee who gave so much of their personal time to aid in planning and conducting the symposium. The contributions of James Ryder and David Mauney are gratefully acknowledged. We also wish to thank Jane Wheeler and the other members of the ASTM staff who provided assistance throughout this endeavor. The readers of this volume will agree that a great deal of useful information emerged at the symposium and is contained herein. We look forward to the next endeavor in this important area of material and structural behavior.

D. W. Hoeppner
University of Missouri, Columbia, Mo. 65201, co-editor.

Survey and Analysis

W. H. Hartt,[1] *J. S. Tennant,*[1] *and W. C. Hooper*[1]

Solution Chemistry Modification within Corrosion-Fatigue Cracks

---

REFERENCE: Hartt, W. H., Tennant, J. S., and Hooper, W. C., "**Solution Chemistry Modification within Corrosion-Fatigue Cracks,**" *Corrosion-Fatigue Technology, ASTM STP 642,* H. L. Craig, Jr., T. W. Crooker, and D. W. Hoeppner, Eds., American Society for Testing and Materials, 1978, pp. 5–18.

ABSTRACT: There exists in the literature several observations indicating that the electrolyte within corrosion-fatigue cracks can become modified relative to the bulk solution. Since the rate of fatigue-crack growth should depend upon electrolyte chemistry near the crack tip, it is important that the conditions under which such modification occurs and the role of influential variables be recognized. This paper represents an initial analysis of how fatigue variables might influence mixing between the crack and bulk solutions. The rationale considers that such mixing is governed primarily by net momentum of the periodically exhausted and ingested electrolyte. It is shown that this momentum should be directly proportional to the crack opening angle, cyclic frequency, and the cube of crack length. Decreasing mean stress also contributes to a momentum increase, with the latter becoming large for stress functions that result in crack closure during a portion of each cycle. Other factors which are considered include temperature, stress-wave form, specimen geometry, test method, and applied current density. The significance of the projected trends is discussed within the frame of commonly employed corrosion-fatigue test procedures.

KEY WORDS: corrosion fatigue, crack propagation, crack chemistry modification, electrolyte momentum, crack opening angle, mean stress, frequencies, crack length, temperature, stress waves, specimen geometry, tests, current density

Nomenclature

α	Crack-opening angle
α_0	Mean crack-opening angle
A	Cross-sectional area of crack at metal surface
a	Crack length
β	Half-angular range of crack opening

---

[1] Professor of ocean engineering, associate professor of ocean engineerning, and research associate, respectively, Department of Ocean Engineering, Florida Atlantic University, Boca Raton, Fla. 33431.

∇	Instantaneous crack-solution volume
J	Net electrolyte momentum
K_{max}	Maximum stress intensity per cycle
K_{min}	Minimum stress intensity per cycle
K_m	Mean stress intensity per cycle
Q	Volumetic flow rate
R	K_{min}/K_{max}
R_e	Reynold's number
ρ	Solution density
ν	Kinematic viscosity of solution
ω	Cyclic frequency
t	Time

Modification of the electrolyte within occluded cells is recognized generally as an important factor with regard to the rate at which localized corrosion takes place [1].[2] Examples where this has been viewed as significant include stress-corrosion cracks, pits, crevices, intergranular-corrosion paths, filiforms, tuberculations, and exfoliations. For freely corroding systems, this modification is usually in the form of acidification of the occluded cell electrolyte, due to hydrolysis of one or more components from the metal or alloy and restricted interchange between this solution and the bulk solution.

For the case of corrosion fatigue, the alternate opening and closing of the crack results in pumping of the electrolyte into and out of the crack on each cycle; and it has been presumed that this promotes mixing of the two solutions (crack and bulk) such that no modification of the crack electrolyte takes place [2,3]. Brown [1] has taken an objective stance with regard to this point, however, by noting that acidification of corrosion-fatigue cracks, as opposed to no modification, should be determined by the extent to which the electrolyte is pumped. As more direct evidence, Barsom [4] has reported a corrosion-fatigue crack pH of approximately 3 for a 12Ni-5Cr-3Mo steel cycled at 0.1 Hz in a near neutral 3 percent sodium-chloride (NaCl)-distilled water bulk solution. Similarly, a pH of less than 3 has been reported by Meyn [5] for Ti-8Al-1Mo-1V fatigued at both 0.5 and 30 Hz.

Modification of crack electrolyte chemistry under conditions of cathodic polarization also may be important with regard to corrosion-fatigue response. For this situation, however, an increase in pH, as opposed to a decrease, is expected. That this is the case is apparent from crevice corrosion-cathodic protection experiments by Peterson and Lennox [6] and from experiments by Pourbaix [7], which were performed in conjunction with stress-corrosion cracking tests by Brown [8]. These latter experiments involved a steel specimen in a 0.001 *M* sodium hydroxide (NaOH)-0.001 *M*

---

[2] The italic numbers in brackets refer to the list of references appended to this paper.

NaCl solution (pH = 10.0), where the electrolyte in contact with part of the metal surface was aerated and the remainder deaerated. For freely corroding conditions, corrosion potential and pH in the aerated portion were approximately −0.34 V (saturated calomel electrode (SCE)) and 10, respectively, whereas for the simulated crevice these values were −0.60 and 2.7. As the specimen was polarized cathodically, however, pH of the occluded region increased; and for potentials below approximately −0.64 V the electrolyte in the deaerated region was basic. Figure 1 presents Pourbaix's data illustrating how stepwise cathodic polarization of this electrode resulted in increasing pH for the crevice solution. Included in this plot are the results of Peterson and Lennox pertaining to stainless steel crevices in a 0.6 *M* NaCl-tap water bulk solution.

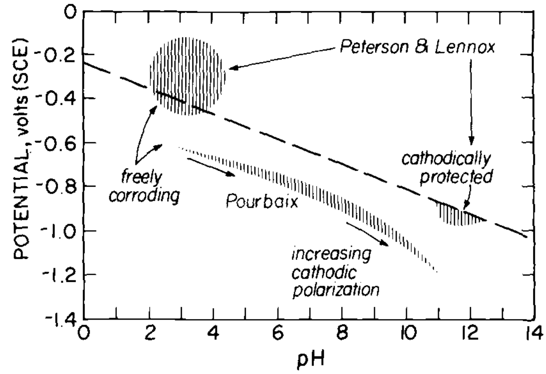

FIG. 1—*Potential −pH data for occluded cells in carbon steel and stainless steel specimens* [6,7].

It has been projected that whether or not a corrosion-fatigue crack propagates is related to the nature of reactions taking place at the crack tip-electrolyte interface [9]. Also, the rate of propagation for an advancing crack is expected to depend upon these same phenomena. On such a basis, chemistry of the electrolyte within a fatigue crack is fundamentally important, and any projection(s) as to the cracking mechanism should be cognizant of this point. The objective of the present paper is to examine the question of corrosion-fatigue electrolyte modification in greater detail than has been attempted previously and to define the effect of various fatigue variables upon occurrence of such modification.

General Consideration

The case of a fluid jet cyclically exiting and reentering a fixed boundary (the metal surface in this case) has been described by Tuck [*10*]. For situations where exit velocity is large, his projection was that a streamline pattern results, as represented schematically for the case of a closing fatigue crack in Fig. 2(*a*). When fluid exitation is complete, the flow becomes circulatory with closed streamlines, as shown in Fig. 2(*b*). The strength of these counter-rotating vortices is directly proportional to the maximum exit velocity.

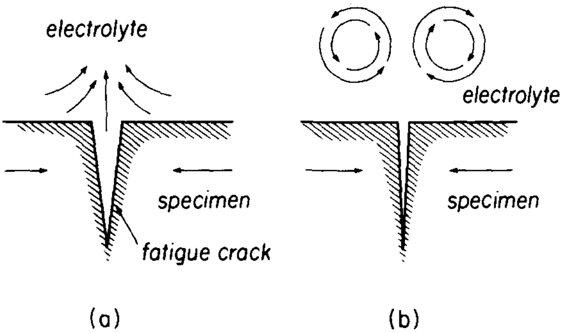

FIG. 2—*Schematic representation of crack and bulk solution flow during closing portion of the stress cycle for cases where net exit momentum is large.*

If vortices of sufficient strength form, then it seems probable that the ejected solution will be transported a sufficient distance from the metal surface and that subsequent reingestion is unlikely. This is particularly true when one considers the profile for ingestion streamlines, which are projected to be as shown in Fig. 3.

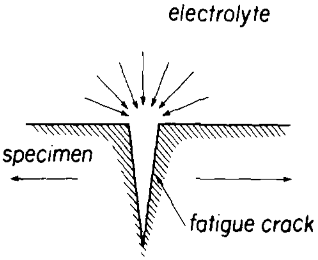

FIG. 3—*Schematic representation of solution flow during the opening portion of the stress cycle.*

For situations where crack-solution exit or reentry momentum is small, solution flow may exhibit viscous behavior. The Reynold's number, R_e, which defines the ratio of inertia to viscous forces, often is employed in such instances. For this case, R_e may be expressed as

$$R_e = \frac{a^2\omega}{\nu} \tag{1}$$

where

a = crack length,
ω = cyclic frequency, and
ν = kinematic viscosity of the fluid.

A high value for R_e then should favor mixing of crack and bulk solutions, but interchange should be minimal when this parameter is small. This is consistent with generalized fluid-dynamic behavior as examined with respect to Reynold's number.

Development of the Model

Consider a corrosion-fatigue crack in an otherwise smooth metal surface, as shown in Fig. 4, and the response of this to the different stress intensity patterns in Fig. 5(*a*) and (*b*). For the case of Fig. 5(*a*) the mean stress intensity, K_m, is sufficiently large compared to the stress intensity range, $K_{\max} - K_{\min}$, that the crack is always open. The latter point is illustrated by the accompanying plot of crack-opening angle, α, as a function of ωt, where the units for ω are radians per second and t is time (in seconds). Figure 5(*b*) represents a second case, where the minimum stress intensity per cycle is such that the crack closes during a portion of the cycle. Assuming a sinusoidal-stress wave, the crack-opening angle in Fig. 5(*a*) may be represented as

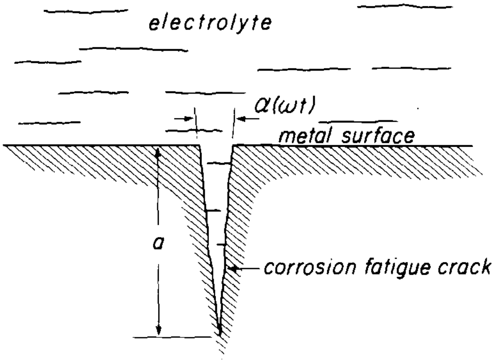

FIG. 4—*Schematic illustration of corrosion-fatigue crack and relevant parameters.*

$$\alpha = \beta \sin \omega t + \alpha_0 \tag{2}$$

where $\alpha_0 - \beta$ is the minimum crack-opening angle per cycle, and $\alpha_0 + \beta$ is the maximum angle. This same expression is applicable to Fig. 5(*b*) but only for the range $\alpha \geq 0$, since the crack-opening angle cannot be negative.

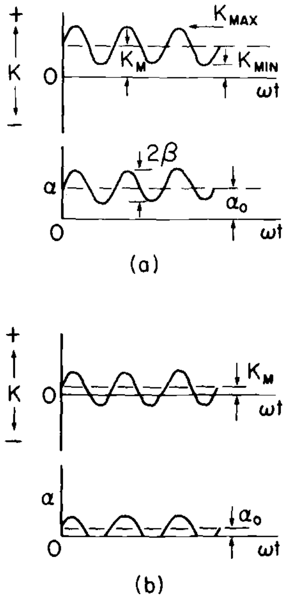

(a)

(b)

FIG. 5—*Assumed stress intensity and crack-opening angle functions for* (a) *a case where the crack is always open and* (b) *a case where the crack is closed during part of each cycle.*

An important question for the aforementioned model pertains to the extent of mixing between the bulk and crack solutions as the crack opens and closes on each cycle. Such mixing may result either from the convective action of the two solutions (bulk and crack) relative to one another or from diffusion or both. With regard to mixing currents, it is appropriate to define the volumetric flow rate, Q, as

$$Q = \frac{d\nabla}{dt} = \frac{d}{dt}\left(a^2 \sin\frac{\alpha}{2} \cos\frac{\alpha}{2}\right) \tag{3}$$

where ∇ is the instantaneous crack solution volume. Assuming $\alpha \ll 1$, this reduces to

$$Q = \frac{a^2}{2}\frac{d\alpha}{dt} = \frac{a^2}{2}\beta\omega \cos \omega t \tag{4}$$

Considering one-dimensional flow and a crack of unit width, the exit velocity, V, averaged across the exit plane (external specimen surface) is

$$V = \frac{Q}{A} = \frac{a^2\,\beta\omega\cos\omega t}{2\,a\,\alpha} \tag{5}$$

where A is the cross-sectional area of the crack at the metal surface. Thus

$$V = \frac{(a/2)\,\beta\omega \cos \omega t}{\beta \sin \omega t + \alpha_0} \tag{6}$$

An alternate parameter of interest, in addition to exit velocity of the crack solution, is the net momentum of this electrolyte during the period that the crack is either opening or closing; and it is considered that this may be influencial with regard to mixing of the crack and bulk solutions. This momentum, J, may be generalized as

$$J = \int \rho \, V d \triangledown \tag{7}$$

where ρ is the solution density. Recognizing that $d \triangledown = AVdt$ and substituting from Eq 6 yields

$$J = \frac{\rho a^3}{4} \int \frac{\dot{\alpha}^2}{\alpha} dt \tag{8}$$

where $\dot{\alpha}$, the first derivative of crack-opening angle with respect to time, equals $\beta\omega\cos\omega t$ (see Eq 2). Incorporation of the latter gives

$$J = \frac{\rho a^3 \beta \, \omega^2}{4} \int \frac{\cos^2 \omega t}{\sin \omega t + \frac{\alpha_0}{\beta}} dt \tag{9}$$

Equation 9 suggests that solution momentum and, presumably, the extent of mixing varies directly with the range of crack-opening angle, 2β (provided α_0/β is maintained constant), and with the cube of crack length.

The dependence of J upon frequency and mean stress, the latter being reflected by the term α_0/β, is apparently complex. Insight into these was provided by numerical integration of Eq 9 between the limits $\pi/2\omega$ and $3\pi/2\omega$, which is the closing portion of the cycle. Thus, Fig. 6 illustrates the variation of net exit momentum as a function of mean stress and for a range of frequencies. More commonly mean stress is expressed by the R parameter, which is defined as $K_{\min}/K_{\max}$. In terms of the present approach, R should be the same as $\alpha_0 - \beta/\alpha_0 + \beta$ for cases where $\alpha_0 > \beta$. Table 1 lists corresponding values for R and α_0/β, thus permiting the two to be correlated. Apparent from Fig. 6 is that solution exit momentum increases modestly with decreasing α_0/β for $\alpha_0/\beta \gtrsim 2$. If, however, the stress or stress intensity function is such that the crack is closed during a portion of each cycle, that is, if $\alpha_0/\beta \leq 1$, then Eq 9 indicates solution momentum

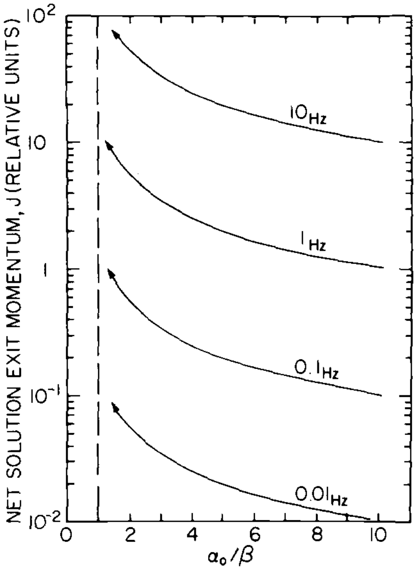

FIG. 6—*Net solution exit momentum as a function of mean stress, α_0/β, and for a range of frequencies.*

TABLE 1—*Relative comparison of* R *and α_0/β values for expressing mean stress condition.*

Stress State	R	α_0/β
Static tension	+1	$+\infty$
$K_{min} = 0$	0	+1
Fully reversed loading	−1	0

to be unbounded. This is consistent also with Eq 6 which shows solution velocity to become infinite as the crack closes. Of course, in the actual physical situation, momentum and velocity must remain finite due to restraints imposed by the bulk solution into which the crack electrolyte exits. But, it probably is correct to state that these parameters (J and V) do achieve a large value as a crack closure situation is approached.

The influence of frequency upon momentum is illustrated in Fig. 7 for a range of α_0/β values. Thus, a linear or power law relationship exists between these two parameters, such that an order of magnitude decrease in frequency results in a corresponding reduction in momentum.

Mixing due to high crack solution momentum for cases where α_0 is near or less than β could be restricted by several factors in addition to the presence of the bulk solution. Precipitation of corrosion products within the crack is one such possibility. This would serve to prop open the crack during

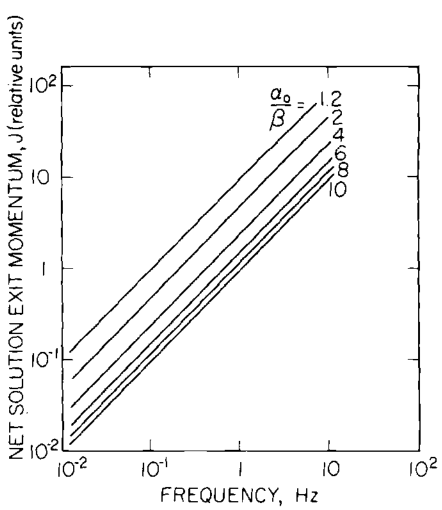

FIG. 7—*Net solution exit momentum as a function of frequency and for a range of mean stress,* α_0/β.

the period that it might normally be closed. Second, corrosion product precipitation just outside the crack could possibly contribute to solution momentum dissipation. Third, asparities (roughnesses) on the fracture faces also could serve to reduce momentum by propping open the crack. The latter should be most apparent when the fatigue fracture exhibits a ductile component and of minimum importance when the fracture involves cleavage.

As a further point, it may be reasoned that for $\alpha_0/\beta < 1$ mixing should become more pronounced as minimum stress becomes increasingly negative, irrespective of the solution momentum. This is due to the crack remaining closed when stress is negative and because there is a time lapse between completion of exhaustion and the beginning of ingestion.

Additional Considerations

Additional factors that are expected to influence modification of the crack electrolyte during fatigue include stress-wave form, temperature, specimen geometry, test method, bulk-solution flow conditions, and applied current density.

Stress-wave form should be important from the standpoint that it influences the rate of crack opening and closing. Thus, a square stress wave is expected to result in greater crack solution momentum and, hence, greater mixing than a sine pattern. While some investigations of the influence of stress wave upon corrosion-fatigue crack growth rate have been carried out [*11,12*], the significance of this parameter remains unclear; and even where a dependence of crack growth rate upon this factor has been noted, it is not obvious that crack solution modification was responsible.

The importance of temperature upon fatigue, of course, has been widely investigated. Significance of this variable with regard to crack chemistry modification is distinct from this, however, and may relate to influence of temperature upon either kinematic viscosity and Reynold's number (Eq 1) or diffusion or both. It is when momentum of the exiting crack solution is small, or when flow is viscous, that any contribution from diffusion should be most pronounced. Of course, diffusional interchange should increase exponentially with temperature. Also, the relative importance of diffusion as compared to convective mixing is expected to increase with decreasing frequency.

It may be reasoned that the amount of mixing that takes place on each cycle also could be influenced by relative velocity between the fatigue specimen and electrolyte. Thus, where such flow is sustained, a boundary layer develops, the thickness of which varies inversely with the relative velocity. For the case where velocity is small, the ejected crack solution may remain mostly within the boundary layer, as shown by Fig. 8(*a*). Alternately, when relative motion between the specimen and electrolyte is great, a significant percent of the crack solution may be displaced on each cycle to beyond the boundary layer and be swept away prior to reingestion (Fig. 8(*b*)).

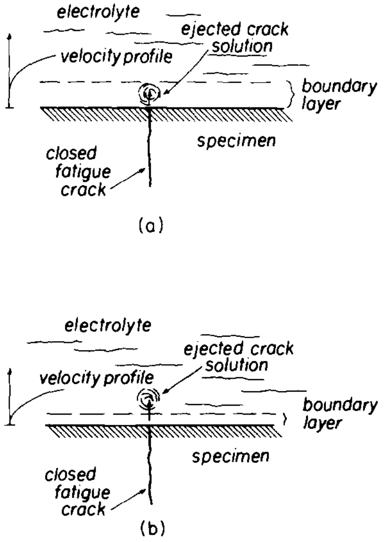

FIG. 8—*Schematic representation of the interaction between exhausted crack solution and the bulk solution for a case where* (a) *the crack solution remains within the bulk solution boundary layer and* (b) *the crack solution extends beyond the bulk solution boundary layer.*

A related possibility is that a relative velocity between the specimen and electrolyte can result from cyclic stressing alone. In this case the flow is probably still sustained, although velocity and direction may vary with time. For the cracked cantilever specimen in Fig. 9, specimen motion may be significant, and this by itself may promote mixing as the crack solution is ejected. Also, the magnitude of this mixing should be a function of position of the crack along the cantilever (distance *d* in Fig. 9), other factors being constant. Any influence of specimen type upon mixing should be less significant for a surface-flawed plate, center-cracked plate or single-edge notch specimen, since for these the fatigue motion or the crack region is generally small compared to the cantilever case.

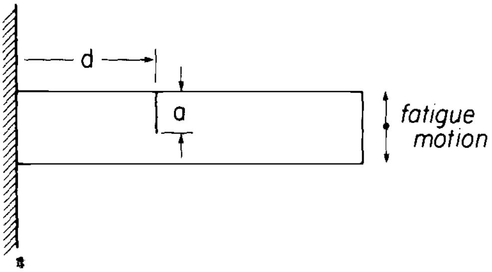

FIG. 9—*Cantilever specimen with fatigue crack.*

Current density associated with corrosion processes within a fatigue crack is yet another factor that should influence local solution-chemistry modification. For freely corroding conditions, it may be reasoned that crack solution modification is more likely to occur for a metal with high rate of corrosion within a fatigue crack than for a metal with low rate of attack assuming the extent of mixing is the same in the two cases. Thus, modification should prevail as long as reactions within the crack proceed more rapidly either than certain reaction products are dissipated or certain reactants replenished or both. Correspondingly, anodic polarization of an active metal in a neutral salt solution, as might result from galvanic coupling, could establish an acid corrosion-fatigue crack even though this same crack solution may not differ from the bulk when the metal is freely corroding. A similar situation should arise for cathodic polarization, except the crack solution pH would in this case be alkaline. It may be reasoned that under conditions of external polarization, crack-chemistry modification may occur, even when the extent of mixing on each cycle is extreme, provided the impressed current magnitude is sufficiently large.

Discussion

Table 2 presents a summary of those factors which are projected as potentially important with regard to crack solution-bulk solution mixing

TABLE 2—*Listing of fatigue variables and the projected influence of each upon crack electrolyte modification or mixing with the bulk solution.*

Fatigue Variable	Influence upon Modification or Mixing
Crack angle opening range, β	mixing is projected to increase linearly with increasing β(mean stress maintained constant)
Mean stress, α_0/β	mixing is projected to increase with decreasing α_0/β and become large when the stress function is such that the crack is closed during a portion of each cycle
Frequency	mixing is projected to increase linearly with increasing frequency
Crack length, a	mixing is projected to increase with the cube of crack length
Temperature	mixing is projected to increase with increasing temperature
Stress wave form	mixing is projected to increase the more rapid the crack opening and closing (constant frequency)
Specimen geometry and test method	fatigue test procedures which enhance relative motion between the crack and bulk electrolyte are projected to enhance mixing
Applied current density	modification of the crack electrolyte is projected to be more likely the greater the applied current density (either anodic or cathodic)

during corrosion fatigue. Here also the role of each factor upon occurrence of mixing is stated. It is not intended that the preceding evaluation of the mixing process be other than very general and simplified. On the other hand, it may be that the present rationale can serve as a starting point for subsequent, more sophisticated and quantitative descriptions. These considerations are, of course, of little value unless they relate to what takes place during an actual corrosion-fatigue process. Thus, experimental verification of the occurrence and significance of crack chemistry modification and the influence of this upon fatigue crack growth rate is particularly important. With exception of the isolated experiments and observations discussed earlier, little data are presently at hand upon which such a correlation can be based. Consequently, development of corrosion-fatigue experiments for the specific purpose of characterizing the various aspects of crack solution chemistry modification seem timely.

It was noted earlier in conjunction with Eq 9 that crack solution momentum and, hence, the tendency for this to mix with the bulk solution is influenced significantly by crack length. This point may be important with regard to the projected singular relationship between corrosion-fatigue crack growth rate and stress intensity range. This follows since the corrosion-fatigue crack environment when the crack is relatively short may be modified in comparison to the bulk; but as the crack extends, the chemistry of the crack solution may become comparable to the bulk. The established procedure of measuring crack length as a function of the number of cycles may amount then to determination of crack growth rate as a function of stress intensity with the local crack environment varying in different phases of the test. This suggests that researchers should specify the crack length corresponding to each crack growth rate data point. Even more appropriate is that different specimens be employed in such a manner that any effect of crack length upon $da/dn - \Delta K$ data can be realized. Resolution of the questions raised by this point should also be realizable by employing constant stress intensity specimens, since these would permit any dependence of crack growth rate upon crack length *per se* to be recognized.

As another point with regard to test procedures, it is noteworthy that numerous corrosion-fatigue crack growth rate determinations have been conducted for an R ratio of 0.1. It can be shown that the corresponding value for α_0/β is approximately 1.2. Interestingly, Fig. 6 suggests that it is in this range that crack solution momentum becomes sensitive to mean stress. Consequently, small variations in experimental techniques or in other influential parameters could result in pronounced differences in the extent of mixing for one test as compared to another.

Crooker [*13*] recently has pointed up the need for standardization of corrosion-fatigue test procedures. Crack solution modification is a factor that has not been considered yet within this context, however. The point has been made in the present paper that crack electrolyte chemistry may be different, not only for one type of specimen or test procedure compared to another, but also for different stages of the same test upon a single specimen. For this reason it is important that the crack solution electrolyte be characterized as a function of fatigue variables, since only after this is accomplished can it be said that standardization of corrosion-fatigue test techniques has been meaningfully accomplished.

Acknowledgments

The authors wish to express appreciation to the National Oceanographic and Atmospheric Administration Sea Grant Project Number 04-3-158-43 for financial support.

References

[*1*] Brown, B. F., *Corrosion*, Vol. 26, 1970, pp. 249-250.
[*2*] Devereaux, O. F., Dresty, J., and Kovacs, B., *Metallurgical Transactions*, Vol. 2, 1971, pp. 3225-3227.
[*3*] Stoltz, R. E. and Pelloux, R. M., *Corrosion*, Vol. 29, 1973, pp. 13-17.
[*4*] Barsom, J. M., *International Journal of Fracture Mechanics*, Vol. 7, 1971, pp. 163-182.
[*5*] Meyn, D. A., *Metallurgical Transactions*, Vol. 2, 1971, pp. 853-865.
[*6*] Peterson, M. H. and Lennox, T. J., *Corrosion*, Vol. 29, 1973, pp. 406-410.
[*7*] Pourbaix, M., *Corrosion*, Vol. 26, 1970, pp. 431-438.

[*8*] Brown, B. F., "The Role of the Occluded Cell in Stress Corrosion Cracking of High Strength Steels," *Rapports Techniques CEBELCOR,* Vol. 112, RT. 170, 1970.

[*9*] Hartt, W. H., Hooper, W. C., and Henke, T. "Fatigue of Notched 1018 Steel in Sea Water," presented at Fourth International Congress on Marine Corrosion and Fouling, 14-19 June 1976, Antibes, France, to be published in conference proceedings.

[*10*] Tuck, E. O., *Journal of Fluid Mechanics,* Vol. 41, 1970, pp. 641-652.

[*11*] Barsom, J. M., *Corrosion Fatigue-Chemistry, Mechanics and Microstructure,* National Association Corrosion Engineers, 1972, pp. 424-433.

[*12*] Selines, R. J. and Pelloux, R. M., *Metallurgical Transactions,* Vol. 3, 1972, pp. 2523-2531.

[*13*] Crooker, T. W., *ASTM Standardization News,* Vol. 3, 1975, pp. 17-19 and 43-44.

C. E. Jaske,[1] *D. Broek,*[1] *J. E. Slater,*[1] *and W. E. Anderson*[2]

Corrosion Fatigue of Structural Steels in Seawater and for Offshore Applications

REFERENCE: Jaske, C. E., Broek, D., Slater, J. E., and Anderson, W. E., "**Corrosion Fatigue of Structural Steels in Seawater and for Offshore Applications,**" *Corrosion-Fatigue Technology, ASTM STP 642,* H. L. Craig, Jr., T. W. Crooker, and D. W. Hoeppner, Eds., American Society for Testing and Materials, 1978, pp. 19-47.

ABSTRACT: The design of fixed platform structures for deeper water and more hostile environments places increased emphasis on the consideration of long-life ($> 10^6$ cycles) corrosion-fatigue behavior of low- and medium-strength structural steels in seawater. An interpretive review of available information on this technical area has been conducted, with separate consideration given to both fatigue-crack initiation and propagation. Emphasis is placed upon weldments because welded tubular joints are the areas of main concern in the fatigue evaluation of conventional offshore platform-type structures. Effects of strain range or range of stress intensity, stress ratio, cycling frequency, and type of loading spectrum are addressed. Also, environmental effects of oxygen level, temperature, pH, cathodic polarization, and high hydrostatic pressure are covered. The merits of cathodic protection in mitigating corrosion-fatigue damage are discussed in detail. Finally, results of this review are used to develop recommendations of the variables to be included in future experimental studies of long-life corrosion-fatigue resistance of such steels in seawater.

KEY WORDS: corrosion fatigue, offshore structures, carbon steels, welded joints, cathodic protection, seawater, crack initiation, crack propagation

The continually increasing demand for petroleum has provided the impetus for seeking and discovering oil in deeper waters and in more hostile environments. It is planned to use fixed offshore structures in such situations. As pointed up by Marshall [*1*][3], long-life fatigue ($> 10^6$ cycles to failure) becomes an increasingly important consideration in the design

---

[1] Senior researcher, research leader, and associate section manager, respectively, Battelle Columbus Laboratories, Columbus, Ohio 43201.

[2] Staff engineer, Battelle Pacific Northwest Laboratories, Richland, Wash. 99352.

[3] The italic numbers in brackets refer to the list of references appended to this paper.

of fixed platforms for these applications because anticipated applied stress histories will have a large number of low-stress level cyclic excursions. Furthermore, the critical areas in the fatigue performance of these structures are the welded-steel tubular joints, which usually are submerged fully in seawater and protected cathodically.

The purpose of this paper is to review the available corrosion-fatigue information on low- and medium-strength structural steels in aqueous seawater and saltwater environments. Salt-air and air-water types of environmental conditions are outside of the scope of this study. Particular emphasis is placed upon (*a*) the low-stress, long-life regime, (*b*) welded steel, and (*c*) cathodic protection. In terms of cyclic fatigue life, N_f, and cyclic crack-growth rate, da/dN, long-life behavior refers to the following regimes

$$N_f > 10^6 \text{ cycles}$$

$$da/dN < 2.54 \times 10^{-8} \text{ m/cycle } (10^{-6} \text{ in./cycle})$$

From the viewpoint of engineering analyses, the fatigue-damage process in metals consists both of fatigue-crack initiation and fatigue-crack propagation. In some instances, one of these components may be much more important than the other, but, in general, they are both of importance. Therefore, both of these aspects of fatigue damage are addressed in this paper. For convenience, each one is discussed separately because most of the available data are reported either in terms of cyclic life or in terms of crack-growth rate.

At long lives, the total number of cycles to failure reported for most small laboratory specimens is predominantly made up of crack initiation. In this context, initiation of a significant size crack is considered to take place when a noticeable (2 to 10 percent) change in specimen load-carrying capacity or specimen compliance occurs. This qualitative definition of crack initiation was kept in mind while reviewing available corrosion-fatigue data and, on this basis, fatigue lives reported in terms of total number of cycles to failure were believed to reflect adequately fatigue-crack-initiation behavior.

On the other hand, crack-propagation data normally are developed using precracked specimens and analyzed using the concepts of fracture mechanics.

Review of Fatigue-Crack-Initiation Resistance

Laird and Duquette [2] reviewed the existing hypotheses of corrosion mechanisms proposed to explain the initial cracking of a metal undergoing corrosion fatigue in an aqueous medium, which can include, but of course is not restricted to, seawater. They classified these possibilities as those involving pitting, preferential anodic dissolution, passive film rupture, and surface adsorption. They found that each had some merit, but not one could explain all of the phenomena included as corrosion-fatigue failures. Thus, a more general, revised hypothesis reflects the combined attack of the environment and cyclic stress and recognizes that the mechanism of crack initiation may be slightly different for different metals and environments.

More germane to the purposes of this review, there are examples in the literature of the role that certain corrosion variables play in the corrosion fatigue of mild steel in saline solutions and seawater. Duquette [*3*] has reviewed many of the data on corrosion fatigue in aqueous media, including seawater and saline solutions. Data included in that review are not discussed here unless they have a direct bearing on the present work.

Available corrosion-fatigue crack-initiation data on mild steels have been developed using constant-amplitude cycling of two types of specimens: (*a*) smooth, unnotched specimens and (*b*) specimens with geometrical discontinuities at either notches or welds. As reported by Marshall [*1,4*], the only fatigue data on actual tubular joints in seawater were those developed by Bouwkamp, at the University of California in 1966, for constant-amplitude loading at lives less than 10^4 cycles to failure. All of the other available data on corrosion fatigue of steel in seawater or saltwater were generated using simply loaded (either axial, cantilever bending, or rotating bending) specimens. The available data [*5-23*] on long-life corrosion fatigue of low and medium strength structural steels are summarized in Table 1. They are discussd in the following paragraphs, which are divided into discussions of corrosion-fatigue crack-initiation behavior for three different types of specimens: (*a*) unnotched (smooth), (*b*) notched, and (*c*) welded.

Crack Initiation in Unnotched Specimens

Data for smooth, unnotched specimens are included in Refs *5* through *15*. All but one of these studies used either saltwater or synthetic seawater solutions. Only the work of Kirk et al [*10*] was conducted in actual seawater, and it indicated an alarmingly low fatigue strength range of only 13.8 MN/m^2 (2 ksi) at 10^8 cycles to failure. In all cases, a continuous decrease in fatigue strength as cyclic life increased (approximately linear on a log-log plot) was observed for unprotected steel. In other words, the knee or fatigue limit usually observed for constant-amplitude cycling of steels in air was not present. This was even true for experiments at an extremely high frequency of 20 kHz, where total test times were less than 14 h for 10^9 cycles [*11,12*].

TABLE 1—*Summary of long-life corrosion-fatigue crack-initiation data on low-*

Type of Steel	Heat Treatment	Tensile Strength, MN/m^2 (ksi)		Type of Specimen
		Ultimate	Yield	
SAE 1020 bar	hot rolled	496 (72)	317 (46)	smooth and notched
ASTM A 245 (0.13C)	hot rolled	... ...	... ...	smooth
0.17C wire	drawn	731 (106)	... ...	smooth
SAE 1015 rod (0.18C)	stress relieved	524 (76)	462 (67)	smooth
SAE 1015 rod (0.18C)	stress relieved	524 (76)	462 (67)	smooth
Mild steel	...	... ...	... ...	smooth
SAE 1020 bar	cold rolled	... ...	... ...	smooth
SAE 1020 bar,	cold rolled	648 (94)	... ...	smooth
ASTM A 537 A	...	552 (80)	... ...	smooth
0.35C	...	607 (88)	324 (47)	smooth and notched
0.44C	normalized	655 (95)	352 (51)	smooth
SAE 1036 rod	normalized	689 (100)	469 (68)	smooth
SAE 1020 bar	cold rolled	... ...	... ...	notched

and medium-strength structural steels in seawater and saltwater.

Type of Loading[a]	Cyclic Frequency, Hz	Type of Environment	Type of Data[b] Developed	Reference
uniaxial, $R = 0$	12.5	air-saturated synthetic seawater with and without cathodic protection	*S-N* curves from 4×10^5 to 5×10^7 cycles	Hudgins et al [*5*]
reversed cantilever bending	29.2	unprotected and protected in synthetic seawater	*S-N* curves from 10^5 to 4×10^7 cycles	Nichols [*6*]
Hiagh-Robertson test machine	...	unprotected in synthetic seawater	*S-N* curves from 5×10^5 to 5×10^7 cycles	Gould [*7*]
reversed bending	30	air-saturated and deaerated 3% NaCl solution at 25 °C	*S-N* curves between 10^5 and 10^7 cycles	Duquette and Uhlig [*8*]
reversed bending	30	anodic currents in deaerated 3% NaCl and pH in air-saturated 3% NaCl at 25 °C	life versus current density and versus pH at 2 stress levels	Duquette and Uhlig [*9*]
rotating cantilever beam	46.7	unprotected in seawater	*S-N* curves from 5×10^6 to 10^8 cycles	Kirk et al [*10*]
reversed axial	20 000	3% NaCl at atmospheric pressure and 6.89 MN/m^2 (1000 psig)	*S-N* curves from 10^6 to 10^8 cycles	Thiruvengadem [*11*]
reversed axial	20 000	3% NaCl at atmospheric and at 13.8 MN/m^2 (2000 psig)	*S-N* curves from 5×10^6 to 10^8 cycles	Jolliff and Thiruvengadem [*12*]
reversed bending	...	unprotected and cathodically protected in synthetic seawater	*S-N* curves between 10^5 and 10^8 cycles	Lyashchenko [*13*]
plane bending	42.5 and 4.08	unprotected in 1% NaCl solution	*S-N* curves from 5×10^5 to 10^7 cycles	Endo and Miyao [*14*]
rotating bending	33.3	3% NaCl solution at room temperature	*S-N* curves from 3×10^5 to 3×10^6 cycles	Radd et al [*15*]
reversed axial	14 200	3% NaCl at 24 °C	*S-N* curve from 10^5 to 10^9 cycles	Thiruvengadem [*16*]

TABLE 1—*Summary of long-life corrosion-fatigue crack-initiation data on low-*

Type of Steel	Heat Treatment	Tensile Strength, MN/m^2 (ksi)		Type of Specimen
		Ultimate	Yield	
SAE 1018 bar	...	... ...	... ...	notched
0.22C	normalized	496 (72)	... ...	notched
0.15C, 0.35C	normalized normalized	434 (63) 572 (83)	193 (28) 345 (50)	notched
ASTM A 441[c]	normalized	524 (76)	345 (50)	notched and as-welded notched
ASTM A 441	normalized	524 (76)	345 (50)	as-welded
ASTM A 537 B	quenched and tempered	... ...	... ...	as-welded
Mild steel	cold rolled	600 (87)	... ...	as-welded
Carbon steel	...	569 (82)	274 (40)	as-welded

[a] *R* indicates stress ratio or ratio of minimum to maximum stress.

[b] *S-N* indicates stress versus number of cycles to failure.

[c] ASTM Specification for High-Strength Low-Alloy Structural Manganese Vanadium Steel.

The effects of cathodic protection in synthetic seawater are covered in three studies [*5,6,13*]. A cathodic protection level of -0.75 V (Ag/AgCl)[4] was found to restore the in-air fatigue resistance of SAE 1020 steel [*5*]. Nichols [*6*] (see Fig. 1)[5] found that a current density of 2150 mA/m^2 (200 mA/ft^2) improved the fatigue resistance of steel produced according to ASTM Specification for Flat-Rolled Carbon Steel Sheets of Structural

---

[4] Term in parenthesis indicates the type of reference electrode: Ag/AgCl = silver/silver chloride, SCE = saturated calomel, and Cu/CuSO$_4$ = copper/copper sulfate.

[5] Design fatigue curves for as-welded steel are shown for comparison purposes in Fig. 1. It should be kept in mind that these are lower bounds to actual data and are intended to include the type of notch effects present in typical weld profiles.

and medium-strength structural steels in seawater and saltwater. —Continued

Type of Loading[a]	Cyclic Frequency, Hz	Type of Environment	Type of Data[b] Developed	Reference
reversed bending	30.8	cathodically protected in seawater	S-N curve from 2×10^6 to 3×10^7 cycles	Hartt et al [*17*]
rotating bending	25	brine drip at 13 and 33°C	S-N curves from 10^5 to 10^8 cycles	Dugdale [*18*]
rotating bending	36.7	1% NaCl at 25°C	S-N curves from 5×10^5 to 10^7 cycles	Endo et al [*19*]
cantilever bending at $R = -0.33$	0.1 and 0.2	unprotected in air and seawater and cathodically protected in seawater	S-N curves from 10^3 to 5×10^8 cycles	Kochera et al [*20*]
cantilever bending at $R = -0.33$	33.3	cathodically protected in seawater	2 data points near 10^9 cycles	Kochera et al [*20*]
axial at $R = 0$, $R = 0.5$	3.67	unprotected in synthetic seawater	S-N curves from 2×10^5 to 2×10^6 cycles	Havens and Bench [*21*]
axial at $R = 0.33$	0.17 and 8.0	unprotected in 3% NaCl drip	S-N curves from 2×10^4 to 10^7 cycles	Marsh et al [*22*]
reversed bending	...	unprotected in air and seawater and cathodically protected in seawater	S-N curves from 10^6 to 10^7 cycles	Walter et al [*23*]

Quality (A 245)[6] in synthetic seawater to levels similar to those observed in air, whereas, a current density of 215 mA/m^2 (20 mA/ft^2) was of little benefit and a current density of 590 mA/m^2 (55 mA/ft^2) was of some benefit. Furthermore, he found that the formation of a calcareous scale consisting of calcium carbonate ($CaCO_3$) and magnesium hydroxide ($Mg(OH)_2$) was an important factor in mitigating corrosion-fatigue damage. A zinc protector of −1.0 V (SCE) was found to restore the in-air fatigue resistance of a 0.35C steel [*13*]. Therefore, it is evident that cathodic protection will significantly improve fatigue-crack initiation resistance of carbon steel in seawater-type solutions.

---

[6] ASTM Specification A 245 has been replaced by ASTM Specification for Hot-Rolled Carbon Steel Sheet and Strip, Structural Quality (A 570) and ASTM Specification for Steel, Cold-Rolled Sheet, Carbon, Structural (A 611).

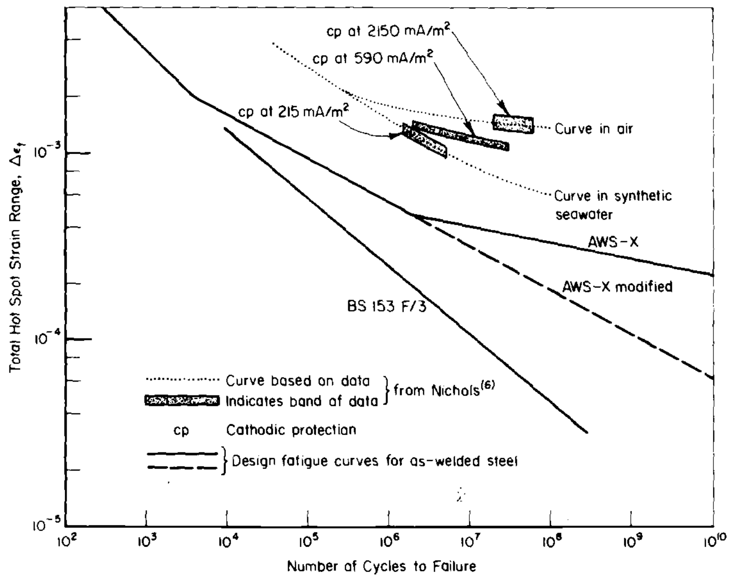

FIG. 1—*Effect of cathodic protection on the reversed bending fatigue behavior of unnotched specimens of ASTM Specification A 245 steel.*

It has been shown that dissolved oxygen plays an important role in the degrading influence of saltwater solutions on the corrosion-fatigue resistance of mild steel [*8*]. The fatigue resistance continually decreased at longer lives for aerated 3 percent sodium chloride (NaCl) solution, but an apparent fatigue limit about the same magnitude as that in air was observed in deaerated 3 percent NaCl solution. The corrosion rate in the deaerated solution was 25.4 μm (0.001 in.) per year, while in the aerated solution, it was 2.54 mm (0.10 in.) per year. These findings indicate that the oxygen content, in a manner similar to its influence on the rate of corrosion, may enhance the initiation of corrosion-fatigue damage.

It also has been shown that high hydrostatic pressures of 6.89 and 13.8 MN/m^2 (1000 and 2000 psig) will reduce the fatigue resistance of SAE 1020 steel in 3 percent NaCl solution at a cyclic frequency of 20 kHz [*11,12*]. Comparable work was not carried out, however, at lower frequencies (for example, less than 50 Hz), where decreasing frequencies would be expected to decrease further cyclic fatigue life. Endo and Miyao [*14*] showed that decreasing from 42.5 to 4.08 Hz for corrosion fatigue in saline solution decreased the cyclic life by a factor of about 2.5 in the range of 10^6 to 10^7 cycles to failure. This frequency effect is felt to be related to the time dependence of corrosion. Failure occurs with fewer total cycles at the lower frequencies, but in about the same or slightly longer times. Any corrosion variable that increases the oxygen content, raises the overall corrosion rate, attacks or disrupts calcareous deposits or corrosion products, or generates a local attack may degrade corrosion-fatigue resistance significantly.

Two studies [*9,15*] have shown the effect of varying pH on corrosion fatigue in saline solutions. Over a broad range of pH, from about 4 to 10, there is little or no effect on fatigue resistance. Very low pH values (less than 4) caused fatigue life to decrease, and very high ones (greater than 10 to 11) gave improved fatigue resistance approaching that expected in air.

Gould [*7*] found that increases in temperature over the range of 15 to 45°C caused small, but corresponding, decreases in fatigue life for tests in artificial seawater. However, no data were developed at low temperatures in the range of 4°C or less that would be representative of cold seawater.

Crack Initiation in Notched Specimens

Relevant corrosion-fatigue data on notched specimens are included in Refs *5, 13,* and *16* through *20.* Cathodic protection was a variable in four of these studies [*5,13,17,20*]. Hudgins et al [*5*] found that cathodic protection restored the in-air, notched-specimen fatigue resistance. Kochera et al [*20*] reported approximately a factor of 3 improvement in cyclic fatigue life (compared to unprotected specimens) for cathodically protected specimens at intermediate fatigue lives (near 10^5 cycles to failure). These lives approached those found for specimens tested in air. Both Lyashchenko et al [*13*] and Hartt et al [*17*] found that cathodic protection could increase the notched-specimen fatigue resistance to levels above those of comparable specimens tested in air. However, only the limited data reported by Kochera et al [*20*] are at low frequencies (0.1 to 0.2 Hz) in the range of those normally anticipated for cyclic loading of offshore structures.

Just as for smooth specimens, Thiruvengadem [*16*] showed that corrosion-fatigue resistance of notched specimens was degraded severely by a 3 percent NaCl solution even at the high cyclic frequency of 14.2 kHz. Dugdale [*18*] showed that increasing the solution temperature from 13 to 33°C reduced the corrosion-fatigue resistance in a brine drip. Just as in the earlier cited study of Gould [*7*], low temperatures (~ 4°C) were not investigated. Endo et al [*19*] have suggested an approach for estimating the combined corrosion resistance and notch sensitivity of steels in a 1 percent saline solution.

One important observation that can be made from examining the results of the unprotected notched-specimen, corrosion-fatigue behavior in saline solutions compared to that in air is that the effects of geometrical stress concentration and corrosion are additive, that is, the corrosive medium will further reduce notched-specimen cyclic life below that observed in air. Thus, corrosion does not simply produce a sharp notch that acts as a stress concentrator, instead, it adds to the detrimental effect of the geometric stress concentration on fatigue life. Both Dugdale [*18*] and Hartt et al [*17*] have noted that one contributing factor to the lowered notched-specimen fatigue strength of mild steel in corrosive media is that non-propagating cracks no longer persist at low stresses (below the apparent fatigue limit in air) as they do in air. Thus, the corrosive attack is thought to keep tiny cracks growing to result in eventual specimen failure, whereas, in air, these cracks normally will stop from propagating in sharply notched mild-steel specimens.

Crack Initiation in Welded Specimens

Only a sparse amount of corrosion-fatigue data is available for welded specimens in seawater-type environments [*20-23*]. These are compared with selected existing design fatigue curves [*24,25*] in Fig. 2. The basis for the American Welding Society (AWS) criteria and their application to the design of tubular joints have been reviewed elsewhere [*4,26*] and the fatigue-design rules used in Great Britain have been described previously [*27,28*]. The AWS-*X* curve was modified to take into account possible long-life corrosion-fatigue effects and the proposed new British Standards

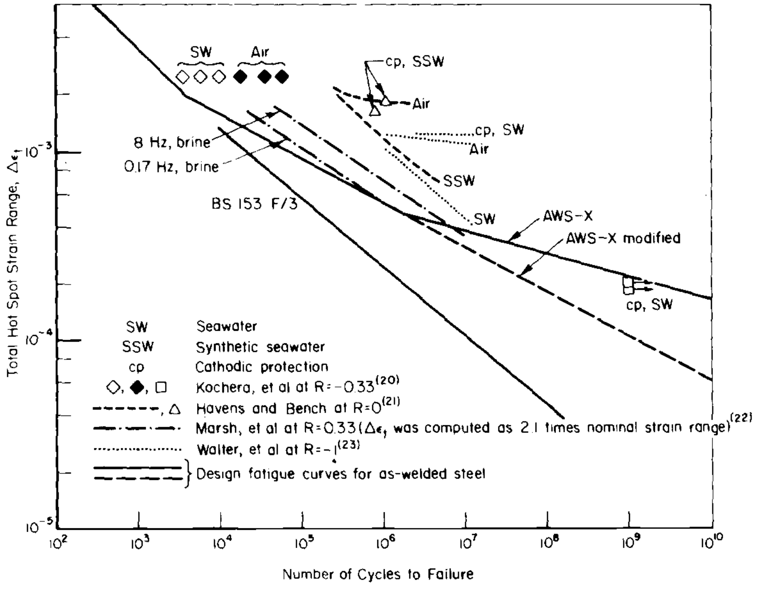

FIG. 2—*Effect of seawater environment of corrosion-fatigue resistance of as-welded carbon steel.*

Institution (BS) 153 F curve was modified by a factor of 3 for use in offshore applications. At less than 10^7 cycles to failure, both the AWS curves and the BS 153 F/3 curve conservatively bound the data, and cathodic protection restored fatigue strength to levels observed in air. The two data points *[20]* near 10^9 cycles to failure indicate that the AWS-*X*-modified curve is conservative and that the BS 153 F/3 curve is extremely conservative when adequate cathodic protection is present. Linear extrapolation (on the log-log plot of Fig. 2) shows that the corrosion-fatigue behavior in freely corroding seawater may fall slightly below the AWS-*X*-modified curve near 10^9 to 10^{10} cycles to failures, whereas the BS 153 F/3 curve would still be very conservative. However, this type of extrapolation may overestimate the degrading effect of seawater at low strain ranges. Thus, corrosion-fatigue data are needed in the region of 10^7 to 10^9 cycles to failure in order to help answer questions as to how much conservatism is included in existing design fatigue curves.

The two data points reported by Kochera et al *[20]* were for specimens that had been cycled 10^9 times without failure. They did have cracks, however, about 0.76 cm (0.30 in.) long by 0.13 cm (0.05 in.) deep. Whether these cracks would have propagated to failure eventually or not is difficult to say. Under deformation controlled cyclic bending, they may have grown enough to lower the stress intensity and consequently cause the crack to cease growing. Thus, their actual fatigue resistance is difficult to assess. Futhermore, no variations in the level of cathodic protection were investigated. Without substantion through additional experimental work, these results are of only limited value.

The work of Havens and Bench *[21]* was conducted at lives less than 2 × 10^6 cycles to failure using unprotected specimens in synthetic seawater. They also conducted comparable experiments on unwelded plates in synthetic seawater that showed about 30 percent greater fatigue strength (at 2 × 10^6 cycles) than the as-welded plates. It also was indicated on the basis of only two tests that cathodic protection improved the corrosion-fatigue resistance of these unwelded plates.

Recently, Walter et al *[23]* have reported results of work on fatigue of welded joints in the region of 10^6 to 10^7 cycles to failure. Compared to air, freely corroding seawater caused a 60 percent reduction in fatigue strength at 10^7 cycles to failure, but the results still fell above the AWS-*X*-modified fatigue curve. However, extrapolation of these seawater results to longer lives indicates that they may fall below the AWS-*X*-modified fatigue curve at 10^9 to 10^{10} cycles to failure. Cathodic protection was found to restore the fatigue resistance to the level observed for the tests conducted in air.

The data of Marsh et al *[22]*[7] were for a very severe splash zone type of

---

[7] As plotted in Fig. 2, the nominal strain values have been multiplied by a factor of 2.1 to account for eccentricity in the lap-welded specimen, giving hot-spot values comparable to other data in Fig. 2.

environment (brine drip with surface drying between each drip), and as would be expected, also showed possibly low long-life fatigue resistance when extrapolated to fatigue lives near 10^9 to 10^{10} cycles. The reduction of cyclic loading frequency from 8.0 to 0.17 Hz caused about a 2.3 factor of reduction in cyclic fatigue life (near 10^8 cycles at 8 Hz). This information provides an assessment of possible worst-case, corrosion-fatigue effects in the splash zone area.

Fatigue-Crack-Propagation Resistance

Fatigue-crack-growth analysis is based largely on the stress-intensity factor, *K*, although some other concepts may prove useful for certain applications. Fatigue-crack-growth behavior usually can be described by the following type of function

$$da/dN = f(\Delta K, R)$$

where ΔK is the range of the stress-intensity factor, and R is the ratio of minimum to maximum stress. Many equations [*29-35*] have been proposed for this relation. None of them is generally applicable, but some are useful for limited application. If the low and high ΔK regions are excluded, the equation

$$\frac{da}{dN} = C(\Delta K)^n, \text{ for constant } R$$

is a reasonable approximation, where C and n are constants (n is usually on the order of 2 to 4).

A vast amount of data has been reported [for example, Refs *20, 36-57*] showing the effect of environment on crack-growth behavior of metals. Much of this information concerns aluminum alloys, titanium alloys, and high-strength steels. Some data have been reported on low- and medium-strength structural steels in saltwater and seawater [*20, 50-57*] as summarized in Table 2 and Fig. 3. For comparison, the band of data for structural steels in air reported by Barsom [*58*] is also shown in Fig. 3.

As illustrated in Fig. 3, the effect of the environment depends upon the magnitude of ΔK. For $R \leq 0.2$, the data of both Bristoll and Opdam [*50*] and Vosikovsky [*55*] indicate a maximum detrimental influence of environment at intermediate levels of ΔK. At high ΔK levels [near 60 to 80 $\text{MN/m}^{3/2}$ (54.6 to 72.8 $\text{ksi}\cdot\text{in.}^{1/2}$)] and at low ΔK levels [less than 10 $\text{MN/m}^{3/2}$ (9.10 $\text{ksi}\cdot\text{in.}^{1/2}$)], the crack-growth-rate curves approach those observed for cycling in air. In fact, Vosikovsky's data [*55*] indicate a slightly elevated threshold level for cathodic-potential conditions, compared to in-air conditions. However, the data of Haagensen [57], which were at a high stress ratio (estimated to be greater than 0.8, based on reported mean stress and crack lengths), show a reduction of the threshold level in seawater environments. This mean-stress or stress-ratio effect is important to keep in mind for welded hardware where residual stress fields may cause the actual stress intensity to be at such high levels. For crack-growth rates between 2×10^{-9} and 10^{-8} m/cycle (7.9×10^{-8} and 3.9×10^{-7} in./cycle), Haagensen [57] also showed that crack-growth rates on specimens in seawater and subjected to narrow-band random loading were close to the constant-amplitude curve in seawater (see Fig. 3) when compared on the basis of the root-mean-square value of ΔK, ΔK_{rms}. This trend is similar to that reported for fatigue-crack growth in air [59-61].

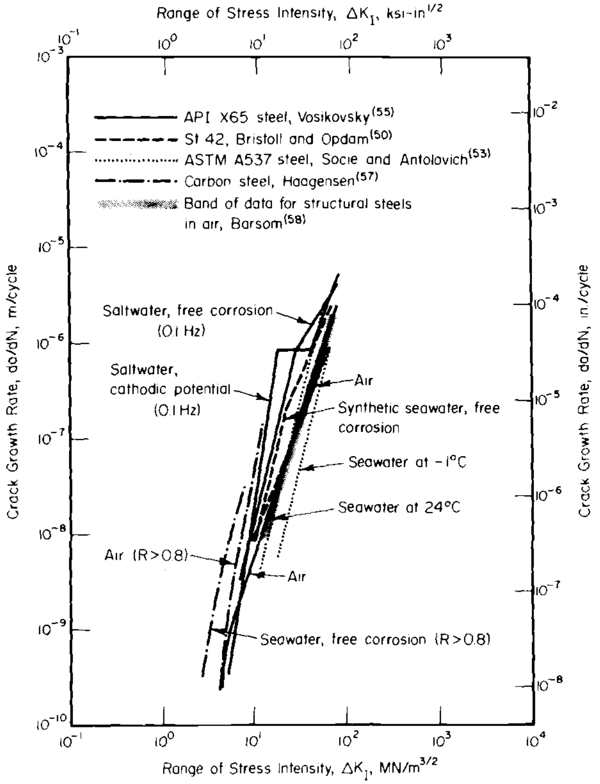

FIG. 3—*Corrosion-fatigue-crack-propagation behavior of low- and medium-strength structural steels in seawater and saltwater.*

The effect of cycling frequency is associated with the environmental effects. At high frequencies, there is less time for environmental action, which means that the crack-growth rate per cycle approaches that found

TABLE 2—*Summary of corrosion-fatigue-crack-growth on low-*

		Tensile Strength, MN/m^2 (ksi)		
Type of Steel	Heat Treatment	Ultimate	Yield	Type of Specimen
St 42	...	...	...	base metal
Mild steel	...	...	...	base metal
ASTM A 387 B[a]	normalized	469 (68)	331 (48)	plate bending, base metal
and A 302 B	normalized	552 (80)	400 (58)	
ASTM A 517 F[b]	quenched and tempered	814 (118)	738 (107)	plate bending, base metal
ASTM A 537	quenched and tempered	565 (82)	427 (62)	single-edge notch, base metal, and weld metal
Mild steel (0.15C)	...	...	...	single-edge notch, base metal
API X65	...	570 (83)	458 (66)	single-edge notch, base metal

and medium-strength structural steels in seawater and saltwater.

Type of Loading	Cyclic Frequency, Hz	Type of Environment	Type of Data Developed	Reference
...	...	air and synthetic seawater	ΔK-da/dN between 1.27×10^{-7} and 2.54×10^{-6} m/cycle (5×10^{-6} and 10^{-4} in./cycle	Bristoll and Opdam [50]
$R = 0.64$ and -1.0	...	brine	ΔK-da/dN at 2.54×10^{-8} m/cycle (10^{-6} in./cycle)	Greenan (NEL) as reported by Pook [51]
cantilever bending, $R = -1.0$	0.08	3½% NaCl solution	strain range—da/dN between 7.62×10^{-8} and 1.02×10^{-5} m/cycle (3×10^{-6} and 4×10^{-4} in./cycle)	Crooker and Lange [52]
cantilever bending, $R = -1.0$	0.08	3½% NaCl solution	strain range—da/dN between 2.54×10^{-7} and 1.02×10^{-5} m/cycle (10^{-5} and 4×10^{-4} in./cycle)	Crooker and Lange [52]
axial	...	3½% NaCl at -1 and 24°C	ΔK-da/dN between 7.62×10^{-9} and 2.54×10^{-8} m/cycle (3×10^{-7} and 10^{-4} in./cycle)	Socie and Antolovich [53]
axial	0.23	3½% NaCl at 30 to 85°C	crack growth at one gross stress level	Telegren and Doruk [54]
axial, $R = 0.2$	15, 10, 1, 0.1, and 0.01	air, 3½% NaCl solution, and distilled water	ΔK-da/dN between 2.54×10^{-10} and 7.62×10^{-6} m/cycle (10^{-8} and 3×10^{-4} in./cycle)	Vosikovsky [55]

TABLE 2—*Summary of corrosion-fatigue-crack-growth on low-*

Type of Steel	Heat Treatment	Tensile Strength, MN/m^2 (ksi) Ultimate	Tensile Strength, MN/m^2 (ksi) Yield	Type of Specimen
ASTM A 441	normalized	524 (76)	345 (50)	plate bending, base metal, and weldment
Mild steel	. . .	430 (62)	315 (46)	double-edge notched plate, base metal
Carbon steel	. . .	444 (64)	586 (85)	single-edge notch, base metal

---

[a] ASTM Specification for Pressure Vessel Plates, Alloy Steel, Chromium-Molybdenum.

[b] ASTM Specification for Pressure Vessel Plates, Alloy Steel, High-Strength, Quenched and Tempered.

[c] Narrow-band random loading as well as constant-amplitude loading.

in dry air. For example, results for a steel base-metal produced according to ASTM Specification for Pressure Vessel Plates, Heat Treated Carbon-Manganese-Silicon (A 537) and a weld metal showed little difference in growth rates between air and 3.5 percent NaCl solution at 24°C [*53*]. Vosikovsky [55] investigated frequencies from 0.01 to 10 Hz; the data for 0.1 Hz are shown in Fig. 3 because this is about the slowest wave-loading frequency anticipated in offshore service. As illustrated in Fig. 4, he found that decreasing the frequency caused a critical crack-growth rate, da/dN_{CR}, to increase. Below this critical level, the ΔK-da/dN curve was the same for all frequencies, and above this level, the ΔK-da/dN curves tended to approach asymptotically the in-air behavior at crack-growth rates near 10^{-5} m/cycle (3.9×10^{-4} in./cycles). An extremely important point to keep in mind is that data developed for high ΔK levels above da/dN_{CR} cannot be reasonably extrapolated to low ΔK levels when such environmental effects are present. If the upper portions of the dotted or dashed curves in Fig. 4 were extrapolated downward, very conservative and unrealistic estimates of actual behavior would be made.

There is no concurrence of opinion as to the cause of the frequency effect. Formation and diffusion of hydrogen ions usually is considered to be *and medium-strength structural steels in seawater and saltwater.*—Continued

Type of Loading	Cyclic Frequency, Hz	Type of Environment	Type of Data Developed	Reference
cantilever bending, $R = -0.33$	0.1 and 0.2	air and seawater both with and without cathodic protection	strain range—*da/dN* between 2.54×10^{-8} and 2.54×10^{-5} m/cycle (10^{-6} and 10^{-3} in./cycle)	Kochera et al [*20*]
axial, $R = 0.6$ and -1.0	. . .	air and 3% NaCl solution with and without cathodic protion	Δ*K*-*N* between 10^6 and 10^9 cycles	Pook and Greenan [*56*]
axial, $R > 0.8$, mean stress = 240 MN/m^2 (34.8 ksi)	6.5 and 20 Hz^c	air and aerated natural seawater	Δ*K*-*da/dN* between 3×10^{-10} and 4×10^{-8} m/cycle (1.2×10^{-8} and 1.6×10^{-6} in./cycle)	Haagensen [*57*]

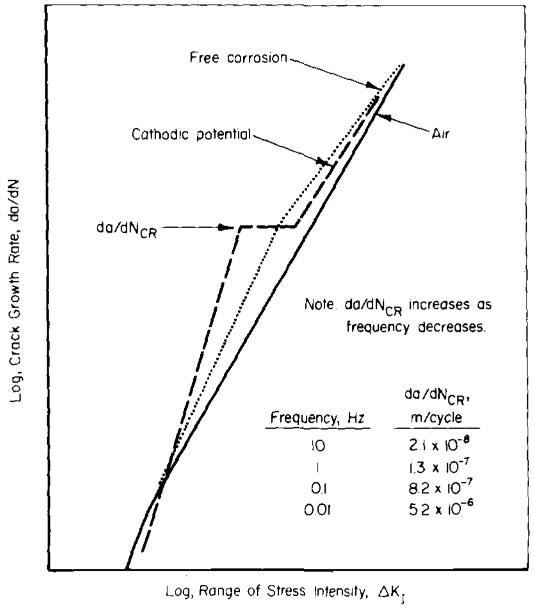

FIG. 4—*Schematic illustration of effect of cyclic frequency on corrosion-fatigue crack-propagation behavior in saltwater based on data of Vosikovsky* [55].

the primary cause. The different properties of the oxide layer formed in aqueous environments sometimes is considered to be of importance. For example, if the oxide layer on the newly formed fracture surface has a lower stiffness, it would give less support to further tearing.

Just as cited earlier for crack initiation, the environmental effect is less at lower temperatures [*53,54*]. In the case of humid air, there are two reasons for the decreased growth rates: (*a*) colder air can contain less water vapor and (*b*) the reaction kinetics are slower at lower temperatures. The latter still holds in aqueous environments as was found for mild steel [*54*] at temperatures from 30 to 85°C and for ASTM Specification A 537 steel [*53*] at temperatures from −1 to 24°C. The latter data are in the temperature range relevant to this study.

There are indications that crack-growth rates in saltwater are accelerated when a cathodic potential is applied [*49,55,62*]. For higher strength steels, this effect is thought to be related to hydrogen embrittlement effects [*62*]. On the other hand, there also is some evidence that the cathodic potential can reduce crack-growth rates significantly in seawater or saltwater to levels observed in air [*20,56*]. Based upon such limited information, it is difficult to assess conclusively the influence of cathodic potential and additional data are highly desirable.

Interpretation of Environmental Effects on Fatigue-Crack Growth

Interpretation of data on the effect of environment is difficult, particularly in some cases where contradictory results seem to have been generated. In order to facilitate an interpretation, consider the waveforms shown in Fig. 5. In the case of low frequency, the time during which the material is subjected to a high ΔK (at same crack size and amplitude) is longer at low frequencies than at high frequencies [Fig. 5(*a*)]. If the load history has different waveforms, the rate at which the material is loaded can be significantly different, even at the same frequencies.

Three quantities are of importance for the environmental effect on fatigue-crack growth: (*a*) time at high K, (*b*) maximum K-level, and (*c*) rate of increase of K (this determines the strain rate at the crack tip). If the time at high K is long [low frequency or Type B waveform in Fig. 5 (*b*)], the time for environmental action is long. Thus, lower frequencies will tend to increase the environmental effect.

If the maximum K-level is high, the growth rates are high anyway and mechanical cracking is well in advance of environmental cracking. Thus, the environmental effect diminishes at high ΔK and at high growth rates. At low ΔK levels, the rate of mechanical crack extension is slow. Thus, the environmental effect can keep pace with the rate at which newly fractured material is exposed at the crack tip, and the corrosive action can increase the amount of crack extension per cycle.

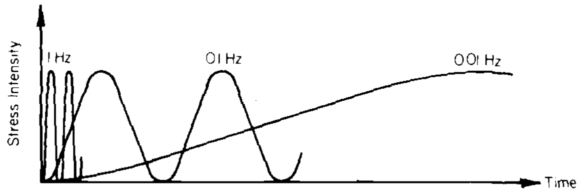

a Stress intensity history.

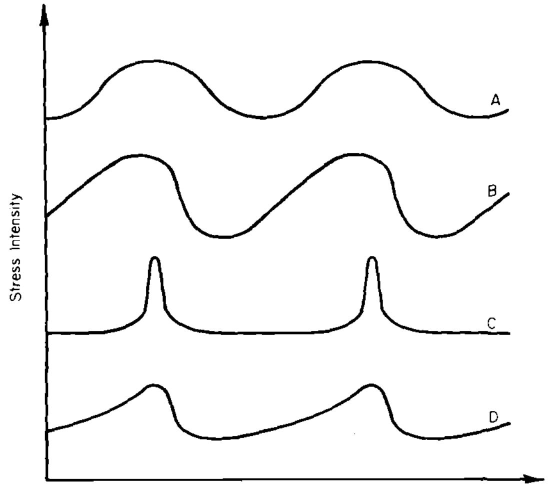

b Different wave forms.

FIG. 5—*Time at load as a function of frequency and waveform.*

If the rate of increase of K is high (high frequency or Waveform C), the strain rate is high. This means that a protective film that may be present at the crack tip may be ruptured, so that the environment can have its effect on crack growth. If the rate of K (strain rate) is low (low frequency or Waveform D), protective films can be rebuilt during straining and mechanical cracking, and the environmental effect may be reduced or absent.

The effectiveness of a protective film depends upon frequency, waveform, and K-level. If tests are limited to a small range of K-levels, the effect found from cathodic protection may be opposite of what would have been found in another range of K-levels.

Some of the data discussd earlier will be reexamined in this light on the basis of Figs. 6 and 7. These figures show Vosikovsky's data [55] plotted in terms of the crack-growth rate with respect to time, da/dt, as a function of frequency. Note that under the absence of any environmental effect, da/dt should be proportional to the frequency (that is the slope in the log-log plot should be equal to 1), since the amount of crack growth per cycle would always be the same.

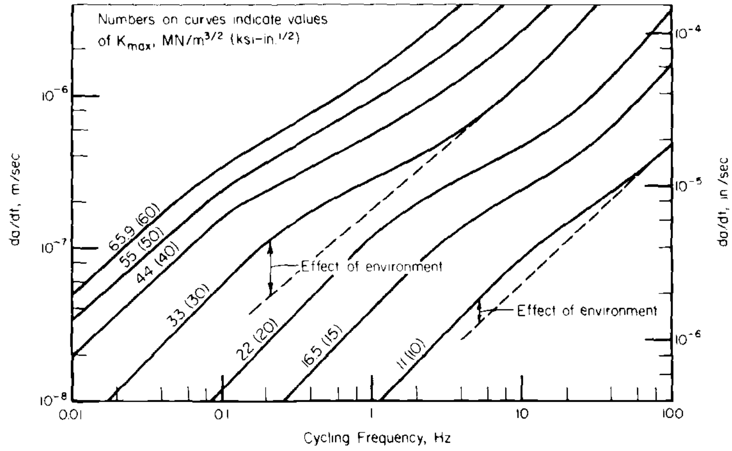

FIG. 6—*Effect of freely corroding saltwater on crack-growth rates in API X65 steel, triangular waveform (up = down),* R = *0.2, from data of Vosikovsky* [55].

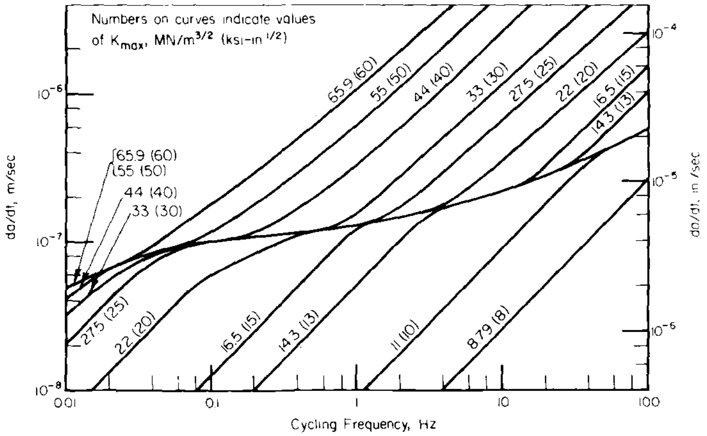

FIG. 7—*Effect of saltwater with cathodic potential on crack-growth rates in API X65 steel, triangular waveform (up = down),* R = *0.2, from data of Vosikovsky* [55].

Consider first Fig. 6. For high frequencies (top right of the figure), the slopes of the lines are equal to 1, independent of the K-level. This is the region where no environmental effect occurs. In the lower left of the figure, the slopes are also equal to 1. This is the region where the environment does affect crack growth, but the environmental effect is independent of the frequency (constant slope) for a given K-level.

The magnitude of the environmental effect is different for different K-levels. At extremely low K, it is relatively small; at extremely high K-level, it can be neglected. As pointed out earlier, the largest effect occurs at medium K-levels. The transition to the region where the environment plays a role depends upon K-level. The higher the K-level, the higher the frequency at which the transition takes place. As discussed in the previous paragraphs, the mechanical crack extension at high K is so large that it requires an extremely low frequency for the environmental action to keep pace with mechanical crack extension.

Figure 7 is a similar diagram for the case of cathodic potential. It shows that cathodic potential is effective, because the transition is postponed to higher frequencies. At a maximum stress-intensity factor, $K_{\max}$, of 8.79 MN/m$^{3/2}$ (8 ksi·in.$^{1/2}$), no transition occurs; protection is fully effective regardless of frequency. Below the transition (lower left), the environmental effect is present, and it is larger than in the case of free corrosion. This can be deduced from the effect of the curves which is much larger in Fig. 7 than in Fig. 6.

The preceding discussion shows the necessity of systematic experiments when evaluating the effect of seawater environment and cathodic protection. If the whole gamut of K-ranges, frequencies, and waveforms are not considered, no general conclusions can be reached. Generalization of limited data sets can be extremely dangerous. Therefore, this review of the data from the literature has been limited to a brief summary of the pertinent results.

Discussion

Based upon the preceding review sections of this paper, the major variables that influence the long-life corrosion-fatigue behavior of low- and medium-strength structural steels in seawater and saltwater are summarized in Table 3. These are listed in approximate order of importance with relation to application to offshore structures. Strain range or range of stress intensity, stress ratio, cyclic frequency, level of cathodic protection, and oxygen level are all important factors that must be kept in mind in assessing corrosion-fatigue resistance for such applications. Temperature, pH level, and pressure are usually of less importance for the range of values normally anticipated in actual service.

Load History Effects

The first three variables listed in Table 3 are associated with the applied stress-strain history in the local area where fatigue damage occurs. Although most of the available data have been developed under constant-amplitude cycling, it is important to keep in mind that such locations in actual structures will be subjected to a variable-amplitude stress-strain history induced by a wide variety of loading conditions. It may be possible to characterize

TABLE 3—*Summary of major variables influencing the long-life corrosion-fatigue behavior of low- and medium-strength structural steels in seawater-type environments.*

	Fatigue-Crack Initiation		Fatigue-Crack Propagation	
Variable	Effect of Variable	References	Effect of Variable	References
Hot spot strain range or range of stress intensity	continuous decrease in fatigue resistance noted as cyclic life increases (no knee or endurance limit) for unprotected steel	*5–16*, and *18–23*	increased da/dN values as values of ΔK increase; strongest environmental effects at intermediate values of ΔK [10 to 80 MN/m$^{3/2}$ (11 to 88 ksi·in.$^{1/2}$)]	*50,51,53,55,* and *57*
Stress ratio	high stress ratios reduce fatigue resistance at low values of $\Delta\epsilon_t$	*21* and *22*	high stress ratios increase crack-growth rates at low values of ΔK	*51,56*, and *57*
Cyclic frequency	slower frequencies cause reduced fatigue resistance for unprotected steel at intermediate values of $\Delta\epsilon_t$	*14* and *22*	decreases in frequency cause increases in crack-growth rates, especially at intermediate values of ΔK	*55*
Cathodic potential	adequate cathodic protection restores fatigue resistance to levels observed in air	*5,6,13,17,20, 21,* and *23*	beneficial in some regimes of frequency and stress-intensity level and detrimental in other regimes; more data are needed over a broad range of important variables	*20,55,* and *56*
Oxygen level	fatigue resistance in deaerated seawater is similar to that in air	*8*	expected to be similar to crack initiation	(none)
Temperature	although decreasing temperature results in increased oxygen levels, the overall effect of decreasing temperature is that fatigue resistance is improved to some extent in range of 13 to 45°C	*7* and *18*	crack-growth rate increased at higher temperatures in range of − 1 to 85°C	*53* and *54*
pH level	over broad range of values (4 to 10), there is little effect of pH on fatigue resistance; low values (< 4) decrease fatigue resistance and high values (> 10) improve fatigue resistance to levels similar to those observed in air	*9* and *15*	no data reported	(none)
Pressure	high hydrostatic pressure causes some reduction in fatigue resistance	*11* and *12*	no data reported	(none)

the loadings of a given sea state as a narrow-band random process and then to accumulate damage for different sea states using Strating's [*63*] pseudo-Miner approach as suggested by Marshall [*4*]. There is evidence that the root-mean-square values of $\Delta\epsilon_t$ or ΔK can be used to relate constant-amplitude to narrow-band random data for both crack initiation [for example, Refs *63,64*] and crack growth [for example, Refs *59-61*], respectively. Although significant changes in spectrum shape usually are not expected in offshore structural applications, it is important to note that if the spectrum shape changes [for example, Ref *65*], the relationship between $\Delta\epsilon_{t_{\mathrm{rms}}}$ and N_f or between ΔK_{rms} and da/dN may not be unique.

Many other approaches to cumulative fatigue damage calculation are available, but it is not the intent to review them here. Rather it is desired to point up that such damage calculations need to be kept in mind so that corrosion-fatigue data developed in the laboratory can be used effectively in design. For example, it is well-known that the local stress-strain history plays an important role in fatigue-crack-initiation damage [for example, Ref *66*] and that retardation of crack growth by overloads plays an important role in fatigue-crack-propagation damage [for example, Ref *67*]. When environmental factors further complicate the damage accumulation process through discontinuities in the basic $\Delta\epsilon_t$ versus N_f and ΔK versus da/dN relationship (for example, see Fig. 4, discussed earlier), the interaction between damage accumulated at high and low load levels becomes even more complex. Thus, experimental studies must be concerned with the broad spectrum of loading histories that will be encountered under actual service conditions.

Cathodic Protection

Considering the wide spread use of cathodic protection as a corrosion mitigation technique for offshore structures [*68-72*], it is important to discuss the effects of cathodic potential on corrosion fatigue in more detail than was done earlier. For completeness, some of the previous observations are repeated in this section of the paper.

A protection level 0.2 to 0.3 V more negative than the free corrosion potential will reduce the corrosion rate of carbon steel by 99 percent [*73*]. On this basis, commonly recommended levels for adequate protection of steel structures are near −0.85-V Cu/$CuSO_4$, −0.78-V SCE, or −0.80-V Ag/AgCl. Since it is difficult to maintain uniform levels of potential over an entire structure, local levels may vary above and below these values. Thus, the effects of both overprotection and underprotection are of interest. Futhermore, increased oxygen level, decreased temperatures, and increased velocity generally will result in the need for increased current densities in order to maintain adequate protection levels.

Glikman [*74*], based on a wealth of data on the effect of environment on the fatigue behavior of steels in aqueous environments, stated that current densities of more than 5380 mA/m^2 (500 mA/ft^2) are needed in 3 percent NaCl to restore the fatigue performance observed in air. Evans and Simnad [*75*] reached similar conclusions for experiments in 0.1 N potassium chloride (KCl). Nichols [*6*] conducted experiments on ASTM Specification A 245 steel in seawater and found that an applied cathodic current of 2150 mA/m^2 (200 mA/ft^2) would restore fatigue performance to that of similar experiments in air. Hudgins et al [*5*] found that a polarization level of −0.75-V Ag/AgCl (−0.81-V Cu/CuSO$_4$) restored the in-air corrosion-fatigue resistance of both smooth and notched specimens of SAE 1020 steel. Lyashchenko et al [*13*] used a more negative potential of −1.0-V SCE to restore in-air fatigue resistance in smooth specimens and yield better-than-air fatigue resistance in notched specimens. Hartt et al [*17*] found that a slightly more negative potential than used by Hudgins et al [*5*], −0.85-V Cu/CuSO$_4$, was necessary to give optimum fatigue resistance in notched specimens of SAE 1018 steel. Walter et al [*23*] showed that cathodic protection restored the fatigue performance of as-welded carbon steel to that observed for comparable experiments in air. Thus, it appears that sufficient and even overprotection by cathodic polarization will improve corrosion-fatigue-crack-initiation resistance, possibly up to levels observed in air. However, Brown [*62*] has pointed up that overprotection (below −0.8-V Ag/AgCl) may decrease fatigue-crack-initiation resistance at lower cyclic frequencies, although these data are based on high-strength steels that are subject to possible hydrogen embrittlement.

Data on the effects of cathodic potential on fatigue-crack growth are inconclusive. There are indications [*62*], based on high-strength steels, that cathodic polarization may be of little benefit to crack-growth resistance and that overprotection (below −0.8-V Ag/AgCl) may be detrimental. These steels are possibly susceptible to hydrogen embrittlement, a problem not expected to be encountered with most low- and medium-strength structural steels. However, for American Petroleum Institute (API) X65 steel, which usually is not considered susceptible to hydrogen embrittlement mechanisms, it was shown that high cathodic potential (near −1.04-V SCE) could increase crack-growth rates (in some regimes of ΔK) by as much as 50 times those observed in air [*55*]. In contrast, studies of structural steels have indicated that cathodic potential at a value of −0.80-V Ag/AgCl [*20*] and from a zinc protector [*56*] will restore crack-growth rates to levels observed in air. This confusing situation can be explained only by conducting further carefully controlled experiments over a wide range of the important variables as mentioned earlier.

Barsom [*76*] has also shown, based on studies of 12Ni-5Cr-3Mo steel in 3 percent NaCl solution, that the effectiveness of cathodic protection decreases as the crack front grows into the material and from the surface. Therefore, it is expected that surface cracks and through cracks may respond differently to cathodic protection, an important point to keep in mind when selecting a crack-growth specimen design for experimental studies.

The data reported by Kochera et al [*20*] and Walter et al [*23*] indicate that cathodic protection probably will improve the fatigue resistance of welded steel in seawater, but no other data for weldments are presently available. Thus, most of the available information is restricted to crack inititation in base-metal specimens. Little conclusive evidence can be assembled for the more realistic situation of welded structures in terms of both fatigue-crack initiation and propagation resistance.

Both Nichols [*6*] and Hudgins et al [*5*] emphasized the influence of calcareous scale formation on corrosion-fatigue behavior. When a cathodic potential is applied to steel in seawater, the pH at the metal surface can rise to levels near 11, leading to the precipitation of calcium and magnesium compounds as a calcareous coating. This coating is valuable because it reduces the current required to protect the steel by (*a*) maintaining a high pH level and (*b*) retarding the diffusion of oxygen to the surface. A tight, adherent coating is apparently quite effective in retarding the initiation of fatigue cracking [*5,6*], but it is not known if such a coating will be useful in retarding fatigue-crack growth once a crack has been initiated. An important point to note for sub-arctic offshore applications is that cold (−2 °C) seawater may cause the dissolution of calcareous scale, as inferred from the observation that such coating would form during summer months and disappear during winter months on platforms in Cook Inlet, Alaska [*77*].

Miscellaneous Variables

The presence of oxygen plays an important role in the corrosion-fatigue damage and any protective measure that inhibits the diffusion of oxygen to the metal surface is expected to improve corrosion-fatigue resistance. In terms of the levels normally expected in seawater (5 to 10 ppm), the bulk effect of such variations is expected to be small because sufficient oxygen will be present in the seawater to cause large reductions in fatigue resistance unless protective measures are employed.

Except for possibly important effects on cathodic protection, temperature variations in the range of 4 to 20 °C are expected to have only a small effect on corrosion fatigue behavior. Normal bulk variations in the pH of seawater are expected to have little influence on corrosion fatigue. High hydrostatic pressure appears to accelerate slightly the chemical processes involved in corrosion-fatigue damage [*12*].

Future Plans

From this review of available data on corrosion-fatigue of low- and medium-strength structural steels in seawater-type environments, it was concluded that an experimental program should be initiated to cover the following primary aspects.

1. Specimens should be weldments made from a carbon-manganese steel typically used in tubular joints of offshore platforms. API Specification 2H steel plate with AWS Class C welds was chosen for initial use.
2. Data on both crack initiation of as-welded specimens at lives to 10^9 + cycles and on crack propagation in precracked specimens at growth rates down to 2.5×10^{-10} m/cycle (10^{-9} in./cycle) should be developed.
3. Actual seawater in the range of 4 to 20°C and with chemistry typical of the deep ocean—approximately 7-ppm oxygen, about 0.030 salinity, and about 7.5 pH—should be used.
4. Three levels of cathodic protection should be employed: (*a*) freely corroding or no protection, (*b*) −0.85-V Cu/$CuSO_4$ or adequate protection, and (*c*) −1.0-V Cu/$CuSO_4$ or overprotection.
5. Initial studies should employ constant-amplitude cycling at 0.2, 1.0, and 10 Hz. Variable-amplitude loading representative of actual service should be used in latter studies.

The first phase of such a program has been initiated at Battelle's Columbus Laboratories. Later phases should be conducted at an ocean-side facility so that an abundant supply of seawater will be readily available.

Acknowledgments

Work described in the paper was performed on a program sponsored by the Offshore Saftety and Anti-Pollution Research (OSAPR) Committee of the American Petroleum Institute (API). The authors thank the following members of the API Technical Advisory Committee on Corrosion-Fatigue Research for their review, comments, and constructive criticism of this work: B. M. Casad, Continental Oil Co., J. E. Hansford, Amoco Production Co., P. W. Marshall, Shell Oil Co., M. L. Peterson, Continental Oil Co., F. W. Schremp, Chevron Oil Field Research Co., and James Storrar, Exxon Production Research Co.

References

[*1*] Marshall, P. W., "Problems in Long-Life Fatigue Assessment for Fixed Offshore Structures," Preprint 2638, American Society of Civil Engineers (ASCE) National Water Resources and Ocean Engineering Conference, San Diego, April 1976.

[*2*] Laird, C. and Duquette, D. J. in *Corrosion Fatigue: Chemistry, Mechanics, and Microstructure,* NACE-2, National Association of Corrosion Engineers, Houston, 1972, pp. 88–177.

[*3*] Duquette, D. J. in *Corrosion Fatique: Chemistry, Mechanics, and Microstructure,* NACE-2, National Association of Corrosion Engineers, Houston, 1972, pp. 12–24.

[*4*] Marshall, P. W., "Basic Considerations for Tubular Joint Design in Offshore Construction," Bulletin 193, Welding Research Council, New York, April 1974.

[*5*] Hudgins, C. M., Casad, B. M., Schroeder, R. L., and Patton, C. C., *Journal of Petroleum Technology*, Vol. 23, March 1971, pp. 283–293.

[6] Nichols, J. L., *Materials Performance*, Vol. 2, No. 2, Feb. 1963, pp. 46-53.

[7] Gould, A. J., *Engineering*, Vol. 141, 1936, pp. 495-496.

[8] Duquette, D. J. and Uhlig, H. H., *Transactions*, American Society for Metals, Vol. 61, 1968, pp. 449-456.

[9] Duquette, D. J. and Uhlig, H. H., *Transactions*, American Society for Metals, Vol. 62, 1969, pp. 839-845.

[10] Kirk, W. W., Covert, R. A., and May, T. P., *Metals Engineering Quarterly*, Vol. 8, No. 4, Nov. 1968, pp. 31-38.

[11] Thiruvengadam, A. in *Stress Corrosion Cracking of Metals—A State of the Art, ASTM STP 518*, American Society for Testing and Materials, 1972, pp. 139-154.

[12] Jolliff, J. V. and Thiruvengadam, A., *Journal of Engineering for Industry*, Vol. 96, No. 3, Aug. 1974, pp. 1085-1088.

[13] Lyashchenko, A. E., Glikman, L. A., and Zobachev, Yu. E., *Soviet Materials Science*, Vol. 9, No. 5, May 1975, pp. 496-499.

[14] Endo, K. and Miyao Y., *Bulletin of JSME*, Vol. 1, 1958, pp. 374-380.

[15] Radd, F. J., Crowder, L. H., and Wolfe, L. H., *Corrosion*, Vol. 16, 1960, pp. 415t-418t.

[16] Thiruvengadam, A., *Journal of Engineering for Industry*, Vol. 88, No. 3, 1966, pp. 332-340.

[17] Hartt, W. H., Fluet, J., and Henke, T., "Cathodic Protection Criteria for Notched Mild Steel Undergoing Corrosion Fatigue in Sea Water," Paper OTC 2380, 1975 Offshore Technology Conference, Houston, May 1975.

[18] Dugdale, D. S., *Metallurgica*, Jan. 1962, pp. 27-28.

[19] Endo, K., Komai, K., and Nakamuro, N., *Bulletin of JSME*, Vol. 13, No. 16, 1970, pp. 837-849.

[20] Kochera, J. W., Tralmer, J. P., and Marshall, P. W., "Fatigue of Structural Steel for Offshore Platforms," Paper OTC 2604, 1976 Offshore Technology Conference, Houston, May 1976.

[21] Havens, F. E. and Bench, D. M., "Fatigue Strength of Quenched and Tempered Carbon Steel Plates and Welded Joints in Sea Water," Paper OTC 1046, 1969 Offshore Technology Conference, Houston, May 1969.

[22] Marsh, K. J., Martin, T., and McGregor, J., "The Effect of Random Loading and Corrosive Environment on the Fatigue Strength of Fillet-Welded Lap Joints," NEL Report 587, National Engineering Laboratory, East Kilbride, Glasgow, Feb. 1975.

[23] Walter, J. C., Olbjorn, E., Alfstad, O., and Eide, G., "Safety Against Corrosion Fatigue Offshore," Publication No. 94, Det Norske Veritas, Hovik, Norway, April 1976.

[24] "Section 10: Design of New Tubular Structures," *Structural Welding Code*, AWS D1.1-75, American Welding Society, Inc., Miami, June 1975, pp. 107-132.

[25] "Specification for Steel Girder Bridges," BS 153: Parts 3B and 4: 1972, Gr 9, British Standards Institution, London, Oct. 1972.

[26] Marshall, P. W. and Toprac, A. A., *Welding Research Supplement*, May 1974, pp. 192s-201s.

[27] Gurney, T. R. and Hicks, J. G., "On Fatigue Design Rules for Welded Structures," Paper OTC 1907, 1973 Offshore Technology Conference, Houston, May 1973.

[28] Gurney, T. R. and Maddox, S. J., *Welding Research International*, Vol. 3, No. 4, 1973, pp. 1-54.

[29] Toor, P. M., *Engineering Fracture Mechanics*, Vol. 5, 1973, pp. 837-880.

[30] Pelloux, R. M. N., "Review of Theories and Laws of Fatigue-Crack Propagation," Technical Report AFFDL-TR-70-144, Air Force Flight Dynamics Laboratory, Dayton, Ohio, 1970, pp. 409-416.

[31] Erdogan, F., "Crack-Propagation Theories," NASA Report CR-901, National Aeronautics and Space Administration, Washington, D.C., 1967.

[32] Foreman, R. G., Kearney, V. E., and Engle, R. M., *Journal of Basic Engineering*, Vol. 89, 1967, pp. 459-464.

[33] Collipriest, J. E. in *The Surface Crack: Physical Problems and Computational Solutions*, American Society of Mechanical Engineers, New York, 1972, pp. 43-62.

[34] Collipriest, J. E. and Ehret, R. M., "A Generalized Relationship Representing the Sigmoidal Distribution of Fatigue-Crack-Growth Rates," Report SD-74-CE-0001, Rockwell International, 1974.

[*35*] Davies, K. B. and Feddersen, C. E., *Journal of Aircraft*, Vol. 12, No. 12, Dec. 1975, pp. 943-947.
[*36*] Hartman, A., *International Journal of Fracture Mechanics*, Vol. 1, 1965, pp. 167-168.
[*37*] Bradshaw, F. J. and Wheeler, C., *International Journal of Fracture Mechanics*, Vol. 5, 1969, pp. 255-268.
[*38*] Dahlberg, E. P., *Transactions*, American Society for Metals, Vol. 58, 1965, pp. 46-53.
[*39*] Frost, N. E., *Applied Materials Research*, Vol. 3, No. 3, July 1964, pp. 131-138.
[*40*] Meyn, D. A., *Metallurgical Transactions*, Vol. 2, 1971, pp. 853-865.
[*41*] Meyn, D. A., *Transactions*, American Society for Metals, Vol. 61, 1968, pp. 52-61.
[*42*] Achter, M. R. in *Fatigue Crack Propagation, ASTM STP 415*, American Society for Testing and Materials, 1967, pp. 181-204.
[*43*] Wei, R. P., *Engineering Fracture Mechanics*, Vol. 1, 1970, pp. 633-651.
[*44*] Hartman, A. and Schijve, J., *Engineering Fracture Mechanics*, Vol. 1, 1970, pp. 615-631.
[*45*] Gallagher, J. P., Ryder, J. T., and Hadley, J. C. in *Mechanical Behavior of Materials*, Vol. III, the Society of Materials Science, Japan, 1972, pp. 328-340.
[*46*] Barsom, J. M., *Engineering Fracture Mechanics*, Vol. 3, July 1971, pp. 15-25.
[*47*] Gallagher, J. P. and Wei, R. P. in *Corrosion Fatigue: Chemistry, Mechanics, and Microstructure*, NACE-2, National Association of Corrosion Engineers, Houston, 1972, pp. 409-423.
[*48*] Dawson, D. B. and Pelloux, R. M., *Metallurgical Transactions*, Vol. 5, March 1974, pp. 723-731.
[*49*] Crooker, T. W., Bogar, F. D., and Cares, W. R., "Effects of Flowing Natural Seawater and Electrochemical Potential on Fatigue-Crack Growth in Several High-Strength Marine Alloys," NRL Report 8042, Naval Research Laboratory, Washington, D.C., Aug. 1976.
[*50*] Bristoll, P. and Opdam, J. J. G., *Oceanology International 75*, Vol. 10, 1975, pp. 3-6.
[*51*] Pook, L. P. in *Stress Analysis and Growth of Cracks., ASTM STP 513*, American Society for Testing and Materials, 1972, pp. 106-124.
[*52*] Crooker, T. W. and Lange, E. A., *Welding Research Supplement*, July 1967, pp. 322s-328s.
[*53*] Socie, D. F. and Antolovich, S. D., *Welding Research Supplement*, June 1974, pp. 267s-271s.
[*54*] Telegeren, A. and Doruk, M., *Engineering Fracture Mechanics*, Vol. 6, 1974, pp. 283-386.
[*55*] Vosikovsky, O., *Journal of Engineering Materials and Technology*, Oct. 1975, pp. 298-304.
[*56*] Pook, L. P. and Greenan, A. F. in *Fatigue Testing and Design*, Vol. 2, The Society of Environmental Engineers, London, April 1976, pp. 30.1-30.33.
[*57*] Haagensen, P. J., "Fatigue Crack Growth of Steel in Air and Sea Water Under Constant Amplitude and Random Loading," Report of Work at SINTEF, University of Trondheim, Trondheim, Norway, Oct. 1976.
[*58*] Barsom, J. M., "Fatigue Behavior of Pressure-Vessel Steel," Bulletin 194, Welding Research Council, New York, May 1974.
[*59*] Smith, S. H. in *Acoustical Fatigue in Aerospace Structures*, Trapp and Forney, Eds., Syracuse University Press, Syracuse, New York, 1965, pp. 331-360.
[*60*] Barsom, J. M. in *Progress in Flaw Growth and Fracture Toughness Testing, ASTM STP 536*, American Society for Testing and Materials, 1973, pp. 147-167.
[*61*] Barsom, J. M. in *Fatigue Crack Growth Under Spectrum Loads, ASTM STP 595*, American Society for Testing and Materials, 1976, pp. 217-235.
[*62*] Brown, B. F. in *Corrosion Fatigue: Chemistry, Mechanics, and Microstructure*, NACE-2, National Association of Corrosion Engineers, Houston, 1972, pp. 25-29.
[*63*] Strating, J., "Fatigue and Stochastic Loadings," Ph.D. thesis, Delft University, Delft, Netherlands, 1973.
[*64*] Bussa, L., "Fatigue Life of a Low Carbon Steel Notched Specimen Under Stochastic Conditions," Advanced Test Engineering Department, Ford Motor Company, Dearborn, Mich., 1967.

[65] Schijve, J., "The Accumulation of Fatigue Damage in Aircraft Materials and Structures," AGARDograph No. 157, Advisory Group for Aerospace Research and Development, North Atlantic Treaty Organization, 1972.

[66] Wetzel, R. M., "A Method of Fatigue Damage Analysis," Technical Report of Scientific Research Staff, Ford Motor Company, Dearborn, Michigan, 1971.

[67] Schijve, J. and Broek, D., *Aircraft Engineering*, Vol. 34, 1962, pp. 314-316.

[68] "Control of Corrosion on Steel, Fixed Offshore Platforms Associated with Petroleum Production," NACE Standard RP-01-76, National Association of Corrosion Engineers, Houston, 1976.

[69] LaQue, F. L. in *Marine Corrosion Causes and Prevention*, Wiley, New York, 1975, pp. 95-163.

[70] Morgan, J., *Materials Performance*, Vol. 14, No. 5, 1975.

[71] McCoy, J. E., *Transactions*, Institute of Marine Engineers, Vol. 82, No. 6, 1970, pp. 210-214.

[72] Compton, K. G. and Craig, H. L., "Cathodic Protection of Offshore Structures," Paper OTC 6, 1969 Offshore Technology Conference, Houston, May 1969.

[73] Jones, D. A., *Corrosion Science*, Vol. 11, No. 6, June 1971, pp. 439-451.

[74] Glikman, L. A., *Corrosion-Mechanical Strength of Metals*, Butterworths, London, 1962.

[75] Evans, U. R. and Simnad, M. T., *Proceedings of the Royal Society*, Vol. A188, London, 1947, pp. 372-392.

[76] Barsom, J. M., *International Journal of Fracture Mechanics*, Vol. 7, No. 2, June 1971, pp. 163-182.

[77] Barrett, S. L. and Taylor, J. M., Jr., "Cathodic Protection Experience in Cook Inlet, Alaska," Paper OTC 2700, 1976 Offshore Technology Conference, Houston, 1976.

Phenomena

G. R. Chanani[1]

Investigation of Effects of Saltwater on Retardation Behavior of Aluminum Alloys

REFERENCE: Chanani, G. R., "**Investigation of Effects of Saltwater on Retardation Behavior of Aluminum Alloys,**" *Corrosion-Fatigue Technology, ASTM STP 642,* H. L. Craig, Jr., T. W. Crooker, and D. W. Hoeppner, Eds., American Society for Testing and Materials, 1978, pp. 51-73.

ABSTRACT: The 2024-T8, 7075-T6, and 7075-T73 alloys were studied in laboratory air and 3.5 percent sodium chloride (NaCl) solution to investigate the effects of a corrosive environment on the retardation behavior of aluminum alloys. Single overload cycles at overload ratios of 1.5, 2.0, and 2.5 were used. The single overloads were found to cause a decrease in constant-amplitude crack-growth in saltwater just as they did in air. Also, the number of delay cycles increased with each increase in overload ratio (OLR) in saltwater just as they did in air. However, the number of delay cycles was larger in air than in 3½ percent saltwater, and the difference was greater for the 7075-T6 alloy than it was for the 2024-T8 and 7075-T73 alloys. The results indicated that a given microstructure and its susceptibility to environmental attack are important in determining its fatigue behavior under variable amplitude loading in a corrosive environment. An alloy which shows superior retardation behavior in air can be inferior in a corrosive environment such as saltwater as was found for the 7075-T6 and 2024-T8 alloys. The difference in the retardation behavior of these two alloys in air was small, while in saltwater, the 2024-T8 alloy was generally superior. Environmental attack similar to that which was observed in the constant-amplitude saltwater fatigue specimens was found by fractographic examination of selected retardation specimens. However, these observations indicated that the general nature of the fractographic features in relation to the OLR and the applied baseline stress-intensity factor is similar in both air and saltwater, except that, at the lower OLR and low K values, the overload markings were not visible in the specimens tested in saltwater. This lack of overload marking was more common in the 7075-T6 alloy because of its high susceptibility to environmental attack.

KEY WORDS: corrosion fatigue, fatigue-crack growth, retardation, fractography, stress corrosion, microstructure, aluminum alloys

The important parameters that can influence fatigue-crack growth are the nature of cyclic stresses at the crack tip, the metallurgical structure

---

[1] Engineering specialist, Metallics Research Department, Aircraft Division, Northrop Corporation, Hawthorne, Calif. 90250.

and properties of the material, and the environmental conditions at the crack tip. Considerable theoretical and experimental work has been performed to determine the crack-growth behavior of various materials under constant-amplitude loading. Recent efforts have concentrated on determining the effects of variable amplitude loading on crack-growth behavior [*1–13*].[2] Research in the last decade or so has shown that load sequences have a considerable effect on fatigue-crack propagation (FCP) [*4–13*]. In particular, the application of a single overload or a few cycles at high tensile loads causes retardation, that is, a decrease in the fatigue-crack growth rate [*4–13*]. However, the influence of an aggressive environment on the retardation behavior has received very little attention. It is recognized generally that a corrosive environment accelerates the constant-amplitude crack-growth rates. Nevertheless, it is not well known as to how the environment affects the retardation behavior. Furthermore, the various models which have been developed to predict FCP behavior under variable amplitude loading are based on constant-amplitude data and plastic-zone size changes at the crack tip [*14–19*]. Since a corrosive environment can affect retardation behavior in various ways, for example, it can both accelerate the constant-amplitude crack-growth rate and remove a portion of the plastic zone during the delay period; it is necessary to establish its effect on the prediction models. This investigation was conducted to determine the influence of a corrosive environment on the retardation behavior of aluminum alloys and to provide information that can be used to predict, with better accuracy, the fatigue life of an aircraft structure under service conditions.

In this investigation, the 2024-T8, 7075-T6, and 7075-T73 alloys were tested in both air and saltwater. The 3½ percent saltwater solution was selected as the corrosive environment because it has been shown to be one of the most corrosive of the typical aircraft test environments [*20*]. Single overload cycles with three different overload ratios (OLR) were used in this work. Fractography was performed to determine the influence of a corrosive environment on the fracture topography of failed retardation specimens and to provide an understanding of fracture mechanisms in a corrosive medium with simple variable-amplitude loading.

Experimental Procedure

The 2024 and 7075 alloys were procured in the T3 and T6 heat treat conditions, respectively. Part of the as-received 7075-T6 material was heat treated to the T73 condition to avoid minor compositional variables, which could otherwise obscure the effects of different 7075 alloy heat treatments on the retardation behavior. The as-received 2024-T3 material was heat

---

[2] The italic numbers in brackets refer to the list of references appended to this paper.

treated to 2024-T8 condition having the same yield strength as the 7075-T73 material. For this purpose, specimens of the 2024-T3 were heat treated using different times at a temperature of 190°C to produce variations in tensile properties within the T8 specification. From the various times and temperatures investigated, an aging treatment of 96 h at 190°C was selected as the best treatment because it produced an average yield strength of 422 MN/m^2, which was within 1 percent of that obtained for the 7075-T73 alloy (419 MN/m^2).

Single-edge notched (SEN) specimens in the LT (RW) orientation, as shown in Fig. 1, were used for this investigation. Single overload cycles with overload ratios of 1.5, 2.0, and 2.5 were used, as shown in Fig. 2.

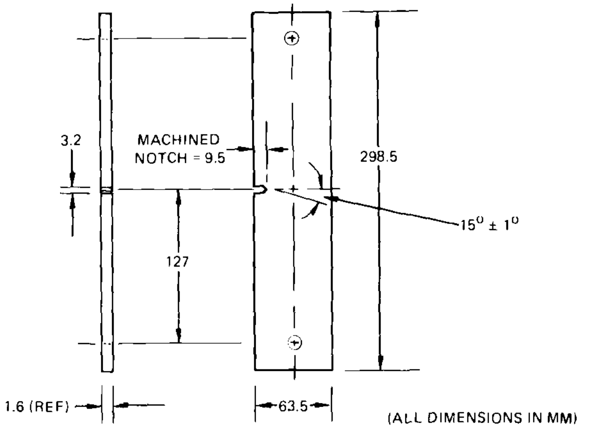

FIG. 1—*SEN aluminum specimen, LT (RW) orientation.*

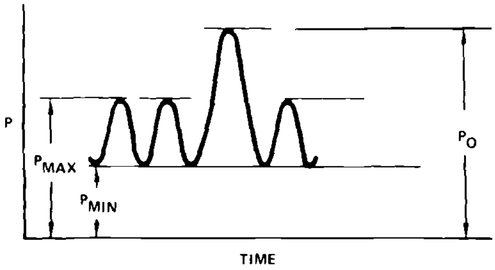

$$\text{OVERLOAD RATIO} = \frac{P_O}{P_{MAX}}$$

$$\%\ \text{OVERLOAD} = \left(\frac{P_O - P_{MAX}}{P_{MAX}}\right) \times 100$$

FIG. 2—*Schematic representation of the test spectrum.*

All tests were conducted with a baseline P_{max} of 2224 N and an R ratio (P_{min}/P_{max}) of 0.1 in a controlled laboratory environment (22 ± 3°C and 50 ± 5 percent relative humidity). Exploratory work showed no significant differences in constant-amplitude crack-growth rates between 1 and 5-Hz tests in air. Hence, the constant-amplitude load cycles for tests in air were applied at a frequency of 5 Hz, while those for tests in saltwater were applied at 1 Hz to obtain the influence of the corrosive environment on retardation. The overload cycles in both media were applied at 0.1 Hz. After the overload cycle, the number of constant-amplitude cycles applied was sufficient for complete recovery of the unretarded crack-growth rate. The crack lengths were measured to an accuracy of ± 0.05 mm with the aid of imprinted photogrids (intergrid spacings of 0.5 mm) and a filar eyepiece in a high-magnification traveling microscope. The saltwater retardation tests were conducted on a continuous basis to avoid the difficulty of measuring crack tip positions on an excessively corroded surface.

Constant-amplitude FCP tests were conducted in both air and saltwater on SEN specimens obtained from the same lot of material as was used in the retardation studies to evaluate the effects of an overload cycle on FCP.

Fractographic examinations of the constant-amplitude FCP and retardation specimens tested both in air and saltwater were performed with a scanning electron microscope (SEM). Fracture surfaces were cleaned by replication and they were then gold shadowed before the SEM examination.

Results and Discussion

The tensile properties of the three alloys used in this investigation are listed in Table 1. The selection of these three conditions provides information about the effect of susceptibility of a microstructure to environmental attack on retardation behavior (susceptible 7075-T6 versus relatively immune 7075-T73 and 2024-T8).

TABLE 1—*Tensile properties of the aluminum alloys.*

Alloy and Heat Treatment	0.2% Yield Strength, MN/m^2	Ultimate Tensile Strength, MN/m^2	% Elongation
7075-T6	504	553	12.5
7075-T73	419	491	12.3
2024-T8	422	471	10.0

NOTES—Flat specimens of 50.8-mm gage length were used. The reported values are an average of three tests.

Figure 3 shows the trend of the constant-amplitude FCP curves obtained for all three materials in air and saltwater. As expected, the FCP rates in

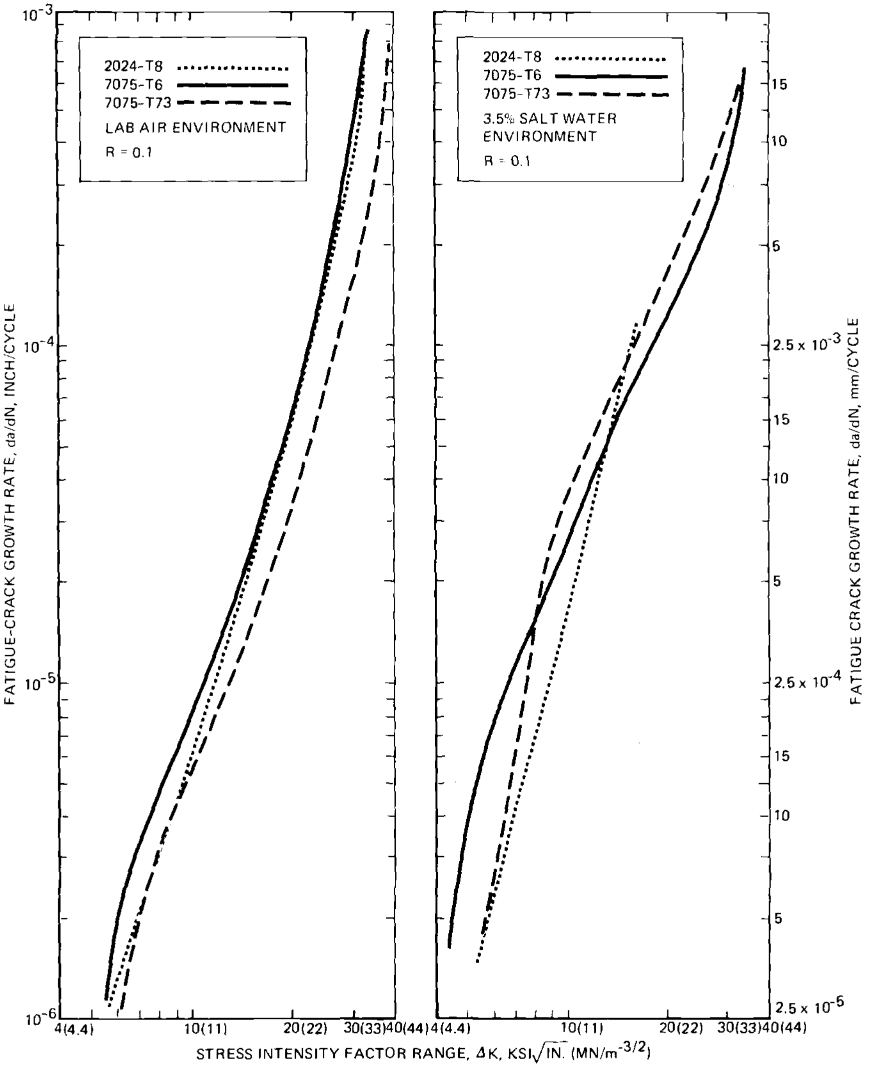

FIG. 3—*General trend of the FCP behavior for all three materials.*

saltwater were faster than those in the air. As described next, data from these curves were used to calculate the degree of retardation, and the specimen fracture surfaces were used to determine the changes in fractographic features due to overload cycles. At low and intermediate crack-growth rates where resistance to environmental attack is important, the 7075-T6 alloy had the poorest FCP resistance because of the susceptibility of this microstructure to environmental attack.

In most of the retardation tests, the overload cycles were applied at similar crack lengths in both the air and saltwater tests. This provided a direct comparison of the test results which were analyzed then in a similar manner. Tables 2 through 4 summarize these results. The number of delay cycles, N^*, and the affected crack length, a^*, refer to the number of cycles and crack length over which the retardation occurred, respectively. Figure 4(*a*) shows schematically how the number of delay cycles and the affected crack length were measured. Figure 4(*b*) shows typical curves of crack length versus number of cycles for the 7075-T73 alloy in both air and saltwater after single overload cycles with an OLR of 2.5. These curves are typical of all of the tests conducted. Because of the inherent scatter in the crack-growth rate after an overload cycle, particularly for the saltwater tests, a small difference in the number of delay cycles between any two tests should not be considered significant.

These results, together with the fractographic results, are described and discussed next.

Retardation Test Results

As can be seen from Tables 2 through 4, the number of delay cycles increased with the increase in the OLR for each alloy in both air and saltwater. Figures 5 through 7 show the amount of delay for each of the three alloys as a function of the baseline K_{max} at a given overload ratio. At an OLR of 1.5, shown in Fig. 5, the delay cycles decrease with an increase in baseline K_{max}, while at OLR values of 2.0 (Fig. 6) and 2.5 (Fig. 7), there is a tendency for a minimum in each curve. The number of delay cycles in air appears to reach the minimum at an approximate K_{max} of 11 and 9 $MN/m^{-3/2}$ for tests at OLR of 2.0 and 2.5, respectively. The minimum in the delay cycle curve for tests in air appears to correspond to a K_0 (overload stress-intensity factor) of about 22 $MN/m^{-3/2}$; at higher values of K_0, the N^* value goes up. Hence, it is possible that the N^* versus K_{max} behavior is somehow related to the value of K_0. This would explain why no minimum number of delay cycles was observed in Fig. 5 for the tests at OLR of 1.5 where K_0 did not exceed 22 $MN/m^{-3/2}$ for any test.

As expected, the number of delay cycles was greater in air than in the 3½ percent saltwater. The difference in the number of delay cycles between air and saltwater tests was greater for the 7075-T6 alloy than it was for the 2024-T8 and 7075-T73 alloys. These results indicate that an alloy with a corrosion-resistant microstructure can change its retardation ranking, depending on the environment in which it is tested. This is demonstrated by making a comparison between the retardation behavior of 2024-T8 and 7075-T6 alloys in air and saltwater. The difference in N^* values in air and saltwater for the 2024-T8 alloy is much smaller than similar differences for the 7075-T6 alloy. This is apparently due to the

TABLE 2—*Summary of retardation results in air and saltwater for 2024-T8 alloy*[a]*.* P_{MAX} *= 2224 N.*

Environment	Specimen	K_0/K_{MAX}, OLR	K_{MAX}, MN/m$^{-3/2}$	a_i, mm	a^*, mm	N^*, 1000	Acceleration[b]
Laboratory air	DT80LC1	1.5	6.7	14.5	0.26	12.5	a
			8.7	18.5	0.071	5	a
			12.2	24.3	0.109	2	a
	DT80LC2	2.0	6.7	14.5	0.83	30	b
			8.7	18.6	0.38	20	b
			10.8	22.3	1.07	15	b
	DT80LC3	2.5	6.8	14.6	0.55	55	b
			8.7	18.6	0.71	65	b
			10.7	22.1	1.57	115	b
3.5% salt water	ET8SW0LC1-2	1.5	6.8	14.7	0.15	6	a
			9.6	20.3	0.23	2	b
			13.7	26.4	0.48	2	b
	ET8SW0LC2	2.0	6.7	14.5	0.25	12.5	a
			9.7	20.3	0.60	8	a
			13.5	26.1	2.27	12.5	a
	ET8SW0LC3	2.5	6.7	14.5	0.48	35	a
			9.6	20.3	1.59	45	a
			13.5	26.1	2.90	45	b

[a] Using 1.6-mm-thick SEN specimens at a frequency of 5 Hz for tests in air and 1 Hz for tests in saltwater.

[b] a = no crack growth during overload cycle and no initial acceleration,
b = crack growth during overload cycle, and
c = initial acceleration after the overload cycle.

TABLE 3—*Summary of retardation results in air and saltwater for 7075-T6 alloy,*[a] P_{MAX} = *2224 N.*

Environment	Specimen	K_0/K_{MAX}, OLR	K_{MAX}, $MN/m^{-3/2}$	a_i, mm	a^*, mm	N^*, 1000	Acceleration[b]
Laboratory air	DT60LC1	1.5	6.7	14.5	0.28	17.5	a
			8.4	18.0	0.25	6	b
			10.2	21.5	0.30	4	a
	DT60LC2	2.0	6.2	13.0	0.10	25	a
			8.1	17.7	0.27	12.5	a
			11.1	22.8	0.54	10	a
			15.1	27.7	3.21	25	b
	DT60LC3	2.5	6.7	14.5	1.09	350	a
			9.6	20.2	2.27	130	a
			13.5	26.1	. . .	arrest	a
3.5% salt water	ET6SW0LC1	1.5	6.7	14.5	0.25	5	a
			9.6	20.2	0.36	2	a
			13.5	26.1	0.41	1	a
	ET6SW0LC2	2.0	6.7	14.5	0.13	6	a
			9.6	20.2	0.66	5	a
			13.5	26.1	1.59	7	a
	ET6SW0LC3	2.5	6.7	14.5	0.53	30	a
			9.6	20.2	1.69	35	a
			13.5	26.1	7.15	40	b

[a] Using 1.6-mm-thick SEN specimens at a frequency of 5 Hz for tests in air and 1 Hz for tests in saltwater.

[b] a = no crack growth during overload cycle and no initial acceleration,
b = crack growth during overload cycle, and
c = initial acceleration after the overload cycle.

TABLE 4—*Summary of retardation results in air and saltwater for 7075-T73 alloy,*[a] P_{MAX} = *2224 N.*

Environment	Specimen	K_0/K_{MAX}, OLR	K_{MAX}, MN/m$^{-3/2}$	a_i, mm	a^*, mm	N^*, 1000	Acceleration[b]
Laboratory air	DT730LC1	1.5	6.7	14.5	0.31	17.5	a
			8.5	18.1	0.23	6	a
	DT730LC2	2.0	5.9	12.7	0.48	55	a
			8.5	18.2	0.64	25	a
			11.2	23.0	1.10	20	b
			16.0	28.7	1.80	25	b and c
	DT730LC3	2.5	6.8	14.7	0.50	90	b
			9.8	20.5	1.06	85	a
			13.8	26.3	4.81	165	b
3.5% salt water	ET73SW0LC1	1.5	6.7	14.5	0.62	15	b
			9.6	20.2	0.42	2	a
			13.5	26.1	0.91	1	b
	ET73SW0LC2	2.0	6.7	14.5	0.73	40	a
			9.2	19.7	1.11	20	a
			13.5	26.1	2.95	12.5	b
	ET73SW0LC3	2.5	6.7	14.5	0.60	35	a
			9.6	20.3	3.12	50	a
			13.5	26.1	7.79	77.5	a

[a] Using 1.6-mm-thick SEN specimens at a frequency of 5 Hz for tests in air and 1 Hz for tests in saltwater.

[b] a = no crack growth during overload cycle and no initial acceleration,
b = crack growth during overload cycle, and
c = initial acceleration after the overload cycle.

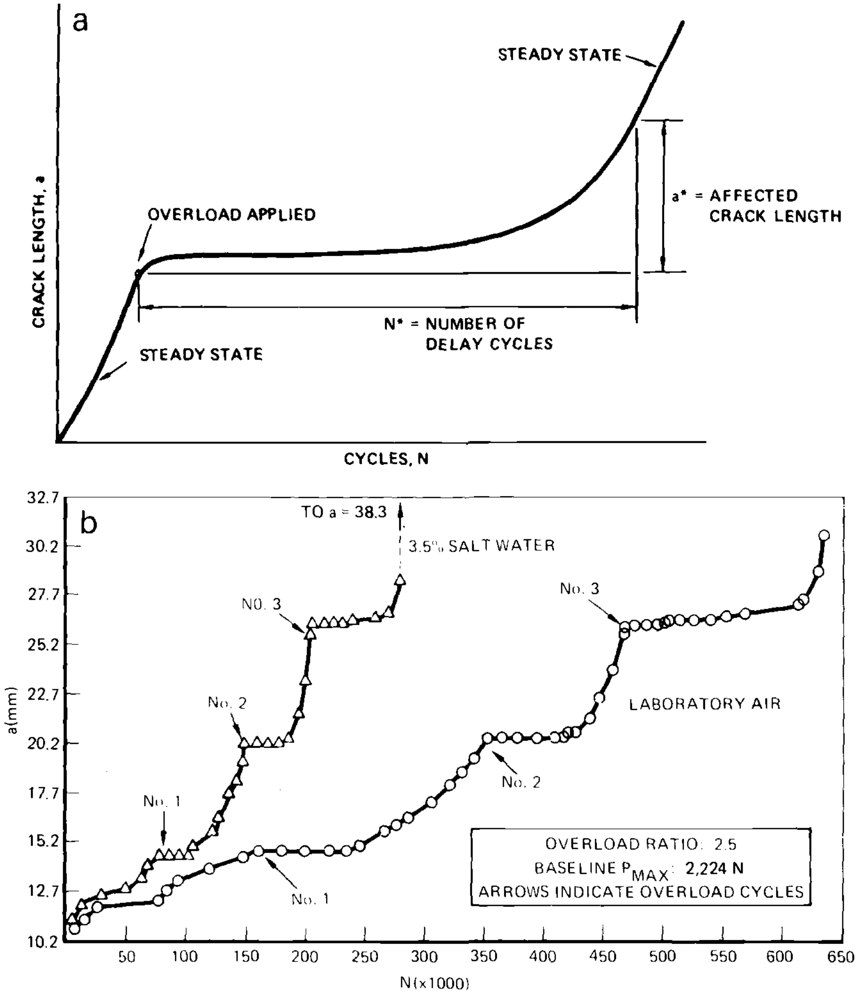

FIG. 4—(a) *Crack-length versus number of cycles resulting from application of a single overload.* (b) *Crack-length versus number of cycles for 7075-T73 alloy at an OLR of 2.5 in both air and saltwater.*

fact that the 7075-T6 alloy is highly susceptible to environmental attack, while the 2024-T8 alloy is relatively immune. This is best illustrated in Fig. 7 at an OLR of 2.5 where the retardation phenomenon is at its maximum.

The affected crack length, a^*, generally is believed to be related to the overload plastic-zone size. The overload plastic-zone size depends on the overload stress-intensity factor, K_0, and increases with increased applied K_0. Hence, a^* also should increase with K_0, as found in most of the cases listed in Tables 2 through 4. However, some inconsistencies do exist in the saltwater data of Tables 2 through 4. These could be due either to

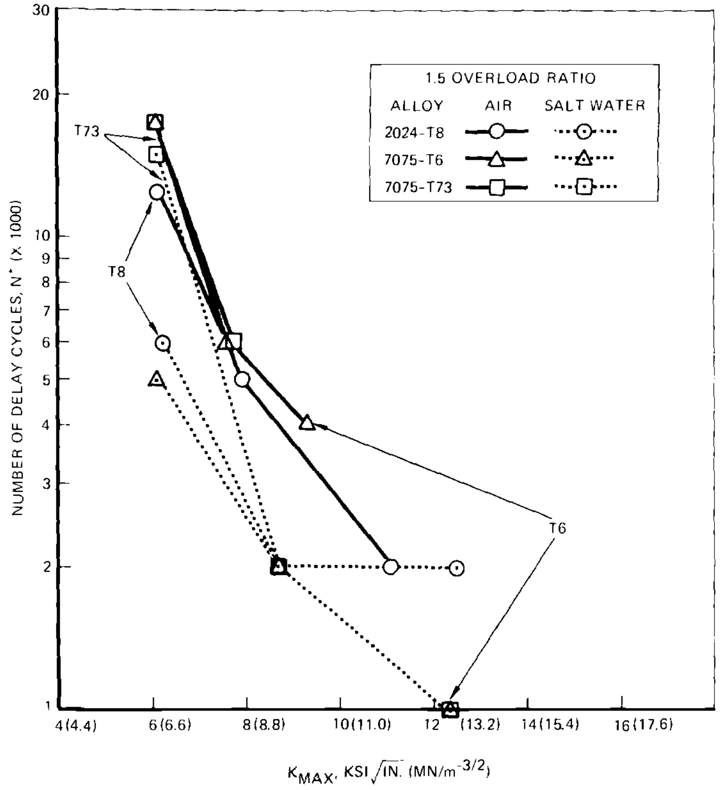

FIG. 5—*Number of delay cycles as a function of baseline stress-intensity factor in air and 3.5 percent saltwater after an OLR of 1.5.*

some complex load-environment-time interaction at the crack tip or to experimental scatter in data. At higher *K* values, the environmental attack at the crack tip is more severe and, hence, a part of the overload plastic zone may be corroded away, which would explain the observed anomaly in affected crack lengths.

The differences between the number of delay cycles in air and saltwater may be attributed to the higher constant amplitude crack-growth rates in saltwater. Thus, it takes fewer cycles for a crack to grow through a given overload plastic zone in saltwater than in air. If the differences could be explained completely due to this growth-rate difference, then crack-blunting would be a minor factor, as indicated by an examination of preliminary results reported earlier [*8*] and also as found by Raju et al [*21*]. Raju et al found that annealing at elevated temperatures eliminated retardation. Since temperature increases do not significantly affect crack-blunting, they concluded that blunting was not a significant factor.

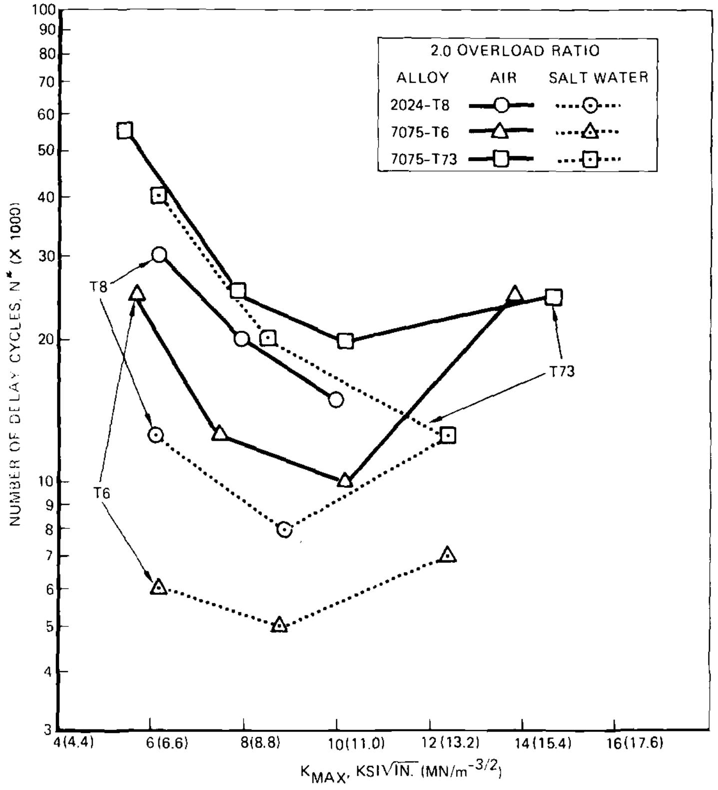

FIG. 6—*Number of delay cycles as function of baseline stress-intensity factor in air and 3.5 percent saltwater after an OLR of 2.0.*

To determine whether or not blunting was a significant factor in these results, the decrease in the average *da/dN* values in the affected crack-length region was compared for each of the two media. The normalized decrease in crack growth (also called degree of retardation), R^*, is defined as: $R^* = (da/dN)/(a^*/N^*)$. Figure 8 shows these values for the 7075 alloy for the lowest (1.5) and highest OLR (2.5). The values of a^* and N^* used to obtain R^* were obtained from Tables 3 and 4. The constant-amplitude *da/dN* values were obtained from the *da/dN* versus ΔK curves shown in Fig. 3. The differences between R^* values at an OLR of 1.5 and those at an OLR of 2.5 were much less for the 2024-T8 alloy than those shown for the 7075 alloys. Examination of Fig. 8 indicates that the higher constant-amplitude *da/dN* rates in saltwater can account for some of the differences in the number of delay cycles, particularly at lower OLR values. However, at higher OLR, the higher *da/dN* rate in saltwater cannot completely account for the observed differences. At present, the mechanism responsible

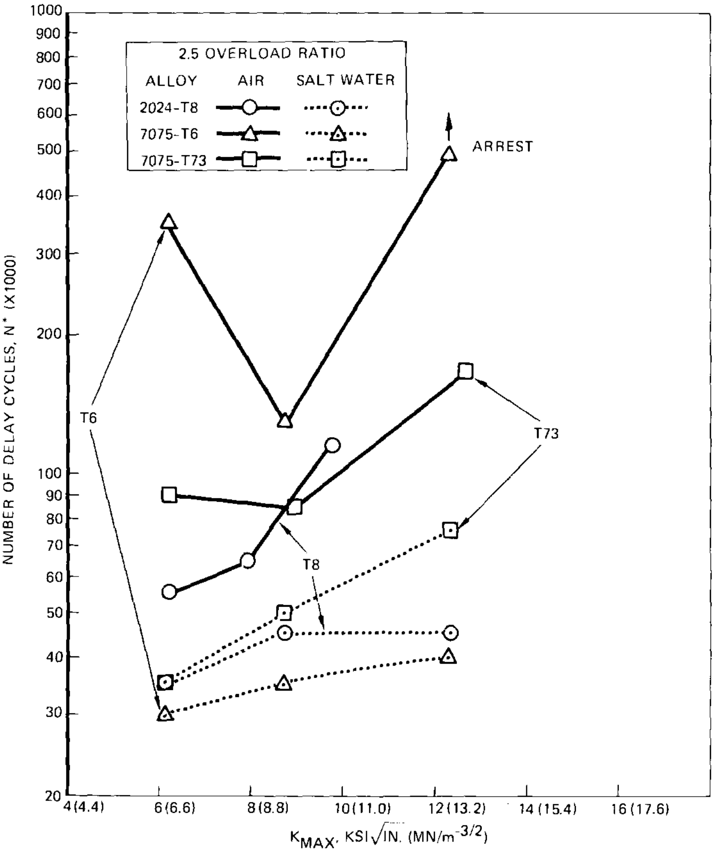

FIG. 7—*Number of delay cycles as a function of baseline stress-intensity factor in air and 3.5 percent saltwater after an OLR of 2.5.*

for these observations are not clearly understood. A possible explanation is described next.

The observed differences could be due either to a high plastic strain at the crack blunting at the higher OLR or to a combination of both plastic energy and crack blunting. At the low OLR, there is less crack blunting and plastic deformation at the crack tip, and hence, the corrosion of a plastically deformed crack tip or resharpening of the blunted crack by an aggressive medium does not play an important role, a conclusion reached earlier based on the results at low OLR [*8*] and also by Raju et al [*21*]. However, at high OLR, both the blunting and the plastic deformation at the crack tip are much greater and, hence, the environmental attack as well as the degree of susceptibility of the alloy to environmental attack can influence the retardation behavior in saltwater. For this reason, it is possible that the heavily blunted crack at the high OLR may have been resharpened

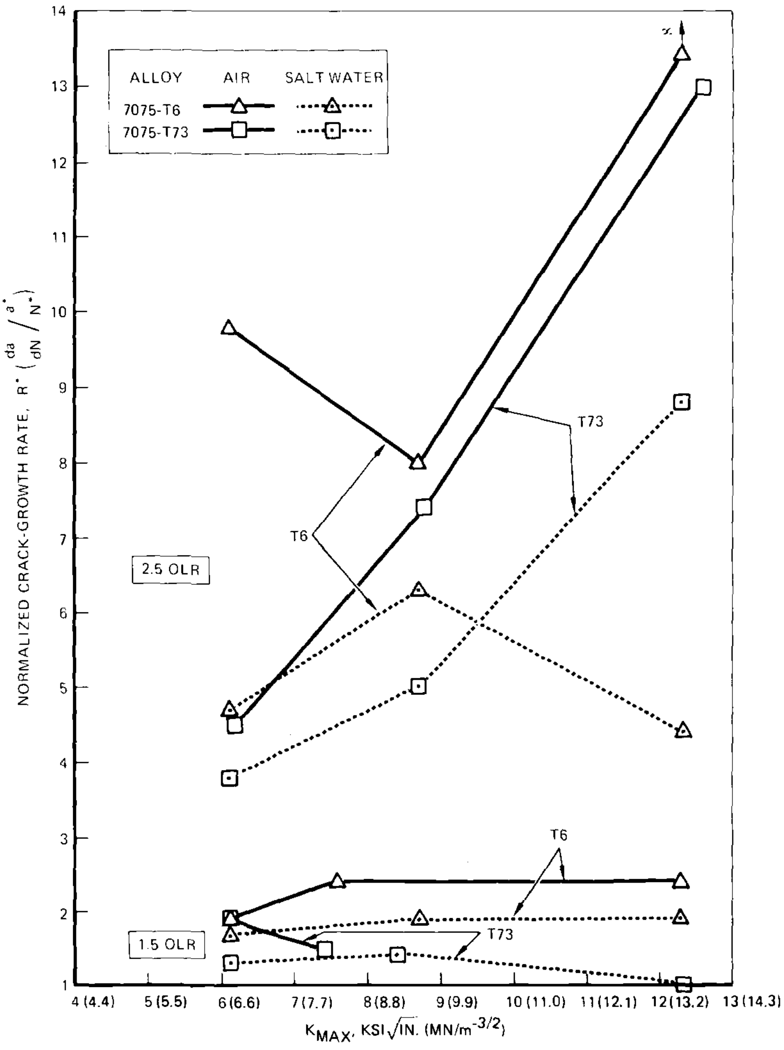

FIG. 8—*The effect of OLR on normalized average crack-growth rate in air and saltwater for the 7075 alloy.*

in the 7075-T6 alloy because of its high susceptibility to environmental attack; and as a result, there is much less retardation in saltwater. Further work is needed to confirm this explanation as well as evaluate other possible mechanisms. In 2024-T8 and 7075-T73 alloys, the difference is much less due to their relative immunity to environmental attack. Thus, it would appear that blunting could be an important, if not a governing, factor in retardation at high OLR. Besides blunting, the high plastic work at the higher OLR also could contribute to the observed differences in delay cycles at high OLR. Nevertheless, these tests indicate the importance of a given microstructure and its susceptibility to environmental attack in determining its fatigue behavior under variable amplitude loading in an aggressive environment. Thus, an alloy which shows superior retardation behavior in air can be inferior to the other alloy in an aggressive environment such as saltwater, as was found for the 7075-T6 and 2024-T8 alloys in this investigation.

Fractographic Results

Fractographic examinations of selected FCP and retardation specimens from each alloy tested in both air and saltwater were performed to provide an understanding of the failure mechanisms in an aggressive medium with a simple variable amplitude loading and to determine the influence of an aggressive environment on the nature and size of the overload region. For this purpose, fractographs were obtained (*a*) before overload, (*b*) in the overload stretch band, and (*c*) at several locations in the retardation zone. In general, environmental attack similar to that which was observed in fracture surfaces of saltwater FCP specimens was found by fractographic examination of saltwater retardation specimens.

The overload cycle causes a stretch band across the thickness of the failed specimens in almost all air tests, while the fracture surfaces of the saltwater retardation specimens showed overload stretch markings only at higher OLR and higher K values. At the lower OLR and lower K values, the overload markings generally were not visible.

The width of the overload-stretch zone and the associated retardation region increased with increased applied K level. In air, it progressed from a barely visible thin line at low K levels to a wide band of overload zone exhibiting dimpling and tunneling at higher K values. This increase in the stretch band size is an indication of the overload plastic-zone size which increases with increased K. In saltwater, the overload markings generally were smaller in magnitude and, hence, may have been removed by the corrosive attack of the saltwater at low OLR values. The nature of the stretch markings in saltwater tests, when visible, was similar to those formed in air.

Figure 9 shows the results for 7075-T6 alloy at an OLR of 2.5 as a function of $K_{\max}$ in air, while Fig. 10 shows similar results in saltwater. These fractographs show, particularly in air, that as the stress-intensity level goes up, the width of the overload zone increases. The overload band or stretch zone associated with the incremental crack-growth during the rising-load portion of the overload cycle is marked by a dimpled region, as in the center of Fig. 9(*c*). The tunneling effect seen in the stretch zone of Figs. 9(*c*) and 10(*c*) is primarily due to the relatively plane-strain condition along the midsection of the specimen. In Fig. 10(*c*), the saltwater en-

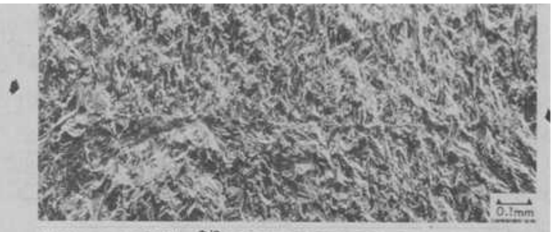

(a) $K_{MAX} = 6.7$ MN/m$^{-3/2}$ CRACK LENGTH AT OVERLOAD = 14.5 mm

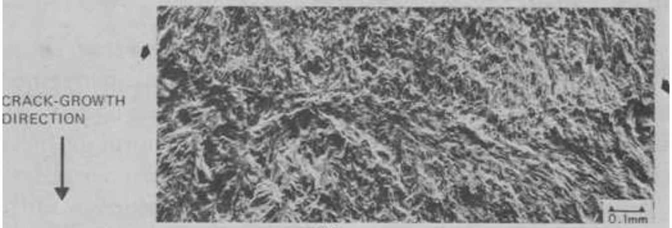

(b) $K_{MAX} = 9.6$ MN/m$^{-3/2}$ CRACK LENGTH AT OVERLOAD = 20.3 mm

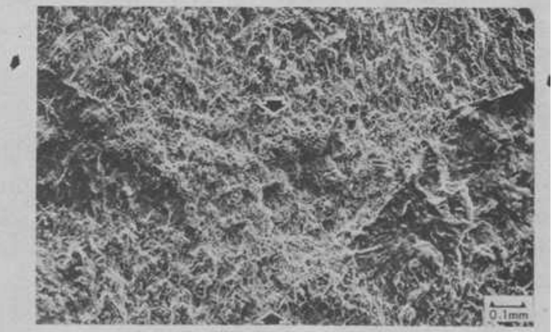

(c) $K_{MAX} = 13.5$ MN/m$^{-3/2}$ CRACK LENGTH AT OVERLOAD = 26.2 mm

BASELINE P_{MAX} = 2,224 N
OVERLOAD RATIO = 2.5

FIG. 9—*Fractographs showing effect of stress intensity on overload marking after a 150 percent overload cycle in 7075-T6 in air.*

vironment also may have influenced the tunneling. Immediately following the stretch marking is the retardation zone marked by a rather smooth topography, characteristic of a very low FCP rate. Proceeding further away from the overload region, the topography of the fracture surface becomes increasingly similar to that which is seen before the overload cycle. This occurs due to the recovery of the constant-amplitude crack-growth rate.

At a baseline K_{max} of approximately 6.6 MN/m$^{-3/2}$, that is, after first overload cycle, a well defined overload stretch marking was not seen in any of the three alloys tested in saltwater even at an OLR of 2.0. Figure 11 shows the fractographic results obtained for both air and saltwater tests

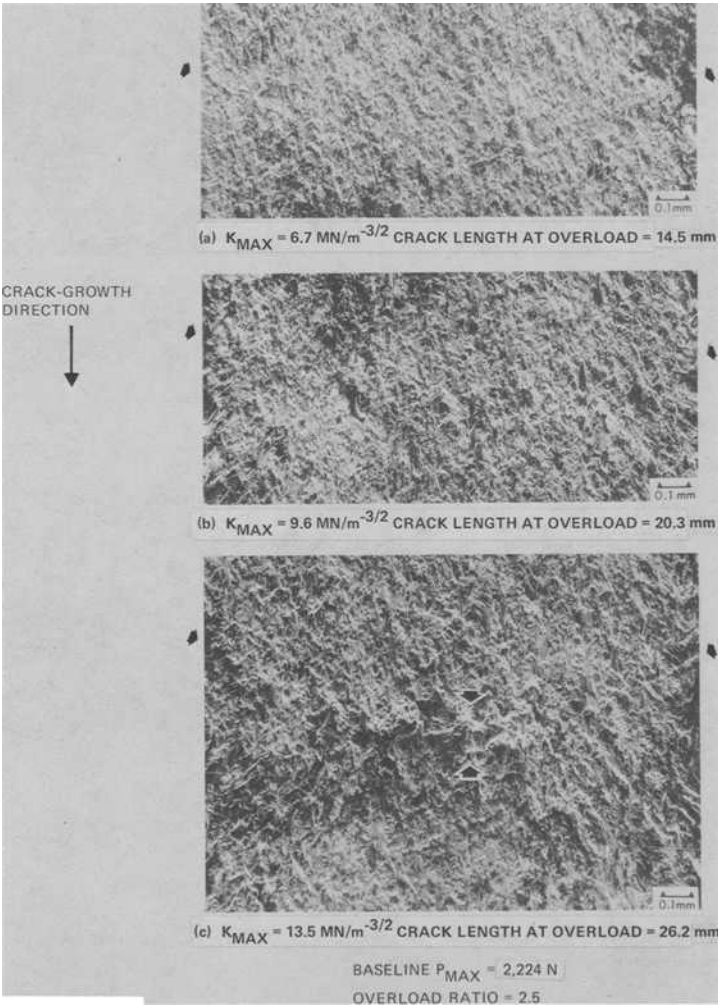

FIG. 10—*Fractographs showing effect of stress intensity on overload marking after a 150 percent overload cycle in 7075-T6 in 3.5 percent saltwater.*

of the 2024-T8 alloy at an OLR of 2.0 and a $K_{\max}$ of 6.7 MN/m$^{-3/2}$. As seen, even in the case of the 2024-T8 alloy which is relatively immune to the environmental attack, the overload marking is not distinct in saltwater, while it is very clear for air. At an OLR of 2.5, the overload markings were just barely visible in the saltwater tests of the 7075-T6 alloy because of its high susceptibility to environmental attack, Fig. 10(*a*), whereas in air, they were very distinct, Fig. 9(*a*).

In the saltwater tests at a baseline $K_{\max}$ of approximately 10 MN/m$^{-3/2}$

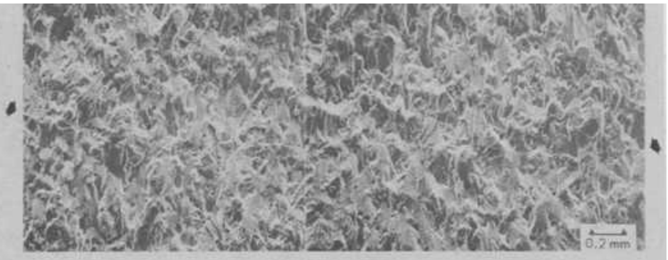

(a) AIR

(b) 3.5% SALTWATER

BASELINE P_{MAX} (K_{MAX}): 2224N (6.7 MN/m$^{-3/2}$)
CRACK-LENGTH AT OVERLOAD: 14.5 MM
OVERLOAD RATIO: 2.0

FIG. 11—*Fractographic features in the vicinity of a 100 percent overload cycle in 2024-T8 in air and saltwater.*

(second overload cycle) and an OLR of 2.0, an overload marking was observed in the 2024-T8 alloy, while a very faint marking was observed in the 7075-T73 alloy and no marking was seen for the 7075-T6 alloy. In the 7075-T6 alloy, pitting and grain boundary attack were seen.

At a baseline K_{max} of approximately 13 MN/m$^{-3/2}$ (third overload cycle), the overload markings were visible in saltwater specimens at both OLR of 2.0 and 2.5, even in the 7075-T6 alloy. Figures 12 through 14 show typical results of the saltwater tests for the three alloys at the two OLR. At a given OLR, the stretch zone, including dimpling, is larger in the 2024-T8 alloy, Fig. 12, than in 7075-T6, Fig. 13, and 7075-T73, Fig. 14, alloys. This observation is similar to that made for testing in air, which indicates that during the overload cycle itself, the environment probably does not play

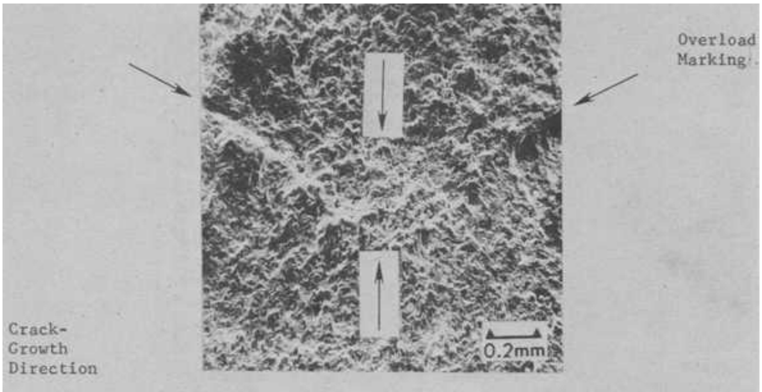

(a) Overload Ratio = 2.0

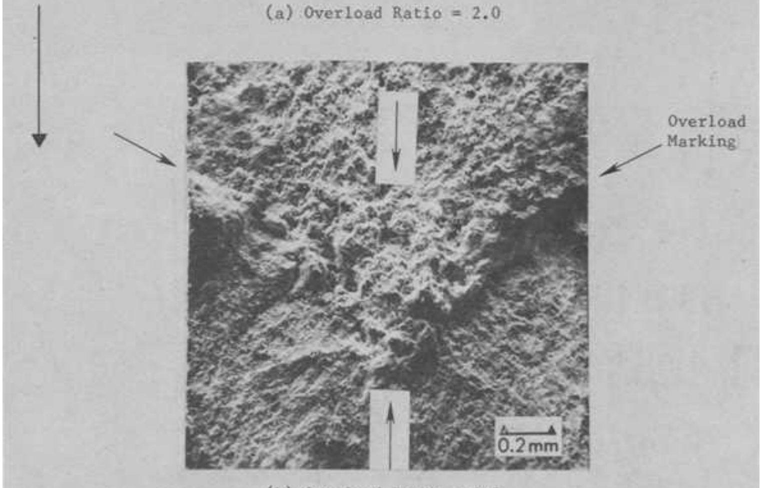

(b) Overload Ratio = 2.5

Baseline P_{max} (K_{max}) = 2224N (13.5 MN/m$^{-3/2}$)

FIG. 12—*Fractographic features in the vicinity of an overload cycle in 2024-T8 at OLR of 2.0 and 2.5 in saltwater.*

as great a role as it does during the crack-growth phase after the overload cycle. This is evidenced by the corroding away of the overload marking in susceptible 7075-T6 alloy, Fig. 13(*a*). Since these fractographs were obtained from those specimens which had experienced relatively high K values, tunneling can be observed. Again, this behavior is similar to that observed in air. Here, too, the 2024-T8 showed the largest amount of tunneling. An increase in OLR from 2.0 to 2.5 at the same baseline K_{max} results in an increase in the stretch zone size, including tunneling just as it did with an increase of K_{max}, as shown in Figs. 9 and 10.

For some of the tests conducted in air, depending on the baseline K, changes in striation spacings were seen across the overload stretch zone.

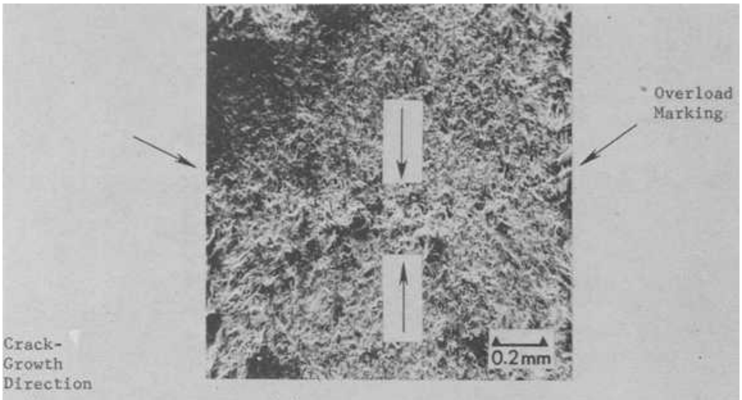

(a) Overload Ratio = 2.0

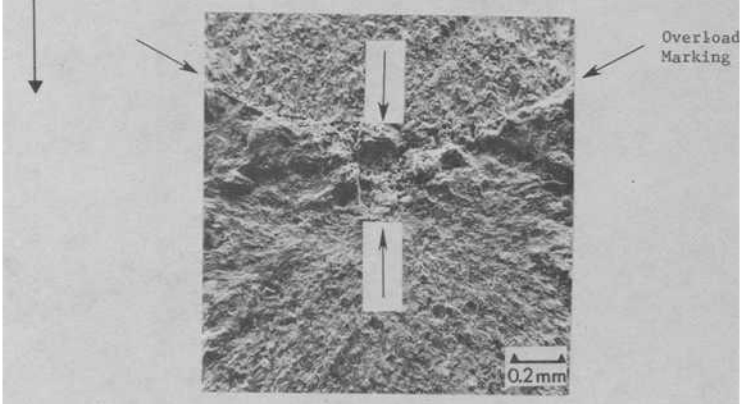

(b) Overload Ratio = 2.5

Baseline P_{max} (K_{max}) = 2224N (13.5 MN/m$^{-3/2}$)

FIG. 13—*Fractographic features in the vicinity of an overload cycle in 7075-T6 at OLR of 2.0 and 2.5 in saltwater.*

No striations were observed in the area immediately after the overload cycle, nor at crack-growth rates below 5 × 10^{-5} mm/cycle for tests conducted in air. Very few striations were observed in the vicinity of the overload cycle for tests conducted in saltwater. The lack of discernible striations for tests in air could be either due to (*a*) abrasion, (*b*) the difficulty in resolving striations using a SEM at crack-growth rates below 5 × 10^{-5} mm/cycle, (*c*) a change in crack-propagation mode, or (*d*) a combination of all these factors. In the case of the saltwater specimens, the striations probably were not seen due to the corroding attack of saltwater. The aggressive environment in these tests apparently did not allow the blunting and resharpening

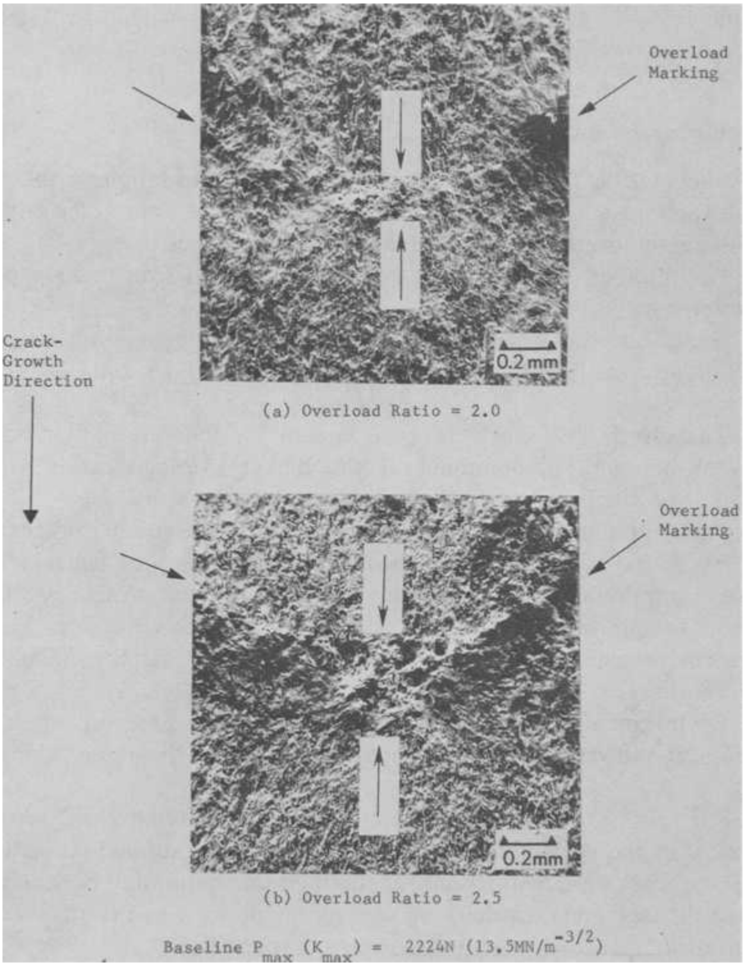

(a) Overload Ratio = 2.0

(b) Overload Ratio = 2.5

Baseline P_{max} (K_{max}) = 2224N (13.5MN/m$^{-3/2}$)

FIG. 14—*Fractographic features in the vicinity of an overload cycle in 7075-T73 at OLR of 2.0 and 2.5 in saltwater.*

mechanisms responsible for striation formation to operate. Nevertheless, for the specimens in which striations were discernible, the agreement between measured *da/dN* and striation spacings was good.

From these observations, it appears that the general nature of the fractographic features in relation to OLR and K_{max} values is similar in both air and saltwater, except that, at the lower OLR and K values, the overload markings were not visible in saltwater. This lack of overload marking was more prevalent in the 7075-T6 alloy, which is highly susceptible to environmental attack. Furthermore, in saltwater tests, the deterioration of fractographic features due to environmental attack was evident and striations were not clearly discernible.

Summary and Conclusions

1. Single tensile overload cycles cause retardation of fatigue-crack growth in saltwater just as they do in air. The number of delay cycles increase with increased overload ratios in both air and saltwater.
2. The number of delay cycles is greater in air than in the 3½ percent saltwater tests.
3. The effect of a corrosive environment on the retardation behavior was much greater in the 7075-T6 alloy than in the 2024-T8 and 7075-T73 alloys.
4. The effect of a corrosive environment on the retardation behavior tends to be more predominant at the higher overload ratios where it could not be attributed to the higher saltwater FCP rates alone.
5. The degree of susceptibility of a microstructure to environmental attack was found to be important in determining its fatigue behavior under variable amplitude loading in a corrosive environment. An alloy which is superior to another alloy in air can be inferior to the same alloy in a corrosive environment such as saltwater, as was found for the 7075-T6 and 2024-T8 alloys.
6. Environmental attack similar to that which is observed on fracture surfaces of saltwater FCP specimens was found on the retardation specimens.
7. For tests in air, the overload cycle causes a stretch band across the thickness of the specimen in almost all of the cases studied. In saltwater, these markings were distinct only at the high OLR and high K values. This lack of distinct overload marking was more common in the 7075-T6 alloy due to its high susceptibility to environmental attack.

Acknowledgments

This work was supported, in part, by the Air Force Materials Laboratory, Air Force Systems Command, U.S. Air Force, Wright-Patterson Air Force Base, Ohio, with D. M. Corbly as the project engineer. Thanks are due to J. Clift and B. J. Mays for performing the mechanical testing and J. Schifando for performing the fractography.

References

[*1*] Schijve, J., "Fatigue Crack Propagation in Light Alloy Sheet Materials and Structures," Report MP-195, National Luchtvaartlaboratorium, Amsterdam, 1960.

[*2*] Hudson, C. M. and Raju, K. N., "Investigation of Fatigue-Crack Growth Under Simple Variable-Amplitude Loading," NASA TN-D-5702, National Aeronautics and Space Administration, March 1970.

[*3*] Hardrath, H. F. in *Fatigue—Interdisciplinary Approach*, Syracuse University Press, Syracuse, N.Y., 1964.

[*4*] Von Euw, E. F. J., Hertzberg, R. W., and Roberts, R. in *Stress Analysis and Growth of Cracks, ASTM STP 513*, American Society for Testing and Materials, 1972, p. 230.

[*5*] Corbly, D. M. and Packman, P. F., *Engineering Fracture Mechanics*, Vol. 5, 1972, p. 479.

[*6*] Rice, R. C. and Stephens, R. I. in *Progress in Flaw Growth and Fracture Toughness Testing, ASTM STP 536*, American Society for Testing and Materials, 1973, p. 95.

[*7*] Shih, T. T., "Fatigue-Crack Growth Under Variable Amplitude Loading," PhD thesis, Lehigh University, 1974.

[*8*] Chanani, G. R., *Metals Engineering Quarterly*, Vol. 15, 1975, p. 40.

[*9*] Jonas, O. and Wei, R. P., *International Journal of Fracture Mechanics*, Vol. 7, 1971, p. 116.

[*10*] Probst, E. P. and Hillberry, B. M., "Fatigue Crack Delay and Arrest Due to Single Peak Tensile Overloads," AIAA Paper No. 73-325, American Institute of Aeronautics and Astronautics, March 1973.

[*11*] Gallagher, J. P. and Hughes, T. F., "The Influence of Yield Strength on Overload Affected Fatigue-Crack Growth Behavior in 4340 Steel," AFFDL-TR-74-28, Air Force Flight Dynamics Laboratory, 1974.

[*12*] Schijve, J. in *Fatigue-Crack Growth Under Spectrum Loads, ASTM STP 595*, American Society for Testing and Materials, 1976, pp. 3-23.

[*13*] Schijve, J., *Engineering Fracture Mechanics*, Vol. 5, 1973, p. 269.

[*14*] Wheeler, O. E., *Transactions*, American Society of Mechanical Engineers, *Journal of Basic Engineering*, Paper No. 71-Met-X.

[*15*] Willenborg, J., Engle, R. M., and Wood, H. A., "A Crack Growth Retardation Model Using and Effective Stress Concept," AFFDL-TM-71-1-FBR, Air Force Flight Dynamics Laboratory, 1971.

[*16*] Porter, T. R., *Engineering Fracture Mechanics*, Vol. 4, 1972, p. 717.

[*17*] Bell, P. D. and Creager, M., "Crack-Growth Analysis for Arbitrary Spectrum Loading," AFFDL-TR-74-129, Air Force Flight Dynamics Laboratory, Oct. 1974.

[*18*] Antolovich, S. D., Saxena, A., and Chanani, G. R., *Engineering Fracture Mechanics*, Vol. 7, 1975, p. 649.

[*19*] Chanani, G. R., Antolovich, S. D., and Gerberich, W. W., *Metallurgical Transactions*, Vol. 3, 1972, p. 2661.

[*20*] Hall, L. R., Finges, R. W., and Spurr, W. F., "Corrosion Fatigue-Crack Growth in Aircraft Structural Materials," AFML-TR-204, Air Force Materials Laboratory, Sept. 1973.

[*21*] Raju, K. N., Ningiah, V., and Rao, B. V. S., *International Journal of Fracture Mechanics*, Vol. 8, 1972, p. 99.

K. Endo[1] *and K. Komai*[1]

Influences of Secondary Stress Fluctuations of Small Amplitude on Low-Cycle Corrosion Fatigue

REFERENCE: Endo, K. and Komai, K., "**Influences of Secondary Stress Fluctuations of Small Amplitude on Low-Cycle Corrosion Fatigue,**" *Corrosion-Fatigue Technology, ASTM STP 642,* H. L. Craig, Jr., T. W. Crooker, and D. W. Hoeppner, Eds., American Society for Testing and Materials, 1978, pp. 74-97.

ABSTRACT: The influences of small superimposed stress fluctuations on low-cycle corrosion fatigue under trapezoidal waveform are varied by the susceptibility of the test materials to stress corrosion cracking (SCC).

The corrosion-fatigue life of the materials which are insensitive to SCC is greatly diminished if small stress fluctuations are superimposed. The crack initiation is shortened somewhat by such a superposition.

In materials sensitive to SCC, the corrosion-fatigue life is almost occupied by the crack growth period, and the crack rate greatly decreases with the superposition of small stress fluctuations under K_{max} higher than K_{ISCC}. Under low K_{max} which is nearly equal to K_{ISCC}, the similar characteristics to that of the materials insensitive to SCC are obtained. The effects of stress change on corrosion fatigue component and SCC component have been discussed.

KEY WORDS: corrosion fatigue, superimposed stress fluctuation, stress corrosion, crack initiation, crack propagation, corrosion potential, fractography, corrosive dissolution

In low-cycle corrosion fatigue, the fatigue strength generally is affected more by the stress waveform than by the stress frequency. On this subject, the authors already have reported in a series of low-cycle corrosion fatigue tests under trapezoidal stress waves. In a single stress cycle, the period of zero stress, the period during which the stress is changed, and the period of application of maximum stress, each has a significant effect on the specimen life [*1*].[2] The damaging effect of the period during which the stress is changing is the most conspicuous, while the protective effect of the stress-

---

[1] Professor and assistant professor, respectively, Department of Mechanical Engineering, Kyoto University, Kyoto, Japan.

[2] The italic numbers in brackets refer to the list of references appended to this paper.

free period and the maximum stress period decrease corrosion-fatigue damage. However, for some materials sensitive to stress corrosion cracking (SCC), the maximum stress period inflicts a very heavy damage to the fatigue life.

In practical conditions, machines and structures frequently operate in corrosive environment under stress of trapezoidal waveform, of extremely low frequency, with secondary stress fluctuations of small amplitude superimposed. For example, a piston crown of a diesel engine is subjected to thermal stress of large amplitude at start and stop, with the superposition of repetitive stress of high frequency in cooling water. In such a case the damages due to the changing stress in cycle are surmised from the results just mentioned.

In the present study, low-cycle corrosion-fatigue tests were performed on a high-strength steel which was insensitive to SCC and a high-strength aluminum alloy which was sensitive to SCC. The test stress was tensile stress of trapezoidal waveform, with the superposition of the secondary sinusoidal stress of small amplitude. Cycle frequency and amplitude of the superimposed stress fluctuations were varied, and their influences on corrosion-fatigue life and crack-growth characteristics were discussed from the fractured surface morphology and the behavior of corrosion potential.

Experimental Procedure

Materials and Specimens

Materials tested were a high-strength steel and a high-strength aluminum alloy. The high-strength steel was insensitive to SCC and the high-strength aluminum was sensitive to SCC. Chemical compositions of these two materials are shown in Table 1. The hot-rolled high-strength steel was used without any heat treatment, while the high-strength aluminum alloy was quenched in water at 0°C (32°F) from 450°C (842°F) after annealing at 560°C (1040°F) for 24 h to raise the susceptibility to SCC and

TABLE 1—*Chemical compositions of test materials, weight percent.*

HIGH STRENGTH STEEL				
C	Si	Mn	P	S
0.17	0.58	0.87	0.016	0.012

HIGH STRENGTH ALUMINUM ALLOY								
Cu	Fe	Si	Mn	Mg	Zn	Cr	Ti	Zr
0.01	0.22	0.06	0.32	2.02	4.08	0.01	0.01	0.17

finally was aged at 70°C (158°F) for 48 h. Mechanical properties at the final conditions are shown in Table 2.

TABLE 2—*Mechanical properties of test materials.*

	Yield Strength, kg/mm^2 (MN/m^2)	Tensile Strength, kg/mm^2 (MN/m^2)	Elongation, %	Reduction of Area, %
High strength steel	51 (500)	63 (617)	24	59
High strength aluminum alloy	24 (235)	35 (343)	15	...

The smooth specimen shown in Fig. 1(*a*) was used to estimate corrosion fatigue lives to fracture under uniaxial stresses. The notch specimens shown in Fig. 1(*b*) and (*c*) were used to measure the crack growth rate in corrosive environment. The double-edge notch specimen was used for

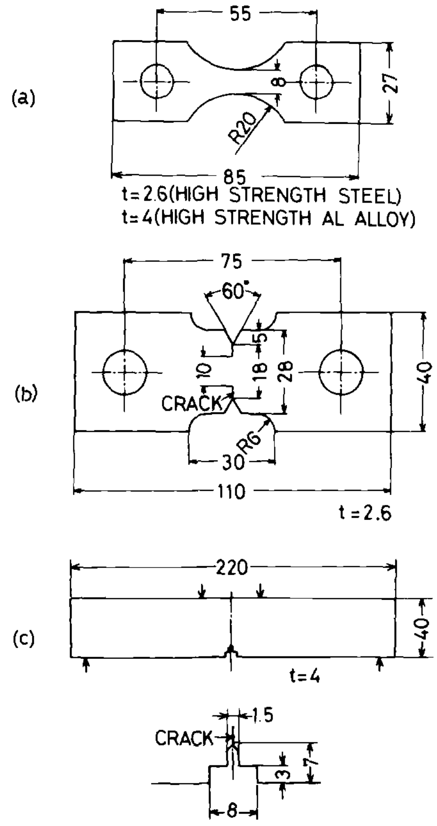

FIG. 1—*Shape and dimensions of specimens.*

the high-strength steel under uniaxial stress. The single-edge notch specimen was used for the high-strength aluminum alloy under in-plane bending. These notch specimens were subjected to pulsating stresses of sufficiently small stress intensity at 1800 cycles per minute (cpm) in air to prepare fatigue cracks 2 ~ 4 mm in length in advance of corrosion-fatigue tests.

Stress Waveform

Stress waveform is shown in Fig. 2. For the high-strength steel, the cycle frequency of the stress of trapezoidal waveform, the primary stress, was 1/60 cpm for smooth specimens and 1/30 cpm for notch specimens.

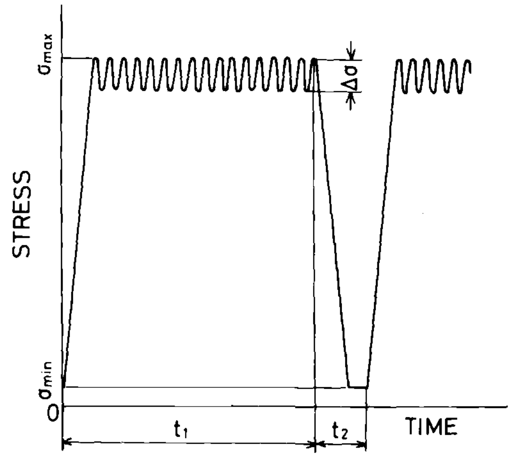

FIG. 2—*Stress waveform.*

The interval, t_1, including the time to increase the stress from zero to maximum stress and the interval t_2, including the time of zero stress, were equal for smooth and notch specimens. The time during which the stress was changed was about 4 min. For the high-strength aluminum alloy, the frequency of the primary stress was 1/30 cpm, and the intervals, t_1 and t_2, were 25 and 5 min, respectively, for smooth and notch specimens. In this case, the stress changing time was about 3 min for the smooth specimen and 1 min for the notch specimen. The minimum stress, σ_{min} was equal to 1 kg/mm^2 (9.8 MN/m^2) for the smooth specimen and the stress ratio, $R = K_{min}/K_{max}$, was 0.1 for the notch specimen. The superimposed stresses of small amplitude, secondary stress, were sinusoidally cycled with frequencies of 200, 40, and 3.9 cpm. The maximum value of the secondary stress was equalized to the maximum value of the primary stress as is shown in Fig. 2. Corrosion-fatigue tests were carried out for a variety of total amplitude of superimposed small wave $\Delta\sigma$ under the constant maximum stress σ_{max}.

Corrosive Environment

A corrosive environment consisting of 1 percent sodium chloride (NaCl) solution in deionized water was poured on the upper surface of a horizontally gripped smooth specimen whose both sides and lower surface were coated by synthetic rubber coating. The precracked notch specimen was immersed in the solution. The length of the corrosion-fatigue crack was measured by a traveling microscope on the surface protected from corrosion with transparent tape. The temperature of the solution was kept constant at 25°C (77°F), and the flow rate was approximately 70 cm^3/min for the smooth specimen and 300 cm^3/min for the cracked specimen.

Corrosion potential of specimens was measured against a saturated calomel electrode (SCE) with a capillary located on the minimum section of the specimens. The potential was recorded on a pen-writing recorder through an electrometer of imput impedance greater than 10^9 Ω.

High Strength Steel

Corrosion-Fatigue Life

The relation between the total amplitude of secondary superimposed stress $\Delta\sigma$ at various cycle frequencies and the lives of corrosion fatigue is shown in Fig. 3 for the high-strength steel under the maximum stress σ_{max} of 60 kg/mm² (588 MN/m²). Since the frequency of the primary stress was

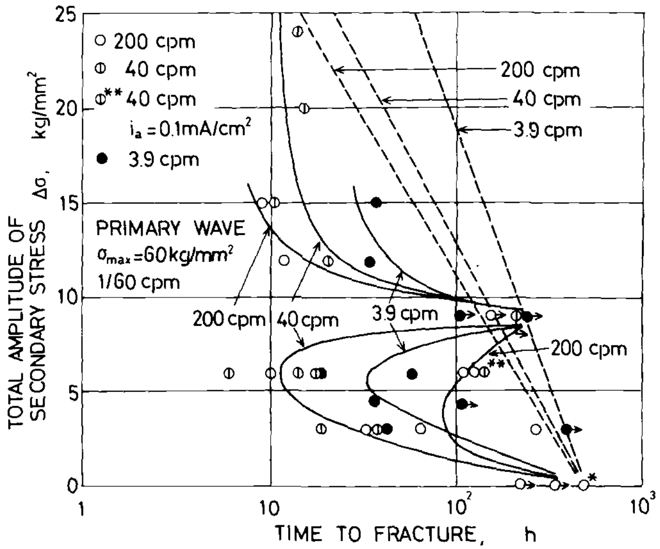

FIG. 3—*Relation between total amplitude of secondary stress and fatigue life.*

1/60 cpm, the life time in hours coincided with the cycles to fracture of the primary wave. As is shown in the figure, the corrosion-fatigue life decreased with a small superposition of $\Delta\sigma$, and it unexpectedly increased at near $\Delta\sigma = 9$ kg/mm^2 (88 MN/m^2). The fatigue lives reduced again as $\Delta\sigma$ grew greater than 9 kg/mm^2. Its lowering was greater at a higher frequency of secondary stress, which is a well known characteristic in usual corrosion fatigue [*2*].

The hollow cirlce with an asterisk under $\Delta\sigma = 0$ shows the number of cycles to fracture at 1/10 cpm. The period spent under maximum stress and the stress-free period were shortened while the changing stress period was the same as the tests at 1/60 cpm. The life cycles at 1/60 cpm can be supposed nearly equal to the one at 1/10 cpm, $N = 4.9 \times 10^2$, because the frequency effect is very small and the period during which the stress is changing has dominant effect in such an extremely low-cycle corrosion fatigue [*1,3*]. The life cycle under the primary wave alone, that is, $\Delta\sigma = 0$, will be equal to the one under $\Delta\sigma = 60$ kg/mm^2, when the effects of waveform and frequency are ignored. The life cycles under $\Delta\sigma = 60$ kg/mm^2 were reduced to the time to fracture at the three frequencies. Broken lines that link the reduced life time under $\Delta\sigma = 60$ kg/mm^2 with the hollow circle with an asterisk under $\sigma_{\max} = 60$ kg/mm^2, $\Delta\sigma = 0$, also are shown in Fig. 3. The straight lines were considered to show the relation between $\Delta\sigma$ and fatigue lives in air [*4*]. However, the damages due to superimposed stress $\Delta\sigma$ of small amplitude appeared extraordinarily greater in corrosion fatigue than those shown by broken lines. It is quite clear that the damages due to superimposed stresses are intense in corrosion fatigue.

All of the fatigue lives under $\Delta\sigma = 9$ kg/mm^2 (88 MN/m^2) lie on the safety side of the straight lines at any frequency of secondary stress. In Fig. 3, the result with ** at 40 cpm under $\Delta\sigma = 6$ kg/mm^2 (59 MN/m^2) shows the life under the anodic current of 0.1 mA/cm^2, which was imposed on the specimen by an auxiliary electrode under current-controlled conditions from the beginning of the test. A remarkably increased fatigue life of about 10 times was obtained under the impression of anodic current. These results will be discussed later.

Corrosion-fatigue cracks propagating in the inclined angle of 45 deg from specimen surfaces were observed sometimes on the cross section of the specimen. However, none of corrosion-fatigue cracks were found on all of the specimen under $\Delta\sigma = 9$ kg/mm^2, though numerous corrosion pits were generated. An example of the cross section under $\Delta\sigma = 9$ kg/mm^2 is shown in Fig. 4.

From the observations just mentioned, the reason why the corrosion-fatigue damages did not increase monotonously with an increase of $\Delta\sigma$ is considered as follows. Under $\Delta\sigma$ smaller than 9 kg/mm^2, the damages by corrosion fatigue were initiated and propagated by only the repetition of primary stress since $\Delta\sigma$ was negligibly small compared with the amplitude

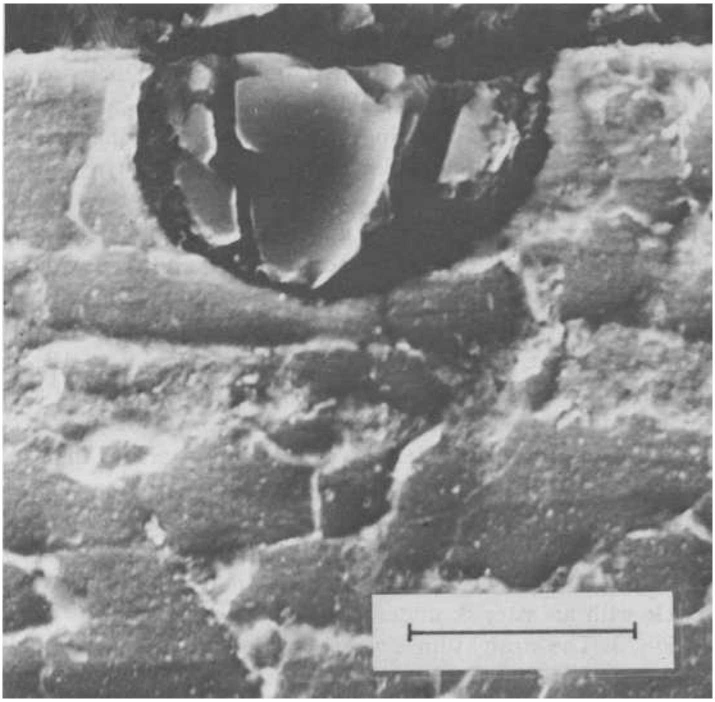

FIG. 4—*Corrosion pit,* $\Delta\sigma = 9$ *kg/mm*^{2}*, 3.9 cpm (scale mark indicates 10 μm).*

of primary stress; and the role of the secondary stress was considered mainly the acceleration of corrosion rate. The surface oxide film which had been weakened by changing stress of the primary wave may have been recovered during a period of maximum stress when $\Delta\sigma = 0$. The recovery of surface oxide film was hindered by the small fluctuation of $\Delta\sigma$. These are proved from a remarkable shift of the corrosion potential to negative (active) side and the increased weight loss of specimens after fatigue tests with an increase of $\Delta\sigma$ as discussed later. The retardation of recovery of oxide films accelerated the fatigue crack initiation during the period of changing stress in the next loading cycle of primary wave. This resulted in a decrease of the corrosion-fatigue life with an increase of $\Delta\sigma$. However, this increased corrosive attack may have removed the nuclei of corrosion-fatigue cracks which were initiated in the loading interval of primary wave. When the removal of crack nuclei is more dominant than the corrosion damage, crack initiation is suppressed and corrosion fatigue lives will be prolonged. In the present experiment, the condition was found under $\Delta\sigma = 9$ kg/mm^2.

When $\Delta\sigma$ becomes greater than 9 kg/mm^2, the mechanical fatigue damages due to the secondary stress are conspicuous. The secondary stress also plays a role to initiate corrosion fatigue cracks, and shortens the fatigue life.

It is affirmed from the behavior under applied anodic current in Fig. 3 that an intensified corrosion attack does not always decrease the corrosion-fatigue life but a suitable acceleration of corrosion rate may increase the life. Under $\Delta\sigma$ = 6 kg/mm^2 (59 MN/m^2) at 40 cpm, the impressed anodic current of 0.1 mA/cm^2 brings about a 10 times increase of fatigue life.

Crack Growth Characteristics of Corrosion Fatigue

The corrosion-fatigue life consists of crack initiation period and crack propagation period. The results in the previous section were mainly on the crack initiation period since the tests were performed on smooth specimens under a very high stress level. Final fracture occurred very soon after discovering cracks on the specimen surface. The crack propagation behaviors also should be studied under corrosion fatigue. Corrosion-fatigue crack rate was measured by using notch and precracked specimens under the trapezoidal waveform of maximum stress intensity factor, K_{max}, superimposed with secondary stress intensity factor, Δk. K_{max} = 96 ~ 108 kg/mm$^{3/2}$ (30 ~ 33.6 MN/m$^{3/2}$) was given in the same changing stress period as the one in the smooth specimen. The cycle frequency of the primary stress was 1/30 cpm and Δk was superimposed at 40 cpm. The ratios of $\Delta k/K_{max}$ were 0.25, 0.15, 0.1, and 0, which are the same as those of $\Delta\sigma/\sigma_{max}$ used in smooth specimen.

The relation between Δk and the crack growth rate against primary wave cycle, dl/dN, is shown in Fig. 5. Under $\Delta k < 10$ kg/mm$^{3/2}$ (3.1 MN/m$^{3/2}$) the crack growth rate seemed nearly constant because of its small value and no influence of the secondary stress was found on crack growth. There was no peculiar feature in crack rate as in fatigue life shown in Fig. 3 even under $\Delta k/K_{max}$ = 0.15 that corresponded to $\Delta\sigma/\sigma_{max}$ = 0.15, $\Delta\sigma$ = 9 kg/mm^2. The balanced condition between the mechanical action and the corrosion attack previously discussed in the smooth specimen at $\Delta\sigma/\sigma$ = 0.15 is known to be due to the retardation of crack initiation.

Photographs of fractured surfaces of precracked specimens by a scanning electron microscope are shown in Fig. 6. The surfaces were obtained with the specimens fractured in liquid nitrogen (N_2) after fatigue testing. Figure 6(*a*) at Δk = 0 shows fatigue striations whose averaged spacing is about 1μm and nearly equal to the crack rate against the primary stress cycle. Figure 6 (*b*) at $\Delta k/K_{max}$ = 0.15 also shows the striations, but the averaged spacing is about 0.2 ~ 0.4 μm, that is, one order smaller than the crack rate against the primary stress. This indicates the effects of the secondary stress on crack growth.

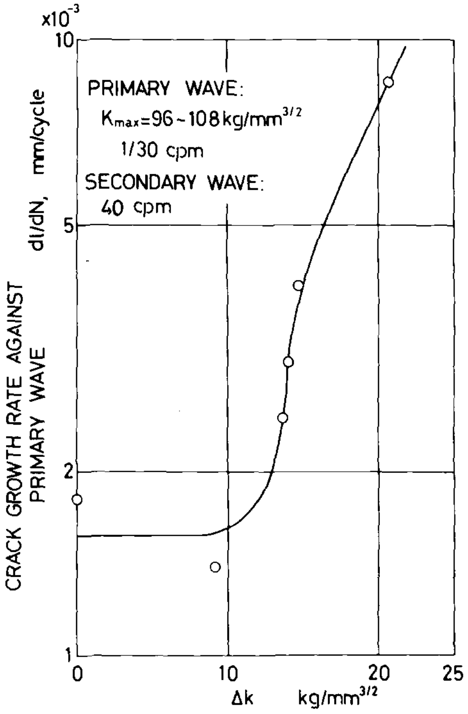

FIG. 5—*Relation between* Δk *of secondary wave and* dl/dN *against primary wave.*

Corrosion Potential

Corrosion potential of a smooth specimen against a SCE has been measured under various values and cycle frequencies of $\Delta\sigma$. An example of the results is shown in Fig. 7. The authors already have reported that the corrosion potential of steel shifts more rapidly in active direction under the greater amplitude of repeated strain and that the corrosion-fatigue damage grows greater when the corrosion potential shifts more rapidly in an active direction [*1*]. In the present experiment, the repetition of only the primary stress shifted the corrosion potential in a more active direction than that under static corrosion. The superposition of secondary waves of $\Delta\sigma$ further accelerated the shift of the potential in an active direction rather than the one under $\Delta\sigma = 0$. After the most active potential under $\Delta\sigma = 6 \sim 9$ kg/mm^2 (59 ~ 88 MN/m^2), the recovery and another shift of the potential appeared with the further increase of $\Delta\sigma$.

The weight loss of the specimen after the fatigue tests is shown in Fig. 8. In accordance with the tendency of corrosion potential, the weight loss increased with the superposition of secondary waves from $\Delta\sigma = 0$ to $\Delta\sigma = 9$ kg/mm^2. In the figure, corrosion rate under static corrosion of carbon steels in salt water [*6*] is shown by a hatched area. The weight loss under

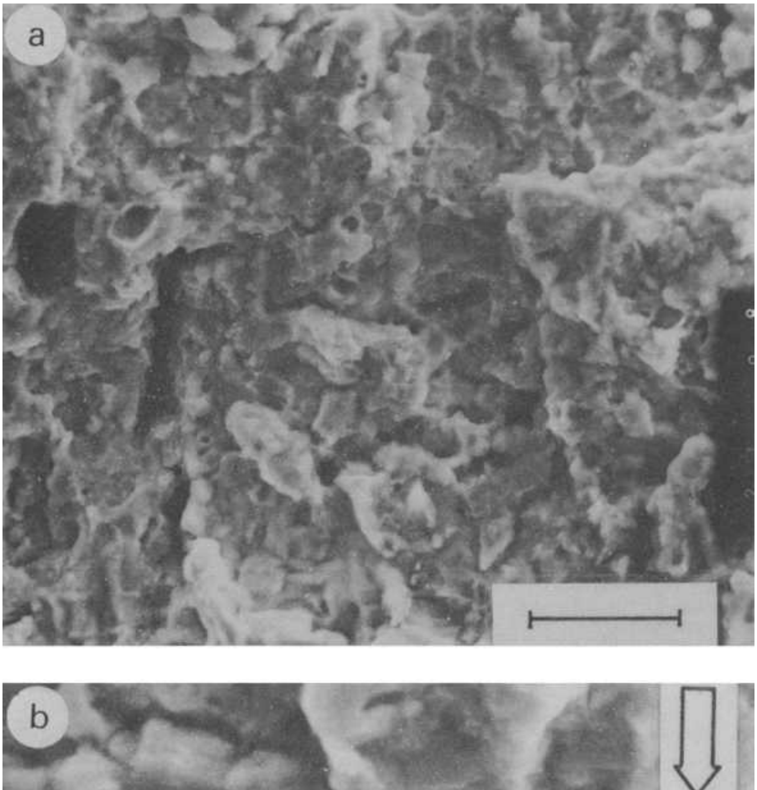

FIG. 6—*Fractured surfaces of precracked specimens.* (a) $\Delta k = 0$ *(scale mark indicates 20 μm).* (b) $\Delta k/K_{max} = 0.15$ *(scale mark indicates 5 μm). Arrow shows direction of crack growth.*

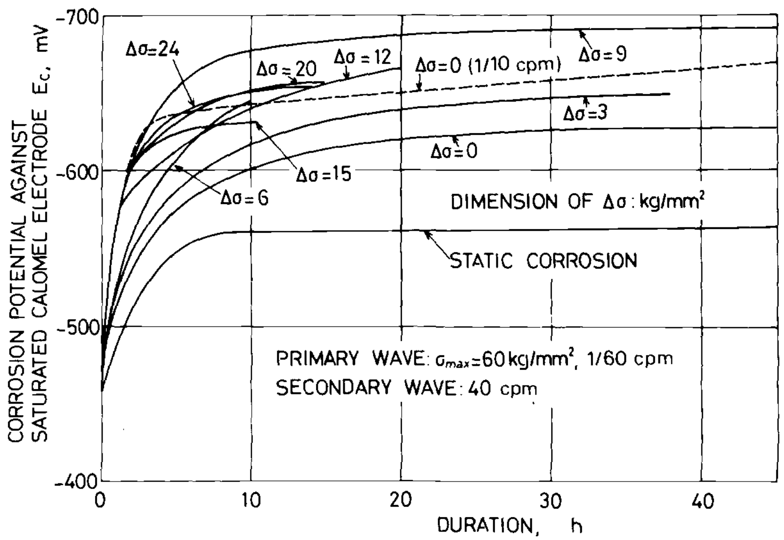

FIG. 7—*Variation of corrosion potential.*

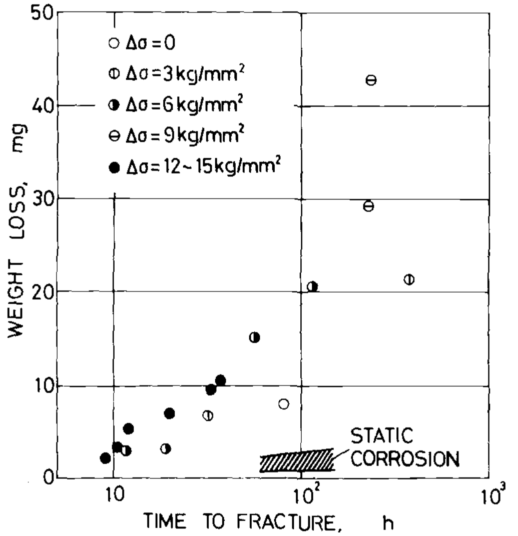

FIG. 8—*Relation between weight loss of specimens and time to fracture.*

the primary stress alone ($\Delta\sigma = 0$) was also greater than that under static corrosion. When secondary waves grew greater than 9 kg/mm^2, fatigue cracks initiated by secondary waves brought localized corrosion attack, and the rate as a whole decreased. The maximum weight loss at $\Delta\sigma = 9$ kg/mm^2 corresponds to the variation of corrosion potential in Fig. 7. Though the corrosion potential under superimposed secondary waves has a partly obscure behavior, the superimposed small waves are concluded to accelerate the corrosive attack. The greater corrosion rate under these conditions alarmed the fracture due to corrosive thinning of materials.

High Strength Aluminum Alloy

Corrosion-Fatigue Life

The high strength aluminum alloy used here is very sensitive to SCC in NaCl solution. The SCC test result of a smooth specimen is shown in Fig. 9. The threshold stress σ_{SCC} was approximated by 28 kg/mm^2 (274 MN/m^2) for 6 × 10^4 min.

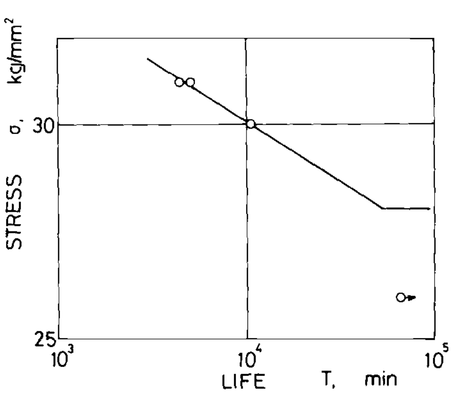

FIG. 9—*Relation between sustained stress and time to fracture.*

The results of the corrosion fatigue test are illustrated in Fig. 10. The relations between $\Delta\sigma$ at 40 cpm and the number of primary stress cycles to fracture under the maximum stress σ_{max} of 31 kg/mm^2 (304 MN/m^2) and 26 kg/mm^2 (255 MN/m^2) are shown. Contrary to the results of the high strength steel, the corrosion fatigue life under σ_{max} = 31 kg/mm^2 increased with the superposition of small $\Delta\sigma$. The increased life, however, decreased as $\Delta\sigma$ grew greater than 5 kg/mm^2 (49 MN/m^2). When $\Delta\sigma$ became considerably greater, the lives were determined solely by $\Delta\sigma$, which was proven from the almost equal life under $\Delta\sigma$ = 20 kg/mm^2 (196 MN/m^2) irrespective of σ_{max}.

The similar characteristics to those of the high strength steel previously described were observed under σ_{max} = 26 kg/mm^2. The life decreased with the superimposed $\Delta\sigma$ of small amplitude, but the decrease was slight in comparison to the case of high strength steel. The maximum stress was smaller than σ_{SCC}, but after the corrosion-fatigue cracks were initiated by

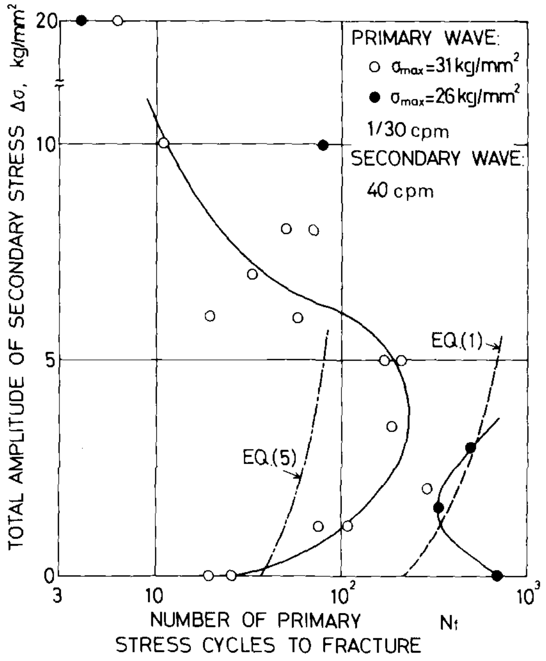

FIG. 10—*Relation between total amplitude of secondary stress and fatigue life.*

the primary stress change of large amplitude, the net stress at crack tips exceeded σ_{SCC}. This brings the intermediate characteristics between the one under $\sigma_{max} = 31$ kg/mm^2 and the one of the high strength steel.

SCC damage under $\sigma_{max} = 31$ kg/mm^2 was computed from the load profile of Fig. 2 when the stress greater than σ_{SCC} was considered to bring about SCC damage. The SCC damage during time interval $a \leq t \leq b$ under the stress pattern $\sigma = f(t)$ is expressed as

$$D_s = \int_a^b \{1/T(\sigma)\}dt = \int_a^b [1/T\{f(t)\}]dt \tag{1}$$

where T is the SCC life, and the final fracture is supposed to occur when D_s reaches unity. From Fig. 9

$$\left.\begin{aligned} T &= 10^{(41.64 - \sigma)/2.89} \text{ (min)} \\ \sigma_{SCC} &= 28 \text{ kg/mm}^2 \text{ (274 MN/m}^2\text{)} \end{aligned}\right\} \tag{2}$$

are obtained. As the SCC damage per one cycle, d_s, equaled D_s/N, the corrosion fatigue life was obtained. The estimated value of N for a variety of $\Delta\sigma$ under $\sigma_{\max} = 31$ kg/mm^2 is shown by a broken curve in Fig. 10. The difference between the estimated value and the experimental one is extraordinarily large especially under $\Delta\sigma = 0$. The differences show the damage of changing stress in primary stress wave on SCC resistance [1].

Corrosion-fatigue tests were carried out by varying the period spent under maximum stress in each trapezoidal stress wave while the period under minimum stress and the changing stress period were kept constant. Figure 11 illustrates the relation between the number of primary stress cycles to fracture, N_f, and the total time of application of maximum stress, Σt_{max}, under $\sigma_{\max} = 31$ kg/mm^2 (304 MN/m^2). The static SCC life is regarded as 1 cycle and the value of $\Sigma t_{\max}$ on the abscissa gives the SCC life. If the damage is caused by SCC during the period spent under maximum stress and the damage due to the primary stress change of trapezoidal form can be ignored, the total time of application of maximum stress, $\Sigma t_{\max}$, must be equal to the life time of SCC even if the period spent under maximum stress in a single cycle is varied. However, the experimental result of $\Sigma t_{\max}$ is decreased remarkably by the stress change of the primary wave, thus proving the conspicuous effect of stress change on SCC damages. This is the main reason for the great difference between the computed broken line and the experimental results in Fig. 10.

Now the damage of the stress change is reduced from Fig. 11 as follows. From Fig. 11, the total time spent under $\sigma_{\max} = 31$ kg/mm^2, $\Sigma t_{\max}$, is expressed as

$$\Sigma t_{\max} = 4790\, N^{-0.495} \text{ (min)} \tag{3}$$

where N shows the number of primary stress cycles. Since the life under static SCC is estimated at 4790 min, N times changes of primary waves are found to correspond to the SCC damage for $4790 - 4790\, N^{-0.495}$ min. If fatigue damage is assumed to accumulate linearly with the progress of stress cycles, the damages due to N times repetitions of primary waves are reduced as

$$(4790 - 4790\, N^{-0.495})/4790 = 1 - N^{-0.495} \tag{4}$$

Consequently the final fracture is supposed to occur when the sum of the damage due to N_f times repetitions of primary waves, $1 - N_f^{-0.495}$, and that of SCC damage due to N_f times of primary waves, $N_f d_s$, reaches unity.

$$\begin{gathered}(1 - N_f^{-0.495}) + N_f d_s = 1 \\ N_f = 10^{-(\log d_s)/1.495}\end{gathered} \tag{5}$$

The broken line in Fig. 10 is thus modified as the chain line. The chain

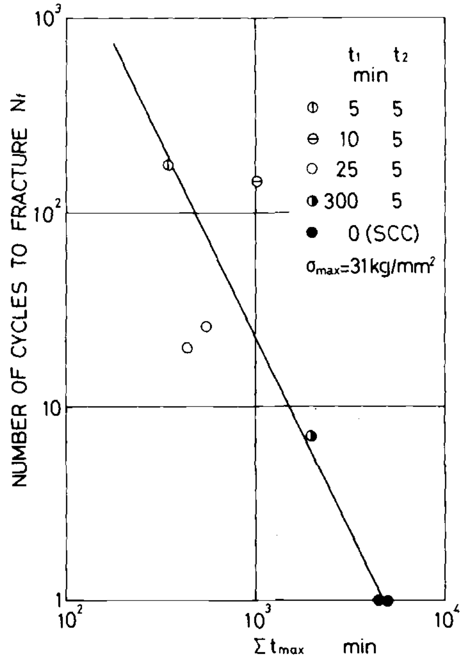

FIG. 11—*Relation between number of primary stress cycles to fracture and total time of application of maximum stress.*

line gives the life close to the experimental one at $\Delta\sigma = 0$. However, the estimated life is found much smaller than the experimental results if small $\Delta\sigma$ is superimposed. This leads to the conclusion that the decrease of SCC damage due to the shrinkage of the high stress portion does not increase fatigue life under the superposition of $\Delta\sigma$ of small amplitude.

Fatigue tests under a variety of $\Delta\sigma$ were interrupted at the primary stress cycles $N = 10$ to observe the specimen surface. Figure 12 shows the surface in the vicinity of minimum cross section under $\sigma_{max} = 31$ kg/mm^2 (304 MN/m^2), $\Delta\sigma = 8$ kg/mm^2 (78 MN/m^2). Muliple distributed cracks with the open mouth perpendicular to principal stress were observed irrespective of the value of $\Delta\sigma$. Plastic-slip deformation due to the primary-stress change of large amplitude does weaken the surface passive films, which enhances SCC crack initiation at the start of fatigue tests. From stress-corrosion cracks formed earlier due to primary stress change, fatigue crack growth was initiated, when the primary stress was greater than σ_{SCC}. In consequence, the corrosion fatigue characteristics of the high strength aluminum alloy should be considered with the crack growth characteristics.

Crack Growth Characteristics of Corrosion Fatigue Combined with SCC

The relation between the range of stress intensity factor of primary wave, ΔK, and the crack growth rate against primary wave cycle, dl/dN, is shown

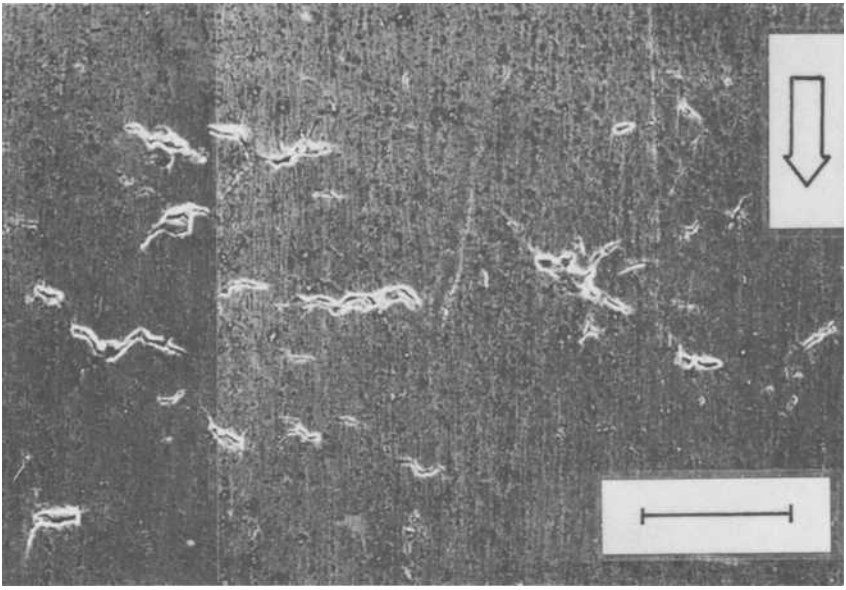

FIG. 12—*Corrosion fatigue cracks,* σ_{max} *= 31 kg/mm*^{2}*,* $\Delta\sigma$ *= 8 kg/mm*^{2}*,* N = *10 (scale mark indicates 200 μm). Arrow shows direction of principal stress.*

in Fig. 13 for a variety of ratios of $\Delta k/K_{max}$. The cycle frequencies of primary and secondary waves were 1/30 and 40 cpm, respectively. The crack rate dl/dN varied remarkably with ΔK at $\Delta k/K_{max} = 0$, since the SCC damage during the period spent under maximum stress was intense. As $\Delta k/K_{max}$ grew to 0.75, dl/dN became insensitive to Δk. This was due to growing influence of the secondary wave.

The relation between Δk and dl/dN is reduced from Fig. 13, which is shown in Fig. 14 with a parameter of K_{max}. When K_{max} was high, the crack rate remarkably decreased with the superpositon of small Δk, then it increased as Δk become greater. The crack rate was determined solely by Δk irrespective of K_{max} under considerably great Δk. These crack growth characteristics exceedingly corresponded to the behavior of fatigue life under σ_{max} = 31 kg/mm^2 shown in Fig. 10. When K_{max} was low, however, the crack rate became insensitive to Δk. Under K_{max} = 75 kg/mm$^{3/2}$ (23.2 MN/m$^{3/2}$) which is near K_{ISCC}, dl/dN was independent upon Δk being smaller than 5 ~ 6 kg/mm$^{3/2}$ (1.5 ~ 1.9 MN/m$^{3/2}$). This result also corresponds well to that of a precracked high strength steel shown in Fig. 5. Under SCC conditons, the influence of superimposed secondary waves is greatly varied by the maximum stress intensity.

Static stress corrosion crack growth characteristics are shown in Fig. 15. Crack growth rate, dl/dt, is expressed as $dl/dt = 2.45 \times 10^{-18} K^{7.26}$. The

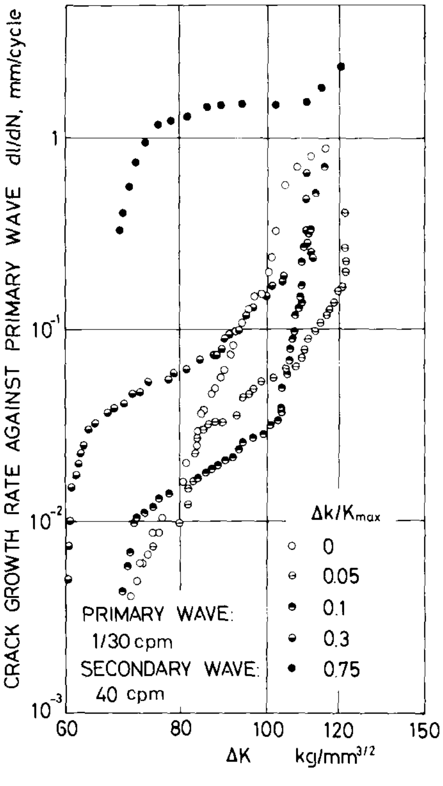

FIG. 13—*Relation between* ΔK *of primary wave and* dl/dN *against primary wave.*

value of K_{ISCC} below which no crack growth has been observed was estimated at 70 kg/mm$^{3/2}$ (21.7 MN/m$^{3/2}$).

SCC crack growth was computed from the load profile of Fig. 2 and the sustained load crack growth data of Fig. 15 with the assumption that the stress intensity greater than K_{ISCC} causes SCC crack growth [*6*]. The fine curves in Fig. 14 are the computed results. The curves correspond to the broken line in Fig. 10, where stress change of the trapezoidal wave is not under consideration. The crack growth of SCC enhanced by stress change is conspicuous at $\Delta k = 0$.

The rise and fall of the crack growth under high K_{max} may be caused by the following phenomena.

1. *Decrease of the SCC Component of Damage Due to the Shrinkage of High Stress Portion by* Δk, *Lowering of Mean Stress*—The decrease of crack growth rate with the increase of Δ*k* may be the effect of the shrinkage of high-stress portion on SCC damage. The crack rate under the superimposed stress fluctuations, however, cannot be estimated by the decrease of SCC damage. For example, *dl/dN* under K_{max} = 120 kg/mm$^{3/2}$ (37.2 MN/m$^{3/2}$),

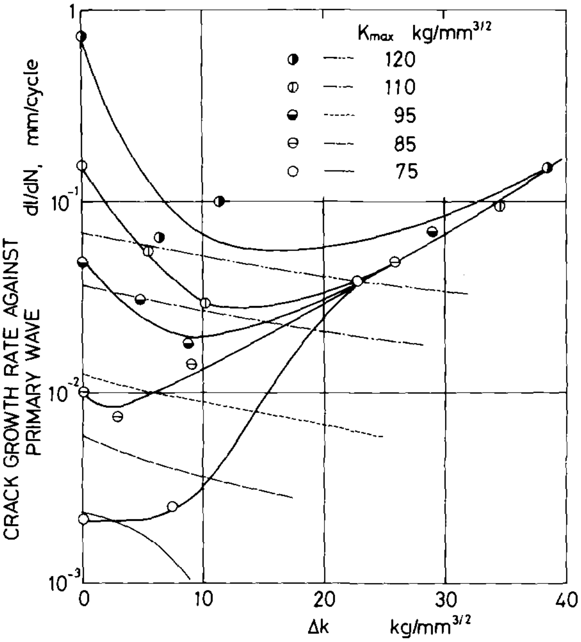

FIG. 14—*Relation between* Δk *of secondary wave and* dl/dN *against primary wave.*

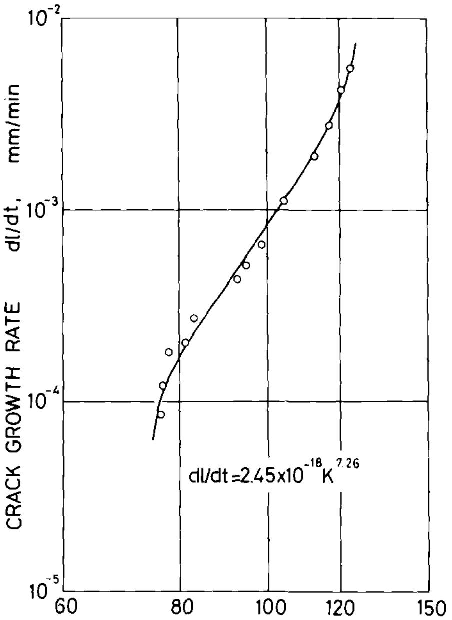

FIG. 15—*Static stress corrosion crack growth characteristics.*

$\Delta k = 10$ kg/mm$^{3/2}$ (3.1 MN/m$^{3/2}$) is smaller than that under $K_{\max} = 110$ kg/mm$^{3/2}$ (34.1 MN/m$^{3/2}$), $\Delta k = 0$. Though the decrease of SCC damage due to the shrinkage of high stress portion predicts the slight lowering of dl/dN shown by the computed curves in Fig. 14, it cannot account for the experimental results.

2. *Lowering of Actual* K *Value at Blunted Crack Tip Due to the Increased Corrosive Dissolution by the Superposition of* Δk—*Influence of Superimposed Stress Fluctuations on SCC Crack Growth*—The superimposed stress fluctuations may promote the corrosive dissolution at SCC crack tips. The actual K value of SCC crack may be lowered from the calculated one for a sharp crack by the blunting of crack tips. This subject will be referred to again in the following fractographical observation.

3. *Influence of Superimposed Stress Fluctuations on Corrosion-Fatigue Crack Growth*—When the superimposed stress fluctuations are great, they also accelerate the crack growth of corrosion fatigue. dl/dN is determined solely by Δk irrespective of $K_{\max}$ under Δk greater than 20 kg/mm$^{3/2}$ (6.2 MN/m$^{3/2}$).

From the consideration mentioned before, the damaging effect of the primary stress change of large amplitude on SCC damage is conspicuous under $\Delta k = 0$. The lowering of the crack rate with the superposition of small Δk is caused mainly by the second phenomenon, rather than the first phenomenon, as is discussed in the fractographical observation.

Fractographical Observation

The fracture area fractions have been estimated on photographs of fractured surfaces (×300). The classification of fractured surface morphologies are as follows.

1. Facet—In this experiment there existed only an intergranular facet
2. Transgranular cracking—Transgranular pattern was caused by not only mechanical stress but also corrosive dissolution
3. Dimple
4. Obscured pattern

The estimation of the fracture-area fraction is abandoned when the fraction of obscured pattern exceeds 0.3.

Figure 16 shows the scanning electron photomicrographs of central portions of fractured surfaces under $K_{\max} = 110$ kg/mm$^{3/2}$ (34.1 MN/m$^{3/2}$). The intergranular facet pattern and the secondary cracks along intergranular zone under $\Delta k = 0$ show SCC damage, where the facet area fraction is 0.75, Fig. 16(*a*). Under $\Delta k = 5.5$ kg/mm$^{3/2}$ (1.7 MN/m$^{3/2}$) the facet area fraction decreased to 0.57 and the corrosion products attached on the surface were observed, Fig. 16(*b*). Under $\Delta k = 10.4$ kg/mm$^{3/2}$ (3.2 MN/m$^{3/2}$) transgranular fracture mode became predominant and the corrosion products were thick, Fig. 16(*c*). Corrosive dissolution at crack tip is considered to

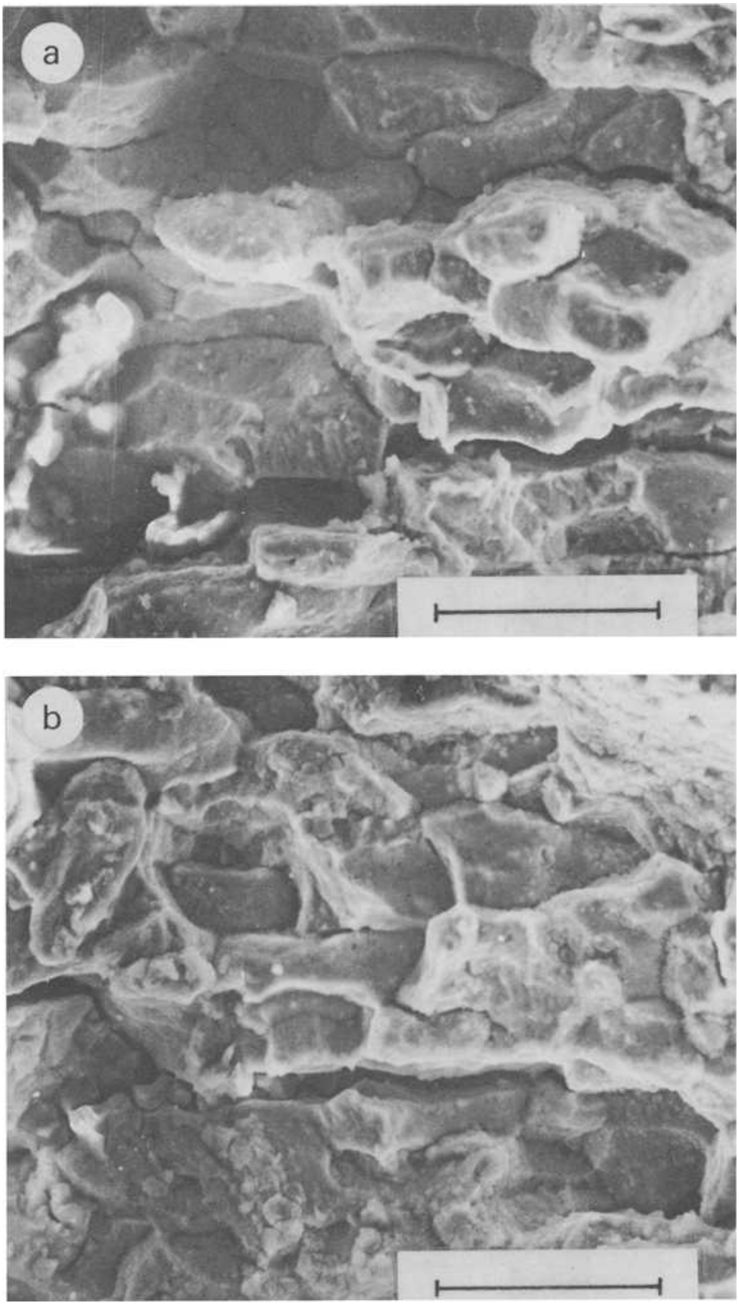

FIG. 16—*Fractured surfaces of precracked specimens.* $K_{max} = 110\ kg/mm^{3/2}$. (a) $\Delta k = 0$. (b) $\Delta k = 5.5\ kg/mm^{3/2}$. *Scale mark indicates 100 μm in all parts of this figure.*

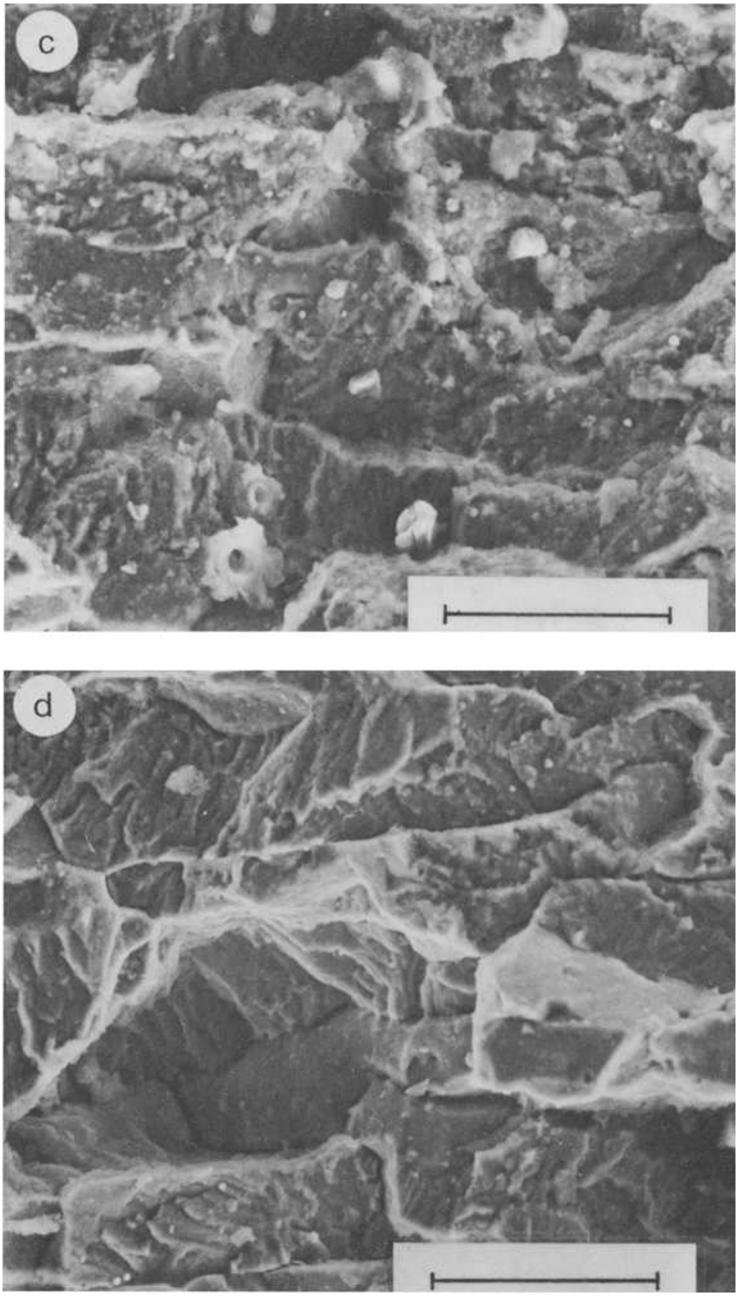

FIG. 16—(*Continued*) (c) $\Delta k = 10.4\ kg/mm^{3/2}$. (d) $\Delta k = 35\ kg/mm^{3/2}$.

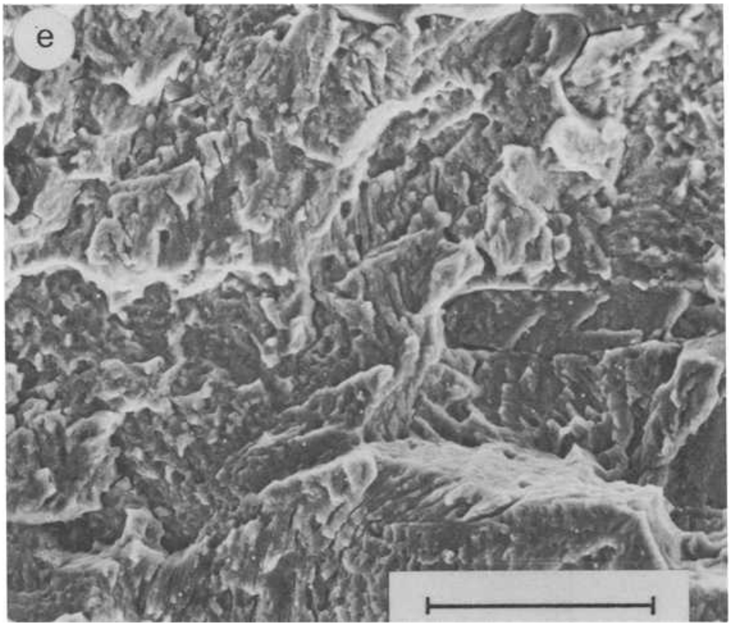

FIG. 16—(*Continued*) (e) Δk = *90.3 kg/mm*$^{3/2}$.

change the fractured surface morphology from facet to transgranular pattern. The lowering of dl/dN with the superposition of Δk attributed to the blunting of SCC crack tip along the intergranular path by the corrosive dissolution. The transgranular pattern observed in this situation differed from that observed under Δk = 35 kg/mm$^{3/2}$ (10.8 MN/m$^{3/2}$), Fig. 16(*d*), which is mechanical transgranular cracking and as a matter of course from fatigue striations under Δk = 90.3 kg/mm$^{3/2}$ (28 MN/m$^{3/2}$), Fig. 16(*e*).

The relations between the fracture area fraction and Δk are shown in Fig. 17 under K_{max} = 80 kg/mm$^{3/2}$ (24.8 MN/m$^{3/2}$) which is near K_{ISCC} and under K_{max} = 110 kg/mm$^{3/2}$ (34.1 MN/m$^{3/2}$) where SCC is predominant at Δk = 0. Under K_{max} = 80 kg/mm$^{3/2}$, dl/dN lowered little with the superposition of small Δk, and the greater part of the fractured surface was always occupied by the transgranular mode. Under K_{max} = 110 kg/mm$^{3/2}$, dl/dN remarkably decreased with the superposition of Δk, and the facet pattern was replaced by the transgranular one with the increase of Δk. Thus the change of the crack rate corresponded well to that of fractured surface morphology. Figure 18 shows a linear relation between dl/dN and the facet area fraction under the small ratios of $\Delta k/K_{max}$ = 0, 0.05, and 0.1.

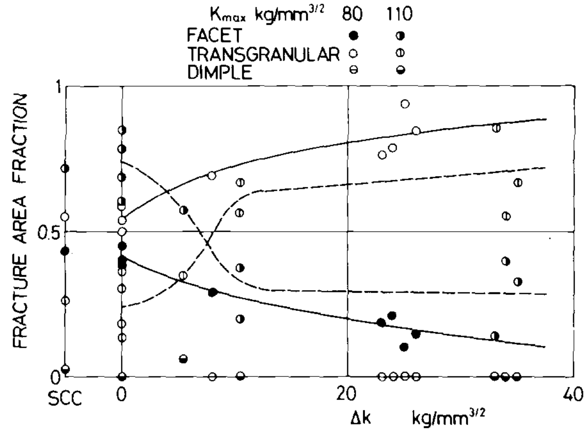

FIG. 17—*Relation between fracture area fraction and* Δk.

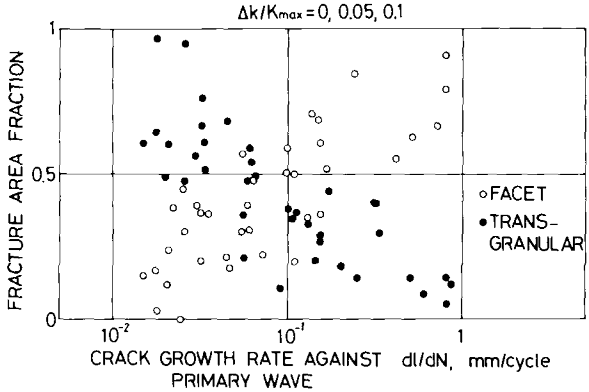

FIG. 18—*Relation between fracture area fraction and* dl/dN.

Conclusions

The influence of small superimposed stress fluctuations on low-cycle corrosion fatigue under trapezoidal waveform is varied greatly by the susceptibility of the test materials to SCC.

The corrosion-fatigue life of the materials insensitive to SCC is decreased remarkably when small stress fluctuations are superimposed. The crack initiation is much enhanced by such a superposition. The decreased fatigue life remarkably increases unexpectedly at near $\Delta\sigma = 9$ kg/mm^2 (88 MN/m^2). The intensified corrosive attack by $\Delta\sigma$ is considered to remove the nuclei of fatigue crack introduced by mechanical-stress repetitions. In this experiment, the removal of crack nuclei became more dominant than the corrosion damage under $\Delta\sigma = 9$ kg/mm^2, and the initiation of corrosion fatigue cracks was suppressed. When $\Delta\sigma$ is greater than 9 kg/mm^2, the fatigue life is decreased again by the fatigue damage of $\Delta\sigma$.

The crack growth rate of corrosion fatigue is insensitive to the superimposed stress fluctuations, Δk, of small amplitude. The crack rate then increases with an increase of Δk greater than 10 kg/mm$^{3/2}$ (3.1 MN/m$^{3/2}$). The increase of fatigue life under $\Delta\sigma$ = 9 kg/mm^2 is due to retardation of crack initiation under an extremely limited condition. The superimposed stress fluctuations increase also the thinning of materials due to corrosion.

In materials sensitive to SCC, the corrosion fatigue life is almost occupied by the crack-growth period, and the crack-growth rate greatly decreases with the superposition of small Δk under K_{max} higher than K_{ISCC}. Under low K_{max} that is nearly equal to K_{ISCC}, the similar growth characteristics to that of the materials insensitive to SCC are obtained. In this case, crack initiation period is dominant, and dl/dN is unchanged under Δk smaller than 5 ~ 6 kg/mm$^{3/2}$ (1.5 ~ 1.9 MN/m$^{3/2}$).

The marked lowering of dl/dN with the superposition of Δk under SCC condition is caused by the superimposed stress effect on SCC crack growth. The superimposed stress fluctuations promote the corrosive dissolution at SCC crack tips, which lowers the actual stress intensity owing to the blunting of crack tip. These results are explained well by fractographical observations.

References

[1] Endo, K. and Komai, K., "Corrosion Fatigue," NACE-2, National Association of Corrosion Engineers, 1972, pp. 437-450.

[2] Endo, K. and Miyao, Y., *Bulletin of Japan Society of Mechanical Engineers*, Vol. 1, No. 4, Nov. 1958, pp. 374-380.

[3] Endo. K., Komai, K., and Nakagaki, K., *Bulletin of Japan Society of Mechanical Engineers*, Vol. 11, No. 47, Oct. 1968, pp. 791-797.

[4] Nakamura, H. and Tanaka, S., *Transactions*, Japan Society of Mechanical Engineers, Vol. 32, No. 244, Dec. 1966, pp. 1755-1761, (in Japanese).

[5] Uhlig, H. H. in *Corrosion and Corrosion Control*, 2nd ed., Wiley, 1971, p. 101.

[6] Wei, R. P. and Landes, J. D., *Materials Research and Standards*, Vol. 9, No. 7, July 1969, pp. 25-27, 44-46.

H. Kitagawa,[1] *T. Fujita,*[1] *and K. Miyazawa*[2]

Small Randomly Distributed Cracks in Corrosion Fatigue

REFERENCE: Kitagawa, H., Fujita, T., and Miyazawa, K., "**Small Randomly Distributed Cracks in Corrosion Fatigue,**" *Corrosion-Fatigue Technology, ASTM STP 642,* H. L. Craig, Jr., T. W. Crooker, and D. W. Hoeppner, Eds., American Society for Testing and Materials, 1978, pp. 98–114.

ABSTRACT: Very small distributed cracks often can be observed on the surfaces subjected to corrosion fatigue. In some cases, the fracture process can be characterized by the interaction and connection of these small distributed cracks. An analysis of such a corrosion-fatigue fracture process is presented by combining the techniques of fracture mechanics, reliability analysis, and graphical display. Many small cracks are measured and their statistical distribution functions, with respect to their sizes and locations, are determined. Using these functions as input data and a condition of the connections of cracks, a statistical simulation of a corrosion fatigue process is performed and its fracture process is output on a two-dimensional graphical display of an x-y plotter. The graphical display facilitates the simulation. The distribution of corrosion fatigue lives can be derived for some cases. Abrupt acceleration of the fracture process by the connection of distributed cracks is demonstrated.

KEY WORDS: corrosion fatigue, crack measurement, fractures (materials), Monte Carlo method, computor display, crack initiation, random crack distribution, fracture mechanics, corrosion fatigue, steels, reliability

Early studies of corrosion fatigue had paid attention to the distributions of small cracks. Recently, several approaches utilizing fracture mechanics and statistical methods [*1-4*],[3] have pointed to the importance of these cracks in corrosion fatigue. The preparation of analyzing this problem included experimental and theoretical basic research on the interaction of closely spaced cracks [*5,6*] and on the simulation of a fracture process by the interaction of cracks [*3,4*].

---

[1] Professor, Institute of Industrial Science, University of Tokyo, and graduate student, Mechanical Engineering, University of Tokyo, respectively, Tokyo, Japan.

[2] Design engineer, Minamisenju-Seisakusho Company, Ltd., Tokyo, Japan.

[3] The italic numbers in brackets refer to the list of references appended to this paper.

In this paper, a new simulation program and improved methods of determination of input data have been developed. A basic method has been constructed for the analysis of a fracture process by crack interaction in corrosion fatigue. The corrosion fatigue behavior of a high strength steel in water was analyzed as an example.

Phenomena, Assumptions, and Procedures of Analysis

Very small, randomly distributed cracks often can be observed on the surfaces of unnotched specimens and parts broken in service, which were or could have been subjected to corrosion fatigue. The authors are trying to analyze the cases where the fracture processes and properties of corrosion fatigue seem to be characterized by these cracks. Of course, these cracks are affected by various environmental, metallurgical, and mechanical factors.

Figure 1(*a*) shows the surface of an unnotched specimen of a rail steel subjected to corrosion fatigue in salt water. Many small cracks were initiated and the specimen was broken by their connection. Figure 1(*b*) shows the surface of a specimen of a high-strength steel corrosion fatigued in distilled water. Many small pits and cracks initiated from the pits are distributed. The stress intensities (K) of most cracks are estimated to be very low in this case, probably below ΔK_{TH}. From the experimental results [*7,8*] on the dependence of small surface cracks upon the K and the relation between $\Delta K \sim da/dN$ in corrosion fatigue, it is deduced that the cracks in Fig. 1(*b*) grew very slowly or hardly at all. In our earlier measurements [*3,4*] in similar conditions, the statistical distribution functions of the crack lengths did not vary through the fatigue life, and the number of cracks increased with the number of applied load cycles. It seem that, when the density of the cracks becomes high enough, the specimen is broken by their connection. When two, three, or several cracks happen to be closely initiated on the way to the breakdown, local interactions and coalescence occur among them. Some examples of interaction can be seen in Fig. 1(*b*). It is assumed that if the density of cracks becomes much higher and their interactions and coalescence succeed, these small cracks grow to a large crack and the specimen is broken. The basic mechanical mechanism of the connection of small cracks is assumed to be an interaction between two closely located cracks. This mechanical process was analyzed by means of linear elastic fracture mechanics. As the sizes and locations of the cracks are random, this stochastic and succeeding process of the initiation, interaction, and coalescence of cracks was analyzed by combining a statistical simulation, a graphic display technique, and statistical measurements of cracks.

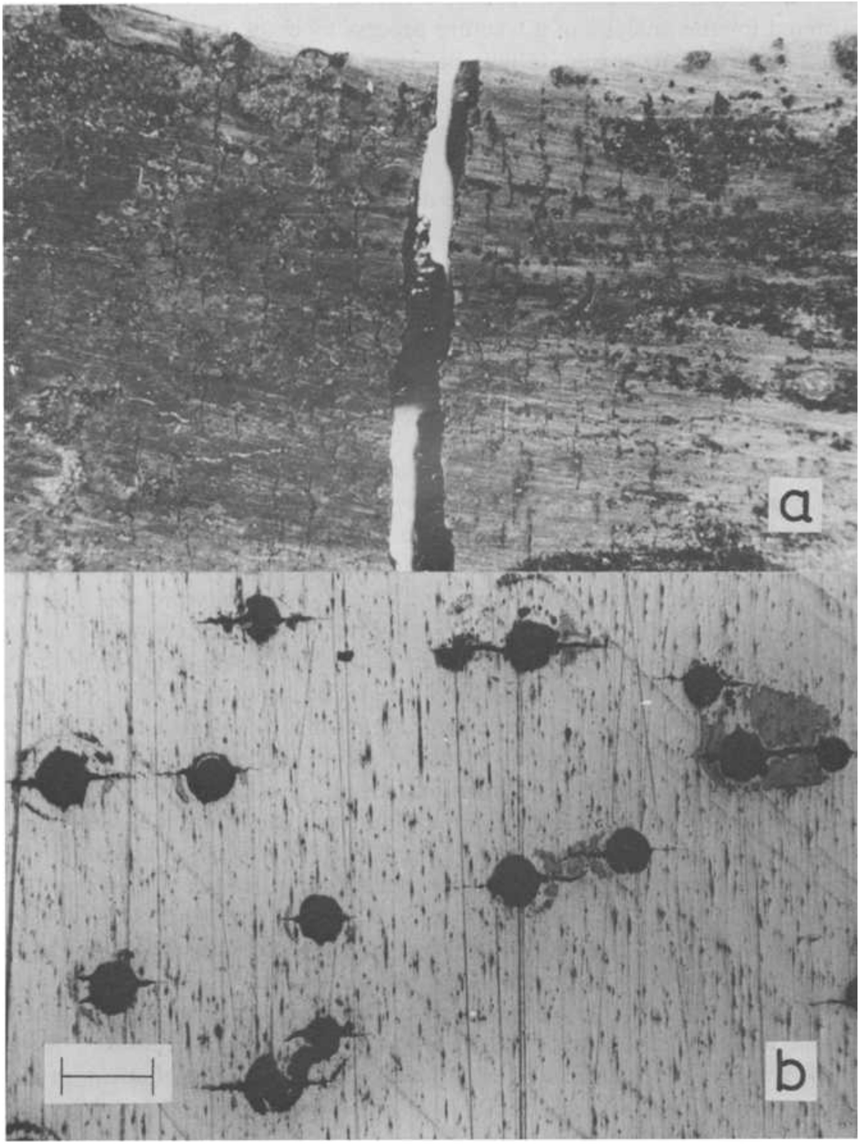

FIG. 1—*General features of the surfaces of the specimens subjected to corrosion fatigue.* (a) *Plate cut from rail steel [0.68C steel, tensile strength 866 MM/m*^{2} *(88 kg/mm*^{2}*), yield strength 445 MN/m*^{2} *(45 kg/mm*^{2}*)] subjected to out-of-plane bending, 25 Hz, in 3 percent sodium chloride aqueous solution, room temperature, stress* $\Delta\sigma$ = *412 MN/m*^{2} *(42 kg/mm*^{2}*),* R = *−1, at 1.54* × *10*^{7} *cycles.* (b) *High strength steel plate [0.10C, 0.19Si, 0.62Mn, tensile strength 530 MN/m*^{2} *(54 kg/mm*^{2}*), yield strength 402 MN/m*^{2} *(41 kg/mm*^{2}*)],* R = *0.04, at 10*^{6} *cycles (about 28 h). Scale mark indicates 200* μ*m.*

Conditions of Interaction and Connection of Cracks

Figure 2(*a*) is a typical example of the interaction and connection of three closely located surface cracks. It is difficult to obtain an exact solution of the *K* values of interacting surface cracks. Then, considering the geometrical similarity between the interaction of surface cracks and that of through cracks to be described later, the corrosion fatigue cracks here will be analogically and approximately interpreted as follows, by using the results of analytical and experimental studies on two-dimensional through cracks. If two cracks are initiated so that their tips are located close enough, the first mode stress intensity factors, K_I, of the closely located

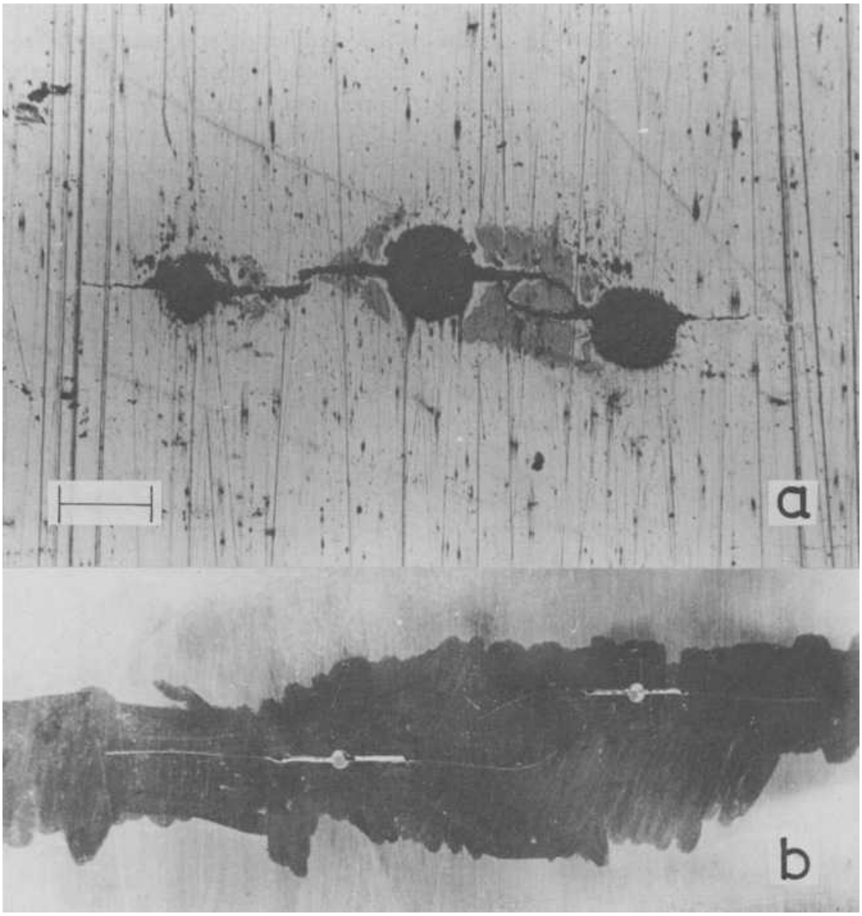

FIG. 2—*Examples of interaction and coalescence of cracks.* (a) *Surface cracks in corrosion fatigue. Scale mark indicates 100 μm.* (b) *Through cracks in fatigue in air.*

tips of the cracks give a higher value by their interaction. The crack tips grow in parallel and pass each other. Then the second mode stress intensity factors, K_{II}, of these tips emerge and increase, and the values of their K_I rapidly decrease by the interaction. On account of the decreasing of K_I and the increasing of K_{II} of the passing tips, the passing tips are curved and approach each other. Subsequently, little change at the surface of the specimen can be observed; but inside the specimen, the cracks are connected to become one large crack. This inside connection is recognized on the fracture surface of the specimen after final fracture. In this paper, this phenomenon is defined as "connection."

Figure 2(*b*) is an example of the interaction and connection of two through cracks in a steel-plate specimen under fatigue loading in air. The interaction and connection in this case are apparently geometrically similar to those of two small surface cracks on the unnotched specimen in corrosion fatigue. Referring to this fact, a pair of two-dimensional interacted through cracks were analyzed as an approximate model of interacted surface cracks, and "interaction factors" (f) (defined in Appendix I) were obtained as the critical condition of the interaction and connection of cracks. The details of the analysis (by fracture mechanics) already had been reported [*3,4,6*]. These are briefly summarized in Appendix I and only the results are used in this paper. Figure 3 is an "equi-interaction factor diagram" or "interaction region diagram" for f = 1.50. The region has been replaced by an approximated polygon for the convenience of computation. It is assumed that when the left tip of another crack falls within the polygon, the interaction occurs and connection soon follows. The value of f as a condition of connection is adjusted and determined

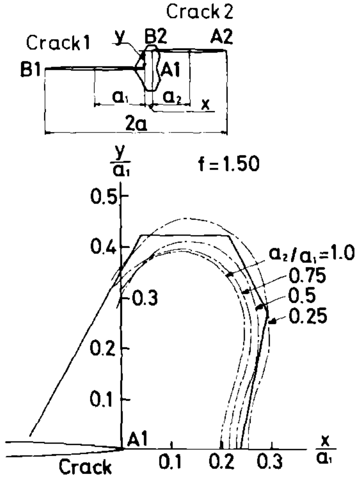

FIG. 3—*Interaction or coalescence region used for the calculation (a crack tip area bounded by a polygon).*

according to the results of the experiments. After the connection, a value for K equivalent to the total crack length $2a$ in Fig. 3 is assumed to apply at the crack tips B1 and A2.

Determination of Statistical Distribution Functions of Cracks

In this section statistical distribution functions of cracks as input data of a statistical simulation analysis have been determined experimentally.

Experimental Conditions

The material of the specimen is a high strength steel plate (thickness: 2.3 mm) which has tensile strength of 530 MN/m^2 (54 kg/mm^2). Environment for corrosion-fatigue tests is distilled water at room temperature supplied into a corrosion chamber and overflowed at the rate of 0.25 cm^3/s and at a pH value of 5.6 to 6.0. Uniaxial, tensile, and sinusoidal wave loads were applied with a frequency of 10 Hz.

In the previous experiments, the specimens were set vertically in a corrosion chamber and the results of distribution of the density of crack initiation sites were inhomogeneous, in spite of the uniform stress distribution, as shown in Fig. 4. In order to obtain a homogeneous distribution, we developed a hydraulic servofatigue testing machine of the horizontal type.

The surface of the specimen was coated except for a central area of 60 by 34 mm of its one side, as shown in Fig. 5. Regions A, B, C and D (10 by 10 mm, respectively) are the regions for the measurements of crack distribution.

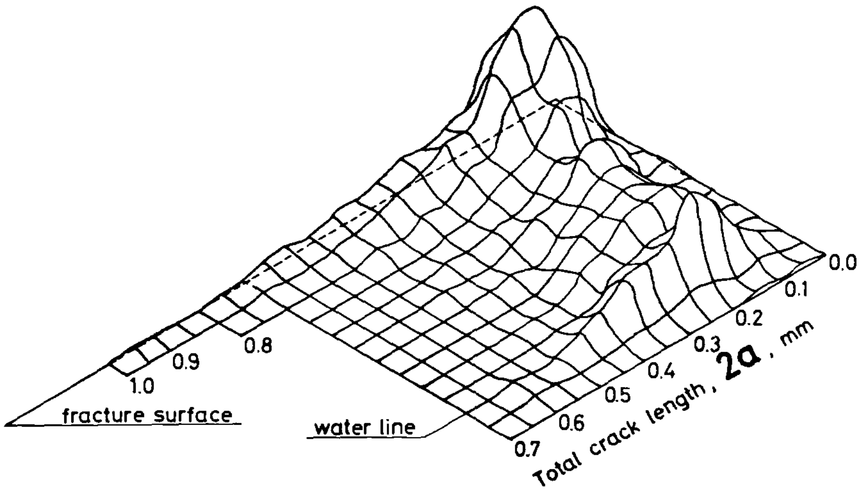

FIG. 4—*Inhomogeneous distribution of crack density on the surface of a vertical specimen subjected to corrosion fatigue of a steel in tap water.*

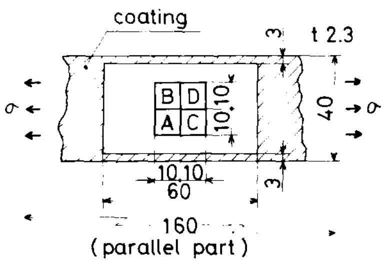

FIG. 5—*The portion subjected to corrosion fatigue and the regions for measurement of cracks (A, B, C, and D).*

After corrosion-fatigue tests, the surface of the specimen was etched with nitric acid and ethyl alcohol and polished with chromium oxide. Then, a grid of 0.5-mm meshes was photoprinted over the surface as shown in Fig. 6. Since the grid is semitransparent, the locations and lengths of cracks

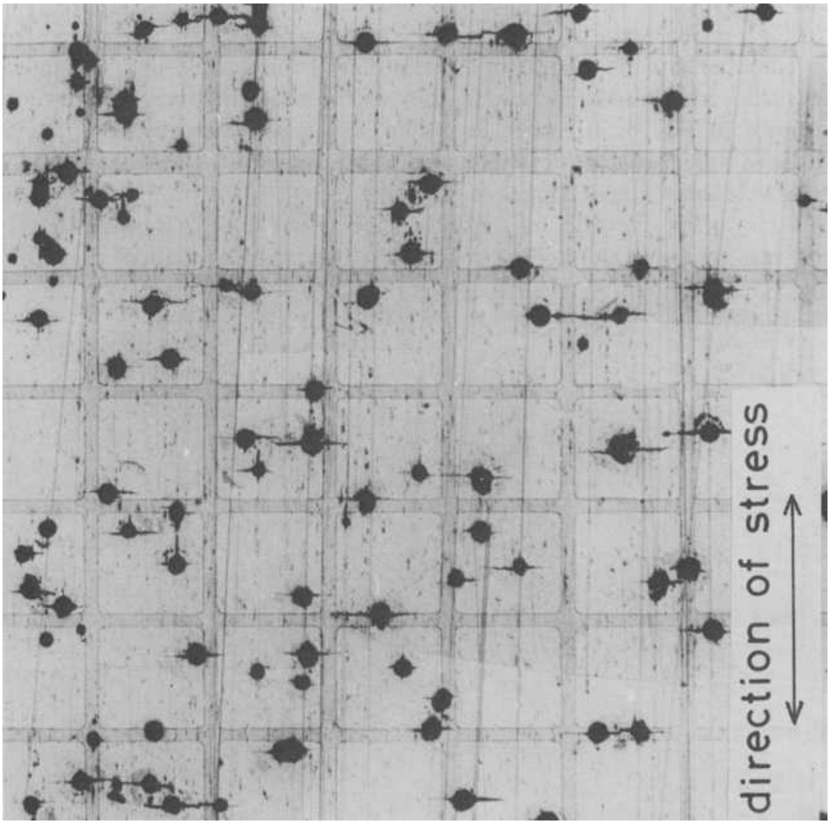

FIG. 6—*Randomly distributed fine cracks and printed grid for measurement.*

could be measured with good accuracy. All of the cracks were parallel to each other and perpendicular to the load.

Distribution of Crack Lengths

Figure 7 shows the distribution of crack lengths observed in one test.

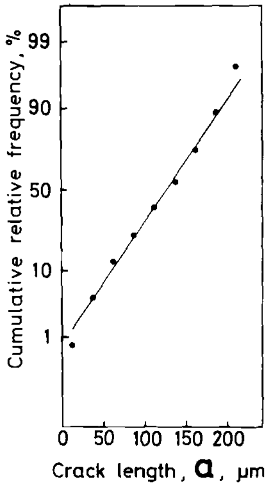

FIG. 7—*Plotting of crack lengths on statistical graph of normal distribution.*

The ordinate shows the frequency. The abscissa values are half-crack lengths. The crack lengths follow a normal distribution. Referring to the results of preliminary experiments [*3,4*], the statistical distribution function of crack lengths did not vary throughout a corrosion fatigue test, as stated in the preceding section. Only the total number of cracks increased linearly with the number of stress cycles [*3,4*].

An example of measurement is shown in the following. The stress range $\Delta\sigma$ was 235 MN/m^2 (24 kg/mm^2), stress ratio, R, was 0.04, and the number of stress cycles at the time of the measurement was one million. The number of cracks measured in the area of 4 by 10 by 10 mm (A, B, C, and D) on this specimen was 1678. The distribution density of the cracks was very high; 420 cracks could be found in the area of 1 cm^2. About 96 percent of the measured crack lengths were within the range of 139 ± 98 μm in half length (mean: 139 μm, standard deviation: 49 μm), and no crack over 260 μm in half length was found.

Distribution of Locations of Cracks

The distribution of the locations of crack initiation is examined by the following function.

$$H = -\sum_{j=1}^{n}\left(\frac{Q_j}{Q_T}\right)\log_2\left(\frac{Q_j}{Q_T}\right) \tag{1}$$

This is "homogeneity function" H, proposed by Masuko [9], as a measure of statistical homogeneity of density in two-dimensional distribution. The details of this function and physical interpretation of the value of H are described in Appendix II. When the values of H are the same for some distributions, their homogeneities are the same.

The value of H function calculated with the results of measurements on the cracks obtained by the experiment described in the previous section is 8.4039, as shown in the first (top) row of Table 1. For the uniform randomness, the theoretical value of H is 8.4608 and almost the same as the experimental result, so that the distribution of the locations of crack initiation was decided to be uniformly random.

TABLE 1—*Evaluation of crack distribution by homogeneity function.*

	Total Number of Cracks, Q_T	Number of Division, n	Calculated Value, H	Theoretical Value, H_{random}	Deviation, D
Experiment	1678	400	8.4039	8.4608	−0.0569
Simulation	397	100	6.4685	6.4505	0.0180

Statistical Simulation of Fracture Process and Graphical Displays

In the previous section, the statistical distribution of the sizes and initiation sites of the randomly distributed cracks has been prepared as input data for the analysis that will be presented now. By means of these input data and the conditions of connection decided before, a statistical simulation by Monte Carlo method can be performed.

Figure 8 is a flow chart for one trial of the simulation. This program is an improved version of the previous one [3,4]. One of the improvements, for instance, is "the exclusion of unfavorable cracks," which means the procedure indicated by the second decision in the flow chart.

First of all, a uniform random number for the distribution function of the locations of crack and a normal random number for the distribution of crack sizes are put into the first two steps as input data based on the experiments, and a crack is initiated. At the next step, each crack tip is examined to determine whether or not the conditions of connection can be satisfied. In the succeeding steps, every unfavorable crack is excluded and the most favorable crack for the connection is selected. Thus, occurrences of connection among all of cracks are examined. If any connection occurs, the circuit turns to the right, and the related cracks are replaced by a

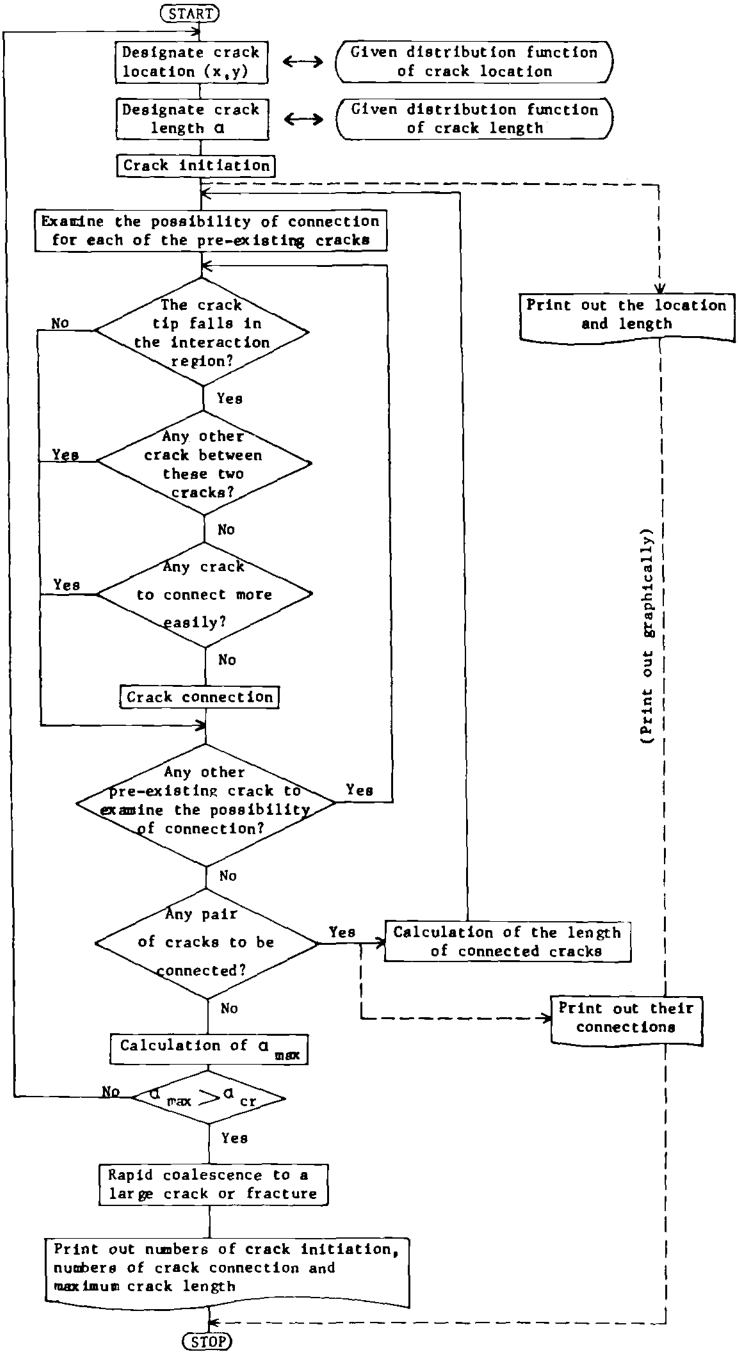

FIG. 8—*Flow chart of the calculation of the simulation model.*

larger crack. Then the circuit goes back and a new possibility of connection is examined again. Thus, connections are successively progressed. When it is judged that no more connection or no connection at all occurs, the maximum half crack length, a_{max}, at that time (for the given number of initiation of cracks, m) is determined. If this a_{max} does not exceed a critical crack length for remarkable growth or fracture, a_{cr}, the next crack is initiated. Cracks are successively initiated one by one in the same way. If a_{max} attains or exceeds a_{cr}, this one trial of fracture process ends.

The extracted results of calculation of one trial using the flow chart are shown in Table 2. Up to 396 cracks, both the number of connections and the maximum crack size, a_{max}, increase gradually with the increase of the number of cracks, m. At the initiation of the 397th crack, however, the number of connections immediately increases up to 34, and also the maximum crack length, a_{max}, abruptly shows a more remarkable increase.

TABLE 2—*Example of a trial of the calculation on the increase of maximum half-crack length and the number of the connection of cracks.*

Number of Crack Initiations, m, per cm^2	Number of Crack Connections, per cm^2	Maximum Half Crack Length, a_{max}, mm
50	0	0.26
100	1	0.36
150	4	0.36
200	4	0.36
250	5	0.36
300	7	0.52
350	11	0.59
397	34	5.07

The results of one trial of this simulation have been output on an x-y plotter too as two-dimensional graphical expressions in addition to the numerical output, as shown in Fig. 9. The number of cracks is increased while keeping them randomly distributed, and, at the 397th crack initiation, they abruptly coalesce along a line. Comparing the outputs on an x-y plotter with actual distribution of cracks, it is possible to detect the imperfections in the simulation model and to improve these imperfections. The procedure of exclusion of unfavorable crack stated before has been proposed by such detection and improvement.

To evaluate the simulation through the examination of statistical homogeneity, the function H was calculated, using the same procedure as was done on the crack distribution obtained by experiments. As shown in the second (bottom) row of Table 1, even in the case of simulation, theoretical values of H for ideal homogeneous random distribution coincided with the value calculated from the output data equivalent to Fig. 9.

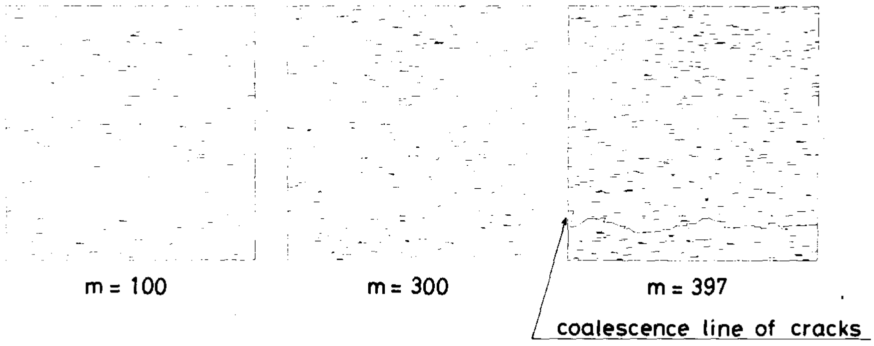

FIG. 9—*Variation of two-dimensional distribution pattern of fine cracks in the area of 10 by 10 mm, as the outputs on an* x-y *plotter from the computation of a statistical simulation of randomly distributed cracks in corrosion fatigue* (m = *the number of crack initiations*).

The procedures stated thus far are for one trial. Many trials have been attempted. Some of these trials are shown in Fig. 10. Each stair-wise line shows one trial. Inducing local connections from time to time and going up stair-wise, a trial goes from the left to the right, and at some number of crack initiations, *m*, an abrupt rapid growth is induced by a rapid chain of connections. The local connections like these can be observed both on the specimen and the graphical display. The lines drawn here are only a part of the trials which were performed actually.

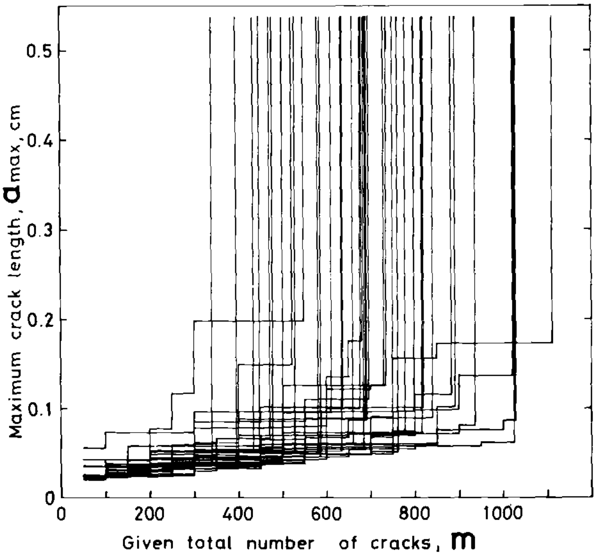

FIG. 10—*Examples of the trials of the simulation; the increase of maximum crack length with the increase of the given total number of cracks.*

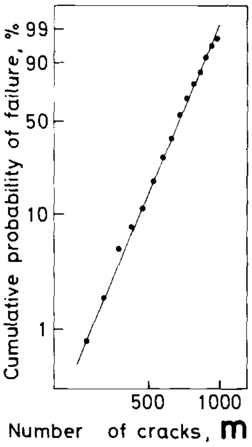

FIG. 11—*Weibull distribution of the probability that* $a_{max} > a_{cr}$ *against the given number of cracks.*

When a figure including all the trials is cut by a vertical line at a value of *m*, the probability of failure at the *m* can be obtained. The probability of failure, *P*, obtained with respect to *m* is shown in Fig. 11. The actual calculation for Fig. 11 was done directly by the numerical output.

If the relation between this value of *m* and the number of load cycles or the test duration, *N*, is given, the relation between *P* and *N* can be obtained, being combined with the $P \sim m$ relation. From this relation of *P* and *N*, one can calculate the statistical distribution function of the number of load cycles to the occurrence of the rapid chain of connections, N_{cr}. In laboratory tests with conventional small specimens, the number of load cycles to fracture, N_f, seems to be nearly equal to this N_{cr}. Referring to the previous tests [*3,4*], there seems to be a linear relation between *m* and *N* as stated in a previous section. In this case, the distribution of corrosion fatigue lives can be derived from the $P \sim N$ relation just mentioned, except for the final crack growth stage.

From the conditions given here, the probability of failure, *P*, against the number of crack initiations, *m*, was obtained as a Weibull distribution. In this case, the crack lengths followed a normal distribution as stated previously. In the previous experiments [*3,4*], the crack sizes followed a logarithmic normal distribution and the probability of failure followed a normal distribution.

Conclusions

In order to analyze a fracture process governed by the interaction and connection of randomly distributed small cracks in corrosion fatigue, a method has been developed by combining (*a*) accurate measurements of distribution functions of the sizes and locations of very small cracks, and their statistical evaluation, (*b*) statistical simulation of such a fracture process, and (*c*) outputs by two-dimensional displays.

Though the construction of a method of analysis was the main purpose, the following important results or conclusions have been additionally obtained.

1. Even for corrosion fatigue in distilled water, cracks of surprising high density, more than 400 cracks/cm^2, were initiated.
2. In spite of the appearance of an irregular inhomogeneous random distribution of small corrosion-fatigue cracks, the density of crack initiation sites followed a uniform random distribution even in a small area of 4 cm^2. In this case, crack sizes followed a normal distribution and the probability of failure followed a Weibull distribution with respect to the number of crack initiations.
3. This analysis suggests a possibility that in some conditions the mechanism of corrosion-fatigue damage during the major part of the specimen's life is characterized by the increase of the number of very small cracks, and at a certain density of cracks their coalescence induces the onset of faster growth of a large crack or a rapid fracture. This suggestion seems to be important for clarification of the mechanism of corrosion fatigue and for the development of protection systems.
4. Fracture mechanics techniques can be applied even to the fracture processes of unnotched smooth specimens or parts when cracks initiate easier, not only to precracked specimens or parts.

Acknowledgments

The authors appreciate the valuable suggestion and cooperation of N. Masuko, University of Tokyo. They also wish to thank T. Ohira for his contribution to the development of a horizontal type fatigue tester for this research, and I. Susuki for his advice based on his experience gained in his pioneering works.

APPENDIX I

Determination of the Degree of Interaction between Two Parallel Cracks by Linear Elastic Fracture Mechanics

Let us consider the stress intensity factors of the first and second modes, K_{I} and K_{II}, at the four crack tips of Crack 1 and Crack 2 in Fig. 12. Referring to the Isida's solution [*10*], the eight values of nondimensional stress intensity factors for each combination of the relative positions of crack center and crack sizes were analyzed [*6*].

Figure 12 shows an example of a set of the computed crack-interaction regions at

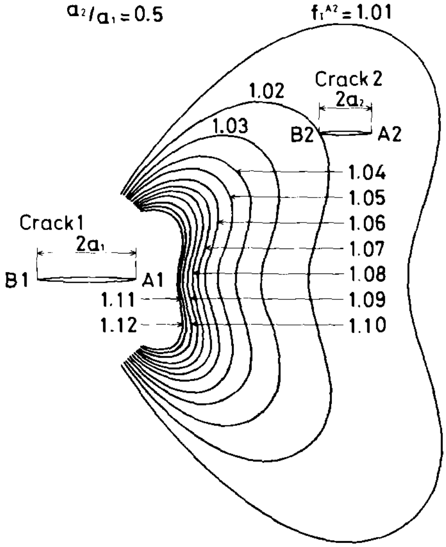

FIG. 12—*Example of equi-interaction factor diagrams.*

a tip A1, within one of which the value of the factor, f, is larger than the value indicated at each curved line. When the left tip B2 of Crack 2 falls on the curved line for $f_I^{A2} = 1.02$ in Fig. 12, the value of K_I at the crack tip A2 is

$$K_I^{A2} = (1.02) \times \sigma\sqrt{\pi a_2} \tag{2}$$

We call f the interaction factor; f_I^{A2} is the interaction factor associated with the effect of the Crack 1 on the stress intensity at A2. Each curved line can be called as an equiinteraction factor diagram. The f is expected to indicate the degree of interaction between a pair of the cracks with geometrical similarity in relative positions and their sizes. The nondimensional crack-interaction region for the given value of f seems to be relatively independent of the absolute values and ratios of crack sizes (see Fig. 3).

APPENDIX II

Evaluation of Uniform Randomness in Two-Dimensional Crack Distribution

Consider an area, S, in which Q_T cracks are distributed. Dividing S into n equal units s ($n = S/s$), let the number of cracks in the jth unit be Q_j ($j = 1, 2, \ldots, n$). Now a homogeneity function of distribution, H, with respect to the location of Q_T cracks is defined as follows:

$$H = -\sum_{j=1}^{n}\left(\frac{Q_j}{Q_T}\right)\log_2\left(\frac{Q_j}{Q_T}\right) \tag{3}$$

This function was originally proposed by Masuko et al [9].

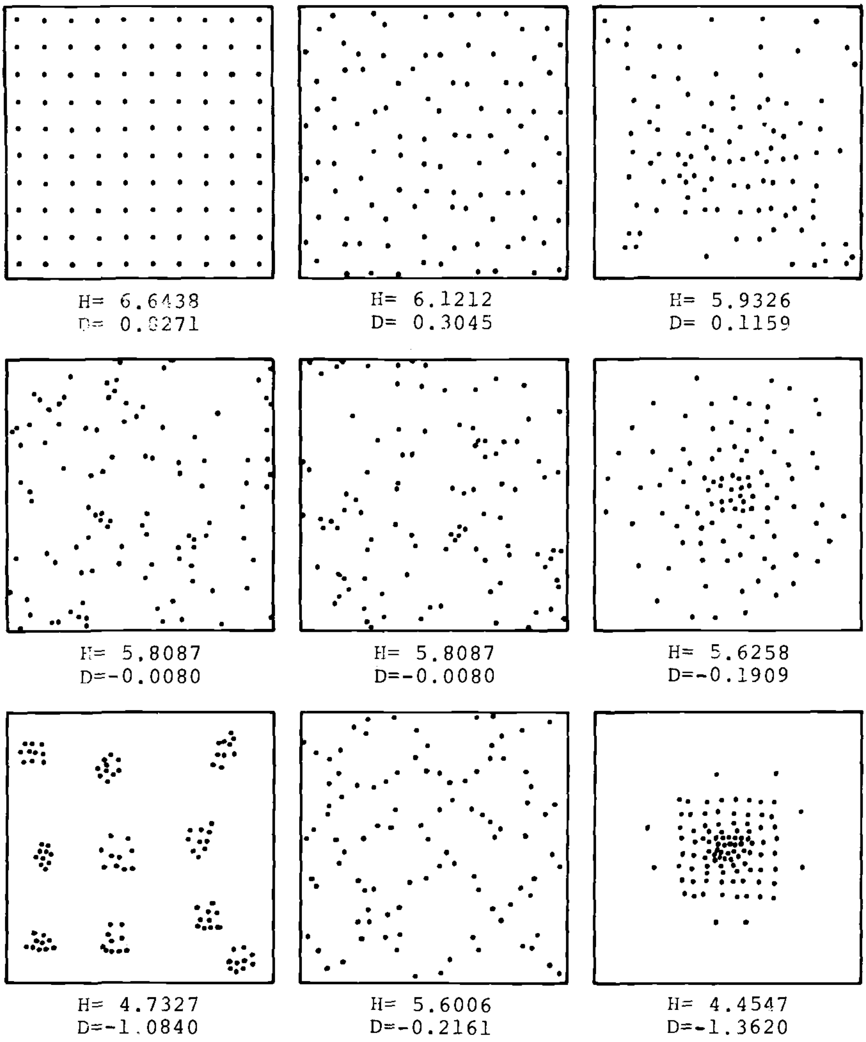

FIG. 13—*Model patterns of two-dimensional distributions and the values of* H *and* D *functions* (n = *100*).

If Q_T cracks are distributed in the area, S, at uniformly random locations and both n and Q_T are large enough and Q_T/n remains constant at a value $\overline{Q}$, the number of the units which contain q cracks, defined by M_q ($\Sigma M_q = n$), are distributed by the Poisson distribution with mean $\overline{Q}$. From Eq 3 we can obtain the theoretical value of H, H_{random}, for this Poisson distribution. This H_{random} is the value of H for an ideal uniformly random distribution.

Some models of pattern of crack distribution ($Q_T = 100$) are displayed in Fig. 13 (Ref *9*). Only the locations of crack centers are plotted. The values of H for each model are calculated for $n = 100$ and attached to each figure. D shows the deviation from the uniformly random distribution ($D = H - H_{\text{random}}$). The smaller the absolute value of D becomes, the more uniformly random the distribution is. The more homogeneous the crack distribution becomes, the larger the values of H and D increase as shown in Fig. 13 ($H - D = H_{\mathrm{random}}$ = constant = 5.8167 for Fig. 13).

References

[*1*] Kitagawa, H. in *Corrosion Fatigue,* Proceedings of the International Conference on Corrosion Fatigue, National Association of Corrosion Engineers and the American Institute of Mining, Metallurgical, and Petroleum Engineers, Conn., 1971, p. 521.

[*2*] Kitagawa, H. and Susuki, I., "Fracture Mechanics Approach to Corrosion Fatigue Strength of Unnotched Steel Specimens—Further Examination," presented at the Meeting on Corrosion Fatigue, University of Manchester Institute of Science and Technology, Manchester, England, 1973.

[*3*] Kitagawa, H. and Susuki, I. in *Reliability Approach in Structural Engineering,* A. M. Freudenthal et al, Eds., Maruzen, Co., Ltd., 1975.

[*4*] Kitagawa, H., Susuki, I., and Yuuki, R., in *Strength and Structure of Solid Materials,* H. Miyamoto et al, Eds., Noordhoff, Co., Ltd., 1976.

[*5*] Kitagawa, H., Isida, M., Ohira, T., and Kuroda, M., *Proceedings,* Third International Conference on Fracture, Vol. 2, Munich, 1973, p. 521, and *Transactions,* Japan Society of Mechanical Engineers, Vol. 42, No. 360, 1976, p. 2281.

[*6*] Kitagawa, H. and Susuki, I., *Proceedings,* Annual Meeting, Japan Society of Mechanical Engineers, No. 740-10, 1974, p. 227.

[*7*] Kitagawa, H. and Takahashi, S., *Proceedings,* International Conference on Mechanical Behavior of Materials, Boston, 1976, p. 627.

[*8*] Kitagawa, H., Takahashi, S., and Fujita, T., *Proceedings,* Spring Meeting, Japan Society of Mechanical Engineers, No. 770-2, 1977, p. 242.

[*9*] Kawarada, H., Masuko, N., and Yanagida, H., *Journal of the Faculty of Engineering,* University of Tokyo, Vol. 31, No. 4, 1972.

[*10*] Isida, M. in *Methods of Analysis and Solutions of Crack Problems,* G. C. Sih, Ed., Noordhoff, 1973, p. 56.

Materials Characterization

C. Amzallag,[1] *P. Rabbe,*[1] *and A. Desestret*[1]

Corrosion-Fatigue Behavior of Some Special Stainless Steels

REFERENCE: Amzallag, C., Rabbe, P., and Desestret, A., "**Corrosion-Fatigue Behavior of Some Special Stainless Steels,**" *Corrosion-Fatigue Technology, ASTM STP 642,* H. L. Craig, Jr., T. W. Crooker, and D. W. Hoeppner, Eds., American Society for Testing and Materials, 1978, pp. 117-132.

ABSTRACT: We have studied the corrosion-fatigue crack initiation and propagation of different types of steels: two austenitic, one austenitic-ferritic, and one ferritic. The testing program had been established in order to define, particularly, the part in corrosion fatigue of electrochemical effects and mechanical damage. Tests were carried out on smooth specimens in rotating bending and on precracked specimens in tension in air, and in a 3 percent aerated solution of sodium chloride.

The capacity of the metal for dissolution and repassivation seems largely responsible for the behavior of the metal in the corrosive solution. This capacity varies notably with the composition of the metal, the loading conditions of the specimens, and the characteristics of the corrosive medium.

KEY WORDS: corrosion fatigue, passive film, electrochemical corrosion, metallographic structures, mechanical properties, rotating-bending tests, crack propagation

The development of new techniques, particularly in the fields of the treatment of polluted water, the use of sea water, oil drilling, etc., has led to an increased interest in corrosion-fatigue phenomena. In fact, corrosion fatigue is an extremely important cause of material damage, doubtless as important as pure fatigue, or corrosion in its various forms.

Corrosion fatigue often is encountered in components used in conditions which do not appear very corrosive; in this respect, corrosion fatigue is analogous to, and as pernicious as, pitting corrosion or stress corrosion.

We can cite the examples of brackish or salted waters and the various acid or saline environments of the chemical industry, which are insufficiently reactive to cause general corrosion but allow the development of localized

---

[1] Engineer, Department of Mechanics, engineer, Department of Mechanics, and engineer, Department of Corrosion, respectively. Creusot-Loire, Centre de Recherches, 42701, Firminy, France.

corrosion in the form of cracks. One cannot help being struck by the close analogies, at least in appearance, which exist between corrosion fatigue cracks and those of stress corrosion, or again between corrosion-fatigue and pitting corrosion. These analogies have attracted the attention of research workers interested in these various aspects *[1,2]*,[2] so that it now seems impossible to study one of these three aspects in isolation, without taking into account their similarities.

We have studied the corrosion-fatigue crack initiation and propagation of different stainless steels in a chloride solution.

The essential characteristic of stainless steels is their ability to be coated by a passive film in liquid media. The most satisfactory representations of the passive state consider it as a dynamic equilibrium state, which results from a continuous competition between passivation and depassivation phenomena *[3,4]*. These phenomena can be accelerated either by mechanical or chemical factors.

In this study, we have attempted to specify the mechanisms leading to the failure of different stainless steels by corrosion fatigue and, particularly, the respective roles of electrochemical corrosion phenomena and mechanical damage.

Experimental Program

In order to demonstrate the effects of metallurgical structure and different mechanical properties, we have studied the behavior of different types of steels: two austenitic, one austenitic-ferritic and one ferritic. The chemical compositions, the heat treatments, and the mechanical characteristics of these steels are listed in Table 1.

It is well known that the nature of the corrosive medium can have a large effect on the kinetics of the corrosion-fatigue phenomena. It is also known that in the case of stainless steels, localized attacks of the stress-corrosion or pitting-corrosion type, are produced characteristically in the presence of chloride ions. Therefore, for simplicity, we have chosen to carry out the tests in a 3 percent aerated solution of sodium chloride (pH = 6). In some cases, to demonstrate the influence of the electrochemical phenomena on the results, a fixed electric potential was imposed on the metal during the test.

Some complementary tests were performed in an acid medium (0.1N, sulfuric acid (H_2SO_4)) in the case of the ferritic steel D.

As previously mentioned, the aim of the program was to try to define the respective roles of corrosion and mechanical failure in the mechanisms of corrosion fatigue. With this objective, we have attempted to separate initiation and propagation phenomena by performing: (*a*) rotating-bending tests

---

[2] The italic numbers in brackets refer to the list of references appended to this paper.

TABLE 1—*Chemical compositions, heat treatments, and mechanical characteristics.*

Steel, AFNOR Designation	Reference Steel	Chemical Composition, weight %							
		C	Si	Mn	Cr	Ni	Mo	N_2	Ti
Z6 CND 17.12	A	0.063	0.51	1.91	16.96	10.70	2.23	. . .	. . .
Z5 CNDT 17.12	B	0.044	0.61	1.66	16.83	11.56	2.16	. . .	0.37
Z3 CNDU 21.7	C	0.023	0.47	1.65	21.10	6.20	2.44	0.049	. . .
Z0 CD 26.1	D	0.001	0.21	0.01	26.21	0.11	1.03	0.007	. . .

Steel, AFNOR Designation	Reference Steel	Heat Treatment	Mechanical Characteristics, at room temperature			
			σ_{ys} (0.2 %), N/mm^2	σ_{ts}, N/mm^2	Elongation, % 50 mm	Reduction, %
Z6 CND 17.12	A	1100°C, 30 mn/water	228	564	68	79
Z5 CNDT 17.12	B	1100°C, 30 mn/water	200	641	66	76
Z3 CNDU 21.7	C	1150°C, 30 mn/water	435	649	41	77
Z 0CD 26.1	D	900°C, 30 mn/water	337	474	43	87

on smooth specimens and (*b*) fatigue crack growth experiments on precracked compact specimens prepared according to ASTM Test for Plane-Strain Fracture Toughness of Metallic Materials (E 399-74).

The geometry of the specimens used is illustrated in Figs. 1 and 2.

The rotating-bending tests and the fatigue crack growth experiments were performed in an immersion cell in which the solution was recirculated. All the metallic parts, other than the specimens, were protected against the effects of galvanic or crevice corrosion.

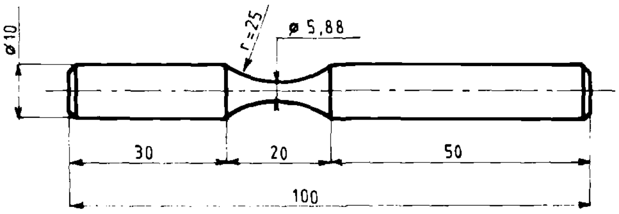

FIG. 1—*Rotating-bending specimen.*

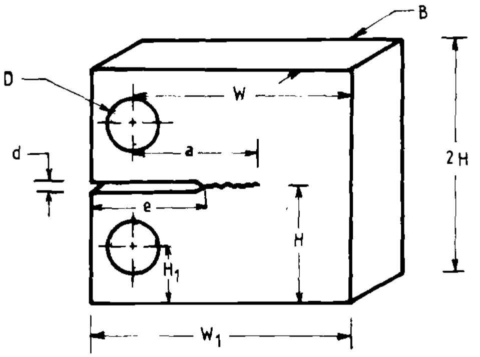

Dimensions (mm)

W = 40
H = 24
D = 10
e = 25
W_1 = 50
H_1 = 13
d = 2
B = 20

FIG. 2—*Compact specimen.*

The rotating-bending tests were performed with 15 specimens to produce the *S-N* curve and to determine, by means of the statistical stair-case method [5], the values at 3×10^7 cycles, of: (*a*) the fatigue limit in air, σ_{DA}, and (*b*) the corrosion-fatigue strength, σ_{DC}. The rotational speed of the specimens was 3000 rpm.

The fatigue crack growth tests were conducted under sinusoidal tension-tension load control, on an MTS, closed loop, hydraulically actuated, servocontrolled mechanical test system. The frequency of tests was from 0.5 to 20 Hz, depending on the case.

In all tests, the specimens were loaded in the environment, and the fatigue crack was initiated and propagated in tension to tension at a constant maximum load and a constant minimum load. The stress ratio, R, ($R = K_{min}/K_{max}$) was 0.1.

The crack usually was initiated and propagated at 20 Hz to a minimum distance of 2 mm from the notch root prior to making crack length measurements, and the frequency then was reduced to the desired test frequency.

Crack lengths were measured through a tempered-glass window, using a traveling microscope. The crack growth rate (da/dN) for a given increment of cracking was calculated by dividing the crack extension (Δa) by the number of cycles in that increment (ΔN). The stress intensity factor (K) was based on the average crack length for that increment using the relationship found in ASTM Test E 399-74 for the compact specimens.

Results and Discussion of the Tests

Rotating-Bending Tests

The results of the rotating bending tests are given in Table 2. The value of each endurance ratio, σ_{DA}/σ_{u} or σ_{DC}/σ_{u}, is shown beside each fatigue limit σ_{DA} or corrosion-fatigue strength σ_{DC} (at 3×10^7 cycles).

Effect of the Metallurgical Structure—The results obtained in air show that the steels can be classified in increasing order of their endurance ratios:

Austenitic steels A and B: 0.55
Austenitic-ferritic steel C: 0.62
Ferritic steel D: 0.74

The results obtained in the chloride medium show that the classification just indicated is the same:

Austenitic steels A and B: 0.42
Austenitic ferritic steel C: 0.45
Ferritic steel D: 0.65

This same relative classification of endurance ratios in air and in corrosive medium is explained by the fact that the steels studied underwent corrosion fatigue in the passive state.

The damage of the materials can be estimated by the decrease of the corrosion-fatigue strength compared with the fatigue limit (Table 3).

The ferritic steel D presents the lowest decrease, because of its high chromium-content, given either a very passive film or at least a passive film which recovers its passivity very rapidly, if damaged.

It is followed by the titanium-stabilized austenitic steel B, which is very resistant to pitting corrosion and stress corrosion in chloride media [*6, 7*], then by the austenitic steel A and the austenitic ferritic steel C.

The resistance to corrosion fatigue in the passive state depends, therefore,

TABLE 2—*Results of the rotating-bending tests.*

Steel, AFNOR Designation	Reference Steel	Air		Corrosive Medium					
				3% NaCl Solution (pH = 6)				H_2SO_4, 0.1N	
				Open Circuit		Imposed Potential		Open Circuit	
		σ_{DA} N/mm^2	σ_{DA}/σ_{ts}	σ_{DC} N/mm^2	σ_{DC}/σ_{ts}	σ_{DC}, N/mm^2	σ_{DC}/σ_{ts}	σ_{DC}, N/mm^2	σ_{DC}/σ_{ts}
Z6 CND 17.12	A	320	0.57	235	0.42	...	...	...	...
Z6 CNDT 17.12	B	335	0.52	270	0.42	...	...	...	...
Z3 CNDU 21.7	C	400	0.62	290	0.45	0 mV 335 50 mV 278	0.52 0.43	...	...
Z 0CD 26.1	D	350	0.74	310	0.65	0 mV 336	0.71	335	0.71

TABLE 3—*Decrease of the corrosion-fatigue strength,* σ_{DC}, *compared with the fatigue limit,* σ_{DA}, *(chloride medium).*

Steel, AFNOR Designation	Reference Steel	$100 \times \frac{\sigma_{DA} - \sigma_{DC}}{\sigma_{DA}}$
Z6 CND 17-12	A	27
Z6 CNDT 17-12	B	19
Z3 CNDU 21-7	C	27
Z0 CD 26-1	D	11

on both the resistance to fatigue in air and thus on the mechanical properties and on the ability to reform the passive film when it is damaged mechanically.

Measurement of the Specimen's Potential—During the corrosion-fatigue tests, the variation in specimen's potential was measured. The saturated calomel electrode was used as reference. The probe was located at 4 mm from the gage length of the specimen for all the tests. For example, Fig. 3 shows the shape of the curves obtained in the case of the austenitic-ferritic steel C for two specimens tested under different stresses (420 and 340 N/mm^2). The free potential of the metal varies with the time; at the beginning of the test, it was about −100 mV and it rose to +100 mV.

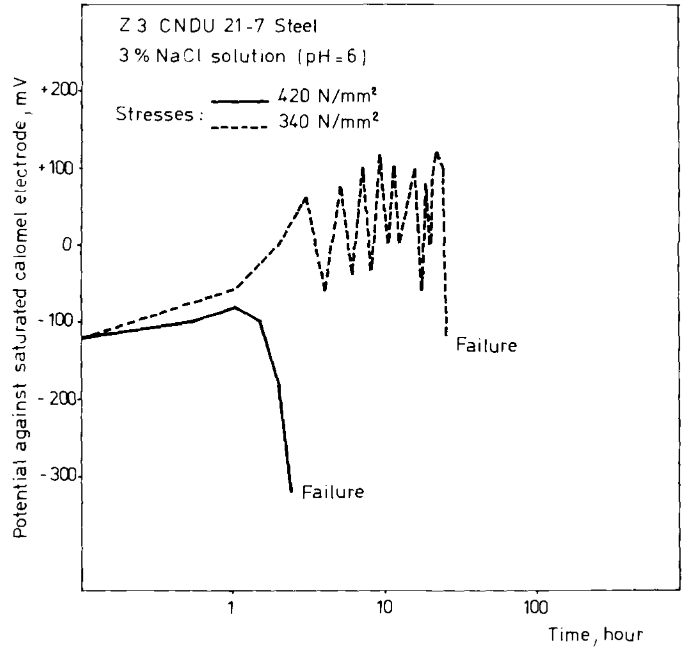

FIG. 3—*Evolution of potential as a function of the life in open circuit.*

The recorded potential is a mixed potential (the result of the anodic and cathodic processes).

The potential can be seen to decrease more quickly at higher stresses. This rapid decrease of the potential under a high load can be due either to the increase of the rate of anodic dissolution or to the increase of anodic areas. This last hypothesis seems the most probable, since the number of crack initiations increases at high stresses. Moreover, tension tests performed at different rates, in chloride media, on analogous materials [*8*], tend to show that, from a certain rate of plastic strain, the rate of anodic dissolution does not increase significantly anymore. This confirms the preponderance of the increase of anodic areas.

In the case of the lowest loads, oscillations in potential were observed which seem to be due to a cycle of depassivation and repassivation.

Similar results have been observed on all the steels studied.

Effect of the Imposed Potential—The current potential curves of the various steels studied were determined by means of potentio-kinetic tests with specimens turning, without applied load, at the same speed as that of the fatigue specimens.

Figure 4 shows, for example, the curve obtained in the case of the austenitic ferritic steel C. From this curve, it can be seen that the metal is passive below 100 mV (saturated calomel electrode (SCE)), whereas pits are not repassivated at potentials above 100 mV (SCE).

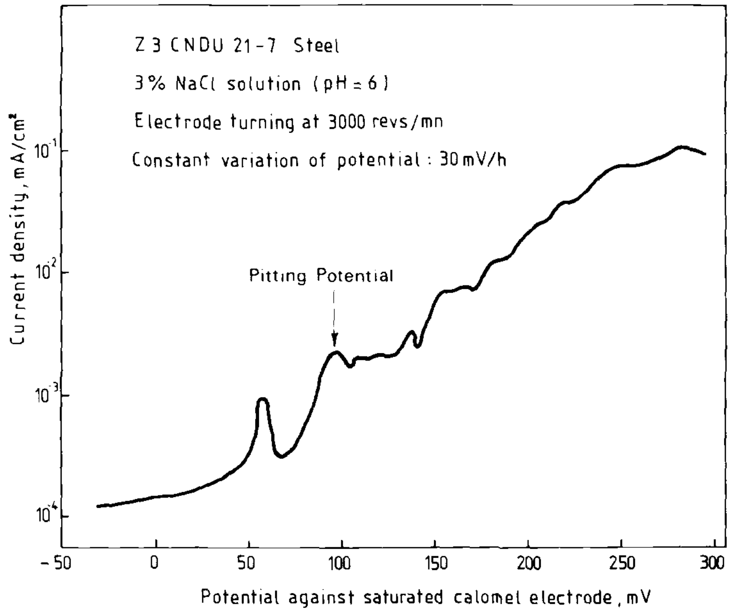

FIG. 4—*Results of potentio-kinetic tests.*

Figure 5 shows the results of the rotating-bending tests obtained on this steel in air and in a chloride medium in open circuit and under imposed potentials of 200, 50, and 0 mV (SCE).

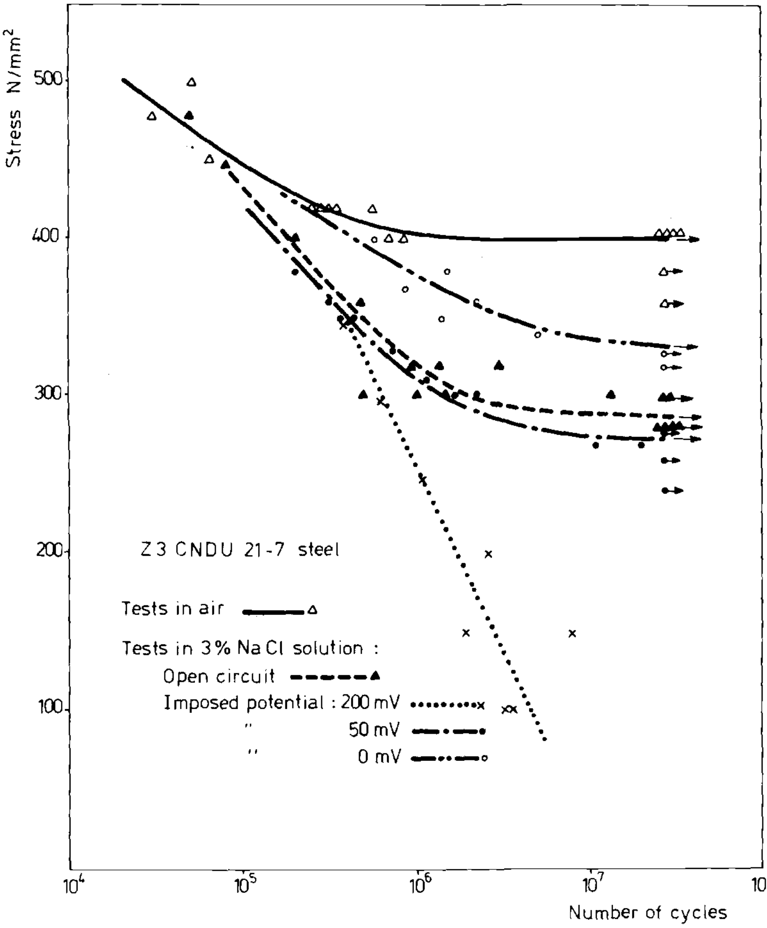

FIG. 5—*Results of the rotating-bending tests.*

The imposed potential of 200 mV (SCE) leads to a considerable drop in the endurance characteristics; it corresponds to a potential level which allows significant localized dissolution.

The results of tests performed under a potential of 50 mV are very close to those made under an open circuit. This potential is within the range where localized corrosion is still possible and could be accelerated by the applied stress because of the damage caused to the passive film.

A significant improvement of the corrosion-fatigue strength occurs when tests are made under a potential of 0 mV; at this potential, the passive film is repaired much more easily. In fact, we can think that, in the passive domain, although the ability of deformation of the film is weak [*9,10*], its reparation is sufficiently rapid.

In the case of the ferritic steel D, the pitting potential is very high (greater than 1200 mV); the evolution of oxygen can be seen without the appearance of pits. Therefore, we have only considered a low potential (0 mV).

The corrosion-fatigue strength obtained under this potential is equivalent to the fatigue limit; this time, the chosen potential corresponds to an extremely stable passive state.

The micrograph of Fig. 6 shows the fracture surface of a rotating-bending specimen tested under a potential of 200 mV. This figure indicates that the crack was initiated at a surface pit. The microfractography of this corrosion pit is given in Fig. 7 where one sees the typical aspect of the interior of the pit in this steel—preferential attack of one of the phases of the alloy.

FIG. 6—*AFNOR Z3 CNDU 21.7 steel, fracture surface of a rotating-bending specimen tested under a potential of 200 mV at σ = 150 N/mm^2. Initiation of the crack at a corrosion-pit.* ×*80.*

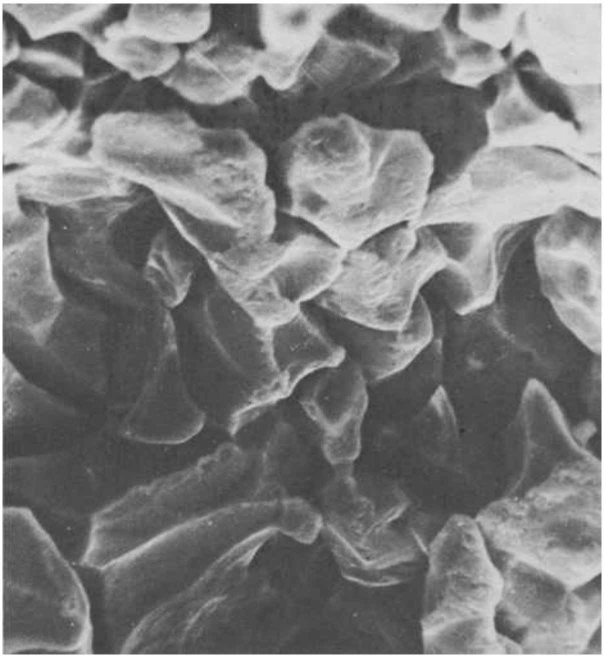

FIG. 7—*AFNOR Z3 CNDU 21.7 steel, aspect of the interior of the pit. (Same specimen as in Fig. 6.* ×*1500.)*

Effect of the Medium—The tests carried out in 0.1N, H_2SO_4 solution, in the case of the ferritic steel D, lead to a value of the corrosion-fatigue strength of 335 N/mm^2, close to the value of the fatigue limit. This result can be explained again by the presence of a very stable passive film in this medium.

To obtain a significant decrease in the corrosion-fatigue strength, the electrochemical conditions of the test (anion or pH) should be modified.

Fatigue-Crack Growth Tests

The influence of the principal parameters studied can be ascertained from the curves produced by the variation of fatigue crack growth da/dN as a function of the variation ΔK of the stress intensity factor.

Effect of the Metallurgical Structure on the Crack-Growth Rate in Air—Figure 8 brings together the fatigue crack growth curves obtained on the four steels, A, B, C, D. This figure shows that: (*a*) crack growth curves of steels A and B are almost identical and (*b*) for values of ΔK greater than 30 MPa $\sqrt{m}$, the lowest crack-growth rate is given by the ferritic steel D, followed by the austenitic-ferritic steel C, and the austenitic steels A and B.

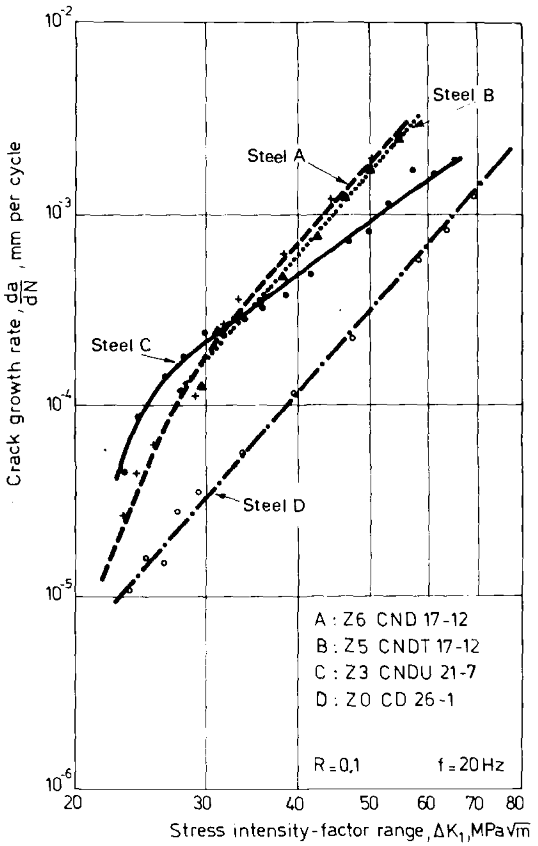

FIG. 8—*Crack growth rates in air.*

Effect of the Corrosive Medium (3 percent sodium chloride (NaCl)) on the Crack-Growth Rate of the Various Steels Studied—Measurements made on the austenitic steels A and B show that, in these steels, at a frequency of 20 Hz, the corrosive solution has no influence on the crack growth rate; the results obtained in chloride solution are identical to those obtained in air.

However, in the case of the austenitic-ferritic steel C, for high values of ΔK, a significant increase in the crack growth rate is observed (Fig. 9), and the lower the frequency, the greater is this increase. A similar result is found in the case of the ferritic steel D (Fig. 10). This increase in crack growth rate can be explained by an acceleration of anodic dissolution under the effect of increasing applied stresses [*3,4*].

Discussion

The measurements of fatigue crack-growth rate in a chloride solution have shown that, at a frequency of 20 Hz, the crack-growth rates are unaf-

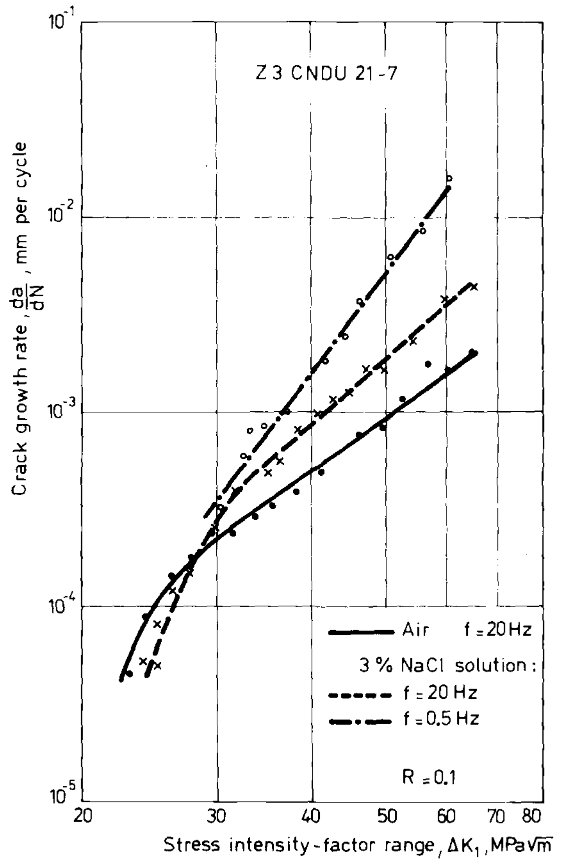

FIG. 9—*Crack growth rates of AFNOR Z3 CNDU 21-7.*

fected by this medium for austenitic steels A and B, but are influenced in the case of austenitic-ferritic and ferritic steels C and D.

A completely opposite effect of this medium was observed for the rotating-bending tests.

These results can be explained by the competition of the mechanisms of depassivation, dissolution, and repassivation which occur differently in the two types of tests.

The rotating-bending tests, performed on smooth specimens, are essentially, for high-cycle fatigue initiation tests [*11,12*], and the values of the corrosion-fatigue strength, in a neutral medium, depend on the stability of the passive film.

In the case of the fatigue crack growth tests, the passive film is destroyed by the propagation of the fatigue crack; there is then competition between the processes of repassivation and metal dissolution.

At the crack tip, a complex phenomenon occurs in which crevice corrosion takes place, by a decrease in pH due to metal ion hydrolysis, simul-

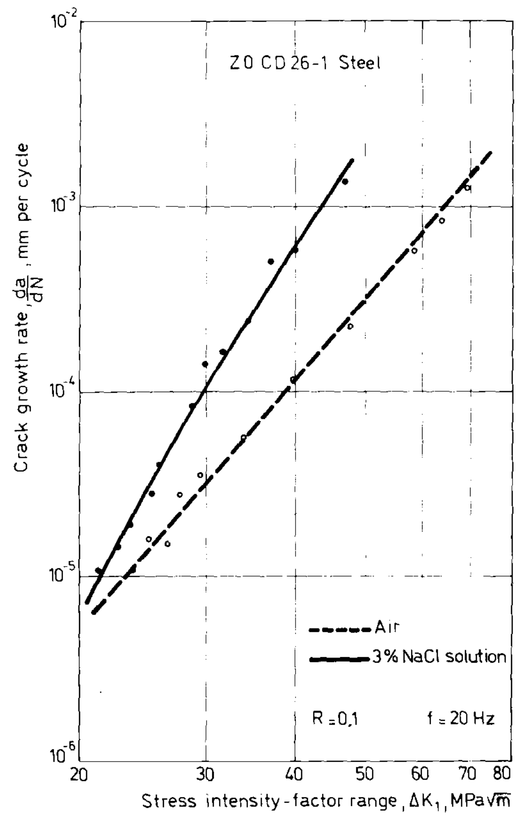

FIG. 10—*Crack growth rates of AFNOR Z0 CD 26-1 steel.*

taneously with mechanical fatigue [*13*]. Therefore, the situation at the crack tip ressembles that of a corrosion-fatigue test performed in a very acid chloride medium.

It is known that, in these conditions, ferritic steels have, in the active state, a very fast rate of dissolution; they are then very sensitive to crevice corrosion (unless the chromium content is at least 30 percent) [*14,15*].

This fact would explain the observed crack growth rates of the ferritic steel D. Thus, as soon as the precracked specimen is loaded, the presence of the fatigue crack would lead to an irreversible deterioration of the passive film, then to a decrease in the pH at the crack tip and the development of localized dissolution. On the contrary, in the case of the austenitic steels which are less sensitive to dissolution in the active state, the frequency of 20 Hz is probably too high to allow the dissolution phenomenon to cause as much damage. This fact is confirmed by some tests performed at low frequencies (<0.01 Hz), in which we have observed an effect of the chloride solution on the austenitic steel A.

The austenitic-ferritic steel, which contains more chromium than the austenitic steels but in which preferential dissolution of one phase can occur, seems to have a behavior intermediate between the austenitic and the ferritic steels.

Conclusion

From the tests performed, a study of the initiation and propagation stages of the fatigue cracks in four stainless steels was possible.

Each of the rotating-bending tests and the fatigue crack growth tests produced a classification of the steels towards resistance to corrosion fatigue. The classifications obtained are different for these two types of tests which, taken individually, do not allow this to estimate the overall resistance of a stainless steel to corrosion fatigue. In fact, the austenitic steel A and the ferritic steel D have a behavior opposite in initiation and in propagation.

From the measurements of potential and the tests made under an imposed potential, the effect of the applied load can be assessed. The region of passivity of the metal seems likely to depend on the stress. In a corrosive medium, with a sufficiently low potential, the values for the corrosion-fatigue strength are found to be the same as the fatigue limit in air.

The overall results show the importance of electrochemical phenomena in the mechanisms of corrosion-fatigue. The capacity of the metal for dissolution and for passivation seems largely to be responsible for the behavior of the metal in a corrosive medium.

This capacity varies notably with the composition of the metal, the loading conditions of the specimens, and the characteristics of the corrosive medium. It appears, moreover, that the rate of dissolution can depend on the applied stress. A stable potential on an uncharged specimen can correspond to a region where dissolution is still possible if the metal is under a high stress.

In the case of the chloride solution with a pH of 6, the ferritic steel D has an extremely stable passive film. When this later is destroyed by a fatigue crack, we observe an acceleration of the metal dissolution rate and, thus, an increase in the rate of fatigue crack propagation.

The austenitic steel A has a lower passivity, which facilitates the initiation of a corrosion-fatigue crack, particularly at corrosion pits [*16,17*]. But once the crack is initiated, a certain amount of repassivation of the metal or a relatively low dissolution rate, leads to propagation rates which are not very different from the rates obtained in air.

All these phenomena obviously depend upon the concentrations of nickel, chromium, and molybdenum in the alloys, and in the present state of our research work, we cannot generalize these results to other stainless steels.

References

[*1*] Speckhardt, H., International Corrosion Conference Series, Vol. NACE-2, National Association of Corrosion Engineers, 1972, pp. 557-568.

[*2*] Spahn, H., International Corrosion Conference Series, Vol. NACE-2, National Association of Corrosion Engineers, 1972, pp. 40-51.

[*3*] Staehle, R. W., International Corrosion Conference Series, Vol. NACE-5, B3, National Association of Corrosion Engineers, 1973.

[*4*] Hoar, T. P., International Corrosion Conference Series, Vol. NACE-5, G11, National Association of Corrosion Engineers, 1973.

[*5*] Dixon, W. J. and Mood, A. M., *Journal of the American Statistical Association,* Vol. 43, 1948, pp. 109-126.

[*6*] Desestret, A., Creusot-Loire-Centre de Recherches d'Unieux, Report 1009, Oct. 1971.

[*7*] Combrade, P., Desestret, A., and McCright, R. D., *Memoires Scientifiques, Revue Mètallurgie,* Vol. 71, No. 12, 1974, pp. 807-822.

[*8*] Desestret, A., Combrade, P., Gauthey, F., Ranvier, J. L., and Paliard, M., Creusot-Loire-Centre de Recherches d'Unieux, Report DGRST 74.1.1118, Oct. 1976.

[*9*] Prazak, M. and Holinka M., International Corrosion Conference Series, Vol. NACE-5, G.20, National Association of Corrosion Engineers, 1973.

[*10*] Petit, M. C. and Desjardins, D., International Corrosion Conference Series, Vol. NACE-5 G.21, National Association of Corrosion Engineers, 1973.

[*11*] Manson, S. S., *Experimental Mechanics,* July 1965.

[*12*] Klimas, S. J., Lesco, D. J., and Freche, J. C., NASA Technical Note TND.3007, Sept. 1965.

[*13*] Brown, B. F. in *The Theory of Stress Cracking in Alloys,* NATO, Brussels, 1971, p. 186.

[*14*] Crolet, J. L. and Defranoux, J. M., *Corrosion Science,* Vol. 13, 1973, p. 575.

[*15*] Barnier, L., Desestret, A., and Vallier, G., Communication au IVe Congrès International de la Corrosion Marine et des Salissures, No. 14.19, June 1976.

[*16*] Weigand, H., Speckhardt, H., and Spahn, H., *Stahl und Eisen,* Vol. 14, 1968.

[*17*] Weigand, H., Speckhardt, H., and Spahn, H., Archir für das Eisenhüterwesen, Vol. 3037, 1969.

J. A. Moskovitz[1] *and R. M. Pelloux*[1]

Corrosion-Fatigue Behavior of Austenitic-Ferritic Stainless Steels

---

REFERENCE: Moskovitz, J. A. and Pelloux, R. M., "**Corrosion-Fatigue Behavior of Austenitic-Ferritic Stainless Steels,**" *Corrosion-Fatigue Technology, ASTM STP 642,* H. L. Craig, Jr., T. W. Crooker, and D. W. Hoeppner, Eds., American Society for Testing and Materials, 1978, pp. 133–154.

ABSTRACT: The corrosion-fatigue behavior of austenitic-ferritic (duplex) stainless steels, which combine high strength, good fracture toughness, and excellent corrosion resistance, is described in detail. The physical metallurgy of this class of alloys is reviewed so that the microstructure of different cast and wrought alloys can be understood in terms of alloy content, heat treatment, and cooling rate. The corrosion and stress corrosion cracking behaviors of duplex stainless steels are discussed and related to their corrosion-fatigue resistance. The results of recent work investigating the effects of various microstructural variables on corrosion-fatigue crack initiation and crack propagation in acidic chloride solution are described. The main structural variables are: volume fraction of austenite and ferrite, microstructural orientation of the different phases, embrittling intermetallic precipitates, and grain boundary carbides. An attempt is made to describe the microstructural features which will give the best corrosion-fatigue resistance in austenitic-ferritic stainless steels.

KEY WORDS: austenitic-ferritic stainless steels, corrosion fatigue, stress corrosion, microstructural effects, fracture (materials)

The problem of insufficient corrosion-fatigue resistance in the standard grades of stainless steels is due to a variety of deficiencies in these various alloy classes. The austenitic alloys, such as Types 304 and 316, have a rather limited fatigue strength because of their low yield strength. Furthermore, they are quite susceptible to stress corrosion cracking (SCC) in a variety of mildly corrosive environments. Ferritic alloys, such as Types 430 and 446, have rather low ductility and low toughness, resulting in high fatigue crack propagation rates at stress intensities greater than half the fracture toughness, K_c. The martensitic alloys, such as Type 410, have higher yield strength and good toughness in the tempered condition, but

---

[1] Research assistant and professor, respectively, Department of Materials Science and Engineering, Massachusetts Institute of Technology, Cambridge, Mass. 02139.

their lower chromium content significantly decreases their corrosion resistance.

The recent need for materials which combine high yield strength, good ductility and toughness, and excellent corrosion resistance has led to the development of austenitic-ferritic stainless steels with superior corrosion fatigue resistance [*1*].[2] These alloys, often referred to as duplex stainless steels, have been used in the chemical and nuclear industries for applications calling for high corrosion, SCC, and corrosion-fatigue resistance. These alloys have the corrosion resistance, ductility, and toughness of austenitic stainless steels, the SCC resistance of ferritic stainless steels, and the high yield strength usually present in two-phase alloys.

One interesting application in which both cast and wrought stainless steels are being used extensively to resist corrosion fatigue is in suction-press rolls in the paper industry. These rolls, which are subjected to high alternating stresses due to rotating bending, operate in an acidic chloride environment known as "white water" [*2*]. Under these service conditions, corrosion-fatigue cracks are initiated at the edges of closely spaced suction holes which serve as stress concentration sites. Suction-press rolls, which can measure as much as 2 m in diameter by 12 m long and 100 mm thick, are either centrifugally cast or fabricated from wrought material (which necessitates welding). When cast materials are used, their corrosion-fatigue behavior is strongly affected by the stresses due to rapid cooling and by the presence of large and small casting defects. On the other hand, welding the wrought alloys leads to the complex problem of phase transformations in the heat affected zone. In both cases, cast or wrought materials, the corrosion-fatigue behavior of the component is a function of the processing history as well as the chemical composition of the alloy.

In this paper, we first will review extensively the literature dealing with the physical metallurgy, corrosion and SCC, and structure-property relationships of austenitic-ferritic stainless steels. Then, we will describe recent research results on the evaluation of the effect of various metallurgical variables on the corrosion-fatigue crack initiation and crack propagation behavior of various commercially available duplex alloys.

Alloy Chemistry and Microstructures

Austenitic-ferritic stainless steels generally contain more than 18Cr, 4 to 10Ni, and less than 0.08C, along with significant amounts of molybdenum, manganese, and silicon. Compositions of commercially available alloys which will be referred to in this paper are listed in Table 1. Typical mechanical properties are listed in Table 2. These alloys are generally water quenched from a temperature of between 1050 and 1150°C, which is

---

[2] The italic numbers in brackets refer to the list of references appended to this paper.

TABLE 1—*Composition of alloys.*

Alloy	C	Cr	Ni	Mo	Mn	Si
Uranus 50	0.02	21.4	6.6	24.	1.9	0.55
3RE60	0.02	18.9	5.2	2.7	1.6	1.6
Alloy 63	0.08	21.5	10.0	3.0	2.0	2.0
VK-A171	0.07	22.2	8.3	1.2	0.76	1.1
VK-A271	0.06	24.6	4.3	0.68	0.71	1.3
IN 744	0.02	25.5	6.1	...	0.45	0.55
	N	**P**	**S**	**Cu**	**Ti**	**Al**
Uranus 50	...	...	...	1.6	0.08	...
3RE60	0.034	0.025	0.05	...	...	...
Alloy 63	0.25	...	...	...	0.50	...
VK-A171	...	0.02	0.031	...	...	...
VK-A271	...	0.02	0.02	...	...	...
IN 744	0.12	...	...	...	0.23	0.12

TABLE 2—*Typical mechanical properties.*

Alloy	Yield Strength, MPa	Ultimate Tensile Strength, MPa	Elongation, %	Reference
Uranus 50	400.0	670.0	35.0	*7*
3RE60	435.0	707.0	39.0	*16*
Alloy 63	373.7	639.1	43.0	*17*
VK-A171	379.2	630.2	36.4	*17*
VK-A271	511.6	634.3	25.6	*17*
IN 744	468.8	696.4	37.0	*18*

usually about 200°C below the austenite solvus. In this temperature range for an alloy of typical composition, the as-quenched alloy will have a metastable microstructure containing anywhere from 20 to 60 percent austenite, which has precipitated from the ferrite upon slow cooling below the austenite solvus. By altering the composition and quenching temperature, the volume fraction of austenite can be varied greatly.

Diagrams have been developed for cast and wrought stainless steels by Schaeffler [*3*], Pryce and Andrews [*4*], and Guiraldenq [*5*], which predict the metastable volume fraction of each phase for a variety of alloying elements. Jolly [*6*] has published a diagram plotting percent ferrite as a function of the ratio of chromium equivalent/nickel equivalent (Fig. 1) and a diagram showing percent ferrite as a function of quenching temperature for Uranus 50 (Fig. 2). From these diagrams it is clear that the metastable volume fraction of austenite in the microstructure is very sensitive to composition, quenching temperature, and cooling rate.

Partitioning of the alloying elements between the two phases is significant

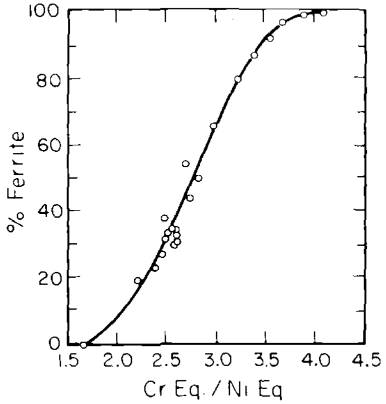

FIG. 1—*Variation in volume fraction ferrite as a function of alloying elements* [6]. *Cr_{eq} = percent chromium + 2× percent molybdenum + 1.5 × percent silicon. Ni_{eq} = percent nickel + percent copper + 15 × percent carbon + 15 (percent nickel − percent titanium/3.5).*

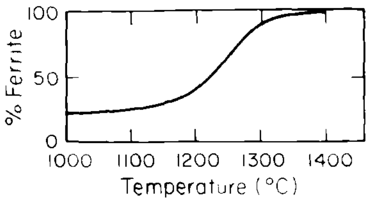

FIG. 2—*Variation in volume fraction ferrite as a function of quenching temperature* [6].

and can be predicted from the iron-chromium-nickel ternary phase diagram. Microprobe analyses of the composition of the two phases [*6–8*] have shown partition ratios (weight percent alloying element in ferrite/weight percent alloying element in austenite) to vary between about 1.8 and 1.2 for ferrite stabilizers and 0.35 and 0.90 for austenite stablizers.

Other phase transformations can occur during slow cooling, heat treatment, or service in the 500 to 1000°C range [*1,6,7,9*]. Chromium-rich ($\simeq$ 45 percent) σ-phase will precipitate between approximately 550 to 950°C, increasing the hardness of the alloy and producing a corresponding decrease in ductility and corrosion resistance. The phenomena known as 475°C embrittlement occurs when a fine intermetallic chromium-rich ($\simeq$ 80 percent) phase forms within the ferrite by spinodal decomposition to α'. In addition to these intermetallic phases, a chromium-carbide of the form $M_{23}C_6$ will precipitate extremely rapidly at the phase boundaries at temperatures below 1000°C. This carbide formation, which depletes the region adjacent to the phase boundaries of chromium, is known as "sensitization."

Austenitic stainless steels are known to undergo both spontaneous and strain-induced martensitic transformations if the temperature is lowered sufficiently [*7,10*]. The formation of strain-induced martensite in the austenite phase will result in marked strengthening and a high work hardening rate. However, Wakasa and Nokamura [*11*] recently have shown for an austenitic-ferritic stainless steel that $M_d = -22°C$ and $M_s = -196°C$, indicating that no martensite will form during room temperature deformation.

Figure 3 shows the microstructure of a typical cast duplex stainless steel,

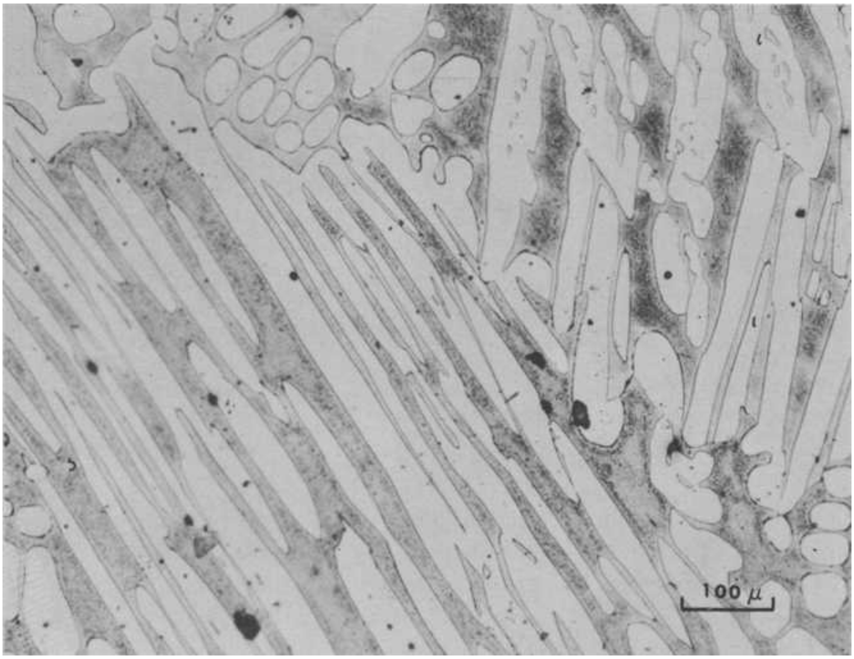

FIG. 3—*VK-A171 microstructure, as received, ~50 percent ferrite. Light austenite islands in dark ferrite matrix, Kalling's reagent,* × *125.*

VK-A171, in the as-recieved condition (quenched from 1050°C), containing approximately 50 percent austenite. When this alloy is reheated to 1250°C, taking all the austenite into solution, and then held at 1150°C for 45 min and water quenched, the volume fraction of austenite is reduced to approximately 15 to 20 percent, as shown in Fig. 4. The microstructure of cast Uranus 50 quenched from 1150°C contains approximately 65 percent austenite and appears very similar to that of VK-A171. Uranus 50 is also produced in the wrought form, and when it is hot rolled at 1150°C, a much finer distribution of the phases results, with the austenite phase

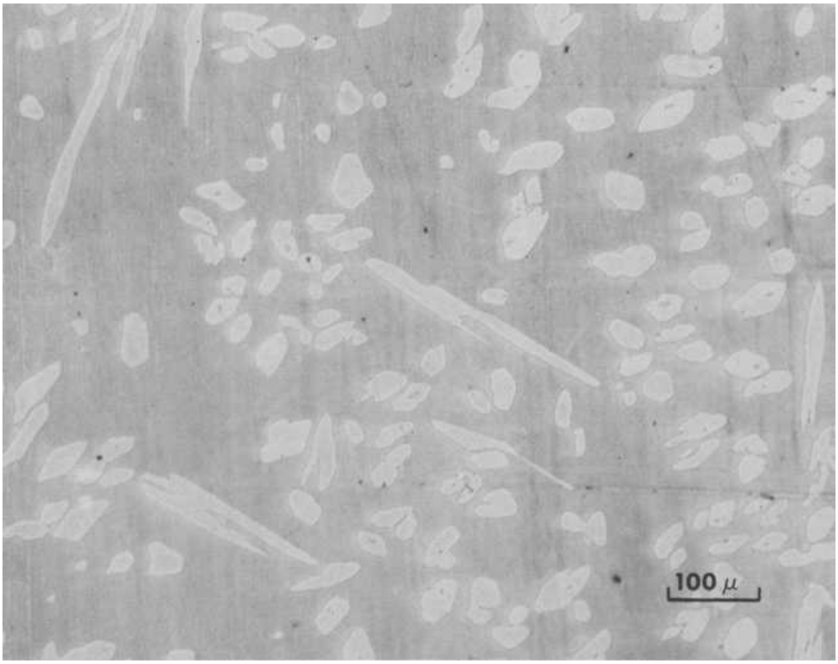

FIG. 4—*VK-A171 microstructure, solutionized at 1250°C, held at 1150°C for 45 min and water quenched, ~80 percent ferrite, Kalling's reagent, ×125.*

elongated in the rolling direction. Figure 5 is a micrograph of wrought Uranus 50 in the rolling plane. Among the other alloys listed in Table 1, 3RE60 and IN 744 are also produced as wrought alloys.

Corrosion and SCC Resistance

Early studies of austenitic-ferritic stainless steels centered around their corrosion and SCC resistance, as they were primarily candidate materials for use in the chemical industry. In weakly oxidizing acid environments, the presence of increasing amounts of ferrite improves corrosion resistance, as the polarization between the austenite and ferrite improves the stability of the passive film [*1,12*]. However, in strongly oxidizing environments, where passivation will not occur, the presence of ferrite detracts from the corrosion resistance, as galvanic action between the two phases can bring about rapid disintegration [*12*]. Ferrite also was found to be beneficial to SCC resistance in chloride environments up to about a 50 percent volume fraction, except for high-carbon nonstabilized (>.08C) alloys [*1*]. The increased resistance imparted by the ferrite was attributed to a "keying

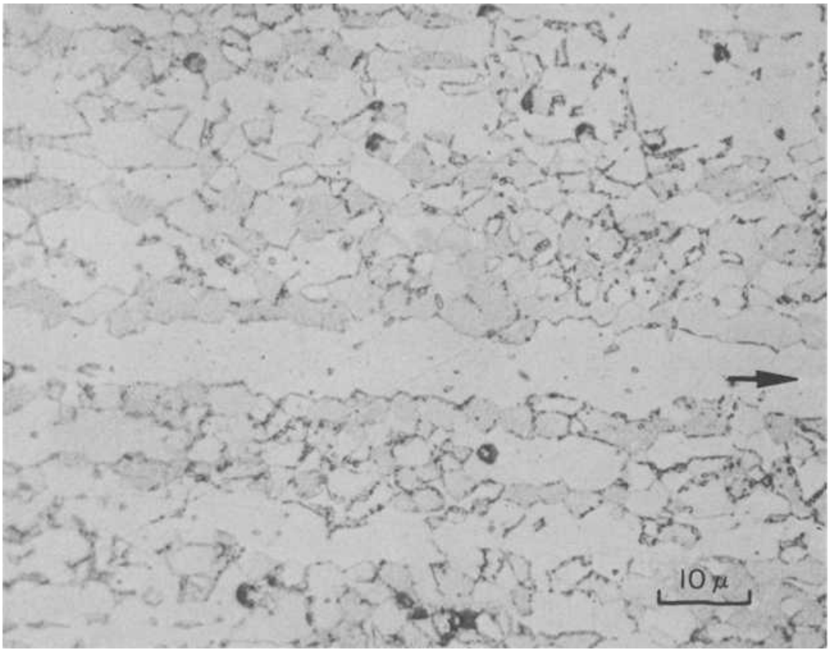

FIG. 5—*Uranus 50 microstructure, wrought, rolling plane, arrow indicates rolling direction, elongated austenite (light) and ferrite (dark) phases, Kalling's reagent, ×1000.*

effect" of the ferrite in slowing down crack propagation by forcing the cracks to propagate around rather than through the ferrite islands.

The SCC in duplex alloys can be both intergranular (IG) and transgranular (TG). The IGSCC occurs primarily along austenite-ferrite phase boundaries and therefore is related closely to IG corrosion resistance. The precipitation of intermetallic second phases and chromium carbides along boundaries generally accelerates IG corrosion and correspondingly causes susceptibility to IGSCC [*7*]. However, there is little correlation between IGSCC and TGSCC resistance. Uranus 50 has been found to be resistant to both forms of SCC, while 3RE60 has been found to be resistant to IGSCC but susceptible to TGSCC [*13*]. Shimodaira et al [*14*], in an extensive study of TGSCC of duplex stainless steels, showed that TGSCC will occur in all duplex alloys, both austenitic-base and ferritic-base, if the applied tensile stress is sufficiently high.

Morphology of Corrosion-Fatigue Crack Initiation and Propagation

One of the most interesting characteristics of austenitic-ferritic stainless steels is their lack of susceptibility to accelerated fatigue crack propagation in aqueous environments. Crack propagation rates at 10 Hz have been found to the the same in air and in acidic chloride solution (pH = 3.5) for Alloy 63, VK-A171, and VK-A271 [*15*], and 3RE60 [*16*]. There is a slight acceleration of crack growth due to a corrosive environment at low growth rates ($< 5 \times 10^{-8}$m/cycle) for IN 744 [*18*]. However, it is well known that the presence of a corrosive environment does decrease the fatigue limit and the fatigue strength at long lifetimes ($> 10^6$ cycles) for these alloys; a typical *S-N* curve is given in Fig. 6 [*19*]. Therefore, we have

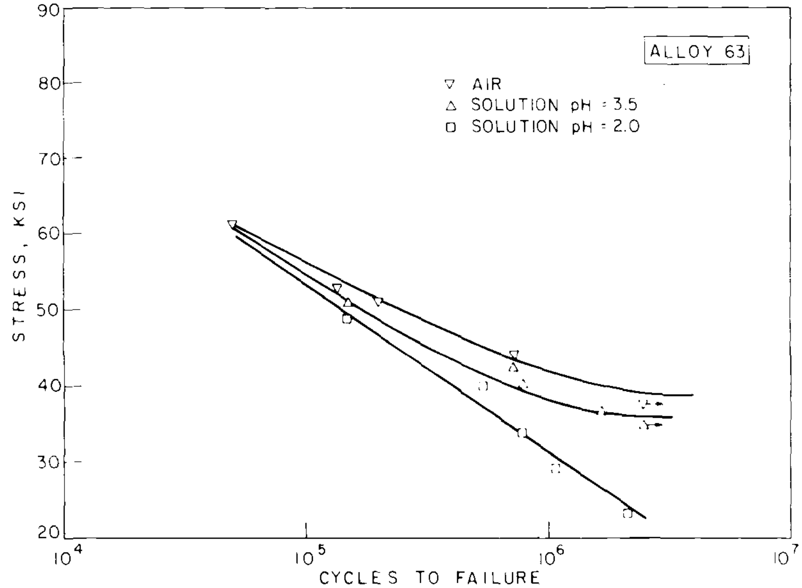

FIG. 6—S-N *curves, Alloy 63, smooth bar,* R = −*1.*

to conclude that corrosion-fatigue effects in these alloys occur primarily in the crack initiation stage. Various studies have dealt with environmental effects on fatigue crack initiation. The most popular theories involve crack initiation either by accelerated dissolution at persistent slip bands (PSB) due to film fupture [*20*] or by changes in the near-surface dislocation arrangement due to surface dissolution, resulting in accelerated PSB formation [*21*]. The relative merits of these conflicting theories have been compared by various authors [*22, 23*], but the dominance of either theory has yet to be shown conclusively.

As environmental effects are known to differ between the initiation and propagation stages, it follows that the role of each individual microstructural phase can also differ in the various stages of the fatigue process and can be affected selectively by the environment. Smooth-bar crack initiation studies performed on typical austenitic-ferritic alloys, described in detail elsewhere

[*19*], have shown that the site at which a fatigue crack initiates can be a function of both stress level and environment, as well as alloy composition and microstructure. The corrosive environment utilized was a simulated "white water" solution, consisting of 0.165 percent sodium chloride and 0.350 percent sodium tetrasulfide (Na_2SO_4) in distilled water, adjusted to a pH of 3.5 with sulfuric acid (H_2SO_4), and was constantly recirculated through an immersion cell during testing. Scanning electron microscope (SEM) micrographs of electropolished specimen surfaces illustrate the following phenomena.

1. For Alloy 63, crack initiation in air occurs mainly at inclusions (Fig. 7) or at phase boundaries, except at high stress levels where initiation occurs at PSB in the austenite. In an acidic chloride solution, crack initiation occurs at PSB in the austenite regardless of stress level (Fig. 8).

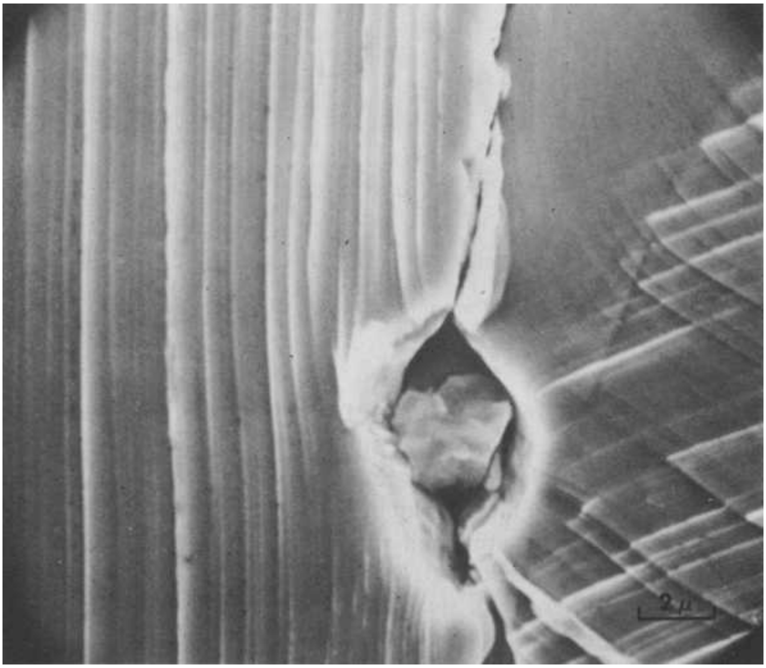

FIG. 7—*Crack initiation at inclusion, Alloy 63, air,* σ_{alt} *= 44 ksi (303 MPa),* ×*4800.*

2. For VK-A171 and VK-A271, crack initiation occurs mainly along phase boundaries in air (Fig. 9) but shows a tendency to occur at PSB in solution (Fig. 10).

3. For IN 744, crack initiation occurs at phase boundaries regardless of environment.

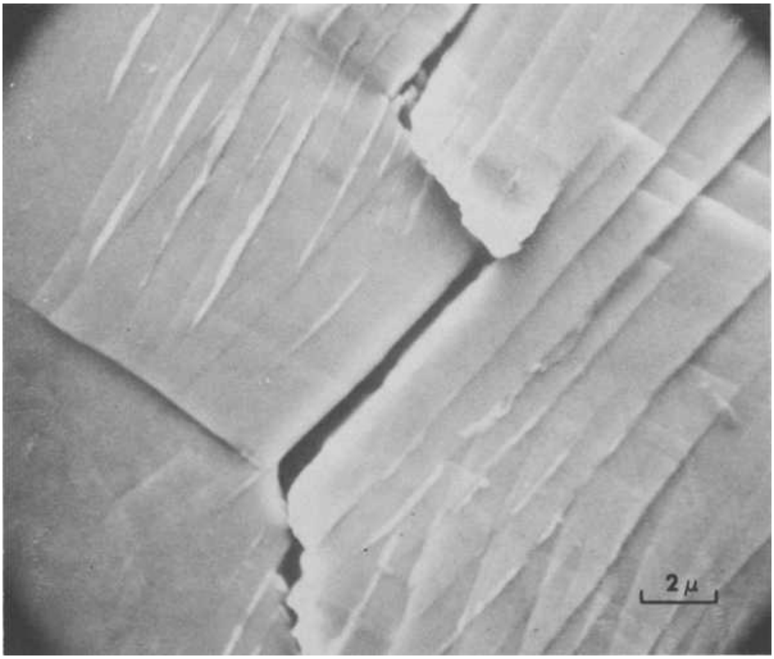

FIG. 8—*Crack initiation at PSB in austenite, Alloy 63, white water,* σ_{alt} *= 51 ksi (352 MPa),* ×*4750.*

These observations can be accounted for by either of the aforementioned crack initiation theories. However, a study of repassivation rate as a function of pH [*24*] shows that there is more rapid repassivation at lower pH. Since any crack initiation mechanism involving film rupture would be slowed down or suppressed by more rapid repassivation, the film rupture theory cannot account for the fact that lower fatigue lifetimes are observed at lower pH. On the other hand, steady-state surface dissolution is unaffected by the repassivation behavior, and it increases with lower pH. Consequently, electrochemically accelerated crack initiation at PSB in austenitic-ferritic stainless steels is believed to be due to a reduction in the resistance to PSB formation brought about by an interaction between the environment and the near-surface dislocation structure. Any environmental acceleration of crack initiation at phase boundaries is less evident, but it may also occur by a mode similar to this accelerated PSB formation because of segregation or precipitation at the boundaries.

Crack initiation and propagation from a sharp preexisting notch is quite similar to low growth rate crack propagation, and therefore it will be considerably less sensitive to a corrosive environment than crack initiation at PSB in smooth bars. The *S*-*N* curves obtained for sharply notched bars

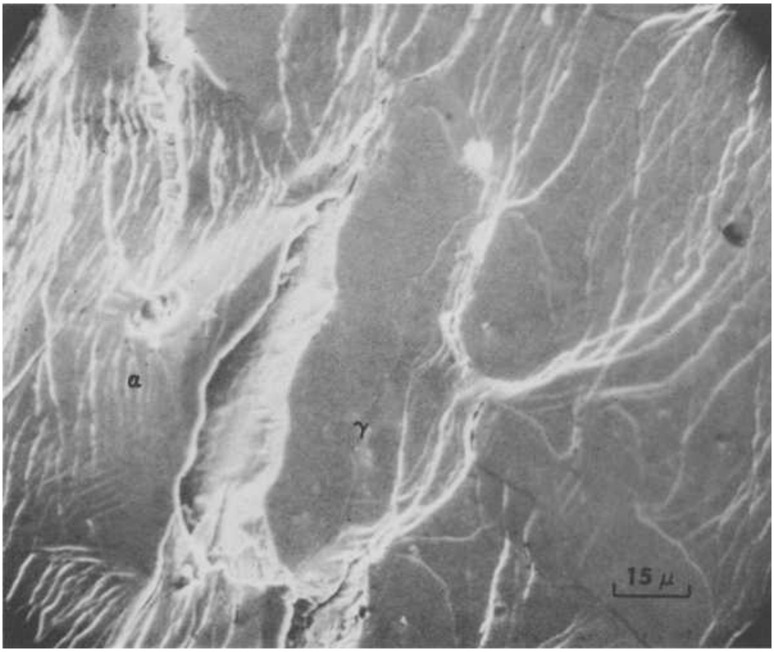

FIG. 9—*Crack initiation at austenite-ferrite phase boundaries, VK-A271, air,* σ_{alt} *= 47 ksi (324 MPa),* × *700.*

of VK-A271 (the detailed experimental procedure is described in Ref *24*), shown in Fig. 11, exhibit some acceleration of crack initiation under a low applied mean tensile stress in a corrosive environment ($R = \sigma_{min}/\sigma_{max} = 0.05$), but this environment effect disappears at higher mean stress ($R = 0.6$). The absence of an environment effect under high applied mean stress and the concomitant increase in crack initiation susceptibility and crack growth rates (Fig. 12) are due to the predominance of purely mechanical fatigue effects which are greatly promoted by high mean stress, specifically the tendency for cleavage-like failure to occur in ferrite phase. Figure 13 is a SEM micrograph of a typical fracture surface obtained at $R = 0.6$ and shows the cleavage-like fracture in the ferrite along with more ductile failure in the austenite, evidence of a keying effect of the austenite in retarding crack propagation. Similar observations have been made by Liljas in studies of 3RE60, in which the keying effect of the austenite also has been observed in polished cross sections showing the path of corrosion-fatigue cracks [*25*]. At lower mean stress levels, there still remains some tendency towards a low energy mode of fracture in the ferrite, as the crack front in the austenite lags behind the crack front in the ferrite, as shown in Fig. 14. Thus

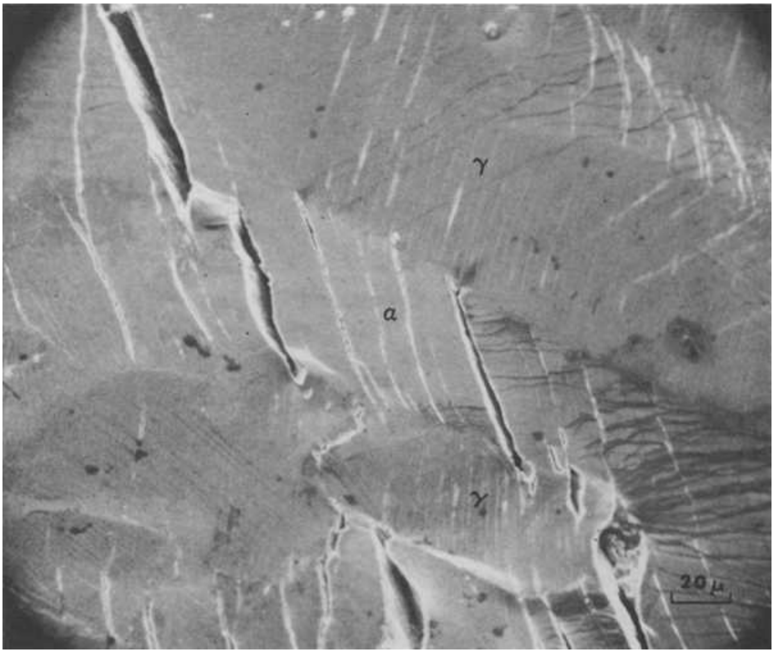

FIG. 10—*Crack initiation at PSB in ferrite, VK-A171, white water,* σ_{alt} *= 44.5 ksi (307 MPa),* ×*400.*

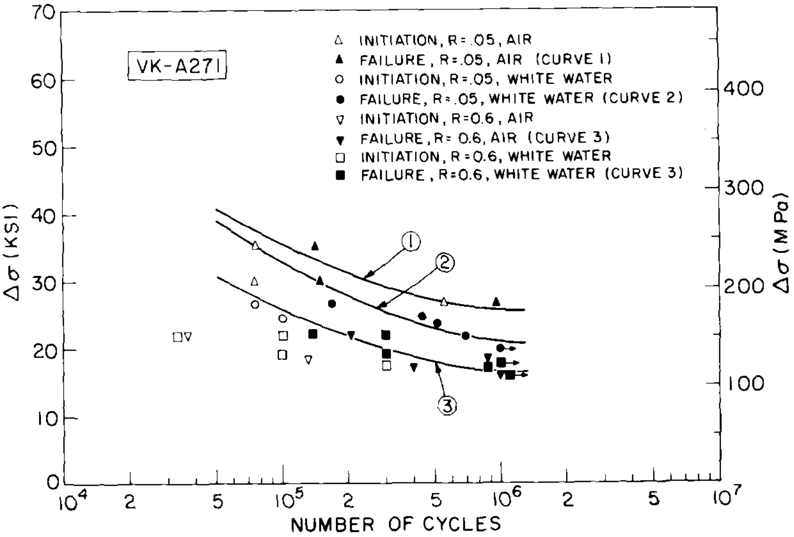

FIG. 11—S-N *curves, VK-A271, notched bar.*

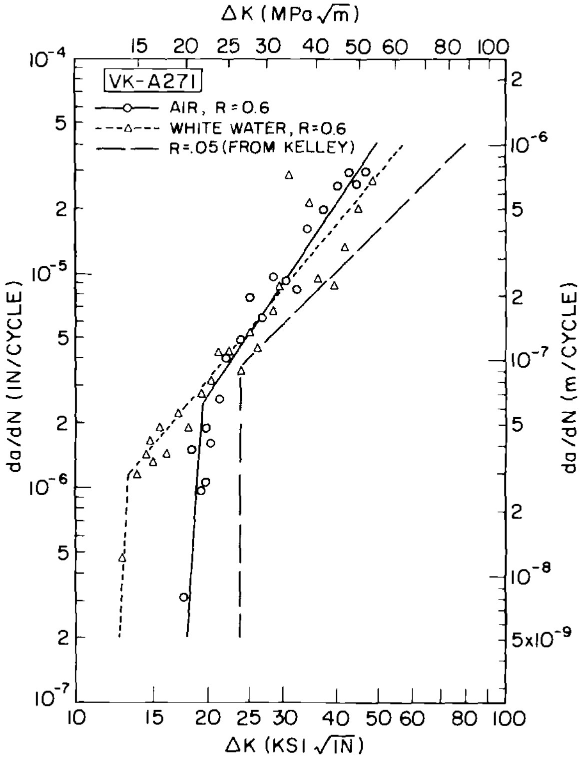

FIG. 12—*Fatigue crack growth rate curves, VK-A271, showing effect of mean stress level.*

it appears that the austenite retards crack propagation but enhances crack initiation in an aggressive environment.

Effect of Varying the Volume Fraction of Austenite and Ferrite

The tendency of one phase to enhance crack initiation and retard crack propagation in corrosion fatigue and vice versa is due primarily to differences in microductility between the two phases [*26*]. A ductile phase (in this case, the austenite) can accommodate a large amount of cyclic plastic deformation before failing by a static mode, but it will undergo extensive slip activity leading to more rapid crack initiation. The stronger but less ductile phase (ferrite) undergoes little slip, but tends to fail by cleavage once a crack is initiated. Also contributing to the difference between the behavior of the two phases are the electrochemical effects discussed by Shimodaira et al [*14*] for SCC. The optimum duplex microstructure therefore should be one which balances all these effects to produce a material which has an austenite phase with higher strength to resist crack initiation and a ferrite phase with better ductility and toughness to resist crack pro-

FIG. 13—*VK-A271 fracture surface,* R = *0.6. Cleavage-like failure in ferrite phase, white water,* ΔK ≃ *20 ksi*$\sqrt{\text{in.}}$ *(22 MPa*$\sqrt{m}$*),* ×*425. Arrow indicates crack growth direction.*

pagation, along with the proper volume fraction of each to give the material both high strength and good toughness, and minimize electrochemical effects. As previously discussed, the volume fraction of each phase can be varied through composition or heat treatment. Thus, when comparing a series of alloys with varying volume fraction ferrite, the approach which maximizes the number of variables held constant yields the most useful comparisons.

Flowers et al [*1*] compared the SCC behavior of commercially available duplex alloys, finding a general trend of increasing SCC resistance with increasing ferrite content (up to 44 percent). However, both composition and heat treatment were different for these alloys, and the magnitude of improved SCC resistance was very much a function of alloy content. In contrast, the SCC study of Shimodaira et al [*14*] utilized only changes in nickel content to vary ferrite fraction, with maximum SCC resistance occurring at 40 percent ferrite. This approach makes the nickel content and therefore the stacking fault energy (SFE) of the austenite approximately the same in each alloy.

Jolly [*27*] has varied the nickel content to examine the effect of ferrite content on mechanical properties. The yield strength increases, the ductility

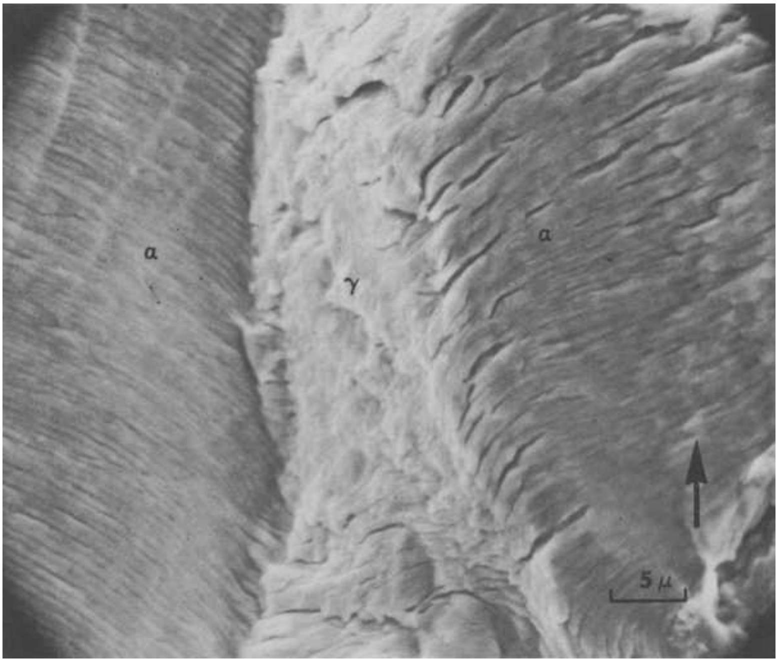

FIG. 14—*VK-A271 fracture surface,* R $= 0.05$, *crack front in austenite lags behind crack front in ferrite,* $\Delta K \simeq 36$ *ksi*$\sqrt{in.}$ *(40 MPa*$\sqrt{m}$*), ×2000. Arrow indicates crack growth direction.*

and toughness decrease continuously with increasing ferrite content, while the ultimate tensile strength increases only up to 25 percent ferrite, becoming constant thereafter. At this volume fraction of ferrite, the austenite phase is not completely continuous, so the ferrite phase limits slip activity in the austenite, retarding crack initiation. Crack propagation is still primarily controlled by the austenite phase, which slows down or arrests the crack locally. An alloy containing 25 percent ferrite thus appears to be very attractive for fatigue resistance, combining maximum tensile strength, crack initiation resistance, and crack propagation resistance.

In a study of fatigue by Hayden and Floreen [*17*], the volume fraction of ferrite was varied from 0 to 100 percent by adjusting the fraction of all major alloy elements along a tie line of the phase diagram, the termini of which are the compositions of the austenite phase and the ferrite phase of the duplex alloy IN 744. The resulting alloys contained austenite and ferrite phases having compositions independent of volume fraction, so the SFE of each phase does not vary between alloys. The mechanical behavior of these alloys therefore should be dependent only upon the volume fraction of each phase and the effect that one phase has upon the other. Figure

15 shows the dependence of the rotating-bending fatigue limit in air at 10^8 cycles as a function of ferrite fraction [*17*]. The alloy with the maximum fatigue strength was IN 744 and contained 57 percent ferrite. Whether these data are also valid for fatigue in a corrosive environment has yet to be determined.

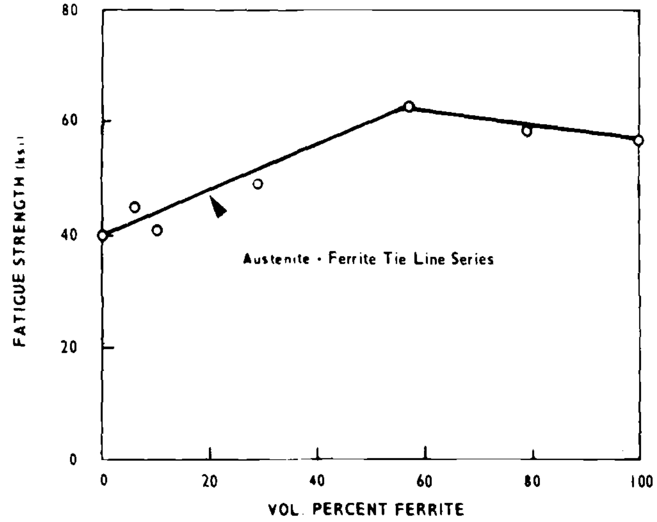

FIG. 15—*Dependence of fatigue limit on volume fraction ferrite, IN 744 tie-line series* [17].

Preliminary attempts to correlate these studies of the dependence of various properties on the volume fraction of austenite and ferrite with actual observations of corrosion-fatigue crack initiation have produced some interesting qualitative results. Smooth-bar fatigue specimens of alloy VK-A171 were annealed at 1250°C and then held at various temperatures and water quenched to produce variations in the austenite volume fraction. As the composition of the alloy is constant, the resulting composition of the austenite and ferrite phases are a function of volume fraction. Fatigue tests were performed in reverse bending as described previously for Alloy 63 [*19*], and observations in the electropolished specimen surfaces were made in the SEM. For alloys containing as little as 15 percent austenite, the slip activity in the austenite is very planar and quite intense, resulting in crack initiation along slip bands in the austenite, as shown in Fig. 16. In addition, deformation twins in the ferrite form cracks where they intersect the austenite-ferrite phase boundaries. As the fraction of austenite increases (and the composition of the phases changes), the slip activity in the austenite becomes less intense, deformation twins cease to form in the ferrite, and the intensity of wavy slip in the ferrite increases greatly, resulting in crack initiation along phase boundaries, as shown previously in Fig.

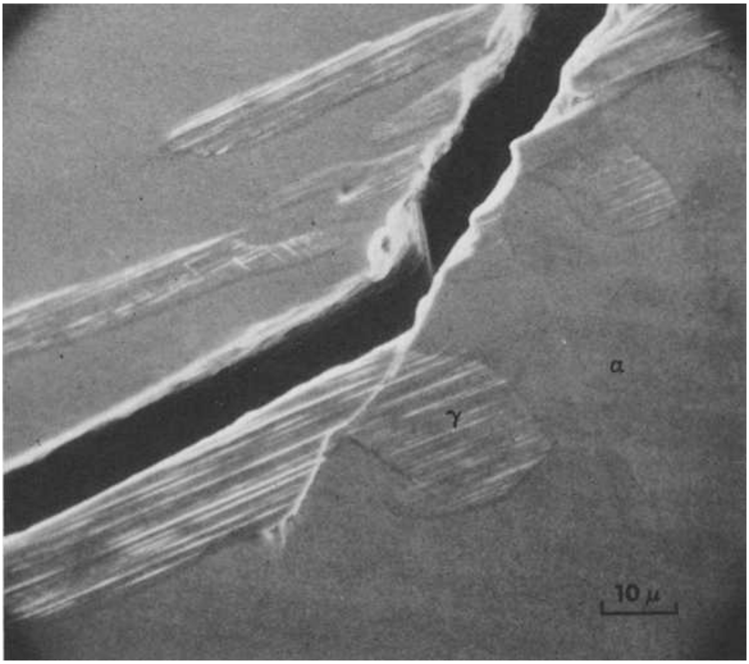

FIG. 16—*Crack initiation at PSB in austenite and at phase boundaries, VK-A171, heat treated to contain 80 percent ferrite, air,* σ_{alt} *= 55 ksi (379 MPa),* ×*900.*

9. These observations reinforce the idea that the actual composition of each phase in a duplex stainless steel is a critical factor in determining the corrosion fatigue behavior of the alloy in addition to the volume fraction of each phase, as was inferred from the SCC study of Shimodaira et al [*14*]. Our current work is aimed at trying to differentiate the effect of composition from the effect of volume fraction in corrosion-fatigue crack initiation and crack propagation of duplex stainless steels.

Effect of Microstructural Orientation

It is well known that grain boundaries and interphase boundaries can act as barriers to a propagating fatigue crack [*27*]. Since a crack growing in the transverse direction of a wrought plate will encounter more boundaries than a crack growing in the longitudinal direction, crack propagation rates are generally greater in the longitudinal direction than in the transverse direction for a wide variety of materials. Other contributing factors are the alignment of inclusions in the longitudinal direction and possible preferred crystallographic orientations arising from hot rolling. Liljas and Fridberg [*16*] have shown that crack propagation rates in air for wrought 3RE60 are twice as great in the longitudinal direction as in the transverse direction. The wrought microstructure of 3RE60 consists of austenite islands elongated in the rolling direction within the ferritic matrix, resulting in a directional distribution of both phases, similar to that previously shown for Uranus 50 (Fig. 5). Therefore, there is a much greater density of boundaries in the transverse direction, resulting in the observed increase in crack propagation resistance.

Tests to confirm this orientation dependence for fatigue in a corrosive environment were performed on 0.125-in. (3.175-mm) thick wrought Uranus 50 specimens, using the single-edge-notch (SEN) specimen geometry described by Barrata et al [*28*]. Specimens tested in solution were contained in an immersion cell through which the previously described white-water solution was constantly recirculated. The resulting crack propagation rate curves, Fig. 17, shows crack growth in the longitudinal direction to be about 1.5 times as rapid as in the transverse direction, independent of

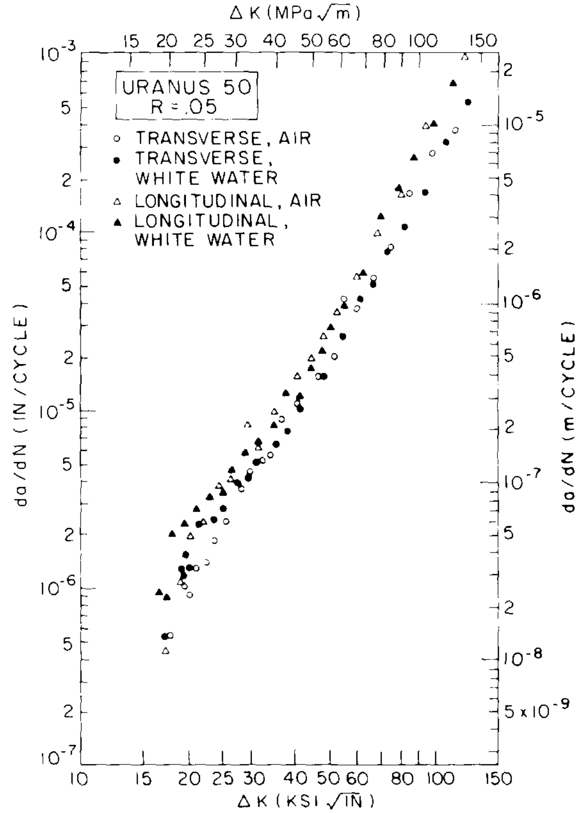

FIG. 17—*Fatigue crack growth rate curves, wrought Uranus 50,* R = *0.05, showing effect of microstructural orientation.*

environment. The SEM examination of the fracture surfaces of longitudinal specimens shows extensive microcracking, possible delamination along phase boundaries, and elongated inclusions, all oriented along the rolling direction. None of these features are observed on fracture surfaces of transverse specimens; the fatigue striations appear to be much more continuous and uniform. These observations account quite well for the measured differences in crack propagation rates. However, crack initiation and very low growth rate crack propagation may be much more dependent upon the nature of the individual phase in which they are occurring, so the orientation effects observed to exist for crack propagation are not necessarily valid for the entire corrosion-fatigue process.

Effect of Lower Temperature Precipitates

The precipitation of intermetallic compounds and carbides during slow cooling below 1000°C can affect the corrosion-fatigue properties of alloys by both mechanical and electrochemical means. Both σ-phase formation and α' precipitation (475°C embrittlement) produce strengthening effects accompanied by losses in ductility and impact resistance [*6*] and therefore can be expected to affect adversely crack propagation resistance while improving crack initiation resistance. The σ-phase precipitation along phase boundaries can also deplete the adjacent regions of chromium resulting in accelerated electrochemical activity in the boundary regions, damaging both initiation and propagation resistance. However, Liljas [*25*] has observed only slight reductions in the corrosion-fatigue resistance of 3RE60 resulting from slow cooling, and no accompanying change in crack propagation mode. The reduction in resistance is a purely mechanical effect, resulting from embrittlement of the ferrite matrix due to σ-phase precipitation. Precipitation of σ-phase at the austenite-ferrite boundaries produces neither adverse mechanical or electrochemical effects. Cooling following σ-phase precipitation was too rapid to produce 475°C embrittlement. The embrittlement effects of these intermetallic compounds are, however, very much a function of the volume fraction of ferrite present, as precipitation occurs primarily in the ferrite and therefore only the mechanical properties of the ferrite are affected [*6*]. Thus in a 50 percent austenitic alloy, the embrittlement effects due to σ or α' precipitation in the ferrite will be diminished somewhat by the presence of the austenite.

Precipitation of chromium carbides at grain boundaries in austenitic stainless steels due to slow cooling is known to cause intergranular attack which can accelerate both SCC and corrosion-fatigue failures [*7*]. This phenomenon is known as sensitization. Slow cooling will also cause chromium carbides to precipitate at austenite-ferrite boundaries in duplex stainless steels. However, Tedmon and Vermilyea [*29*] have observed that during further cooling following chromium carbide precipitation, the volume fraction of austenite continues to increase, causing the phase boundaries to migrate away from the carbide precipitates. This boundary movement results in a replenishing of chromium in the sensitized boundary regions, so that IG attack and IGSCC due to sensitization are not observed. Due to this effect, precipitation of chromium carbides should not be detrimental to the corrosion-fatigue resistance of austenitic-ferritic stainless steels. This same effect may also account for the observed absence of detrimental electrochemical effects due to σ-phase formation at phase boundaries in 3RE60 [*25*].

Summary

The corrosion-fatigue behavior of austenitic-ferritic stainless steels has been shown to be very much a function of alloy microstructure. Better control of the volume fraction of austenite and ferrite, microstructural orientation, and the formation of embrittling intermetallic precipitates will lead to more reliable corrosion-fatigue resistance in these alloys. At present, cast duplex alloys suffer from very nonuniform microstructures, resulting in large data scatter and poor reliability. The detrimental effects of large surface residual stress resulting from quenching of large cast components further limit corrosion fatigue resistance. In contrast, the fabrication of large components from wrought alloys offers increased microstructural control, including the opportunity to utilize beneficial orientation effects, along with the elimination of residual stresses due to quenching. The detrimental effect of intermetallic compounds and chromium carbides which precipitate during welding of wrought alloys are not as significant as believed previously for alloys containing a reasonable amount of austenite. Therefore, wrought alloys are becoming more attractive than cast alloys in most applications.

However, there still remains the need to characterize many of the effects discussed in this paper more fully. Further studies will center on the variation in the modes of corrosion-fatigue crack initiation and crack propagation produced by changing the volume fraction of austenite and ferrite along a tie-line series and on the electrochemical polarization effects that the austenite and ferrite phases have upon each other. The dependence of the deformation behavior of each phase upon the composition of the phase also must be explored further, as this has been shown to affect greatly crack initiation. Eventually, a complete understanding of the complex mechanical and electrochemical interactions which occur during corrosion fatigue of duplex stainless steels will emerge, and austenitic-ferritic stainless steels with superior corrosion fatigue resistance will become available.

Acknowledgments

The authors wish to acknowledge the support of Valmet Oy of Finland for the majority of this research, and to thank the Sandusky Foundry and Machine Company, Kubota Ltd. of Japan, and Creusot-Loire of France for furnishing material for testing. J. A. Moskovitz also wishes to thank the International Nickel Company for fellowship support.

References

[*1*] Flowers, J. W., Beck, F. H., and Fontana, M. G., *Corrosion*, Vol. 19, 1963, p. 1864.

[*2*] Vadas, R. M. and Thompson, R., *Pulp and Paper Magazine of Canada*, Vol. 72, 1971, p. T336.

[*3*] Schaeffler, A. L., *Metal Progress*, Vol. 56, 1949, p. 680.

[*4*] Pryce, L. and Andrews, K. W., *Journal of the Iron Steel Institute*, Vol. 195, 1960, p. 415.

[*5*] Guiraldenq, P., *Memoires Scientifiques de la Revue de Metallurgie*, Vol. 64, 1967, p. 907.

[*6*] Jolly, P., *Bulletin du Cercle d'Etudes des Metaux*, Vol. 12, 1973, p. 317.

[*7*] Gordon, G. M., *Proceedings of International Conference on SCC and Hydrogen Embrittlement of Iron Base Alloys*, Unieux, Firminy, France, 1973, in press; also published as No. 73NED105, G. E. Technical Information Series, General Electric Co., Pleasanton, Calif., 1973.

[*8*] Hayden, H. W. and Floreen, S., *Metallurgical Transactions*, Vol. 1, 1970, p. 1955.

[*9*] Jolly, P. and Hochmann, J., *Memoires Scientifiques de la Revue de Metallurgie*, Vol. 70, 1973, p. 117.

[*10*] Lecroisey, F. and Pineau, A., *Metallurgical Transactions*, Vol. 3, 1972, p. 387.

[*11*] Wakasa, K. and Nakamura, T., *Scripta Metallurgica*, Vol. 10, 1976, p. 129.

[*12*] Nair, F. and Semchyshen, M., *Corrosion*, Vol. 19, 1963, p. 2104.

[*13*] Clarke, W. L., Danko, J. C. and Gordon, G. M., No. 74NED57, G. E. Technical Information Series, General Electric Co., Pleasanton, Calif., 1974.

[*14*] Shimodaira, S., Takano, M., Takizawa, Y. and Kamide, H., *Proceedings of International Conference on SCC and Hydrogen Embrittlement of Iron Base Alloys*, Unieux, Firminy, France, 1973, in press.

[*15*] Kelley, C. E., Vestola, J., Sailas, V., and Pelloux, R. M., *TAPPI*, Vol. 58, 1975, p. 80.

[*16*] Liljas, M. and Fridberg, J., "Avesta 3RE60—A New Stainless Steel For Suction Rolls," presented at International Seminar on Pulp and Paper Industry Corrosion Problems, Chicago, 1974.

[*17*] Hayden, H. W. and Floreen, S., *Metallurgical Transactions*, Vol. 4, 1973, p. 561.

[*18*] Lemaignan, C., "Fatigue Crack Propagation in Microduplex Stainless Steel IN 744," S.M. thesis, Massachusetts Institute of Technology, Cambridge, Mass., 1973.

[*19*] Moskovitz, J. A., "Mechanisms of Corrosion Fatigue Crack Initiation in Cast Stainless Steels," S.M. thesis, Massachusetts Institute of Technology, Cambridge, Mass., 1975.

[*20*] Pyle, T., Rollins, V., and Howard, D., *Journal of the Electrochemical Society*, Vol. 122, 1975, p. 1445.

[*21*] Duquette, D. J. and Uhlig, H. H., *Corrosion*, Vol. 25, 1969, p. 839.

[*22*] Laird, C. and Duquette, D. J. in *Corrosion Fatigue: Chemistry, Mechanics and Microstructure*, National Association of Corrosion Engineers, Houston, 1972, pp. 88-113.

[*23*] Pelloux, R. M., Stoltz, R. E., and Moskovitz, J. A., *Materials Science and Engineering*, Vol. 25, 1976, p. 193.

[*24*] Moskovitz, J. and Pelloux, R. M., *Proceedings of the Second International Conference on Mechanical Behavior of Materials*, Boston, 1976, in press.

[*25*] Liljas, M., "Influence of Precipitates on Corrosion Fatigue Properties of a Duplex Stainless Steel," internal document, Avesta Jernverks AB, Avesta, Sweden, 1975.

[*26*] Pelloux, R. M. and Stoltz, R. E., *Proceedings of Fourth International Conference on the Strength of Metals and Alloys*, Nancy, France, 1976, in press.

[27] Jolly, P., "Mechanical Properties of Austeno-Ferritic Alloys in the Fully Annealed Condition and After Heat Treatments of Long Duration," internal document, Creusot-Loire Centre de Recherches d'Unieux, Unieux, Firminy, France, 1974.

[28] Baratta, F. I., Bluhm, J. I., Driscoll, G. W., and Matthews, W. T., *International Journal of Fracture Mechanics*, Vol. 7, 1971, p. 203.

[29] Tedmon, C. S., Jr. and Vermilyea, D. A., *Metallurgical Transactions*, Vol. 1, 1970, p. 2043.

R. Ebara,[1] *T. Kai,*[1] *and K. Inoue*[1]

Corrosion-Fatigue Behavior of 13Cr Stainless Steel in Sodium-Chloride Aqueous Solution and Steam Environment

---

REFERENCE: Ebara, R., Kai, T., and Inoue, K., "**Corrosion-Fatigue Behavior of 13Cr Stainless Steel in Sodium-Chloride Aqueous Solution and Steam Environment,**" *Corrosion-Fatigue Technology, ASTM STP 642,* H. L. Craig, Jr., T. W. Crooker, and D. W. Hoeppner, Eds., American Society for Testing and Materials, 1978, pp. 155-168.

ABSTRACT: To clarify the influence of sodium-chloride (NaCl) content and steam environment on fatigue strength of 13Cr stainless steel, rotating-bending fatigue tests were conducted. Fatigue strength at 10^7 cycles in 3 percent NaCl aqueous solution was 70 percent lower than that in air. The lower the NaCl content, the longer the fatigue life is in the same stress level. The degree of the influence of steam on fatigue life decreases with decreasing the stress, and no influence was found in the fatigue limit. Corrosion pits and subcracks were found in all tested environments except air.

Corrosion pits were also observed at crack initiation region on fracture surface. Striation was predominant at fatigue life lower than 6×10^5 cycles in 3 to 3×10^{-3} percent NaCl and 2×10^4 cycles in steam environment.

At longer fatigue life, intercrystalline fracture pattern was predominant.

KEY WORDS: stainless steels, corrosion fatigue, *S-N* diagrams, corrosion pits, subcracks, striations, intercrystalline fractures, crack initiation, crack propagation

It is comparatively rare to find information on corrosion fatigue behavior of 13Cr stainless steel. Furthermore, it is unknown how impurities' contents in corrosive environment influence the appearance of surface and fracture surface. The main purpose of this paper is to present observation results on corrosion pits, subcracks, and fracture surfaces of the fatigue-

---

[1] Doctor of engineering and researcher, Strength Research Laboratory; researcher, The First Experimental Laboratory; and doctor of engineering and head, Strength Research Laboratory; respectively, Hiroshima Technical Institute, Mitsubishi Heavy Industries, Ltd., Hiroshima, 733, Japan.

tested specimen in sodium chloride (NaCl) aqueous solution with a 3 to 3 × 10^{-4} percent NaCl content and steam environment.

Experimental Procedure

The material used in this investigation was martensitic stainless steel, austenitized at 970°C for ½ h, oil quenched, tempered at 720°C for ½ h, and water cooled. Chemical compositions and mechanical properties of the tested steel are shown in Table 1. The conventional rotating-bending fatigue testing machine (98 N·m) operating at 3600 rpm was employed using a specimen of the form shown in Fig. 1(*a*). The prepared environment consisted of distilled water and a 3 to 3 × 10^{-4} percent NaCl aqueous solution made by changing the NaCl content in the distilled water. The solutions were piped to the midsection of the specimen at a speed of 2 cm^3/min. The environmental temperature for the majority of tests was 15°C, and some of the tests were conducted at 80°C. A Wöhler type machine (55.8 N·m, 3600 rpm) built in the laboratory was used for generating the steam, and the (steam plus 3 percent NaCl) environmental test formed the specimen shown in Fig. 1(*b*). Steam from a generator built in the laboratory was sent to the acrylic resin made chamber mounted in the machine with a notched section. A "V" ring was employed to seal off the notched section from the atmosphere. All tests were conducted with nearly saturated steam with a temperature of 100°C and 1 atm. The (steam plus 3 percent NaCl) environment was prepared by sending steam to the chamber and simultaneously piping 3 percent NaCl to a notched section by use of a glass tube with a helical form. The analyzed NaCl content in an exhausted solution from a chamber was 1.7 percent. Before the test, all specimen surfaces were polished with #4 emery paper after machining carefully to a minimum diameter of 10 ± 0.01 mm and were degreased by acetone. Crack propagation path, surface corrosion pits, and fracture surface were observed by optical and JEOL 15 kV scanning electron microscopes (JSM-P 15).

Results and Discussion

An *S-N* curve obtained in various NaCl contents in aqueous solutions is shown in Fig. 2. Fatigue strength in 3 percent NaCl solution at 10^7 cycles is 70 percent lower than that in air. The lower the NaCl content, the longer the fatigue life is (Fig. 3). This inclination is similar to the results on nickel-chromium-molybdenum steel.[2] It is seen in Fig. 4 that even a 3 × 10^{-4} percent NaCl content has an influence on the fatigue strength of this steel. From these results it is anticipated that at long range fatigue life

---

[2] Rollins, V., Arnold, V., and Lardner, E., *Metallurgia,* Vol. 75, 1967, pp. 149-154.

TABLE 1—*Chemical compositions and mechanical properties of tested material.*

	Chemical Compositions, %							Mechanical Properties					
Material	C	Si	Mn	P	S	Cr	Mo	Yield Strength, 0.2% offset, MPa	Tensile Strength, MPa	Elongation in 50 mm, %	Reduction of Area, %	Charpy 2 mm U Notch, Impact Value, N·m/cm^2	HB
SUS410J1[a]	0.10	0.26	0.46	0.021	0.006	12.40	0.51	650.4	765.2	25.6	68.2	262.6	229

[a] The material was austenitized at 970°C for ½ h, oil quenched, tempered at 720°C for ½ h and water cooled.

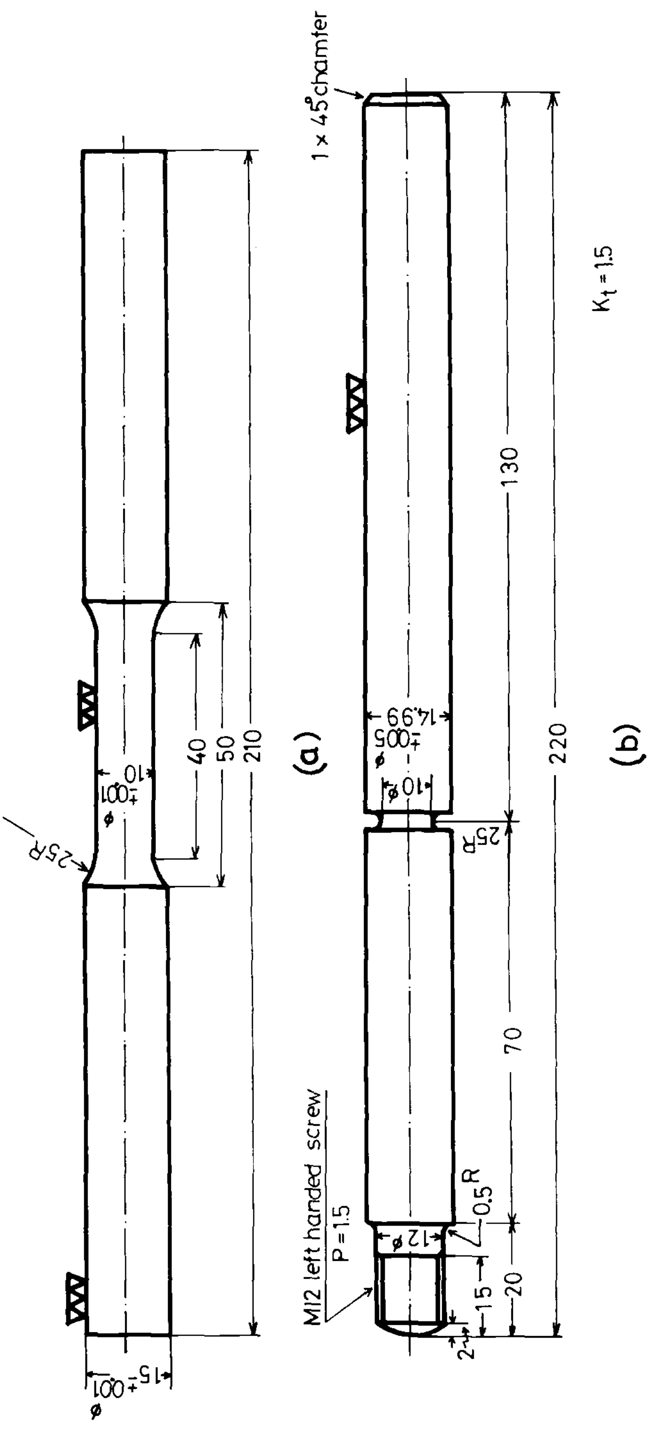

FIG. 1—*Fatigue specimen, unit, in millimetres.*

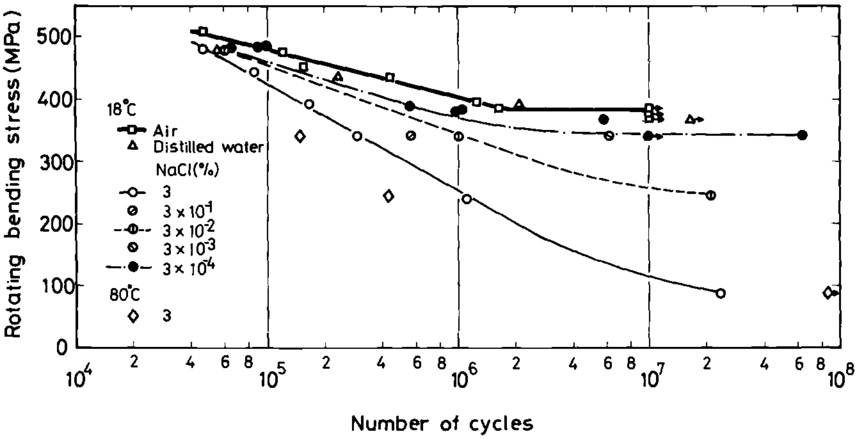

FIG. 2—S-N *curve in various environments.*

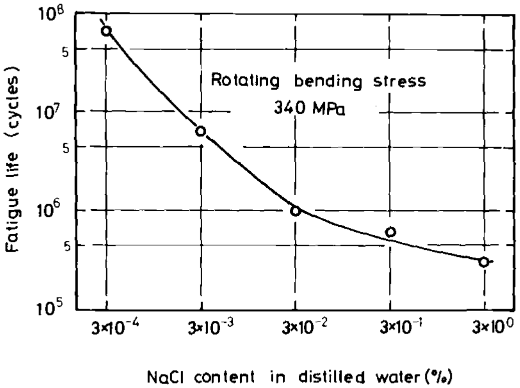

FIG. 3—*Influence of NaCl content in distilled water on fatigue life at rotating bending stress of 340 MPa.*

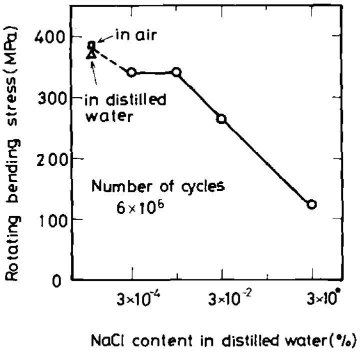

FIG. 4—*Influence of NaCl content on fatigue strength at number of cycles of 6* × *10^6.*

region ($N > 10^9$ cycles), fatigue strength decrease will be more prominent in an environment containing even a small Cl^- content. Fatigue strength decrease due to distilled water was not seen. However, the influence of steam on fatigue strength was recognized, and the fatigue life ratios decreased with decreasing the stress to unity at the endurance limit (Fig. 5).

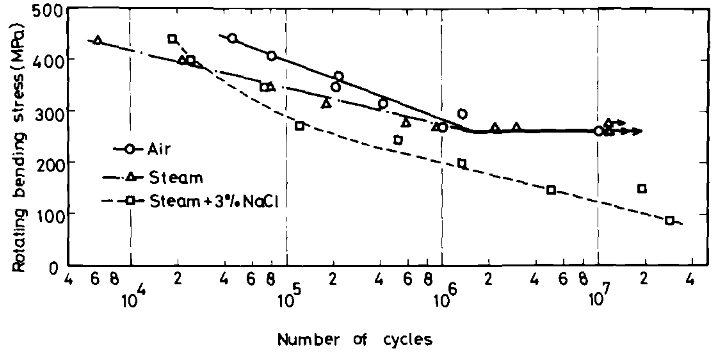

FIG. 5—S-N *diagram in steam and (steam plus 3 percent NaCl) environment.*

It is reported that the fatigue strength of 13Cr stainless steel in steam environment was 20 percent lower than that in air.[3] But in this experiment it is said that the effect of the nonmetallic inclusion was prominent. It is seen that the (steam plus 3 percent NaCl) environment acted as an agressive environment, and it prominently decreased fatigue strength at a low stress level. These differences of fatigue strength decrease at a lower stress level in steam and (steam plus 3 percent NaCl) may be noticeably related to the difference of corrosion fatigue mechanism in a mild and agressive environment.

Corrosion pits and subcracks found in 3 percent NaCl aqueous solution are shown in Fig. 6. Except for the fairly large pits indicated by *a* in Fig. 6(*a*), many corrosion pits the size of few micrometres were found on the specimen near the fracture surface shown in *a* (Fig. 6(*b*)). The mark *b* in the same figure shows the linkage of corrosion pits associated with subcracks. These corrosion pits and subcracks were found on the specimen surface in all tested environments except air. However, it was very rare to find such corrosion pits on specimen surfaces tested in distilled water. Typical examples of corrosion pits and subcracks found in 3×10^{-3} and 3×10^{-4} percent NaCl aqueous solution are shown in Fig. 7. These corrosion pits also appeared on fracture surfaces as shown in Fig. 7. Figure 8(*a*) shows subcracks found on a cross section axially cut. The heads of these cracks were round which characterized typical corrosion fatigue (Fig. 8(*b*)).

---

[3] Ouchida, H., *Kikai-gakkai Ronbun-shu,* Vol. 19, 1953, pp. 27–34.

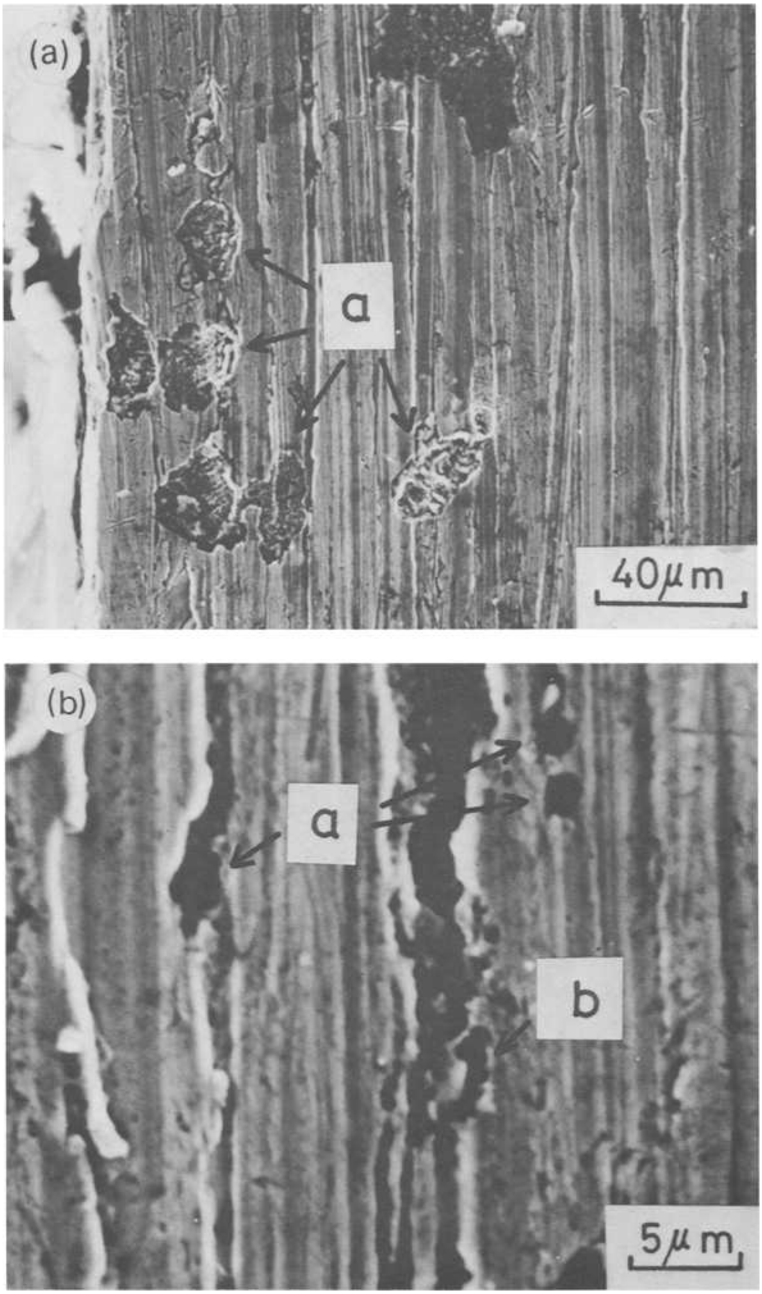

FIG. 6—*Corrosion pits and subcracks in 3 percent NaCl aqueous solution. Rotating bending stress = 90 MPa and number of cycles = 2.5 × 10^7.*

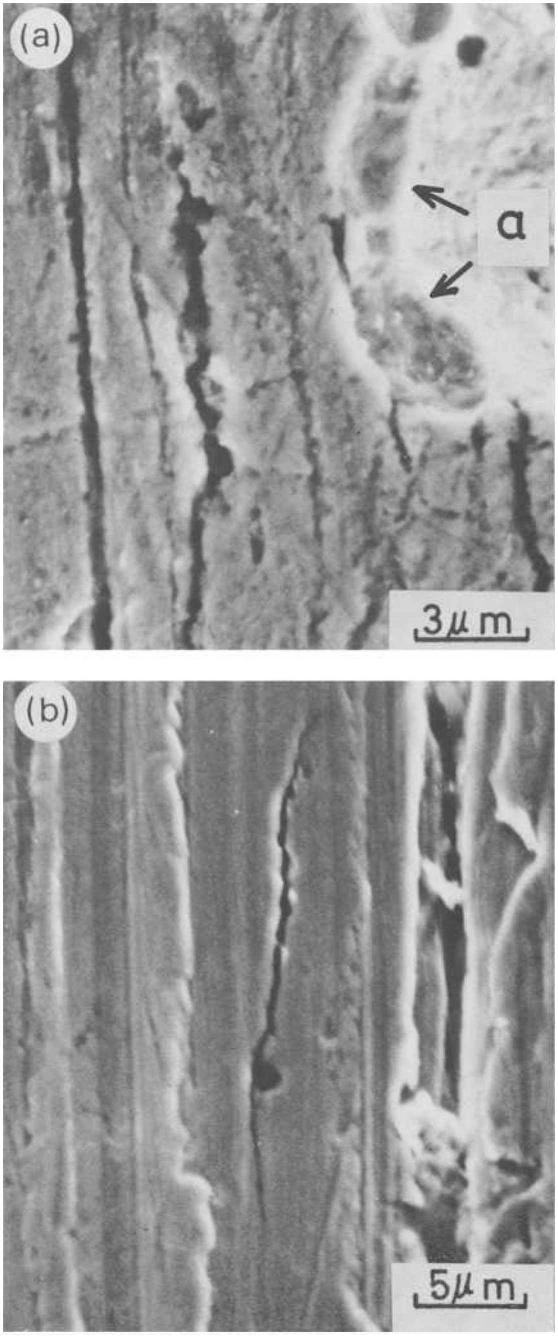

FIG. 7—*Corrosion pits and subcracks in NaCl aqueous solution:* (a) *3×10^{-3} percent NaCl, rotating bending stress = 342 MPa, and number of cycles = 6.4×10^{6};* (b) *3×10^{-4} percent NaCl, rotating bending stress = 342 MPa, and number of cycles = 6.3×10^{7}.*

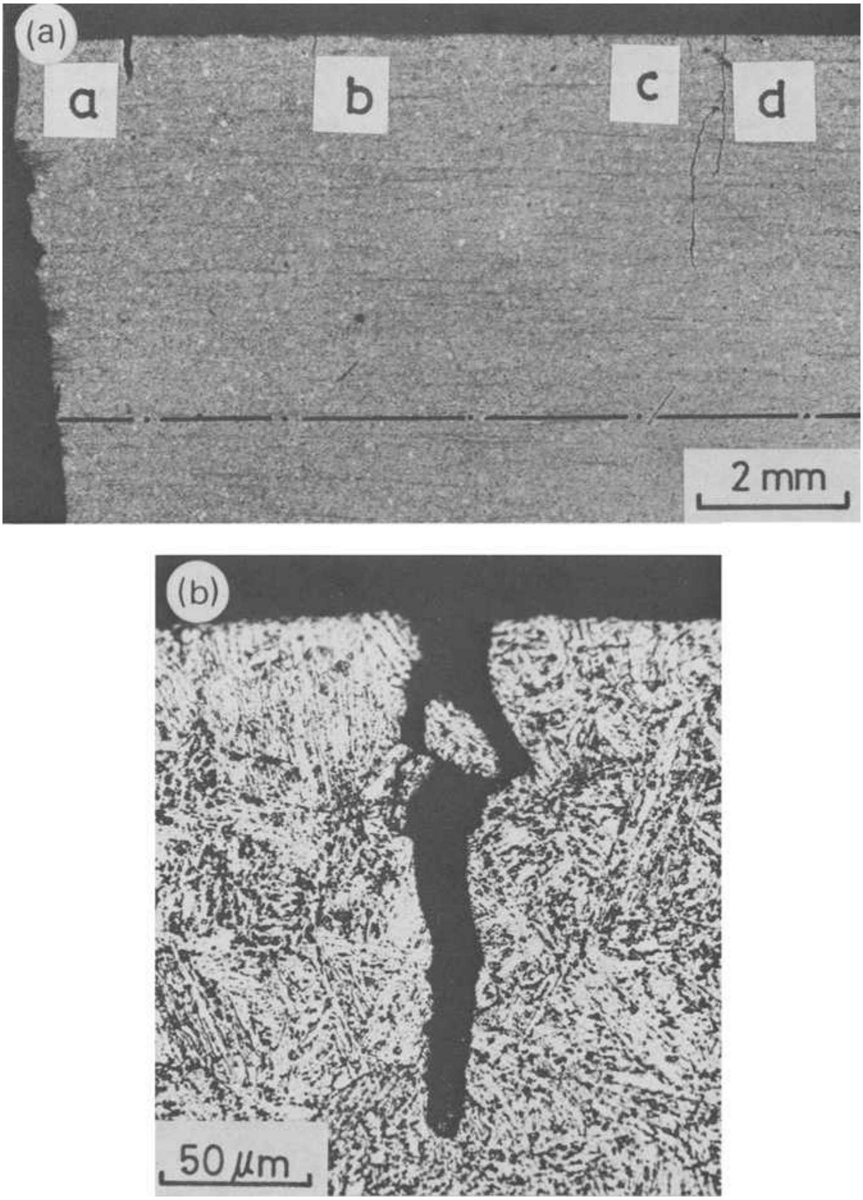

FIG. 8—*Subcracks on cross section (3 percent NaCl):* (a) *rotating bending stress = 391 MPa, and number of cycles = 1.6 × 10^5;* (b) *rotating bending stress = 480 MPa, and number of cycles = 4.5 × 10^4. a, b, c, and d show subcracks.*

It was also found that intergranular crack propagation was observed frequently on the fracture surface at lower stress levels. Striation was predominant on fracture surfaces in air, distilled water, and 3×10^{-4} percent NaCl aqueous solution. In other environments intergranular fracture predominantly appeared at longer fatigue life. Figures 9 and 10 are typical examples of fracture surfaces in 3 percent NaCl and steam, respectively. These fractographical results are summarized in Tables 2 and 3. The arrows in Fig. 11 shows corrosion pits found at the crack initiation point on the fracture surface in (steam plus 3 percent NaCl) environment. The same phenomenon was confirmed in another experiment[4] of this steel in 3×10^{-2} percent NaCl aqueous solution. One of the examples is shown in Fig. 12. From the aforementioned results it might be concluded that in the environment containing the NaCl fatigue crack of 13Cr stainless steel these cracks initiate at corrosion pits and propagate with intercrystalline fracture predominantly. It might be mentioned that the Cl^- concentration in the bottom of the corrosion pits promotes the crack propagation. The oxygen effect must be taken into consideration when pursuing the corrosion fatigue mechanism of the martensitic stainless steel. Clark[5] has reported that the oxygenated steam does not influence the fatigue crack initiation of Type 403 stainless steel. However, the influence of oxygen on long range fatigue life is still unknown. Further work is needed to make clear the influence of oxygen on fatigue strength of 13Cr stainless steel.

Conclusions

1. Although the influence of distilled water on fatigue strength of 13Cr stainless steel was not recognized, the influence of NaCl content in distilled water was prominent. The fatigue strength in 3 percent NaCl aqueous solution was 70 percent lower than that in air. The lower the NaCl content, the longer the fatigue life is. Fatigue strength decrease due to the 3×10^{-4} percent NaCl was 15 percent at 10^7 cycles.

2. Influence of steam on fatigue strength of 13Cr stainless steel was recognized, and the fatigue life ratios decreased by decreasing the stress to unity at the endurance limit. Prominent decrease of fatigue strength was recognized at a low stress level in the (steam plus 3 percent NaCl) environment.

3. Corrosion pits and subcracks were found in all tested environments except air. Furthermore, they were prominently observed in the environment containing NaCl. Corrosion pits were observed frequently at the crack initiation region on the fracture surface.

---

[4] Ebara, R., unpublished work.

[5] Clark, W. G., Jr. in *Fracture Toughness and Slow-Stable Cracking, ASTM STP 559,* 1974, pp. 205-224.

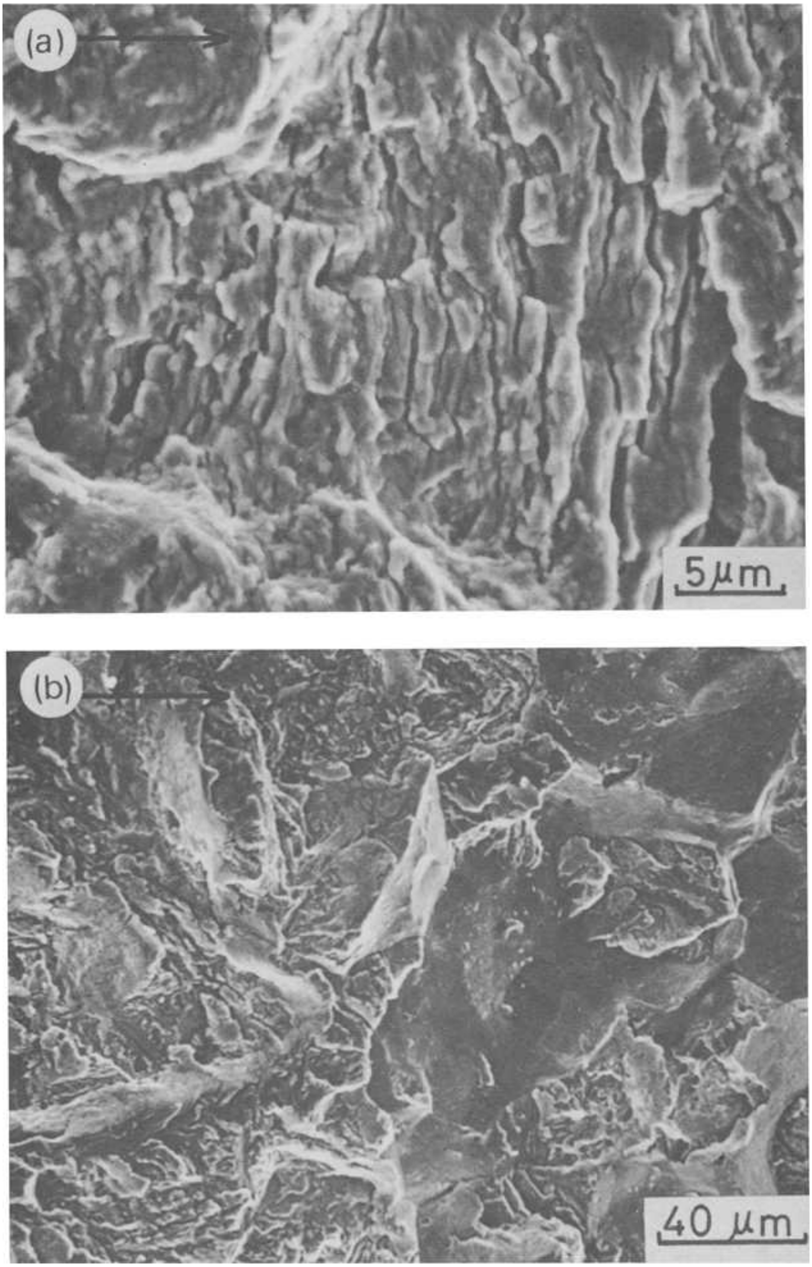

FIG. 9—*Fracture surface in 3 percent NaCl aqueous solution:* (a) *3.8 mm from the initiation point, rotating bending stress = 391 MPa, and number of cycles = 1.6 × 10^5;* (b) *1.8 mm from the initiation point, rotating bending stress = 242 MPa, and number of cycles = 1.1 × 10^6. Arrow shows crack propagation direction.*

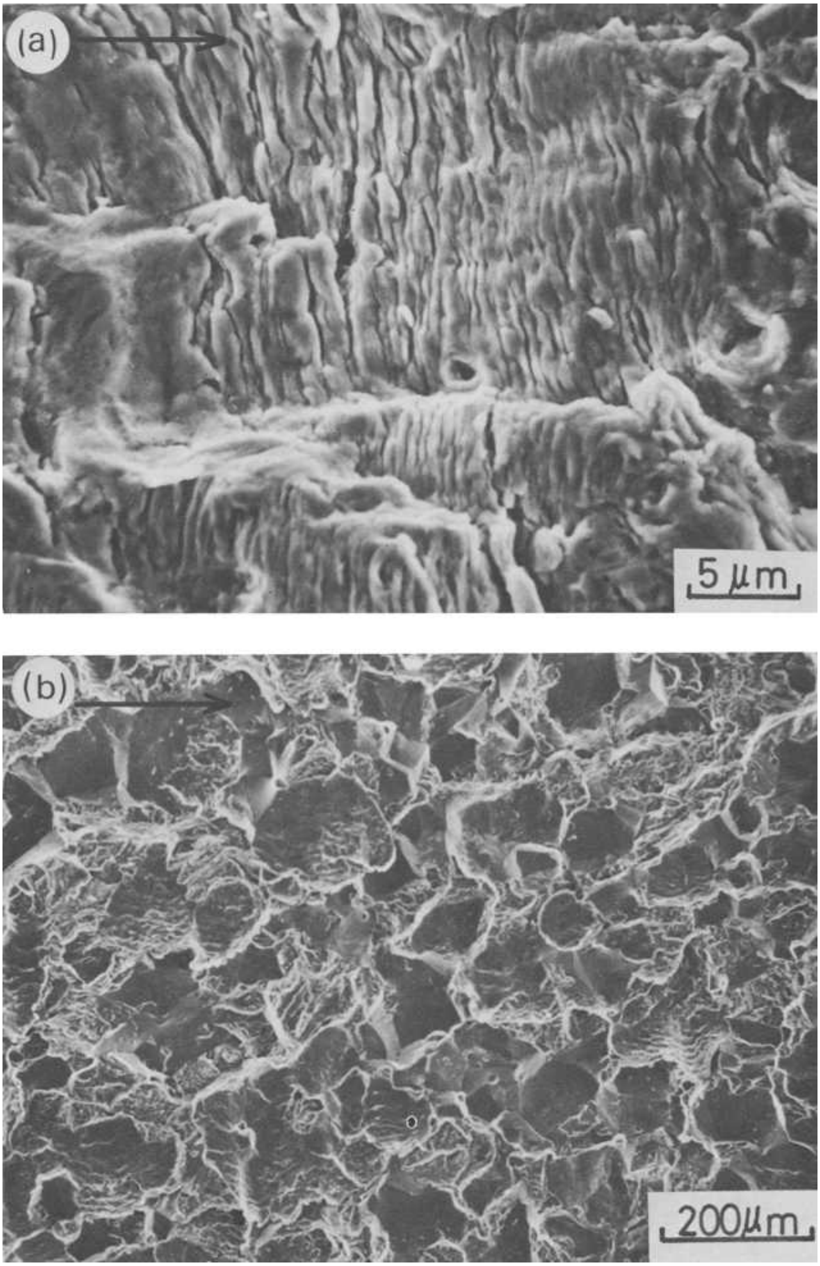

FIG. 10—*Fracture surface in steam environment:* (a) *14 mm from initiation point, rotating bending stress = 440 MPa, and number of cycles = 6.2 × 10^3;* (b) *2.5 mm from initiation, rotating bending stress = 271 MPa, and number of cycles = 3 × 10^6.*

TABLE 2—*The results of fractography in various environments.*

Environment	$N<6\times10^5$	$6\times10^5\leq N<10^8$
Air	striation	striation
Distilled water	striation	striation
3×10^{-4}% NaCl	striation	striation
$3\sim3\times10^{-3}$% NaCl	striation	intergranular

TABLE 3—*The fractographical results in steam and (steam plus 3 percent NaCl).*

Environment	$N<2\times10^4$	$2\times10^4\leq N<10^8$
Air	striation	striation
Steam	striation	intergranular
Steam plus 3% NaCl	striation	intergranular

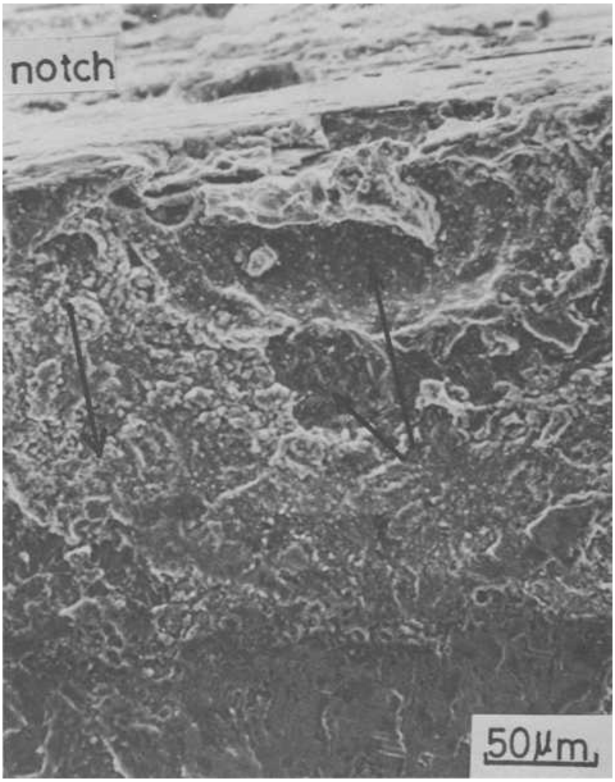

FIG. 11—*Fracture surface in (steam plus 3 percent NaCl) environment: rotating bending stress = 88 MPa, and number of cycles = 2.8 × 10^7. Arrow on the left-hand side shows crack propagation direction.*

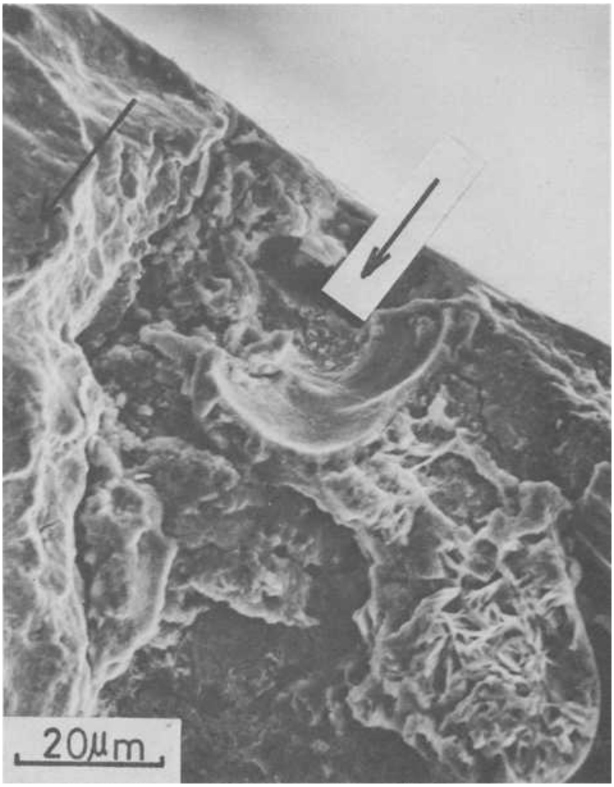

FIG. 12—*Corrosion pit at initiation point in* 3×10^{-2} *percent NaCl aqueous solution: rotating bending stress = 183 MPa, and number of cycles =* 5.1×10^{7}. *Arrow on the left-hand side shows crack propagation direction.*

4. Striation was predominant at fatigue life lower than 6×10^5 cycles in 3 to 3×10^{-3} percent NaCl and 2×10^4 cycles in steam and (steam plus 3 percent NaCl) environment. During longer fatigue life, an intercrystalline fracture pattern was predominant. In the other environments, striation was predominant.

Acknowledgments

The authors wish to acknowledge the work of T. Yamada who performed the fatigue tests.

Joseph Zola[1]

Influence of Advanced Ingot Thermal-Mechanical Treatments on the Microstructure and Stress Corrosion Properties of Aluminum Alloy Forgings

---

REFERENCE: Zola, J., "**Influence of Advanced Ingot Thermal-Mechanical Treatments on the Microstructure and Stress Corrosion Properties of Aluminum Alloy Forgings,**" *Corrosion-Fatigue Technology, ASTM STP 642,* H. L. Craig, Jr., T. W. Crooker, and D. W. Hoeppner, Eds., American Society for Testing and Materials, 1978, pp. 169-188.

ABSTRACT: A new approach, the application of microstructure control to products possessing an optimized alloy chemistry, has been taken to develop an improved combination of properties in 7000 series wrought aluminum products. The technique developed is an ingot (intermediate) thermal-mechanical treatment (ITMT) process which optimizes the combination of static strength, fracture toughness, fatigue strength, and stress corrosion resistance of commercial aluminum alloy die forgings. Previously, high fracture toughness had been achieved in wrought products by sacrificing tensile strength or stress corrosion properties. The ITMT processes produce either a recrystallized grain structure by thermal treatments prior to working at lower-than-conventional (warm) working temperatures or an altered grain structure by hot working the previously recrystallized structure. In both cases, the resulting grain morphology is desirable for good fracture toughness. Results of testing forging material show that ITMT on a high purity 7475 alloy produces advantageous fatigue crack propagation rates in 3.5 percent salt solution in comparison to 7075-T73, and stress corrosion resistance equivalent to 7075-T73 in addition to attractive tensile properties and high fracture toughness.

KEY WORDS: corrosion fatigue, thermal-mechanical heat treatment, crack propagation, stress corrosion resistance, forging, microstructure

In recent years an intensive effort has been made to develop an optimum combination of static strength, toughness, and stress corrosion resistance in 2000 and 7000 series wrought aluminum products by concentrating on

---

[1] Senior stress engineer, Boeing Vertol Company, Philadelphia, Pa. 19142.

alloy chemistry and alloy processing. At this point in time it was clear that the key to unlocking future improvements in this combination of properties is the application of microstructure control to products possessing an optimized alloy chemistry.

On the basis of this conviction, a program was conceived and conducted to develop industrial techniques for producing improved aluminum alloy forgings in sizes applicable to helicopter hardware which will possess combinations of static strength, fracture toughness, fatigue performance, and resistance to stress corrosion cracking superior to that of commercial 7075-T73 forgings.

These techniques involve thermal or mechanical treatment, or both, in the ingot processing stages of forging.

Ingot Processing

It has been known for some time that a fine, recrystallized grain structure in sheet is a desirable microstructure for high toughness. In sheet form, these structures usually are obtained by cold rolling prior to and recrystallizing during solution heat treatment. Producing plate and forgings in a similar manner by cold-working prior to solution heat treatment has not been possible with today's alloys and fabrication procedures, largely because limited ductility prohibits introduction of sufficient cold work. Hence, commercially available, thick-section wrought products often have an unrecrystallized, highly elongated lamellar grain structure which, although desirable for some properties in some directions, is considered detrimental to fracture toughness in the short-transverse direction.

Recently, Conserva et al and Waldman et al[2,3] developed novel processes specifically designed to produce a fine-grained, recrystallized structure in 7XXX alloy plate. These processes, referred to as intermediate thermal-mechanical treatments, (ITMT) include establishing a preliminary structure amenable to recrystallization by applying appropriate thermal treatments prior to working at lower-than-conventional working temperatures (in the case of 7X75 plate, the warm-working temperature was 500°F). The warm working introduces relatively high degrees of strain hardening which promote recrystallization to a relatively fine-grained equiaxial grain structure during a subsequent high-temperature thermal treatment. The ITMT methods produce products that have either a recrystallized grain structure or an altered grain structure produced by hot working the previously recrystallized structure; the latter procedure elongates the recry-

[2] Conserva, M., DiRusso, E., and Gatto, F., *Alumino e Nuovo Metallurgia*, Vol. 9, 1968, pp. 441-445.

[3] Waldman, J., Sulinski, H., and Markus, H., "New Processing Techniques for Aluminum Alloys," presented at the Army Materials Technology Conference on Solidification Technology, Wentworth by the Sea, New Hampshire, Oct. 1972.

stallized grains. The resulting grain morphology is desirable for good fracture toughness, and the general fabrication method involved in achieving this structure is commercially feasible for forgings.

Forging Microstructure

There were 29 different ITMT processes used to fabricate small hand forgings, and the two most promising processes were selected for scale up to larger forgings. Three forgings with section thicknesses of 6.7 (17), 2.0 (5.08), and 1.0 in. (2.54 cm), respectively, were fabricated for each of the ITMT practices. Microstructures and forging practices for ITMT 1 are shown in Figs. 1 through 3. Microstructures and forging practices for ITMT 2 are shown in Figs. 4 through 6. Grain dimensions are given in Table 1.

Specimens were fabricated from the forgings to measure fatigue crack propagation rates and stress corrosion resistance. Results were compared with test results for conventional 7075-T73 specimens fabricated from forgings which are identical to the ITMT forgings in size.

Fatigue Crack Propagation Rate Tests in 3.5 percent Salt Solution

The objective of these tests is to obtain fatigue crack propagation rate data over a range of stress conditions representative of those expected in the service life of helicopter hardware.

Specimen Configuration and Preparation

Eight fatigue crack propagation rate compact specimens were fabricated from blanks cut from selected locations in the forgings. These locations are centered with respect to the thickness of each blank (*t*/2 location).

In order to measure crack growth, a grid consisting of approximately 40 lines with a nominal spacing of 0.040 in. (0.1 cm) was photographically applied to one side of each specimen.

Test Procedure and Test Setup

All testing was conducted at a load frequency of 5 Hz at stress ratio $R = +0.05$ and with the specimen immersed in 3.5 percent salt solution.

Loads were applied to the specimen and monitored by a load cell in series with the specimen. Load control was provided to permit no greater than ±1.5 percent variation of the cyclic range of load for the duration of each test. In cases where precracking loads higher than the test crack propagation loads were required, care was taken to step down to the test

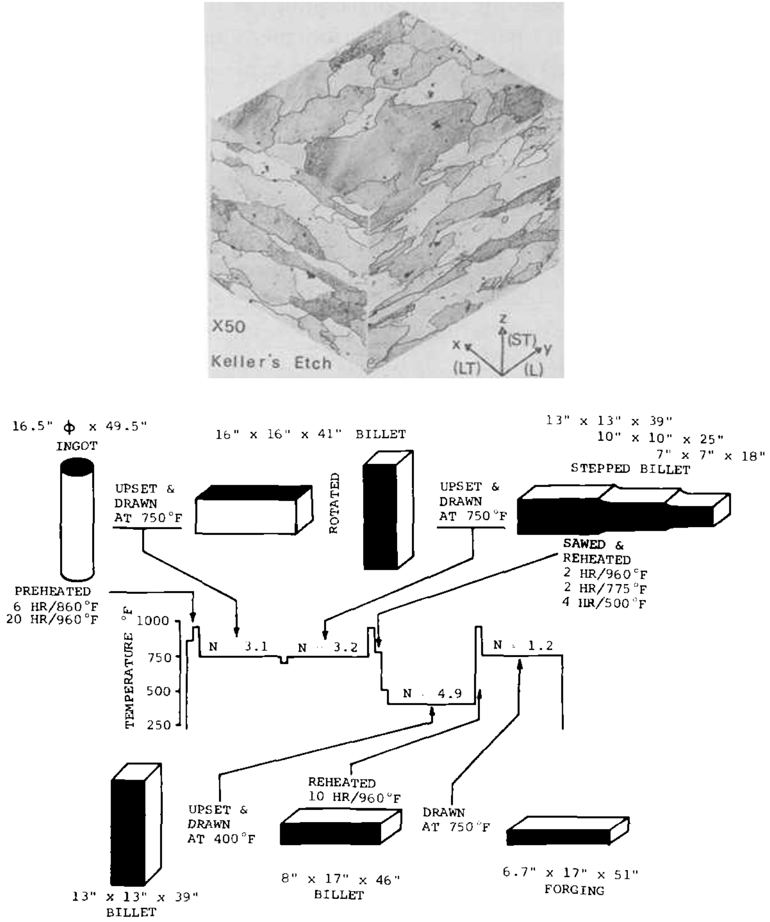

FIG. 1—*Microstructure properties and forging practice for 6.7-in.-thick 7475-ITMT1 forging.*

loads in small increments and to let the crack grow to a length such that the prior load would not influence the crack-growth data.

Crack growth was monitored visually by observing the intersection of the crack front with the grid lines previously described. Dye penetrant and optical magnification of various power (×15 and ×45) were used as aids in following the crack. The salt solution was contained in a transparent container surrounding the crack and the crack was viewed through the container. Periodic checks were made to ensure that cracking was progressing uniformly on both sides of the specimen.

Basic crack growth data, consisting of crack length and number of fatigue cycles, were reduced by computer to determine the fracture-mechanics

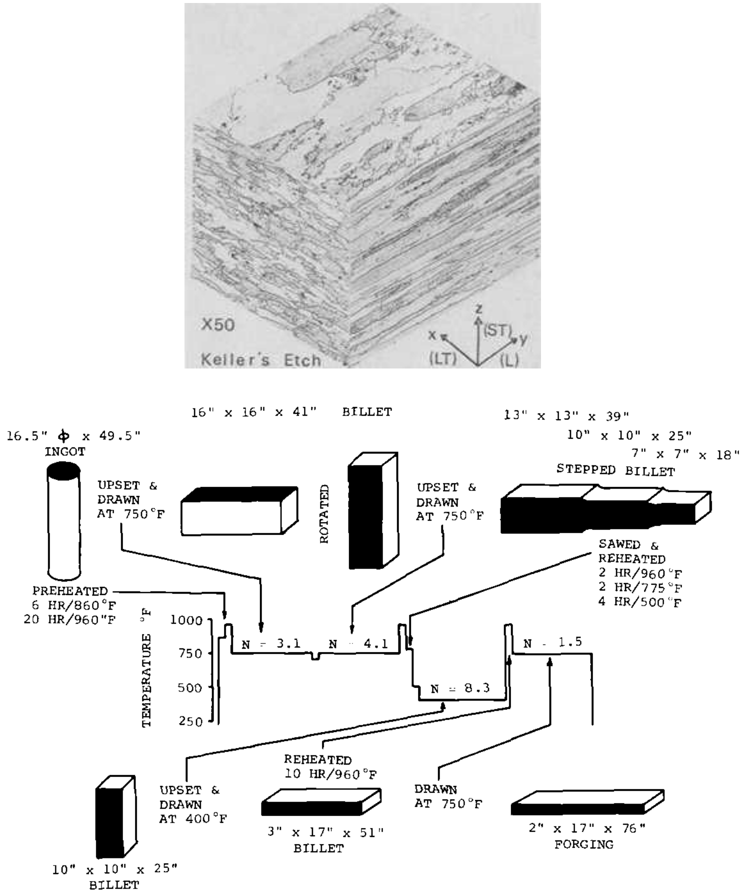

FIG. 2—*Microstructure properties and forging practice for 2-in.-thick 7475-ITMT1 forging.*

parameters of stress intensity range factor, ΔK, and crack growth rate, $\Delta a/\Delta N$.

The stress-intensity range was calculated using the following expression from ASTM Test for Plane-Strain Fracture Toughness of Metallic Materials (E 399)

$$\Delta K = \frac{\Delta P}{BW^{1/2}}\left[29.6\left(\frac{a}{W}\right)^{1/2} - 185.5\left(\frac{a}{W}\right)^{3/2} + 655.7\left(\frac{a}{W}\right)^{5/2}\right.$$

$$- 1017.0\left(\frac{a}{W}\right)^{7/2} + 638.9\left(\frac{a}{W}\right)^{9/2}\Bigg]$$

where

ΔP = load range, $P_{\max} - P_{\min}$,
a = average crack length,
B = average thickness of specimen, and
W = average width of specimen per ASTM Test E 399.

Test Results

The results of the fatigue crack propagation rate tests are presented in Figs. 7 through 11 as plots of stress intensity factor range, ΔK, versus fatigue crack propagation rate, $\Delta a/\Delta N$.

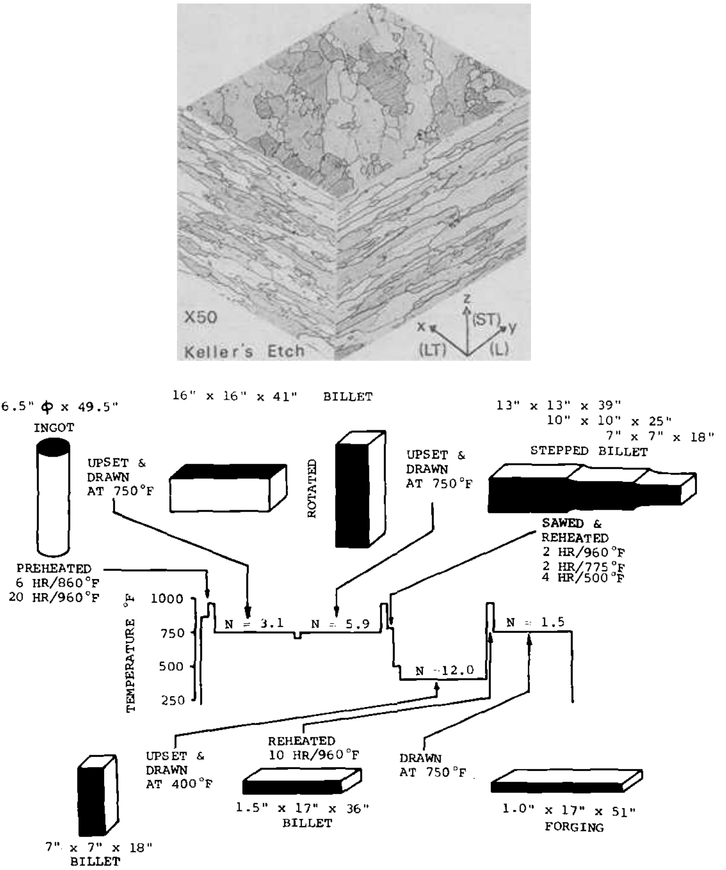

FIG. 3—*Microstructure properties and forging practice for 1-in.-thick 7475-ITMT1 forging.*

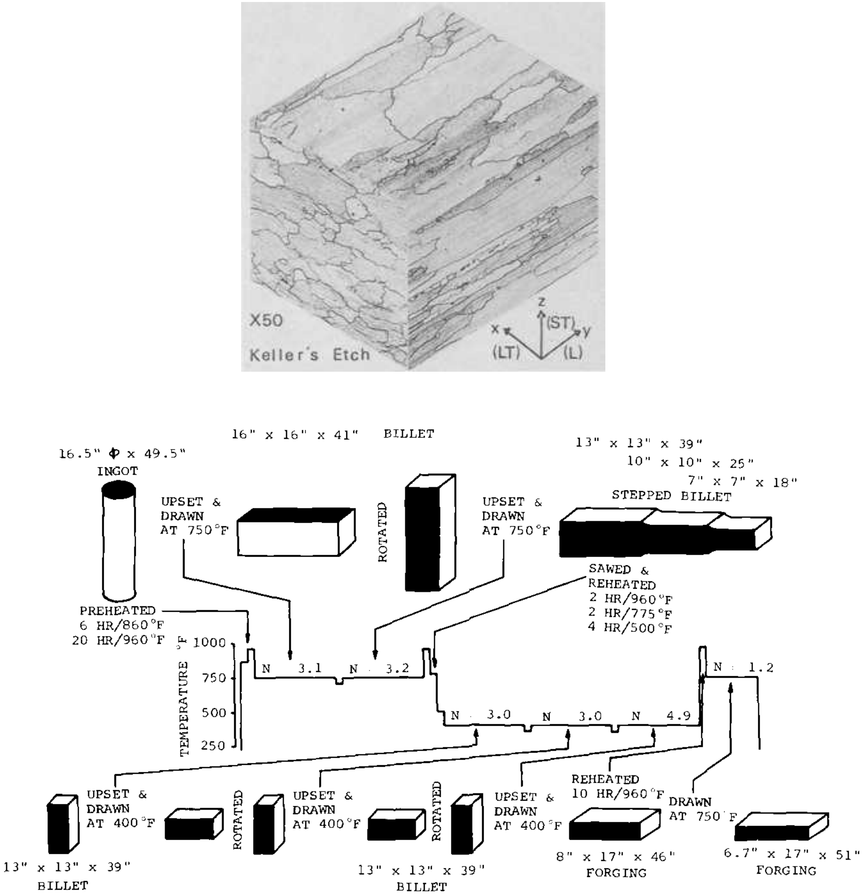

FIG. 4—*Microstructure properties and forging practice for 6.7-in.-thick 7475-ITMT2 forging.*

For each of the materials, a 3.5 percent salt solution was found to increase the crack growth rates above those obtained in an air environment. The crack growth rate of 7475-ITMT 1 in salt solution is approximately three times the rate in air. This is also true for 7475-ITMT 2 and for conventional 7075-T73.

As shown in Figs. 7 and 8, in a 3.5 percent salt solution, 7475-ITMT1 and 7475-ITMT2 demonstrate the same crack propagation rates. In comparison to 7075-T73, the crack propagation rates of ITMT alloys are faster, but this is offset by the fact that ITMT alloys have the capability to maintain stable crack growth rates at high values of stress intensity factor range, ΔK. This cannot be achieved in a conventional 7075-T73 alloy.

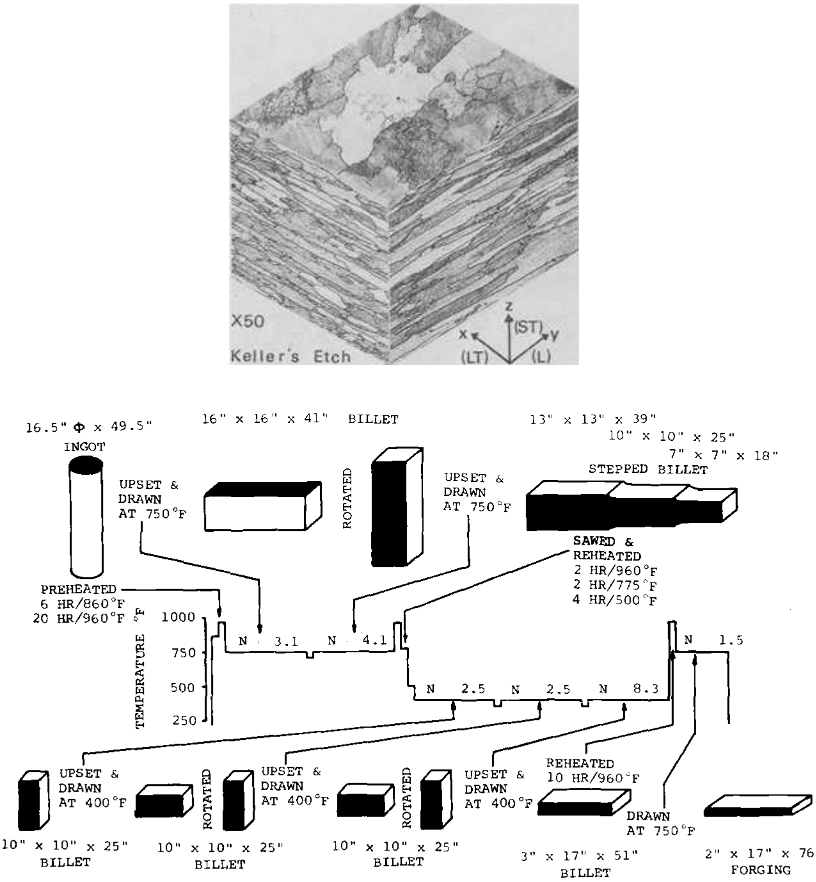

FIG. 5—*Microstructure properties and forging practice for 2-in.-thick 7475-ITMT2 forging.*

Longitudinal and short-transverse specimens were tested from the 6.7 in. (17 cm) thick forgings. In 3.5 percent salt solution, no significant differences were found in the crack growth rates of ITMT material loaded parallel to the grain (longitudinal) and ITMT material loaded transverse to the grain (short transverse), Fig. 3.

This applies to both ITMT1 and ITMT2, and is a distinct advantage over the conventional 7075-T73 material which demonstrates short-transverse crack growth rates 33 percent faster than longitudinal crack growth rates (Figs. 7 and 8).

A thickness effect is apparent in the longitudinal direction in ITMT alloys; the crack propagation rates of ITMT alloys are 33 percent faster than 7075-T73 in 1-in. (2.54-cm) forging and 100 percent faster in 2-in. (5.08-cm) forgings. See Figs. 10 and 11.

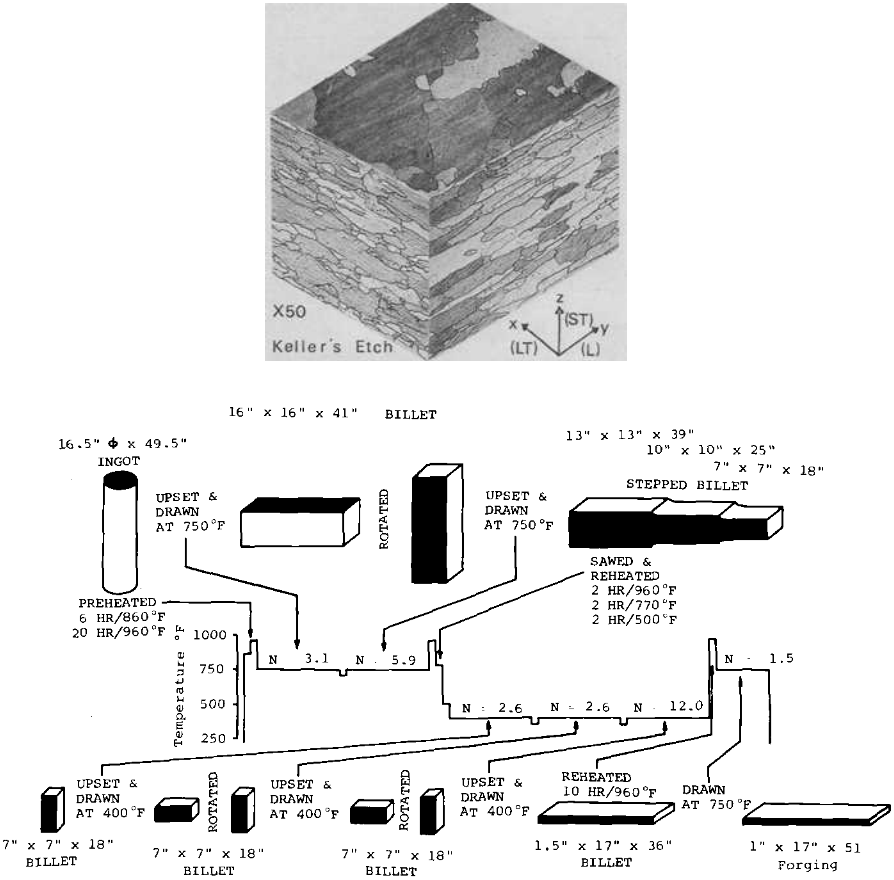

FIG. 6—*Microstructure properties and forging practice for 1-in.-thick 7475-ITMT2 forging.*

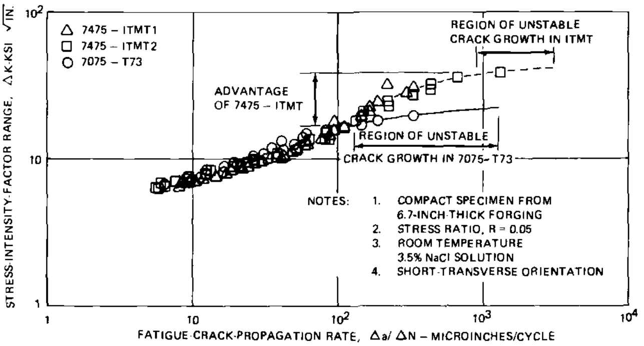

FIG. 7—*Comparison of short-transverse fatigue crack growth rates for 6.7-in.-thick forgings.*

TABLE 1—*Fabricating details for 7475 hand*

Finished Hand Forging				Initial Forging of 16.5 θ × 49-in. ingot at 750°F[a,e]	
	Grain Dimensions				
Specimen	Thickness, mm	Width, mm	Length, mm	Type of Forging Operation	Reduction, N^d
					6.7-in.-thick
438170	0.042	0.083	0.125	upset and draw	3.1
				upset and draw	3.2
438173	0.036	0.083	0.200	upset and draw	3.1
				upset and draw	3.2
					2.0-in.-thick
438169	0.010	0.029	0.067	upset and draw	3.1
				upset and draw	4.1
438172	0.015	0.071	0.250	upset and draw	3.1
				upset and draw	4.1
					1.0-in.-thick
438168	0.013	0.062	0.091	upset and draw	3.1
				upset and draw	5.9
438171	0.020	0.091	0.143	upset and draw	3.1
				upset and draw	5.9

NOTE—Reprinted from Zola, J. C., "Improvement of Helicopter Forgings by Controlled Solidification and Thermal-Mechanical Treatments," AVSCOM Report No. 76-41, Boeing Vertol Company, Phila., Pa., March 1977.

[a] Ingot preheated 6 h at 860°F, plus 20 h at 960°F, prior to forging at 750°F.

[b] Billet reheated 2 h at 960°F, furnace cooled to 775°F, soaked 2 h at 775°F, furnace cooled to 500°F, and soaked 4 h at 500°F prior to warm forging at 400°F.

[c] Forging reheated 10 h at 960°F after warm forging at 400°F and prior to forging at 750°F.

[d] Reduction, N = original thickness in direction of greatest reduction/final thickness in direction of greatest reduction.

[e] Composition of ingot: 1.55Cu, 2.37Mg, 5.73Zn, 0.06Fe, 0.04Si, 0.04Cr, 0.02Ti, 0.002Be.

The results of the short-transverse grain direction are particularly significant and demonstrate that ITMT alloys are superior in performance to 7075-T73 in thick forgings. Crack propagation rates in 7075-T73 show a directionality effect, and in the short-transverse direction the 7075-T73 cannot sustain stable crack growth rates at the higher stress intensity levels attainable by the ITMT alloys. This, plus the fact that the longitudinal crack growth rates of ITMT are equal to (and not faster than) the transverse rates means that the short-transverse growth rates govern the alloy selec-

forgings produced by ITMT-type procedures.

Warm Forging of Billet at 400°F^b			Forging of Recrystallized Billet 750°F^c			
Initial Size, in.	Type of Forging Operation	Reduction, N^d	Initial Size, in.	Type of Forging Operation	Reduction, N^d	Finished Size of Forging, in.
Hand Forgings						
13 by 13 by 39	upset and draw	4.9	8 by 17 by 46	draw	1.2	6.7 by 17 by 51
13 by 13 by 39	upset and draw	3.0				
	upset and draw	3.0				
	upset and draw	4.9	8 by 17 by 46	draw	1.2	6.7 by 17 by 51
Hand Forgings						
10 by 10 by 25	upset and draw	8.3	3 by 17 by 51	draw	1.5	2.0 by 17 by 76
10 by 10 by 25	upset and draw	2.5				
	upset and draw	2.5				
	upset and draw	8.3	3 by 17 by 51	draw	1.5	2.0 by 17 by 76
Hand Forgings						
7 by 7 by 18	upset and draw	12.0	1.5 by 17 by 36	draw	1.5	1.0 by 17 by 51
7 by 7 by 18	upset and draw	2.6				
	upset and draw	2.6				
	upset and draw	12.0	1.5 by 17 by 36	draw	1.5	1.0 by 17 by 51

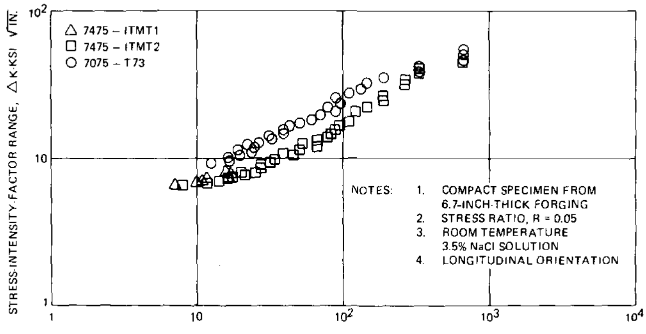

NOTES:
1. COMPACT SPECIMEN FROM 6.7-INCH-THICK FORGING
2. STRESS RATIO, R = 0.05
3. ROOM TEMPERATURE 3.5% NaCl SOLUTION
4. LONGITUDINAL ORIENTATION

FIG. 8—*Comparison of longitudinal fatigue crack growth rates for 6.7-in.-thick forgings.*

tion in a practical application. On this basis, one would select the ITMT alloy.

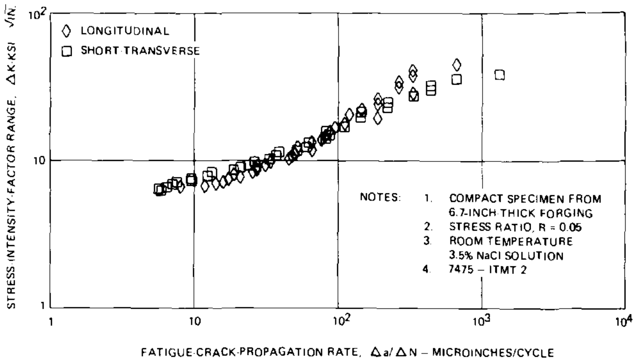

FIG. 9—*Comparison of fatigue crack growth rates for the longitudinal and short-transverse grain directions in 6.7-in.-thick 7475-ITMT2 forgings.*

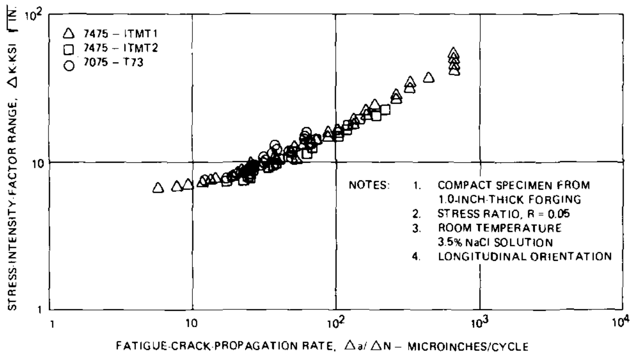

FIG. 10—*Comparison of fatigue crack growth rates in 1-in.-thick forgings.*

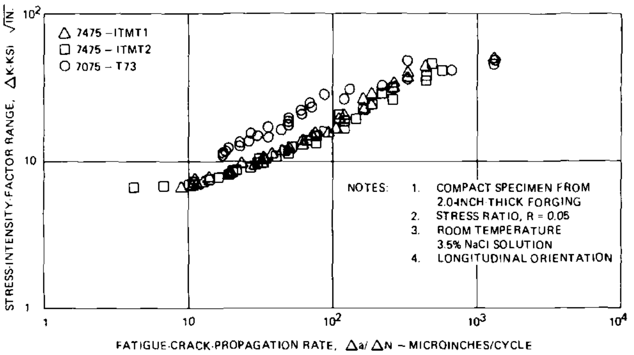

FIG. 11—*Comparison of fatigue crack growth rates in 2-in.-thick forgings.*

Stress Corrosion Tests

Samples of 6.7 (17), 2.0 (5.08), and 1.00 in. (2.54 cm) thick 7075 and 7475 hand forgings solution heat treated, quenched, and artificially aged 24 h at 250°F were aged additionally 2 to 9 h at 350°F. Longitudinal 0.125 in. (0.32 cm) diameter threaded-end tension specimens were machined from the *t*/2 location of all of the samples of forgings. Short transverse 0.125 in. (0.32 cm) diameter threaded-end tension specimens were machined from the samples of 6.7 (17) and 2.0 in. (5.08 cm) thick forgings, and short transverse 0.75 in. (1.91 cm) diameter C-rings were machined from the samples of 1.0 in. (2.54 cm) thick forgings. The specimens were stressed at 25 (172), 35 (241), or 45 ksi (310 MPa) and exposed to a 3.5 percent sodium chloride (NaCl) solution by alternate immersion, according to Federal Test Method Standard No. 151B, Metals: Test Methods, Method Number 823, for 84 days. The second-step aging times at 350°F, the stresses at which the specimens were exposed, and the results of the corrosion test are summarized in Table 2 for the 6.7 in. (17 cm) thick forgings, in Table 3 for the 2.0 in. (5.08 cm) thick forgings, and in Table 4 for the 1.00 in. (2.54 cm) thick forgings.

Stress-corrosion acceptance criteria and minimum tensile properties are well established for 7075-T73 products. Figure 12 demonstrates that a second-step aging of 8 h at 350°F resulted in the 1 (2.54) and 2 in. (5.08 cm) thick 7075-T73 forgings being aged to electrical conductivities well above the specified minimum of 38 percent of the international annealed copper standard (IACS) and to yield strengths well above the guaranteed minimum of 56 ksi (386 MPa) specified for forgings up to 3 in. (7.62 cm) thick. The 6.7 in. (17 cm) thick 7075-T73 forging given a second-step aging of 8 h at 350°F also displayed an electrical conductivity well above the specified minimum of 38 percent IACS. Figure 12 provides some evidence that the nominal aging practice provides sufficient latitude within the specification limits for successful commercial production of 7075-T73 forgings.

Although a minimum electrical conductivity and minimum tensile properties have not been specified for 7475-T73 forgings, the multiple second-step aging times that were used in the investigation permit a comparison of the tensile properties and electrical conductivity of the 7075-T73 and the 7475-T73 forgings at comparable levels of resistance to stress corrosion. From Figs. 13 and 14, it is evident that the fabrication procedures used in this investigation produced longitudinal yield strengths in the 7475-T73 forgings that were above the minimum value of 56.0 ksi (386 MPa) specified for 7075-T73 hand forgings of thicknesses less than 3.0 in. (7.62 cm), but that for an equivalent resistance to stress-corrosion cracking the 7475-T73 forgings had strengths lower than those of the 7075-T73 forgings included for comparison. Based on these limited data for 7475-T73 forg-

TABLE 2—*Resistance to corrosion of 6.7-in.-thick*

		Longitudinal Tensile Properties				Days to Failure of 1/8-in. Longitudinal Stressed at 45 ksi		
Specimen	2nd-Step Aging at 350°F, h	Ultimate Tensile Strength ksi	Yield Strength ksi	Elongation, %	Electrical Conductivity, % IACS	Specimen L2	Specimen L3	Specimen L4
7075 Hand Forging, Unrecrystallized								
437701-32	2	78.3	68.2	14.0	36.6	OK 84	OK 84	OK 84
437701-33	4	77.2	67.1	14.0	38.7	OK 84	OK 84	OK 84
437701-34	6	72.8	61.0	14.0	40.7	OK 84	OK 84	OK 84
437701-35	8	70.2	58.0	14.0	42.1	OK 84	OK 84	OK 84
7475 Hand Forging, Recrystallized Plus								
438170-2	2	76.7	68.3	16.0	36.2	OK 84	OK 84	OK 84
438170-3	4	75.6	67.0	14.0	38.6	OK 84	OK 84	OK 84
438170-4	6	73.9	64.4	16.0	40.1	OK 84	OK 84	OK 84
438170-6	9	73.7	63.2	14.0	40.3	OK 84	OK 84	OK 84
7475 Hand Forging, Recrystallized								
438173-2	2	78.6	70.0	14.0	35.2	OK 84	OK 84	OK 84
438173-3	4	74.2	65.6	18.0	39.0	OK 84	OK 84	OK 84
438173-4	6	73.5	64.6	16.0	39.7	OK 84	OK 84	OK 84
438173-6	9	70.2	59.0	18.0	40.5	OK 84	OK 84	OK 84
7475 Hand Forging, Unrecrystallized								
438176-2	2	82.9	75.6	12.0	35.2	OK 84	OK 84	OK 84
438176-3	4	77.0	70.7	6.0	37.7	OK 84	OK 84	OK 84
438176-4	6	75.9	67.6	10.0	38.9	OK 84	OK 84	OK 84
438176-6	9	67.6	60.0	6.0	40.4	OK 84	OK 84	OK 84

NOTES—1. Forgings heat treated, quenched in cold water, aged 24 h at 250°F plus indicated time at 350°F as 2-in.-thick sawed sections.

2. 7075 heat treated at 880°F, 7475 heat-treated at 960°F.

3. Yield strength = 2.0 percent offset.

Reprinted from Zola, J. C., "Improvement of Helicopter Forgings by Controlled Solidification and Thermal-Mechanical Treatments," AVSCOM Report No. 76-41, Boeing Vertol Company, Phila., Pa., March 1977.

ings, it would appear that minimum tensile properties for 7475-T73 forgings would have to be lower than those that have been specified for 7075-T73 forgings. Furthermore, Fig. 15 shows that the minimum electrical conductivity of 38 percent IACS will not be applicable to 7475-T73 forgings fabricated by the studied procedures. The 7475-T73 forgings require aging to higher electrical conductivities to obtain the same resistance to stress corrosion that 7075-T73 forgings display at an electrical conductivity of 38 percent IACS.

Conclusions

It is apparent that ITMT is a process which can be applied to 7000 series

7075-T7X and 7475-T7X hand forgings.

ϕ Tensile Bars Exposed Stressed to Alternate Immersion (Method 823) for 84 Days

Short-Transverse Stressed at 45 ksi			Short Transverse Stressed at 35 ksi			Short Transverse Stressed at 25 ksi		
Specimen N2	Specimen N4	Specimen N6	Specimen N5	Specimen N8	Specimen N11	Specimen N1	Specimen N7	Specimen N9
F51	F2	F5	F72	OK 84	OK 84	OK 84	OK 84	OK 84
OK 84	OK 84	OK 84	OK 84	OK 84	OK 84	OK 84	OK 84	OK 84
OK 84	OK 84	OK 84	OK 84	OK 84	OK 84	OK 84	OK 84	OK 84
OK 84	OK 84	OK 84	OK 84	OK 84	OK 84	OK 84	OK 84	OK 84
Hot-Worked (*7475-TMTI*)								
F4	F3	F2	F4	F4	F3	F10	OK 84	F9
F81	F80	OK 84	OK 84	OK 84	OK 84	OK 84	OK 84	OK 84
OK 84	OK 84	OK 84	OK 84	OK 84	OK 84	OK 84	OK 84	OK 84
OK 84	OK 84	OK 84	OK 84	OK 84	OK 84	OK 84	OK 84	OK 84
Plus Hot-Worked (*7475-TMT2*)								
F3	F2	F2	OK 84	F2	F2	F10	F10	F3
F16	F30	F9	F62	F78	F5	OK 84	OK 84	F78
F46	OK 84	F80	OK 84	OK 84	OK 84	OK 84	OK 84	OK 84
OK 84	OK 84	OK 84	OK 84	OK 84	OK 84	OK 84	OK 84	OK 84
F2	F2	F2	F2	F2	F2	F2	F10	OK 84
F10	F3	OK 84	F24	OK 84	F84	OK 84	F83	OK 84
F30	F10	not exposed	F25	F37	not exposed	F83	OK 84	OK 84
OK 84	OK 84	OK 84	OK 84	not exposed	OK 84	OK 84	OK 84	OK 84

aluminum alloy forgings to produce a combination of properties which collectively demonstrate an improvement over the untreated alloy properties. This is achieved with the incurrence of a fabrication cost increase. In summary, the following average properties have been demonstrated by test:

Property	7075-T73	ITMT1	ITMT2
Ultimate tensile strength, ksi (MPa)	73(503)	73(503)	72(496)
Elongation, percent	13	17	16
Reduction in area, percent	32	46	50
Fracture toughness K_Q or K_{Ic}, ksi$\sqrt{\text{in.}}$ (MNm$^{-3/2}$)	40(36)	46(42)	49(45)
Fatigue crack propagation rate in 3.5% NaCl		improved over 7075-T73 on basis of short-transverse orientation properties	
Stress corrosion resistance	equivalent performance; all three alloys passed 84-day alternate immersion test at average ultimate tensile strength values		

TABLE 3—*Resistance to corrosion of 2-in.-thick*

		Longitudinal Tensile Properties				Days to Failure of 1/8-in. Longitudinal Stressed at 45 ksi		
Specimen	2nd-Step Aging at 350°F, h	Ultimate Tensile Strength, ksi	Yield Strength, ksi	Elongation, %	Electrical Conductivity, % IACS	Specimen L2	Specimen L3	Specimen L4
							7075 Hand Forging,	
437701-22	2	83.7	73.4	12.0	36.0	OK 84	OK 84	OK 84
437701-23	4	78.0	69.0	14.0	39.2	OK 84	OK 84	OK 84
437701-24	6	76.3	65.4	14.0	39.6	OK 84	OK 84	OK 84
437701-25	8	73.3	61.7	16.0	41.0	OK 84	OK 84	OK 84
						7475 Hand Forging, Recrystallized		
438169-2	2	82.0	74.9	14.0	37.2	OK 84	OK 84	OK 84
438169-3	4	79.6	71.0	16.0	39.3	OK 84	OK 84	OK 84
438169-4	6	79.4	70.2	16.0	40.7	OK 84	OK 84	OK 84
438169-6	9	76.0	65.6	14.0	41.5	OK 84	OK 84	OK 84
						7475 Hand Forging, Recrystallized		
438172-2	2	80.3	72.0	14.0	38.0	OK 84	OK 84	OK 84
438172-3	4	80.7	71.0	14.0	40.1	OK 84	OK 84	OK 84
438172-4	6	76.4	67.3	16.0	40.5	OK 84	OK 84	OK 84
438172-6	9	75.1	63.9	14.0	42.3	OK 84	OK 84	OK 84
							7475 Hand Forging,	
438175-2	2	82.3	74.6	16.0	36.6	OK 84	OK 84	OK 84
438175-3	4	79.6	71.7	16.0	39.7	OK 84	OK 84	OK 84
438175-4	6	75.2	65.3	16.0	40.6	OK 84	OK 84	OK 84
438175-6	9	73.4	63.9	16.0	42.2	OK 84	OK 84	OK 84

NOTES—Forgings heat-treated, quenched in cold water, aged 24 h at 250°F plus indicated time at 350°F.
7075 forging heat treated at 880°F, 7475 forgings heat treated at 960°F.
Yield strength = 0.2 percent offset.
Reprinted from Zola, J. C., "Improvement of Helicopter Forgings by Controlled Solidification and Thermal-Mechanical Treatments," AVSCOM Report No. 76-41, Boeing Vertol Company, Phila., Pa., March 1977.

The ITMT offers an alternative to the more costly powder metallurgy techniques and high purity processes.

Acknowledgments

I wish to acknowledge Dr. Jeffrey Waldman of Frankford Arsenal, U.S. Army, and U.S. Army Aviation Systems Command (AVSCOM), St. Louis, Mo., for technical guidance and financial support of this program. In addition, J. Staley and J. Vruggink of Alcoa Technical Center are to be recognized for their significant contributions by providing fabrication facilities and fabrication expertise to this program.

7075-T7X and 7475-T7X hand forgings.

ϕ Tensile Bars Exposed Stressed to Alternate Immersion (Method 823) for 84 Days								
Short Transverse Stressed at 45 ksi			Short Transverse Stressed at 35 ksi			Short Transverse Stressed at 25 ksi		
Specimen N2	Specimen N4	Specimen N6	Specimen N5	Specimen N8	Specimen N11	Specimen N1	Specimen N7	Specimen N9
Unrecrystallized								
F3	F34	F43	F72	F10	F72	F10	F3	OK 84
OK 84	OK 84	OK 84	OK 84	OK 84	OK 84	OK 84	OK 84	OK 84
OK 84	OK 84	OK 84	OK 84	OK 84	OK 84	OK 84	OK 84	OK 84
OK 84	OK 84	OK 84	OK 84	OK 84	OK 84	OK 84	OK 84	OK 84
Plus Hot-Worked (*7475-TMT1*)								
F2	F2	F2	F2	F2	OK 84	F3	F3	F3
F46	F54	F6	F60	OK 84	F52	OK 84	OK 84	OK 84
F66	F60	F58	F71	OK 84	F80	OK 84	OK 84	OK 84
OK 84	OK 84	OK 84	OK 84	OK 84	OK 84	OK 84	OK 84	OK 84
Plus Hot-Worked (*7475-TMT2*)								
F2	F2	F2	F3	F2	F3	F2	F3	OK 84
F4	F5	F33	F57	F58	F61	OK 84	OK 84	OK 84
F54	OK 84	F27	OK 84	F64	F58	OK 84	OK 84	OK 84
F57	defect in specimen	F80	OK 84	OK 84	OK 84	OK 84	OK 84	OK 84
Unrecrystallized								
F3	F3	F3	F8	F30	F30	OK 84	OK 84	OK 84
F19	F24	F5	F26	F30	F30	F57	F58	OK 84
not exposed	not exposed	OK 84	OK 84	OK 84	F30	OK 84	OK 84	OK 84
OK 84	OK 84	OK 84	OK 84	OK 84	F84	OK 84	OK 84	OK 84

TABLE 4—*Resistance to corrosion of 1-in.-thick 7075-T7X and 7475-T7X hand forgings.*

		Longitudinal Tensile Properties				Days to Failure of Specimens Exposed Stressed to Alternate Immersion (Method 823) for 84 Days						
						Longitudinal 1/8-in. ϕ Tensile Bars Stressed at 45 ksi			Short Transverse Stressed at 45 ksi		0.75-in. ϕ C-Rings Stressed at 35 ksi	
Specimen	2nd-Step Aging at 350°F, h	Ultimate Tensile Strength ksi	Yield Strength[c] ksi	Elongation, %	Electrical Conductivity, % IACS	Specimen L2	Specimen L3	Specimen L4	Specimen C1	Specimen C2	Specimen C3	Specimen C4
					7075 Hand Forging, Unrecrystallized[a,b]							
437701-12	2	82.2	72.9	14.0	36.3	OK 84	OK 84	OK 84	OK 84[e]	OK 84[e]	not exposed	not exposed
437701-13	4	79.9	69.5	16.0	37.4	OK 84	OK 84	OK 84	OK 84[d]	OK 84[d]	not exposed	not exposed
437701-14	6	78.7	68.0	14.0	38.4	OK 84	OK 84	OK 84	OK 84[d]	OK 84[d]	not exposed	not exposed
437701-15	8	74.5	62.7	16.0	40.6	OK 84	OK 84	OK 84	OK 84	OK 84	not exposed	not exposed
					7475 Hand Forging, Recrystallized Plus Hot Worked (7475-TMT1)[a,b]							
438168-2	2	81.9	74.6	16.0	37.9	OK 84	OK 84	OK 84	OK 84[d]	OK 84[d]	OK 84[e]	OK 84[d]
438168-3	4	81.0	72.7	16.0	40.0	OK 84	OK 84	OK 84	OK 84	OK 84	OK 84	OK 84[d]
438168-4	6	78.5	69.3	16.0	41.0	OK 84	OK 84	OK 84	OK 84	OK 84	OK 84	OK 84
438168-6	9	74.3	65.4	18.0	41.9	OK 84	OK 84	OK 84	OK 84	OK 84	OK 84	OK 84
					7475 Hand Forging, Recrystallized Plus Hot Worked (7475-TMT2)[a,b]							
438171-2	2	80.0	73.4	16.0	38.3	OK 84	OK 84	OK 84	F51DA	F51DA	OK 84[e]	OK 84[e]
438171-3	4	79.0	71.6	16.0	40.2	OK 84	OK 84	OK 84[e]	OK 84	OK 84[d]	OK 84[d]	OK 84
438171-4	6	77.0	67.8	16.0	41.0	OK 84	OK 84	OK 84	OK 84	OK 84	OK 84	OK 84
438171-6	9	74.6	64.4	16.0	42.1	OK 84	OK 84	OK 84	OK 84	OK 84	OK 84	OK 84
					7475 Hand Forging, Unrecrystallized[a,b]							
438174-2	2	83.8	76.6	14.0	37.0	OK 84	OK 84	OK 84	OK 84[e]	OK 84[d]	not exposed	not exposed
438174-3	4	80.2	72.4	14.0	39.1	OK 84	OK 84	OK 84	OK 84	OK 84	not exposed	not exposed
438174-4	6	77.4	69.0	18.0	40.1	OK 84	OK 84	OK 84	OK 84	OK 84	OK 84	OK 84
438174-6	9	74.8	64.9	18.0	41.3	OK 84	OK 84	OK 84	OK 84	OK 84	OK 84	OK 84

NOTE—Reprinted from Zola, J. C., "Improvement of Helicopter Forgings by Controlled Solidification and Thermal-Mechanical Treatments," AVSCOM Report 76-41, Boeing Vertol Company, Phila., Pa., March 1977.

[a] Forgings heat treated, quenched in cold water, aged 24 h at 250°F plus indicated time at 350°F.

[b] 7075 forging heat treated at 880°F, 7475 forgings heat treated at 960°F.

[c] Yield strength = 0.2 percent offset.

[d] Specimen did not fail but contained severe directional pitting.

[e] Specimen did *not* fail but contained small directional cracks.

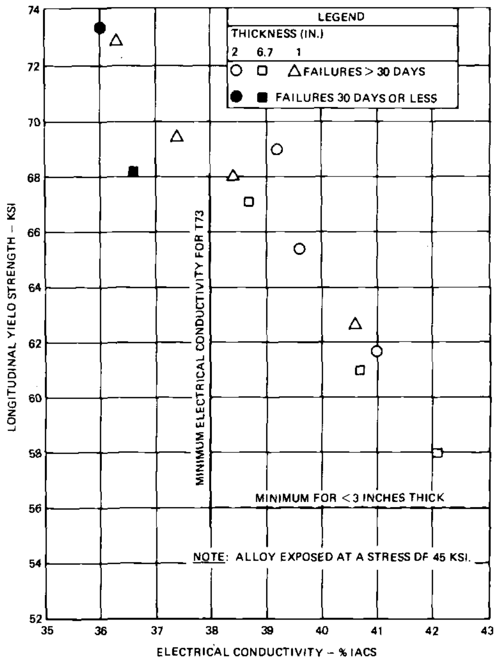

FIG. 12—*Longitudinal yield strength versus electrical conductivity for unrecrystallized 7075 aluminum alloy.*

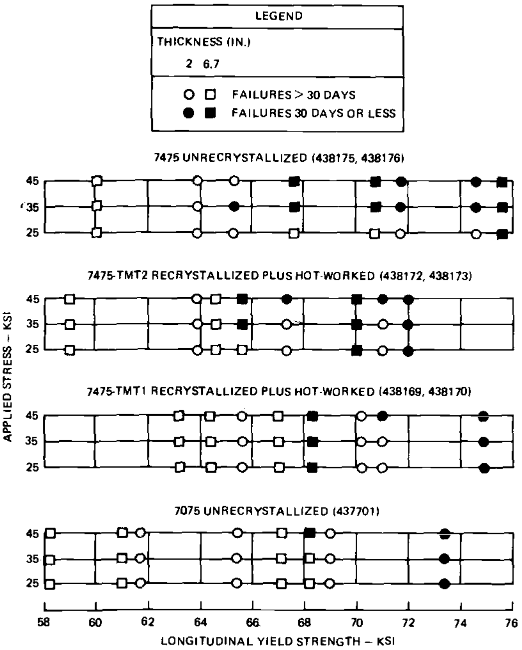

FIG. 13—*Applied stress versus longitudinal yield strength for aluminum alloy.*

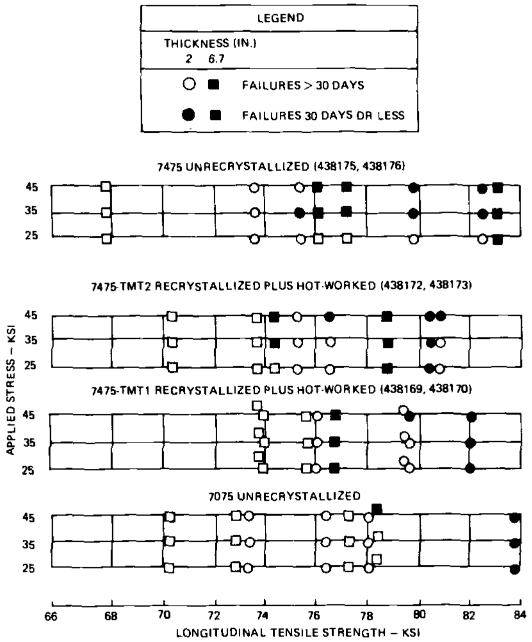

FIG. 14—*Applied stress versus longitudinal tensile strength for aluminum alloy.*

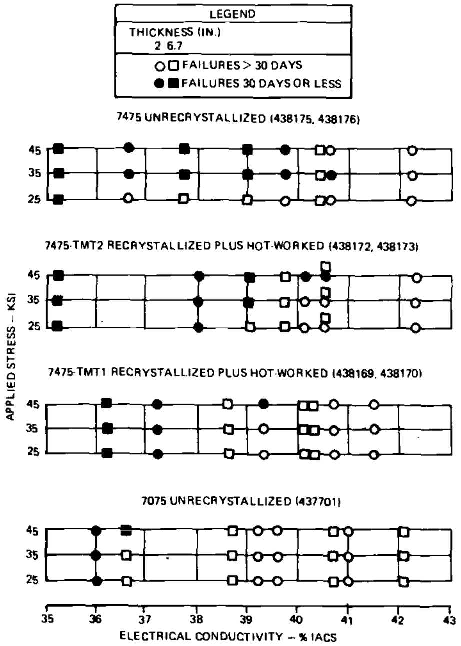

FIG. 15—*Applied stress versus electrical conductivity for aluminum alloy.*

T. W. Crooker,[1] F. D. Bogar,[2] and W. R. Cares[3]

Effects of Flowing Natural Seawater and Electrochemical Potential on Fatigue-Crack Growth in Several High-Strength Marine Alloys

REFERENCE: Crooker, T. W., Bogar, F. D., and Cares, W. R., "**Effects of Flowing Natural Seawater and Electrochemical Potential on Fatigue-Crack Growth in Several High-Strength Marine Alloys,**" *Corrosion-Fatigue Technology, ASTM STP 642,* H. L. Craig, Jr., T. W. Crooker, and D. W. Hoeppner, Eds., American Society for Testing and Materials, 1978, pp. 189-201.

ABSTRACT: Fatigue crack propagation studies were conducted on specimens of four high-strength marine alloys to determine the sensitivity of fatigue-crack growth rates to seawater and electrochemical potential. The materials studied included HY-130 steel, 17-4 PH steel in several combinations of melt processing and temper, Ti-6Al-2Cb-1Ta-0.8Mo, and 5456-H116 aluminum. Fatigue testing was conducted at low cyclic frequency, and the fatigue data are presented in terms of fatigue-crack growth rate (*da/dN*) versus crack-tip stress-intensity factor range (ΔK). Specimens were exposed to fresh flowing natural seawater under freely corroding and potentiostat-controlled electrochemical conditions while undergoing corrosion-fatigue testing. The results of this investigation reveal significantly distinct differences among the four alloys under the conditions of corrosion fatigue. Both seawater and potential acted to accelerate crack growth rates in the ferrous alloys, which proved to be much more sensitive to seawater and negative potential than the nonferrous alloys studied. The titanium alloy exhibited no measurable sensitivity to either seawater or negative potential. The aluminum alloy exhibited only moderate sensitivity to seawater and beneficial effects from both positive and negative potentials. These exploratory studies indicate that high-strength marine alloys exhibit widely differing responses to corrosion-fatigue crack growth and that high-strength steels currently aimed for marine service are among the alloys most deleteriously affected.

KEY WORDS: corrosion fatigue, crack propagation, high-strength alloys, fracture mechanics, steels, titanium alloys, aluminum alloys, seawater, electrochemistry

---

[1] Head, Fatigue Criteria Section, Engineering Materials Division, Naval Research Laboratory, Washington, D.C. 20375.

[2] Research chemist, Naval Research Laboratory, Marine Corrosion Research Laboratory, Key West, Fla. 33040.

[3] Research chemist, Pullman Kellogg, Research and Development Center, Houston, Tex. 77084.

The U.S. Navy has initiated development of new classes of advanced surface ships, such as hydrofoil and surface effect ships, which require weight-critical structures. These weight-critical structures demand the utilization of high-strength marine alloys which are inherently more highly flaw sensitive than the more forgiving traditional naval materials, and thus more susceptible to such failure mechanisms as fatigue, environmental crack growth, and fracture. Experience to date with early prototype ships strongly suggests that fatigue and environmental crack growth, in fact, do pose genuine threats to the structural integrity of these new classes of high-performance ships [*1*].[4] The present study was undertaken to begin development of the technology base on the effects of flowing natural seawater and electrochemical potential on fatigue-crack growth in several candidate high-strength marine alloys for advanced ship applications.

At present little is known regarding the combined effects of seawater and potential on fatigue-crack growth in marine alloys. However, experience to date with existing prototype ships has demonstrated the necessity for crack-growth estimates in establishing design criteria and maintenance intervals during service. Therefore, information of the type presented herein is directly applicable to current problems in advanced ship design.

Description of Materials

The materials studied in this investigation included HY-130 steel, three specimens of 17-4 PH steel, Ti-6Al-2Cb-1Ta-0.8Mo, and 5456-H116 aluminum. All of the materials studied were received as 1-in. (25.4-mm) thick rolled plate. The three specimens of 17-4 PH consisted of a vacuum-melted (VM) material in the H1050 temper plus an argon-oxygen melted (AOM) material in the H1050 and H1150 tempers. The fatigue crack propagation characteristics of these three 17-4 PH steels in an ambient air environment are described in detail in Ref *2* and similar information on the HY-130 steel are reported in Ref *3*. The tensile properties of the six materials studied are given in Table 1.

Experimental Procedures

All of the corrosion-fatigue data reported herein were obtained in flowing fresh natural seawater at the U.S. Naval Research Laboratory (NRL) Marine Corrosion Research Laboratory in Key West, Fla. Fatigue-crack growth tests were conducted using single-edge-notch (SEN) cantilever specimens, Fig. 1, except for limited reference data taken from Refs *2* and *3*, as noted. Fracture mechanics stress-intensity factors for the cantilever specimens were calculated using the Kies expression [*4*]. All specimens

---

[4] The italic numbers in brackets refer to the list of references appended to this paper.

TABLE 1—*Tensile properties.*

	0.2% Yield Strength		Ultimate Tensile Strength		Elongation,	Reduction in Area,
Material	MPa	ksi	MPa	ksi	%	%
HY-130	1015	147.2	1054	152.9	18.8	20.0
17-4 PH VM-H1050	1059	153.6	1105	160.3	16.0	62.0
17-4 PH AOM-H1050	1124	163.0	1178	170.8	12.5	47.2
17-4 PH AOM-H1150	931	135.0	1025	148.6	14.2	48.0
Ti-6Al-2Cb-1Ta-0.8Mo	789	114.5	865	125.5	12.0	27.6
5456-H116	214	31.1	371	53.8	22.7	20.0

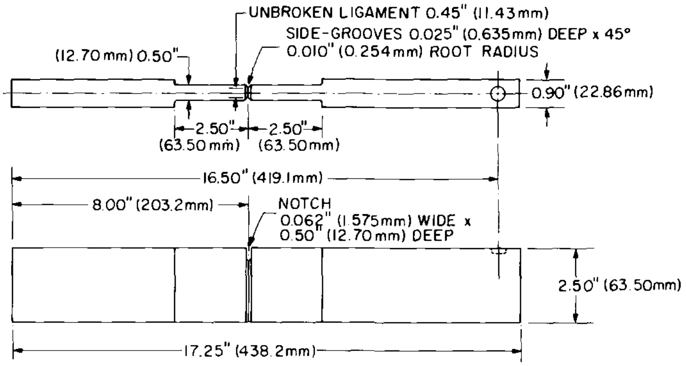

FIG. 1—*Details of the SEN cantilever specimen.*

were oriented with the edge crack parallel to the final rolling direction of the material, in the ASTM-designated T-L orientation [*5*].

The cantilever specimens were cycled under constant load, zero-to-tension, with the stress ratio, $R = 0$. All tests were conducted at a cyclic frequency of 10 cycles per minute (cpm) (0.167 Hz), unless otherwise noted. One corrosion-fatigue test on HY-130 steel was conducted at 1 cpm (0.0167 Hz), and some ambient air environment reference data for 17-4 PH and HY-130 steels taken at higher frequencies are included from Refs *2* and *3*. Although the electrohydraulic testing machines used for the corrosion-fatigue tests conducted at the Key West laboratory did not feature closed-loop control systems, the waveforms employed can be considered to be approximately triangular for comparison purposes.

For the corrosion-fatigue tests, natural seawater was taken directly from the ocean and immediately passed through a polyurethane enclosure cell, placed around the specimen test section, in a single-pass mode at a flow rate of approximately 200 ml/min. The corrosion cell had a plexiglas viewing area for optical observation of crack growth. Measurement of the fatigue-crack length was performed by a slide-mounted optical micrometer focused on the root surface of one side groove of the specimens.

Electrochemical potentials were applied by means of a potentiostat device. Potentials were measured versus a silver/silver chloride (Ag/AgCl) reference electrode. The freely corroding potentials of the various materials studies are given in Table 2.

TABLE 2—*Freely corroding potentials versus Ag/AgCl.*

Material	HY-130	17-4 PH VM	17-4 PH AOM	5456-H116 Al	Ti-6Al-2Cb-1Ta-0.8Mo
Potential, mV	−665	−300	−200	−950	−300

Results

The results of this investigation are shown in Figs. 2 through 7. These figures are logarithmic plots of crack growth rate (*da/dN*) versus stress-intensity factor range (ΔK) for the six materials included in this investigation. Each plot includes a reference curve generated in a laboratory am-

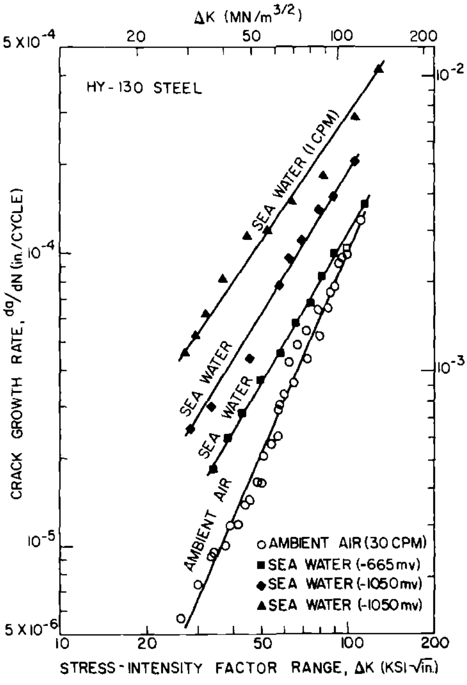

FIG. 2—*Corrosion-fatigue crack growth data for HY-130 steel.*

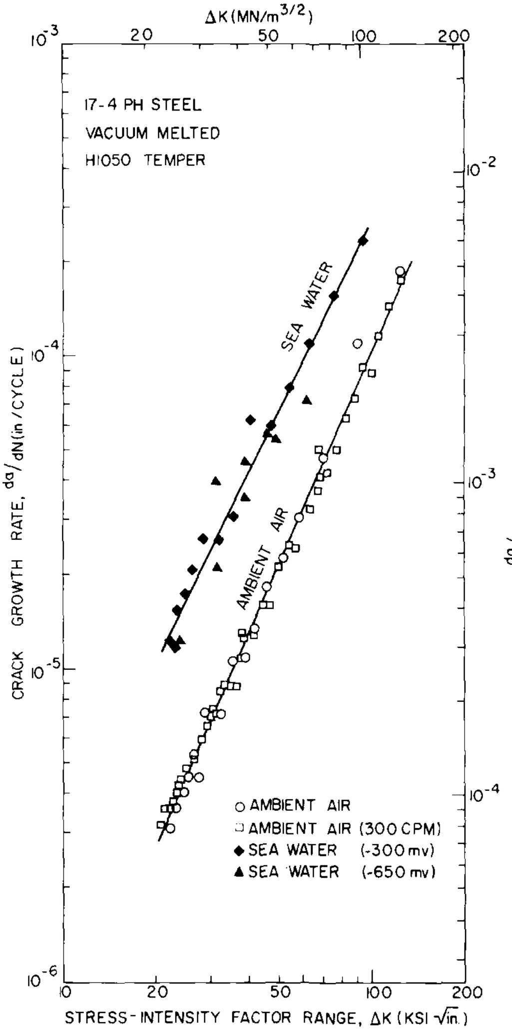

FIG. 3—*Corrosion-fatigue crack growth data for 17-4 PH VM-H1050 steel.*

bient air environment (relative humidity ~50 percent) plus data generated in flowing natural seawater under freely corroding conditions and under various applied electrochemical potentials.

A wide variety of responses to seawater and electrochemical potential were noted among the six materials:

1. No effect of either seawater or negative potential (Ti-6Al-2Cb-1Ta-0.8Mo)
2. Deleterious effect of seawater with no effect of negative potential (17-4 PH VM steel)

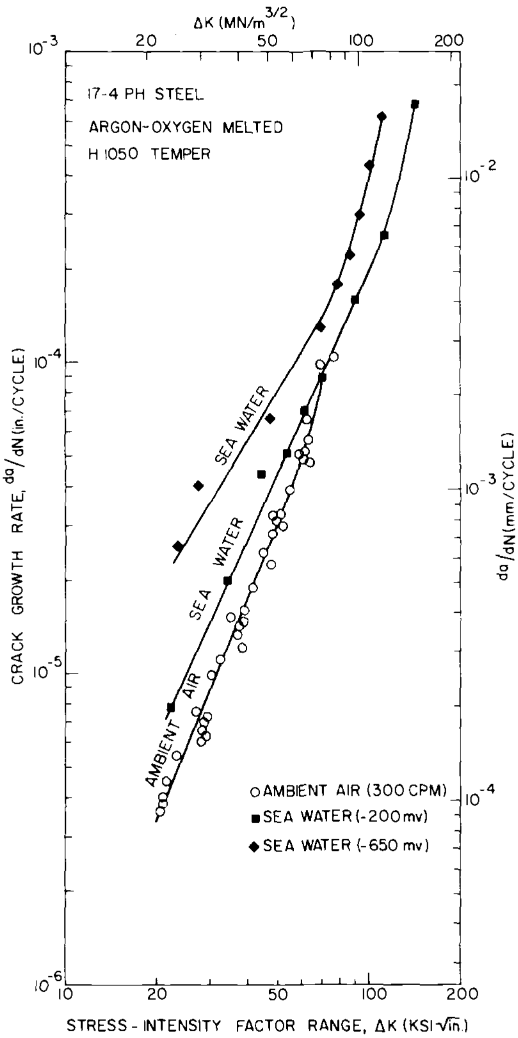

FIG. 4—*Corrosion-fatigue crack growth data for 17-4 PH AOM-H1050 steel.*

3. Deleterious effect of seawater with beneficial effect of either positive or negative potential (5456-H116 aluminum)
4. Deleterious effect of seawater with deleterious effect of negative potential (17-4 PH AOM steels)
5. Deleterious effect of seawater and negative potential with a further deleterious effect of reduced cyclic frequency (HY-130 steel)

The magnitudes of the environmentally and electrochemically induced accelerations in crack growth rates varied from negligible to an order of

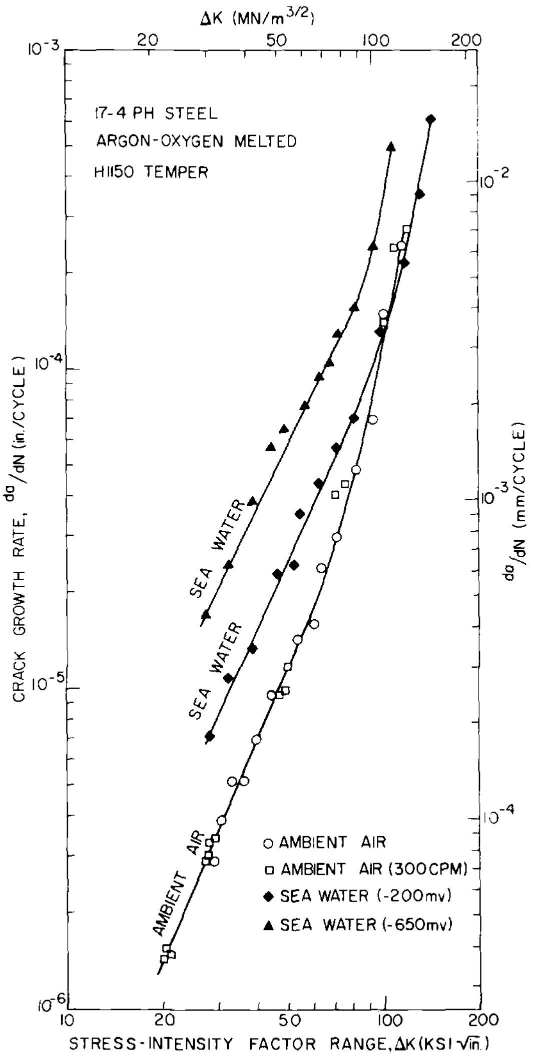

FIG. 5—*Corrosion-fatigue crack growth data for 17-4 PH AOM-H1150 steel.*

magnitude, with the greatest accelerations occurring in the ferrous alloys at lower ΔK values under negative potential and at reduced cyclic frequency.

Discussion

Ambient Air Environment

The da/dN-versus-ΔK curves generated in an ambient air environment

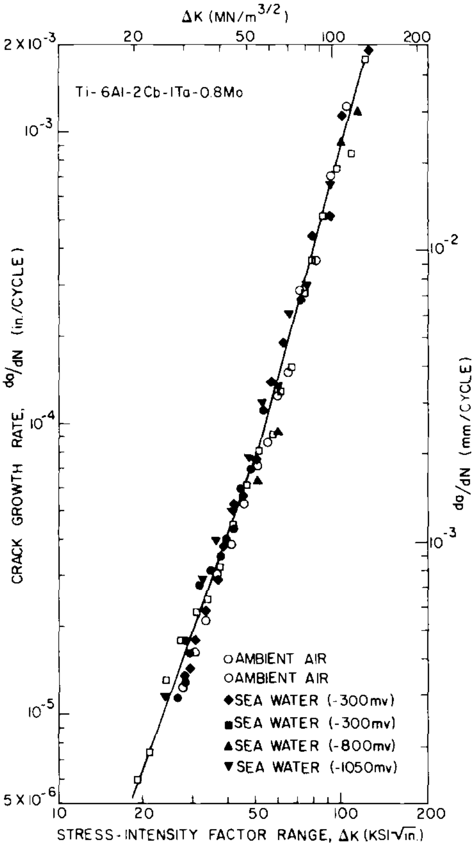

FIG. 6—*Corrosion-fatigue crack growth data for Ti-6Al-2Cb-1Ta-0.8Mo alloy.*

provide the reference basis against which environmental and electrochemical effects are judged. Wherever possible, these reference curves are based upon data from more than one test or have been compared against data from other investigators. For instance, the HY-130 ambient air reference curve shown in Fig. 2 was taken from data on part-through-cracked and center-through-cracked specimens at a frequency of 30 cpm as reported in Ref *3*. Subsequently, additional tests were performed on this material using compact tension specimens cycled at 300 cpm which confirmed these results in ambient air, as reported in Ref *6*. For the 17-4 PH VM-H1050 material, Fig. 3, the reference curve consists of data generated using SEN cantilever specimens cycled at 10 cpm at the Key West Laboratory, plus data generated using pin-loaded SEN tension specimens cycled at 300 cpm at the Naval Research Laboratory in Washington, as reported in Ref *2*. A similar combination of data is used to provide the reference curve for

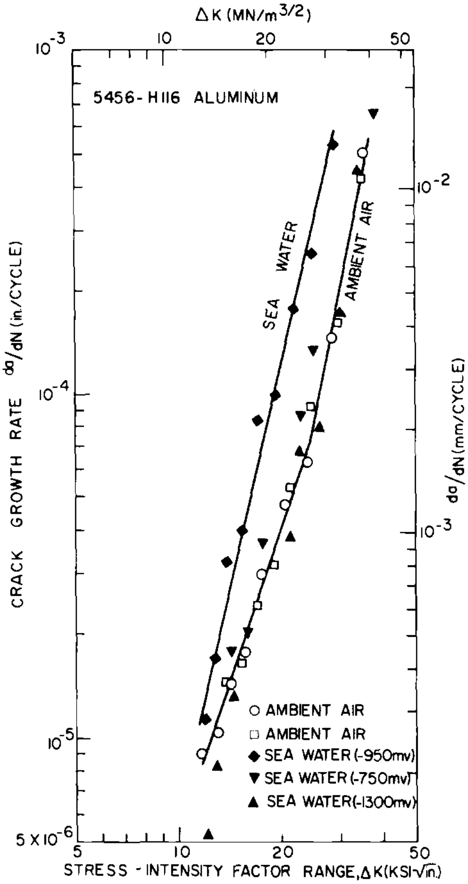

FIG. 7—*Corrosion-fatigue crack growth data for 5456-H116 aluminum alloy.*

the 17-4 PH AOM-H1150 material, Fig. 5. For the Ti-6Al-2Cb-1Ta-0.8Mo alloy, Fig. 6, the data generated in this investigation are in excellent agreement with the results of other studies on this material conducted under U.S. Navy sponsorship [*7,8*]. Finally, for the 5456-H116 alloy, Fig. 7, the ambient air reference curve is in good agreement with previous work on a 5456-H321 alloy reported in Ref *9*.

Freely Corroding Seawater Environment

With the exception of the Ti-6Al-2Cb-1Ta-0.8Mo alloy, all of the materials studied exhibited some degree of environmentally accelerated crack growth rates in the natural seawater environment under freely corroding conditions. The most significantly affected material under this condition was the 17-4 PH-VM H1050 steel, Fig. 3, which exhibited increases in crack growth rates by as much as a factor of five due to freely corroding seawater. For the remaining materials (that is, HY-130 steel, 17-4 PH AOM steels in both tempers, and the 5456-H116 aluminum) the freely corroding natural seawater environment resulted in an approximate doubling of crack growth rates.

However, in judging these effects for the 17-4 PH steels, it must be kept in mind that the air environment reference curves for these materials differ significantly. This aspect has been discussed in detail in Ref *2*, where it was noted that AOM-H1050 material exhibits notably poorer resistance to fatigue crack growth in ambient air than the other two 17-4 PH steels. Thus, this material, Fig. 4, has an air environment reference curve which lies well above the reference curves for the other two 17-4 PH steels, Figs. 3 and 5. Therefore, it would appear that the freely corroding seawater has somewhat of an "equalizing effect" on these 17-4 PH steels, that is, more strongly affecting the initially superior materials and less strongly affecting the initially inferior material.

Potentiostated Seawater Environment

The application of electrochemical potential to specimens of the various materials being fatigued in seawater provided very marked differences in response among the alloys under investigation. This strongly suggests that the mechanisms of environmentally accelerated fatigue crack growth differ among the various materials.

With the exception of one test on the aluminum alloy, all of the potentials applied by means of the potentiostat device were more negative than the freely corroding potentials. For the ferrous alloys, negative potentials of the magnitudes examined here are of great practical significance for advanced ship applications. Cathodic protection systems utilizing zinc anodes or coupling between steel foils and an aluminum hull are encountered in marine structures and produce negative potentials in the range of values utilized in these studies.

For three of the four ferrous materials studied, negative potential had a markedly adverse effect on crack growth rates, generally accelerating crack growth rates by a factor of two or more over those measured under freely corroding conditions. Overall, the combined effects of seawater and negative electrochemical potential tended to accelerate crack growth rates by a factor of approximately five in the HY-130 steel and the two 17-4 PH AOM steels. Effects of this magnitude become highly significant in crack growth estimates for design purposes. However, in some situations such crack growth acceleration effects are difficult to avoid because some degree of negative potential is often necessary to reduce surface pitting or crevice corrosion in ferrous alloys.

Unlike the other steels examined, the 17-4 PH VM material, Fig. 3, did not exhibit acceleration in crack growth rate due to negative potential. No explanation for this behavior is readily available. However, two observations are relevant. First, this material did respond more strongly to freely corroding conditions than the other steels studied. Also, an apparent lack of response to negative potential in this steel also has been noted in another investigation [*8*].

The HY-130 steel, Fig. 2, exhibited further increases in crack growth rates by reducing the cyclic frequency under potentiostated conditions to 1 cpm, resulting in crack growth rates as much as an order of magnitude greater than those measured in ambient air in this material. Frequency effects of this type are well recognized in steels [*10–12*]. In fact, the crack growth rates seen here are in good agreement with those measured in HY-80 steel by Gallagher at similar values of ΔK, frequency and potential [*10*]. Both Gallagher [*10*] and Vosikovsky [*12*] have shown that crack growth rates even continue to increase at cyclic frequencies below 1 cpm, with some of Vosikovsky's data on a low-alloy steel showing increases in crack growth rates by as much as a factor of 100 over ambient air data due to the combined influences of salt water, negative potential, and low cyclic frequency below 1 cpm.

The responses of the nonferrous alloys to potential was quite different. The Ti-6Al-2Cb-1Ta-0.8Mo alloy exhibited no response either to seawater or seawater plus potential, thus indicating its attractiveness as a marine alloy. The aluminum alloy exhibited a moderate acceleration in crack growth rates due to freely corroding seawater, but the application of either negative or positive potentials in seawater had beneficial effects and reduced crack growth rates back to values near the ambient air reference curve. These observations are in contrast to those of Speidel et al on 7079-T651 aluminum [*13*], where potentials negative from the freely corroding potential were seen to reduce crack growth rates in corrosion fatigue and positive potentials produced an acceleration. However, further interpretation of many of the observations presented cannot be rationalized without an understanding of the mechanisms involved.

Comparisons with Stress Corrosion Cracking Characteristics

Some general comparisons with the stress corrosion cracking (SCC) characteristics of the materials studied are in order. It has become customary to delineate corrosion-fatigue crack propagation into two regimes involving K_{max} levels below or above K_{Iscc} [*10*]. Fatigue cycling above K_{Iscc} implies significantly accelerated crack growth rates resulting from the dual superposition of an SCC mechanism plus a fatigue mechanism [*14*], whereas cycling below K_{Iscc} implies a lesser degree of environmental acceleration resulting from a singular mechanism of crack growth.

Although only one of the actual materials studied in this investigation was specifically tested to determine its K_{Iscc} characteristics, a review of existing data on similar materials suggests that nearly all of the *da/dN*-versus-ΔK data from this study involve corrosion-fatigue cycling "below K_{Iscc}." Fujii [*15*] has done an extensive study on SCC in VM 17-4 PH steels as a function of yield strength and potential utilizing the same plate sample of materials as was used in this study. His data suggest that for the H1050 temper utilized in this study, the K_{Iscc} values for both the freely corroding and -650 mV conditions lie above 100 ksi$\sqrt{\text{in.}}$ (110 MPa·m$^{1/2}$) and thus beyond the upper limit of the corrosion-fatigue curve for this material, as shown in Fig. 3. For the 17-4 PH AOM materials and the HY-130 steel, published data [*16*] plus recent unpublished work [*17*] suggest that all but the very upper portions of the corrosion-fatigue *da/dN*-versus-ΔK curves in Figs. 2, 3, and 5 lie below the estimated K_{Iscc} values. For the nonferrous alloys studied, related information on SCC characteristics of these materials suggests that they exhibit little or no sensitivity to SCC [*18,19*].

Summary and Conclusions

Corrosion-fatigue crack growth studies were conducted on a selected group of high-strength marine alloys in flowing natural seawater under low cyclic frequency at various controlled levels of electrochemical potential. The materials studied included: HY-130 steel, VM 17-4 PH steel in the H1050 temper, AOM 17-4 PH steel in the H1050 and H1150 tempers, Ti-6Al-2Cb-1Ta-0.8Mo, and 5456-H116 aluminum alloy. The results are presented in terms of a *da/dN*-ΔK fracture mechanics format. These results are as follows.

1. The corrosion-fatigue response of these alloys to natural seawater and electrochemical potential varies widely depending upon the particular alloy. Effects range from negligible to seriously deleterious.
2. Generally, the high-strength steels (HY-130 and 17-4 PH) currently committed to U.S. Navy programs are among the most seriously affected by corrosion fatigue.
3. The nonferrous marine alloys (Ti-6Al-2Cb-1Ta-0.8Mo and 5456-H116 aluminum) exhibited very promising responses to the conditions of corrosion fatigue utilized in this investigation.

Acknowledgments

The authors wish to acknowledge the assistance of C. W. Billow, G. W. Jackson, and W. E. King in preparing specimens and conducting tests. The financial support of the U.S. Naval Material Command is gratefully acknowledged.

References

[1] Vanderveldt, H. H., Crooker, T. W., and Corrado, J. A., *Naval Engineers Journal,* April 1976, pp. 97-104.

[2] Crooker, T. W., Hasson, D. F., and Yoder, G. R. in *Fractography, ASTM STP 600,* American Society for Testing and Materials, 1976, pp. 205-219.

[3] Sullivan, A. M. and Crooker, T. W., *Transactions,* American Society of Mechanical Engineers, *Journal of Pressure Vessel Technology,* Vol. 98, Series J, No. 2, May 1976, pp. 179-184.

[4] Kies, J. A., Smith, H. L., Romine, H. E., and Bernstein, H. in *Fracture Toughness Testing and Its Applications, ASTM STP 381,* American Society for Testing and Materials, 1965, pp. 328-353.

[5] Goode, R. J., *Materials Research and Standards,* Vol. 12, No. 9, Sept. 1972, pp. 31-32.

[6] Sullivan, A. M. and Crooker, T. W., *Engineering Fracture Mechanics,* Vol. 9, No. 1, 1977, pp. 159-166.

[7] Smith, H. L., U.S. Naval Research Laboratory, private communication.

[8] Miller, D. D., The Boeing Company, private communication.

[9] Crooker, T. W., *Transactions,* American Society of Mechanical Engineers, *Journal of Engineering Materials and Technology,* Vol. 95, Series H, No. 3, July 1973, pp. 150-156.

[10] Gallagher, J. P., "Corrosion Fatigue Crack Growth Above and Below K_{Iscc}," NRL Report 7064, U.S. Naval Research Laboratory, 1970.

[11] Barsom, J. M., *Engineering Fracture Mechanics,* Vol. 3, 1971, pp. 15-25.

[12] Vosikovsky, O., *Transactions,* American Society of Mechanical Engineers, *Journal of Engineering Materials and Technology,* Vol. 97, Series H, No. 4, Oct. 1975, pp. 298-304.

[13] Speidel, M. O., Blackburn, M. J., Beck, T. R., and Feeney, J. A., *Corrosion Fatigue,* National Association of Corrosion Engineers, 1972, pp. 324-343.

[14] Wei, R. P. and Landes, J. D., *Materials Research and Standards,* Vol. 9, No. 7, July 1969, pp. 25-28.

[15] Fujii, C. T. in *Stress Corrosion Cracking—New Approaches, ASTM STP 610,* H. L. Craig, Jr., Ed., American Society for Testing and Materials, 1976, pp. 213-225.

[16] Sandoz, G. in *Stress Corrosion Cracking in High Strength Steels and in Titanium and Aluminum Alloys,* B. F. Brown, Ed., U.S. Naval Research Laboratory, 1972, pp. 79-133.

[17] Fujii, C. T., U.S. Naval Research Laboratory, private communication.

[18] Fujii, C. T., "Stress Corrosion Cracking Properties of Thin-Plate Titanium Alloys," Report of NRL Progress, U.S. Naval Research Laboratory, 1976, pp. 10-12.

[19] Bogar, F. D. and Fujii, C. T., "Stress Corrosion Cracking Properties of Two Aluminum-Magnesium Alloys," NRL Memorandum Report 2724, U.S. Naval Research Laboratory, Jan. 1974.

J. T. Ryder,[1] *W. E. Krupp,*[1] *D. E. Pettit,*[1] *and*
D. W. Hoeppner[2]

Corrosion-Fatigue Properties of Recrystallization Annealed Ti-6Al-4V

REFERENCE: Ryder, J. T., Krupp, W. E., Pettit, D. E., and Hoeppner, D. W., "**Corrosion-Fatigue Properties of Recrystallization Annealed Ti-6Al-4V,**" *Corrosion-Fatigue Technology, ASTM STP 642,* H. L. Craig, Jr., T. W. Crooker, and D. W. Hoeppner, Eds., American Society for Testing and Materials, 1978, pp. 202-222.

ABSTRACT: The corrosion-fatigue crack growth properties of recrystallization annealed (RA) Ti-6Al-4V were studied in room-temperature laboratory air, dry air, high-humidity air, sump-tank water, and 3.5 percent sodium chloride (NaCl) solution environments. The alloy was characterized by chemical, microstructural, and tensile properties. Corrosion fatigue tests were conducted using wedge-opening-load (WOL), center-cracked-through (CCT) and part-through-cracked (PTC) specimens. Frequency and environmental interactions were studied as well as the effects of orientation and stress ratio. The effect of frequency was to increase the fatigue crack growth rate as the frequency was decreased. A severe effect of frequency was noted in sump-tank water and saltwater where at low frequencies, crack growth rates increased to such a high level that failure occurred at $K_{\max}$ levels significantly below those expected. Fractographic studies showed no apparent cause of this phenomenon.

KEY WORDS: crack propagation, corrosion fatigue, titanium, frequencies, environments

The problem of subcritical flaw growth and subsequent fracture of aircraft structural materials has been recognized as a challenge in maintenance of aircraft structural integrity [*1*].[3] Recent experience in military aircraft has indicated that a greater amount of information pertaining to the fracture and subcritical flaw growth behavior of engineering materials is required in order to prevent early failures and ensure the safe service life of a structural component [*2*].

This report summarizes corrosion-fatigue crack propagation studies conducted for Ti-6Al-4V titanium in the recrystallization-annealed (RA) con-

---

[1] Research scientist, group engineer, and research scientist, respectively, Lockheed-California Company, Rye Canyon Research Laboratory, Burbank, Calif. 91520.

[2] Professor of engineering, University of Missouri, Columbia, Mo. 65201.

[3] The italic numbers in brackets refer to the list of references appended to this paper.

dition. The report is based upon the results of a contract [3] supported by the U.S. Air Force, Air Force Materials Laboratory, Wright-Patterson Air Force Base, Ohio. This titanium alloy was chosen for study as typical of the newer generation of high-toughness titanium alloys being used in aircraft structural applications.

This fatigue crack propagation study was separated into two main tasks. The first task was determination of the influence of cyclic frequency on the fatigue crack growth behavior of this titanium alloy in the suspected most aggressive environment of those to be tested, here selected as 3.5 percent sodium chloride (NaCl) solution. This initial frequency screening was conducted using through-cracked wedge-opening-load (WOL) specimens. Based on these results, test frequencies for the second task were determined. In the second task, the influence of environment (laboratory air, dry air, high humidity, sump-tank water, and 3.5 percent NaCl solution), test frequency, hold time, orientation, and stress ratio on fatigue crack growth behavior was evaluated.

For these fatigue crack propagation tests, surface flaws were used as the main flaw geometry because of the frequency with which they are encountered in service problems. In addition, through-cracked, center-cracked tension (CCT) panels were also tested for comparison with the part-through-cracked (PTC) results to examine the effect of crack orientation within the parent material.

Material Characterization

Chemistry and Microstructure

The Ti-6Al-4V alloy was purchased in two product forms: 9.5 by 910 by 2440-mm (3/8 by 36 by 96-in.) plate as Heats K8732 and K9548, and 3.2 by 910 by 2440-mm (1/8 by 36 by 96-in.) plate as Heat 304616. Both materials were purchased to Rockwell International Specification ST0170LB00032, Revision B, for the RA condition, even though this normally does not include material less than 4.75 mm (0.187 in.) thick. The heat treatment sequence for the 9.5-mm (3/8-in.) material included heating at 954°C (1750°F) for 1½ h and air cooling. For the 3.2-mm (1/8-in.) material, a production anneal at 954°C (1750°F) for 1½ h, air-cool anneal at 760°C (1400°F) for 1 h, and air-cool heat treatment sequence were used. The chemical analysis results for plates from each heat of material is presented in Table 1.

The three-dimensional composite microstructural models from the surface and midplane of the 3.2-mm (1/8-in.) plate showed an equiaxed primary α microstructure separated by transformed β (acicular α). Approximately 85 percent of the microstructure consisted of primary α. A slight amount of banding was noted at the midplane of the plate. The three-

TABLE 1—*Chemical analysis of Ti-6Al-4V(RA) products by weight.*

	Heat	Al	V	Fe	C	O	N	H
9.52-mm (3/8-in.) plate	K8732	6.3	4.1	0.16	0.022	0.15	0.011	0.006
	K9548	6.4	4.0	0.14	0.026	0.13	0.014	0.010
3.8-mm (1/8-in.) plate	304616	6.1	4.0	0.19	0.020	0.14	0.013	0.010

dimensional models of the 9.5-mm (3/8-in.) plate showed equiaxed primary α separated by retained β at the grain boundary. A slight amount of banding also was noted at the midplane of this plate product.

Tensile and Fracture Toughness Properties

Flat tension specimens were machined from the 3.3- and 9.5-mm (1/8- and 3/8-in.) plates and tested in accordance with ASTM Tension Testing of Metallic Materials (E 8). Table 2 lists the average tensile results from various laboratories for the plates. Both heats showed strong directionality with the longitudinal direction having a higher strength. A section of the 9.5-mm (3/8-in.) plate was used for standard X-ray analysis to determine the crystallographic texture of the plate. The results showed a strong texture in the material, the basal hexagonal planes being oriented parallel to the rolling direction. This texture was consistent with the very high tensile strength in the transverse orientation and the significantly lower tensile strength in the longitudinal orientation.

TABLE 2—*Tensile results for Ti-6Al-4V(RA) materials.*

Product Form	Ultimate Tensile Strength, MPa (ksi)		Yield Strength 0.2% Offset, MPa (ksi)		Elongation, % in 50.8 mm (2 in.)
9.52-mm (3/8-in.) plate					
Heat K9548					
Longitudinal	911.5	(132.2)	827.4	(120.0)	12.9
Transverse	1082	(157.0)	999.7	(145.0)	15.0
Heat KB732					
Longitudinal	944.6	(137.0)	859.8	(124.7)	14.0
Transverse	1061	(153.9)	957.7	(138.9)	14.0
3.18-mm (1/8-in.) plate					
Longitudinal	1071	(155.3)	1019	(147.8)	10.3
Transverse	1079	(156.5)	1029	(149.2)	11.0

Fatigue Crack Propagation Test Procedures

Three specimen geometries were used in this fatigue crack propagation study: the WOL specimen (Fig. 1), used for frequency screening tests; the PTC specimen (Fig. 2), used for the majority of the tests; and the CCT specimen (Fig. 2), used as a secondary specimen geometry. Stress intensities for the WOL geometry were calculated using the typical equation for WOL coupons [4]. For PTC specimens, stress intensity was computed using the equation of Irwin [5]. No back surface correction was used for basic analysis of the surface flaw due to the large number of proposed

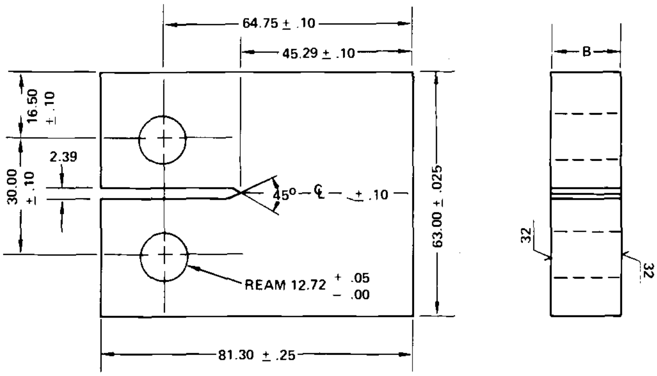

(All Dimensions in mm)

FIG. 1—*WOL specimen configuration.*

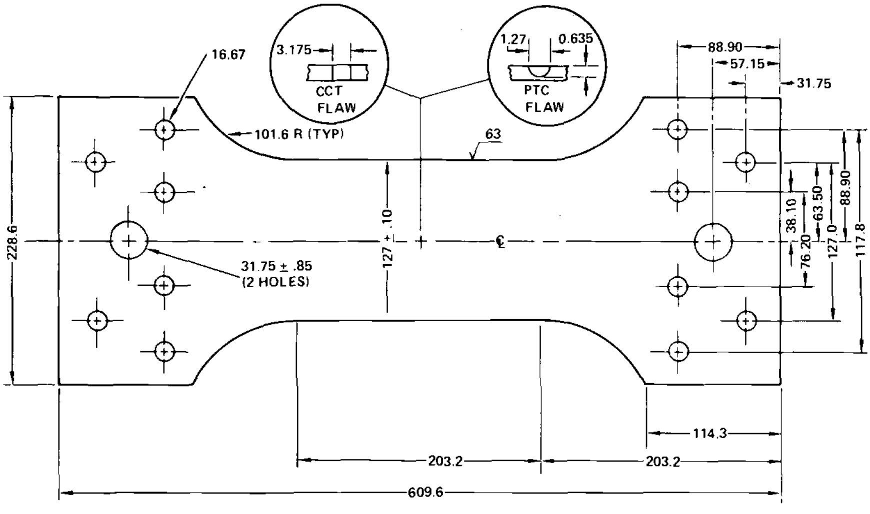

(All Dimensions in mm)

FIG. 2—*PTC and CCT specimen configuration.*

corrections available, none of which have been shown to be applicable for fatigue crack propagation studies over a range of materials and testing conditions. For the range of crack lengths used in the majority of this program, a maximum 10 percent difference in K would have resulted from applying a correction factor, and, in general, the difference would be much less than 10 percent. The CCT specimen geometry was the same as that for the PTC specimen with the exception of the starter crack which was a 3.18-mm (1/8-in.)-diameter slotted hole in the center of the panel. For CCT specimens, stress intensity was computed using the equation of Federson [*6*].

Prior to testing, all specimens were fatigue precracked at 20 Hz at a load ratio of $R = +0.1$ in laboratory air. Loads were stepped down such that the final 0.5 mm (0.020 in.) of growth occurred at a maximum stress intensity equal to that at which subsequent testing was to be started. All precracking and fatigue crack propagation tests were conducted in closed-loop electrohydraulic testing machines. Each machine was equipped with peak and valley detectors which controlled the load to ±1 percent on both the maximum and minimum loads, any excedance of these levels resulting in a dumping of the load signal to zero and the sounding of an alarm. The test waveform used was the sine wave.

All of the fatigue crack propagation tests were conducted at room temperature 22 ±2°C (72 ±5°F) in controlled environments. These environments were:

laboratory air	laboratory air at 40 ±10 percent relative humidity
dry air	10 percent or less relative humidity obtained by enclosing the specimen in a moisture-proof container with freshly dried desiccant as per Military Specification for Desiccants, Activated, Bagged, Packaging Use and Static Dehumidification (MIL-D-3464D, Type I)
high humidity	environment of ≥85 percent relative humidity achieved by bubbling argon gas through distilled water
sump tank residue water	sump tank residue water [*7*] consisting of distilled water with the following additions (±1%): $CaCl_2$ 50 ppm; $CrCl_3\cdot 6H_2O$ 1 ppm $CdCl_2$ 1000 ppm; $CuCl_3\cdot 2H_2O$ 1 ppm $HgCl_2$ 50 ppm; $FeCl_3$ 5 ppm NaCl 100 ppm; $MnCl_2\cdot 4H_2O$ 5 ppm $ZnCl_2$ 10 ppm; $NiCl_2\cdot 6H_2O$ 1 ppm $PbCl_1$ 1 ppm
3.5 percent NaCl solution	solution made by adding NaCl to deionized water such that a 3.5 percent NaCl solution was achieved.

The environments were circulated around the entire crack region of each specimen. The high humidity environment was contained by placing a clear plastic bag around the entire crack region of the specimen. A chamber formed of silicon rubber and clear glass was installed around the crack for the 3.5 percent NaCl liquid environment. The 3.5 percent NaCl solution was circulated continuously past the crack region at the rate of 7.886 × 10^{-3} m^3/s (0.008 gal/min).

Crack length measurements were made on the front surface of the PTC specimen until crack breakthrough occurred and on front and back surfaces of the WOL and CCT specimens. Crack lengths were measured to ±0.0254 mm (±0.001 in.) using a toolmaker's microscope and appropriate illumination. For PTC specimens, the maximum stress ratio was lowered periodically for 0.5 mm (0.02 in.) of growth to mark the crack length. Following completion of each test, the specimen was fractured and correlations made between surface crack length, $2C$, and corresponding crack depth, a, as measured from fracture surface markings. Fracture surfaces of all specimens were sprayed with a clear plastic lacquer subsequent to failure to preserve the fracture surface for subsequent fractography.

All data analyses were performed by computer programs using as input measured $2C$ values as determined from the fracture surface markings for each specimen. The computer analysis computed incremental crack growth tensity expressions for each specimen type. Crack-depth values for PTC specimens were computed by hand, based on the correlation of $a/2C$ versus measured $2C$ values as determined from the fracture surface markings for each specimen. The computer analysis computed incremental crack growth rates, da/dN or dC/dN depending on specimen type, and stress intensity parameters at average crack length in the specific crack length interval. A tabulation of the results was printed out and a plot of da/dN or dC/dN versus the alternating stress intensity factor, ΔK, printed.

Results

The experimental variables studied included environment, frequency, orientation, stress ratio, and microstructure. The test matrix is summarized in Table 3. Results of these tests are discussed in the following subsections. In the figures which accompany these subsections, smooth curves through the data are shown to aid in visualizing trends. Specific data points for each coupon are plotted in Ref *3*. Trend curves were used because the large number of data points per coupon would have unnecessarily cluttered the graphs. The data scatter for each coupon was generally quite small as indicated for some of the data sets in Fig. 3.

Environment/Frequency Effects

Results of frequency screening tests in 3.5 percent NaCl solution using

TABLE 3—*Summary of fatigue crack propagation tests for Ti-6Al-4V(RA) material.*

	Environment					Test Frequency, Sine Wave, Hz			Hold Time, Trapezoidal Wave			Orientation				Stress Range	
Material Specimen Geometry	Dry Air	Lab Air	High Humidity	Sump-Tank Water	3.5% NaCl	0.1	1	10	½ min	1 min	5 min	WR	WT	RT	RW	0.1	0.5
9.5-mm (3/8-in.) plate																	
WOL		X		X	X	X	X	X	X	X	X	X				X	
CCT			X		X	X		X				X				X	X
PTC	X		X		X	X	X	X					X	X		X	X
3.2-mm (1/8-in.) plate																	
CCT		X			X	X		X				X			X	X	X

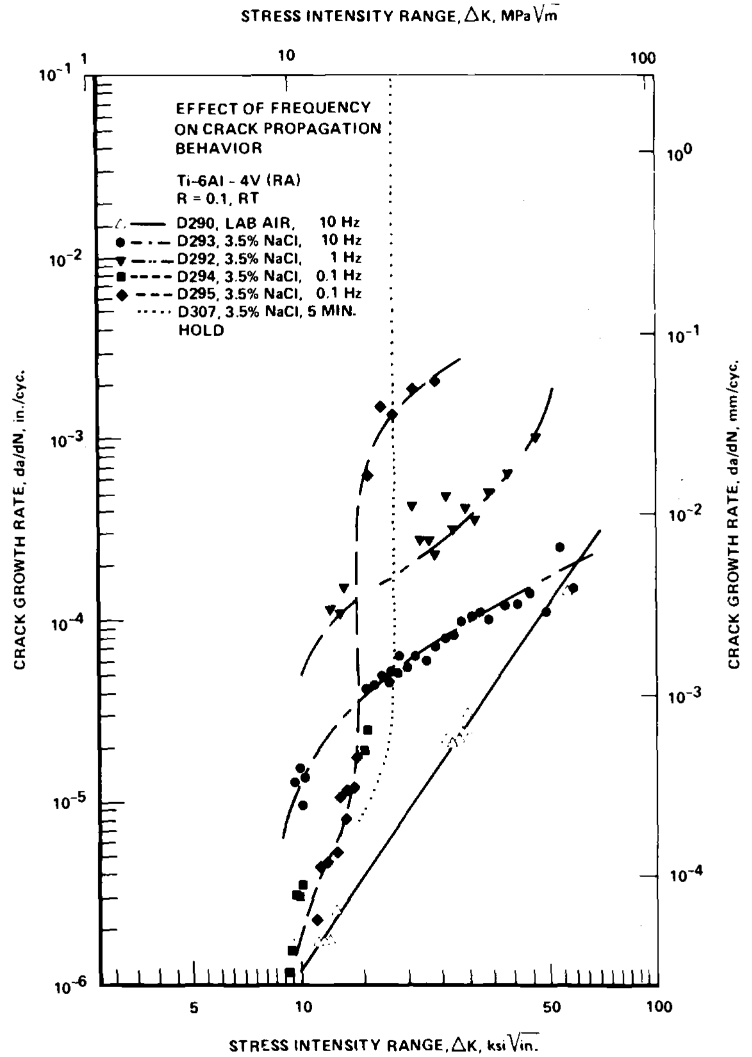

FIG. 3—*Frequency screening results for 9.5-mm (3/8-in.) Ti-6Al-4V(RA) WOL specimens, R = 0.1, WR orientation, in 3.5 percent NaCl.*

WR oriented WOL specimens from the 9.5-mm (3/8-in.) plate are presented in Fig. 3. A strong influence of the 3.5 percent NaCl solution environment, primarily at midrange, was observed at 10 Hz when compared with the laboratory air 10-Hz results. As the frequency was lowered from 10 to 1 Hz in 3.5 percent NaCl solution, the crack growth rate increased by a factor of 4 to 10 above the 10-Hz 3.5 percent NaCl solution results. At a frequency of 0.1 Hz, rapid acceleration of *da/dN* was observed at

$\Delta K \sim$ 17.6 MPa $\sqrt{m}$ (16 ksi $\sqrt{in.}$). This effect was similar to that noted previously for Ti-6Al-6V-2Sn in the solution treated and overaged (STOA) condition [*8, 9*]. There was, however, some indication of a leveling off of the rates at ~5.08 × 10^{-5} m/cycle (2 × 10^{-3} in./cycle) for ΔK >22 MPa $\sqrt{m}$ (20 ksi $\sqrt{in.}$).

The 0.1-Hz curve in 3.5 percent NaCl solution crossed below the 10-Hz 3.5 percent NaCl solution curve at low ΔK values and exhibited fatigue crack growth rates which approached the 10-Hz air results. Introduction of a 5-min hold-time trapezoidal wave in 3.5 percent NaCl solution showed a similar result to that of the 0.1-Hz test, without any evidence of a leveling off of rates above $\Delta K \sim 22$ MPa $\sqrt{m}$ (20 ksi $\sqrt{in.}$). For the trapezoidal waveform, rapid acceleration in *da/dN* occurred at $\Delta K \sim$ 10.8 MPa $\sqrt{m}$ (18 ksi $\sqrt{in.}$), a small difference probably due to material variations from specimen to specimen. In essence, the hold-time curve was nearly vertical.

When frequency screening was conducted in sump-tank water, the results shown in Fig. 4 were obtained. Again the crack growth rates increased with decreasing frequency. The rates in sump-tank water at each frequency were generally lower than the comparable rates in 3.5 percent NaCl solution, as shown in Fig. 5. However, when a trapezoidal waveform was applied with a hold time at maximum load varying from 0.5 to 5 min, see Fig. 4, the sump-tank water crack growth rates exhibited rapid acceleration at $\Delta K \sim 18.7$ MPa $\sqrt{m}$ (17 ksi $\sqrt{in.}$), similar to those observed in 3.5 percent NaCl solution.

The similarity of the sump-tank water hold-time data (the results of hold time from 0.5 to 5 min were identical) with the 3.5 percent NaCl solution 0.1 Hz and hold-time results is shown in Fig. 6. This excellent agreement showed that while sump-tank water was somewhat less aggressive then 3.5 percent NaCl solution at higher frequencies (0.1 to 10 Hz) the effect of sump-tank water was equivalent to that of 3.5 percent NaCl solution at lower frequencies. As a result, 3.5 percent NaCl solution test conditions may provide a realistic screening test where real-time frequencies must be considered for structures in which sump-tank water or other environments might be contacted.

Results of tests on CCT specimens (WR orientation) of 9.5-mm (3/8-in.) material are presented in Fig. 7. The 10-Hz results for the CCT specimen agreed well with the previous 10-Hz data from the WOL specimens. Rapid acceleration of the 0.1-Hz data was noted again for CCT specimens and, while occurring at a lower level of $\Delta K \sim 11$ MPa $\sqrt{m}$ (10 ksi $\sqrt{in.}$) than for WOL specimens, the data exhibited previously observed trends.

Center-cracked tension specimen results for 3.2-mm (1/8-in.) sheet material showed no difference in results between the WR and RW orientations at 10 Hz in either high humidity or 3.5 percent NaCl solution. Results at 0.1 Hz in 3.5 percent NaCl solution showed previously established trends, although the rapid acceleration region did not occur until $\Delta K \sim$

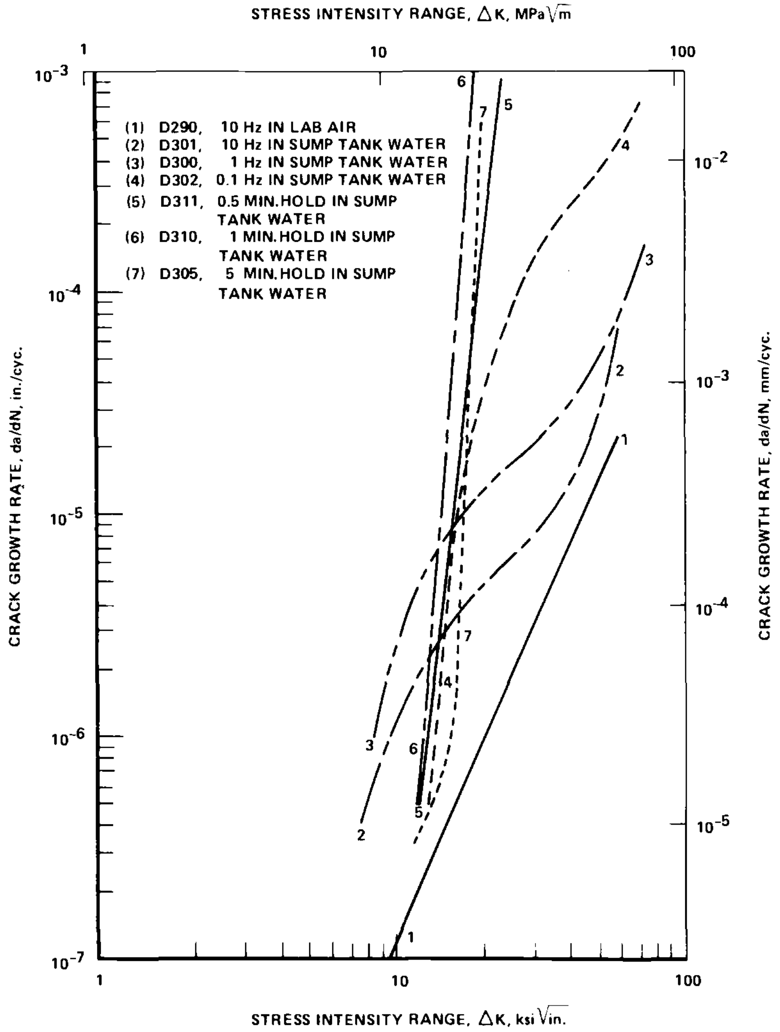

FIG. 4—*Frequency screening results for 9.5-mm (3/8-in.) Ti-6Al-4V(RA) WOL specimens,* R = *0.1, WR orientation, in sump-tank water.*

28.6 MPa $\sqrt{m}$ (26 ksi $\sqrt{in.}$). A comparison with the 9.5-mm (3/8-in.)-CCT specimen results, Fig. 8, showed that 10-Hz 3.5 percent NaCl solution results were quite similar for the two thicknesses, while at 0.1 Hz, the 9.5-mm (3/8-in.)-thickness rates were substantially higher. The 9.5-mm (3/8-in.) thickness had lower crack growth rates than the 3.2-mm (1/8-in.) material at 10 Hz in high humidity for ΔK $\sqrt{17.6}$ MPa $\sqrt{m}$ (16 ksi $\sqrt{in.}$).

Results of the 9.5-mm (3/8-in.) PTC specimens (WT orientation) showed

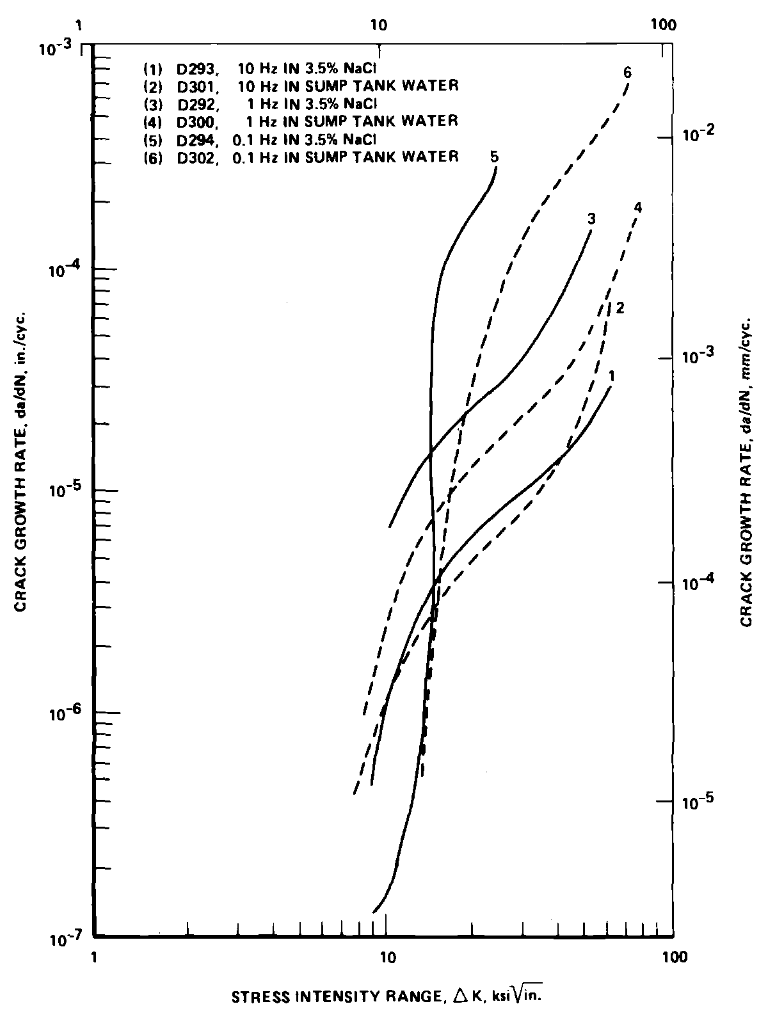

FIG. 5—*Effect of environment on fatigue crack growth behavior of 9.5-mm (3/8-in.) Ti-6Al-4V(RA) WOL specimens,* R = *0.1, WR orientation.*

only a small effect on crack growth rate due to changes in frequency from 10 to 0.1 Hz in the high humidity environment. However, as frequency was lowered in the 3.5 percent NaCl environment, large increases in fatigue crack growth rate were observed. At 0.1 Hz in 3.5 percent NaCl solution, rapid *da/dN* acceleration occurred between $\Delta K \sim 11$ to 19.8 MPa $\sqrt{m}$ (10 to 18 ksi $\sqrt{in.}$). Comparisons of 9.5-mm (3/8-in.)-PTC data (WT orientation) with the 9.5-mm (3/8-in.)-CCT data (WR orientation) are shown in Fig. 9. Figure 9 shows a good agreement between tests run on different

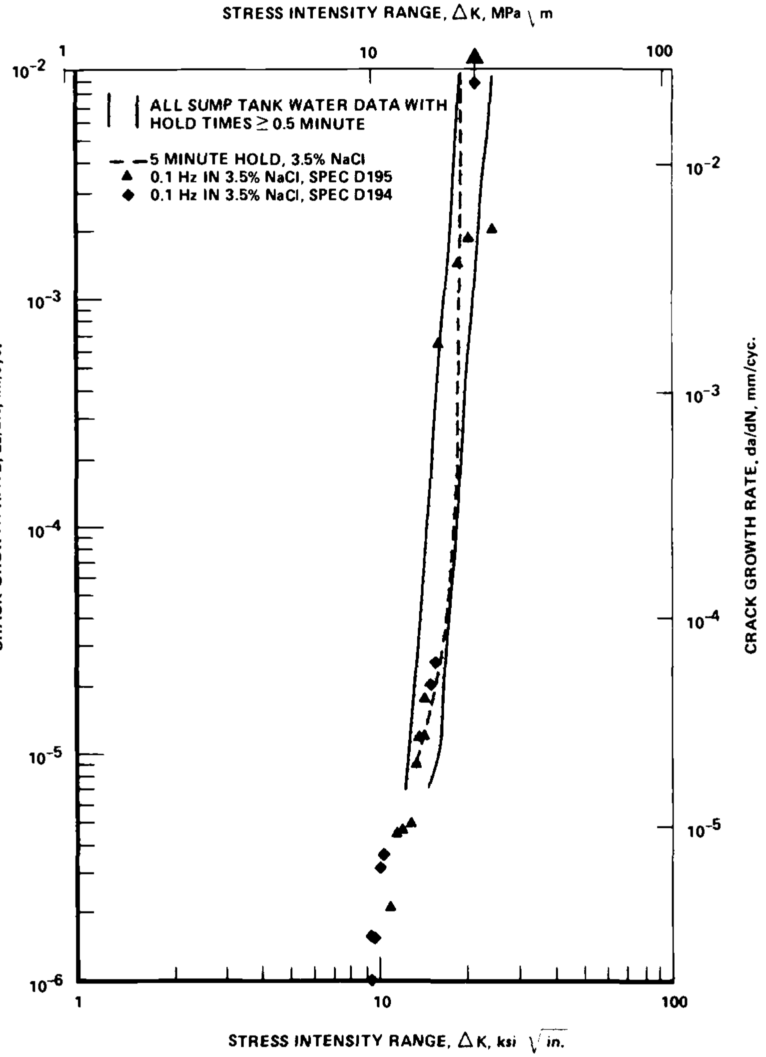

FIG. 6—*Comparison of sump-tank water and 3.5 percent NaCl test results for 9.5-mm (3/8-in.) Ti-6Al-4V(RA) WOL specimens,* R = *0.1 WR orientation.*

specimen and flaw geometries in similar environments. A comparison of results for 9.5-mm (3/8-in.)-PTC specimens in WT and RT orientations showed that the growth rates were nearly the same when tested at 10 Hz in high humidity, but the WT orientation was more susceptible to corrosion fatigue when tested in 3.5 percent NaCl.

One of the PTC specimens (D 56) showed an unexpected decrease in *da/dN* at high ΔK values. This decrease was due to a rapid change in

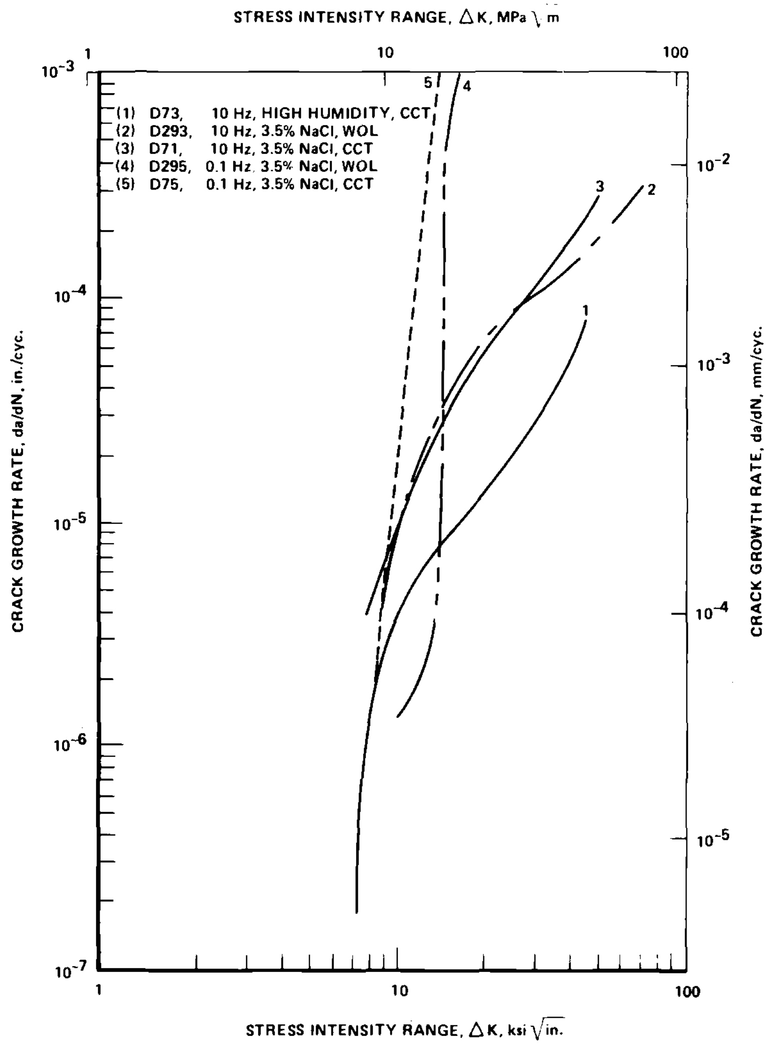

FIG. 7—*Frequency screening results for 9.5-mm (3/8-in.) Ti-6Al-4V(RA) CCT and WOL specimens,* R = *0.1, WR orientation.*

crack shape at high ΔK values. This was observed in highly aggressive environments or in low frequency tests where the surface crack growth rate begins to accelerate faster than the growth in the crack depth. As a result the *a/2C* ratio decreased markedly during this time even though the crack length was growing rapidly, particularly on the surface, and resulted in a slowing of the *da/dN* rate, that is, the crack depth growth rate. This behavior was indicative of a lower resistance to the corrosion fatigue process in the WR direction as compared to the WT direction.

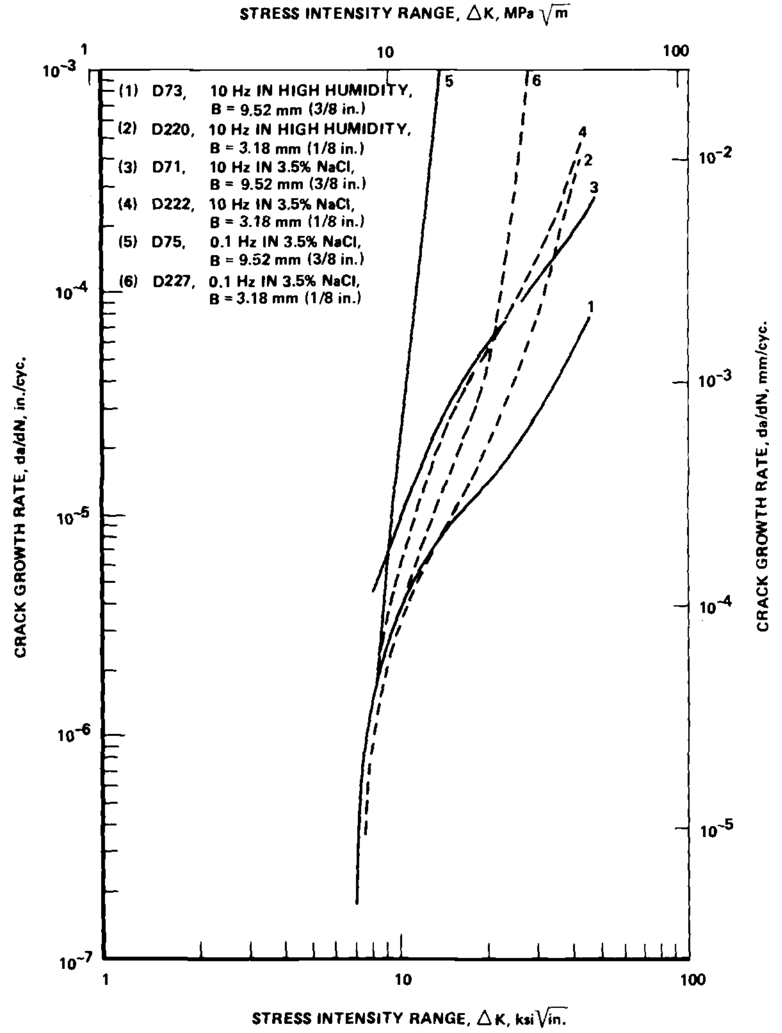

FIG. 8—*Effect of thickness on fatigue crack propagation results for T-6Al-4V(RA) CCT specimens,* R = *0.1, WR orientation.*

Stress Ratio Effects

Figure 10 shows typical stress ratio results for 9.5-mm (3/8-in.) Ti-6Al-4V(RA) CCT panels (WR orientation). For the 9.5-mm (3/8-in.) material, the effect on crack growth rate of changing the stress ratio from +0.1 to +0.5 followed trends observed in other titanium alloys [*8-11*]. At R = +0.5, the 10-Hz curves in high humidity and 3.5 percent NaCl solution showed a significant increase in crack growth rate at high and low ΔK

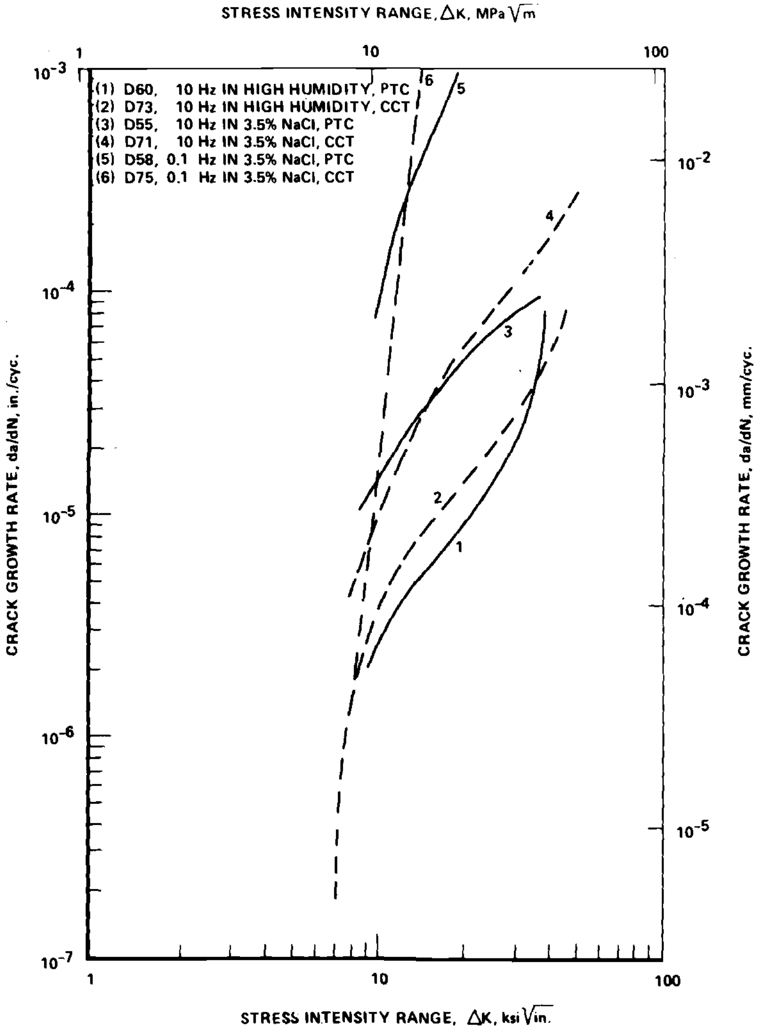

FIG. 9—*Comparison of PTC and CCT fatigue crack propagation results for 9.5-mm (3/8-in.) Ti-6Al-4V(RA),* R = *0.1.*

levels when compared to $R = +0.1$ data, the effect being somewhat less at intermediate ΔK levels. The 3.2-mm (1/8-in.)-thickness results also showed the same effect of stress ratio. Virtually no effect of stress ratio in the range $9.9 \leq \Delta K \leq 16.5$ MPa $\sqrt{m}$ ($9 \leq \Delta K \leq$ 15 ksi $\sqrt{in.}$) was observed. However, increasingly large effects occurred as ΔK decreased or increased beyond this range. In general, the effect of stress ratio on crack growth rate in 3.2-mm (1/8-in.)-thick panels was less than that observed in 9.5-

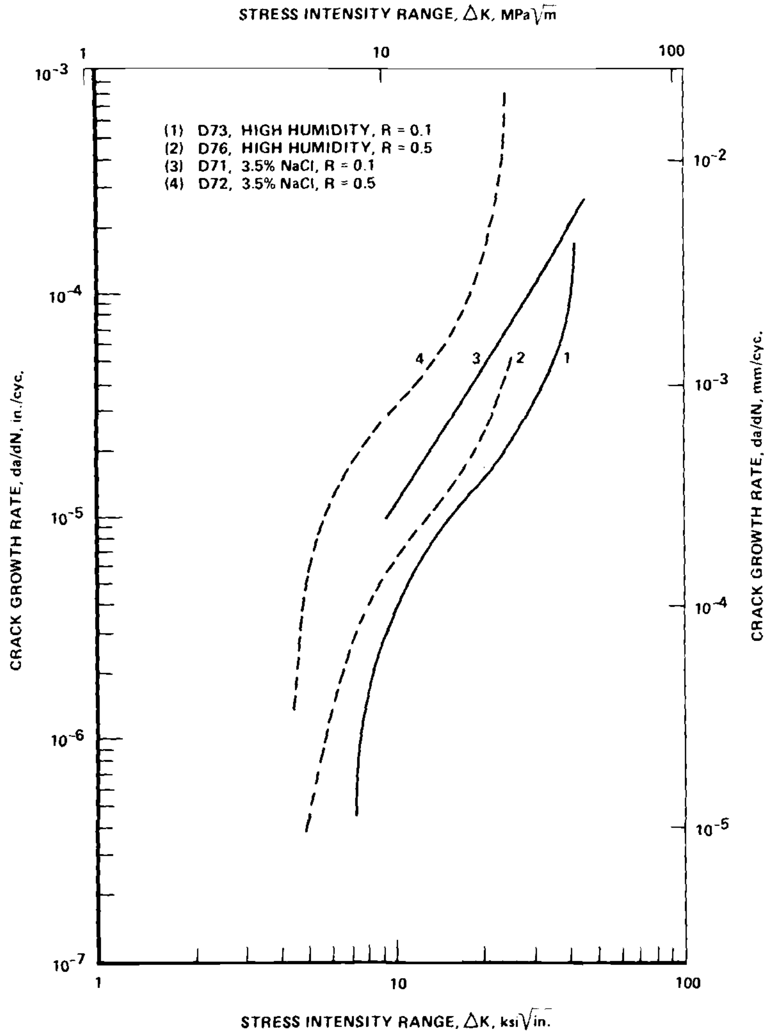

FIG. 10—*Effect of stress ratio on 9.5-mm (3/8-in.) Ti-6Al-4V(RA) CCT specimens at 10 Hz, WR orientation.*

mm (3/8-in.) panels. No difference was observed between WR and RW orientations for the 3.2-mm (1/8-in.) material.

Results of 9.5-mm (3/8-in.)-PTC specimens of Ti-6Al-4V(RA) (WT orientation) were more difficult to interpret than the previous through-the-thickness crack data. As shown in Fig. 11, 10-Hz 3.5 percent NaCl solution data showed a marked deceleration in *da/dN* at high *ΔK* levels. As previously discussed, this was due to the rapid change in crack shape, the *a/2C* ratio sometimes changing from 0.45 to 0.3 in this region. As a result

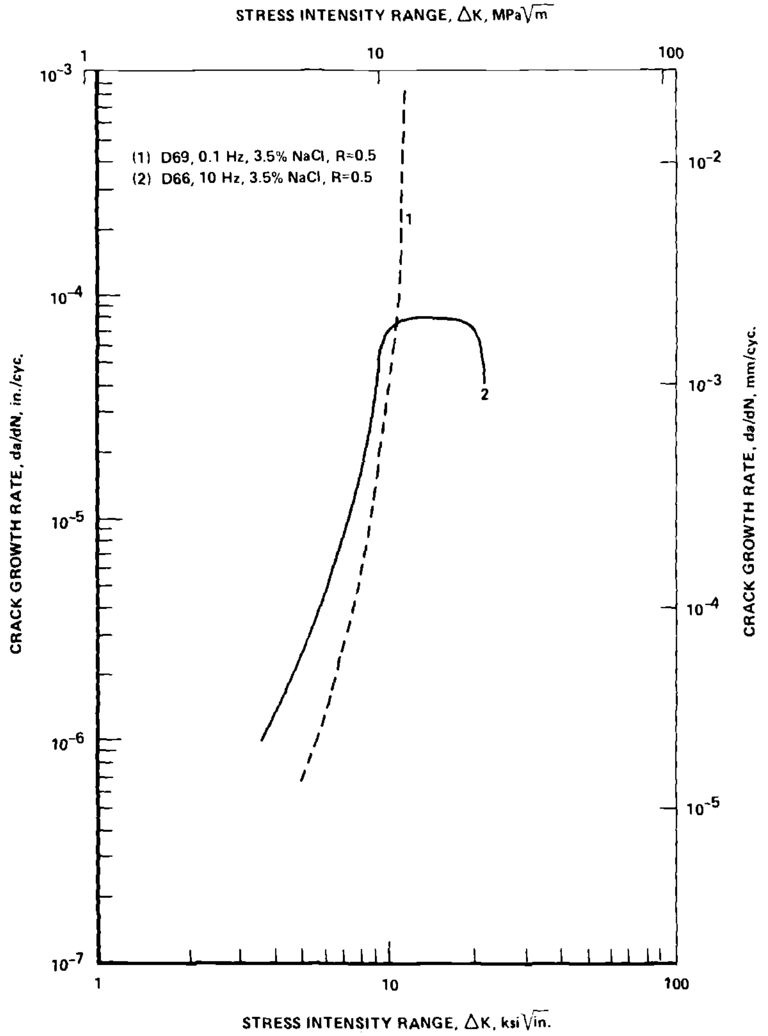

FIG. 11—*Fatigue crack propagation results for 9.5-mm (3/8-in.) Ti-6Al-4V(RA) PTC specimens,* R = *0.5 in 3.5 percent NaCl, WT orientation.*

the *dC/dN* versus ΔK plot was examined for these three specimens. The resulting curves agreed reasonably well with the CCT results, as would be expected since both measurements were in the WR orientation. This would indicate a greater susceptibility to corrosion-fatigue crack growth in the WR direction as compared to the WT orientation. Whether this effect is due to a back surface interaction with environment or a material effect remains unknown.

Discussion

This fatigue crack propagation study showed the same general frequency effect in 3.5 percent NaCl solution as observed in other titanium alloys [*8-11*]. Application of a trapezoidal waveform with a 5-min hold time in 3.5 percent NaCl solution resulted in a similar curve to that of the 0.1-Hz 3.5 percent NaCl solution results. This indicated that the detrimental effect of the 3.5 percent NaCl solution essentially had saturated at 0.1 Hz.

In sump-tank water, a frequency effect, similar to but less severe than that noted in 3.5 percent NaCl solution, was observed. The application of a trapezoidal wave with hold times from 0.5 to 5 min yielded a common curve for all hold time tests in this range; the hold-time results in sump-tank water corresponding to the same curve as the 5-min hold time results in 3.5 percent NaCl solution. These results indicated that, while the crack propagation rates in sump-tank water at a given test frequency were lower than in 3.5 percent NaCl, the effect of both environments saturated to a common lower bound. The only difference was that the 3.5 percent NaCl solution effect saturated at ~0.1 Hz while hold times ≥0.5 min were required to saturate the effect of sump-tank water.

At slow frequencies in detrimental environments (including high humidity), this alloy showed a frequency effect typified by a crossover at low ΔK levels of the slow frequency (0.1 Hz) *da/dN* curve with the 10 Hz *da/dN* data in the same environment. As a result, the ΔK level at which a rate of 2.54×10^{-3} mm/cycle (1×10^{-5} in./cycle) occurred was at a significantly high ΔK value for 0.1 Hz than for 10 Hz. This effect was discussed in detail in Ref *3* and also was reported by Dawson and Pelloux [*12*]. Kraft has suggested a physical explanation of this cross-over effect [*13*] and used the data of Ref *14* for Ti-6A1-4V(RA) material to support his conclusion. Essentially, to quote Kraft [*13*], the effect of frequency and environment on crack propagation is analyzed as a special case of the tensile ligament instability model. The model is discussed further by Kraft in Ref *15*.

Fractographic studies were conducted to determine the causes of the instability in crack growth which occurred at the lower frequencies in sump-tank water and 3.5 percent NaCl. These studies showed that at 10 Hz in laboratory air and 3.5 percent NaCl, the fracture surfaces were dominated by ductile rupture. At low frequency in both sump-tank water and 3.5 percent NaCl, the crack growth instability region had much larger amounts of cleavage than the earlier lower rate regions. The transition region between a relatively stable crack growth region of rates 2.5×10^{-7} to 2.5×10^{-6} m/cycle (10^{-5} to 10^{-4} in./cycle) to one where rates exceeded 10^{-4} m/cycles (10^{-2} in./cycle) was extremely abrupt. In general, the Ti-6A1-4V(RA) alloy fracture morphology showed increasingly large amounts of cleavage at higher rates.

To investigate further the causes of the instability in crack growth rate at low frequencies in saltwater and sump-tank water, transmission electron microscope (TEM) fractographs and metallographic sections of representative specimens were taken. Four regions of a low-frequency specimen were examined from just before the instability region to the region just prior to fracture. The fractographs showed that in each region striations, ductile rupture, and cleavage were observed. As expected, the fatigue striation spacing increased as the crack growth rate increased. The increasing amount of cleavage corresponded to the observed large jump in crack growth rates at a relatively low ΔK.

Metallographic sections were taken perpendicular to the crack at three regions along the crack-fracture line. As the crack progressed, the fracture plane remained smooth until, abruptly, a transition occurred; the crack growth rates greatly accelerated, and the crack front became rough with large secondary cracks. The presence of large secondary cracks below the main fracture surface was noted. The features for the high growth rate regions were typical of high growth rate regions, but the large amounts of secondary cracking, rough fracture surface, and accompanying rates usually are associated with a high ΔK, not the relatively low ΔK at which the transition in behavior occurred. No apparent intrinsic material changes occurred in the transition region, the cause of the abrupt rate change apparently being associated with the increased tendency for cleavage to occur. This behavior has also been observed elsewhere [*16*].

The type of secondary cracking observed in corrosion fatigue is similar to that observed by Cowgill et al [*17*] for stress corrosion of Ti-8Al-1Mo-1V where secondary cracking along the α-β interface and in the coarse α also occurred. These results are consistent with other work which showed that in typical α-β alloys, transgranular cleavage normally occurs in the α phase [*18-20*] on or near the *(0001)* planes [*17*] and occasionally at the α-β interface [*17-21*]. The effect of the microstructural parameters that have been observed indicates that the acicular α microstructure has better resistance to corrosion fatigue cracking than larger equiaxed α microstructures. This is believed to be due to smaller α particle size which requires additional cleavage cracks to be developed to extend the primary crack a given increment. However, the effectiveness of the acicular microstructure is also dependent on the strength and characteristics of the β matrix material.

One can hypothesize that the instability in growth rate was caused by exceeding some externally induced energy threshold. This energy threshold might be reached by the input of a large amount of mechanical driving force (that is, high ΔK) or by environmental/mechanical attack and interactions at low ΔK levels provided that frequencies are low enough to allow sufficient time for the environmental degradation to occur. This would explain the instabilities in crack rate observed at low frequencies in aggressive environments and also why the rates under hold-time conditions in sump-tank water were about the same as those in 3.5 percent NaCl solution at 0.1-Hz and 5-min hold times.

Summary and Conclusions

Results of fatigue crack propagation tests showed a strong frequency effect in 3.5 percent NaCl solution. An unexpected instability in crack growth rate at low ΔK and low frequency was observed. The application of a trapezoidal waveform with a 5-min hold time in 3.5 percent NaCl resulted in a curve similar to that of the 0.1-Hz 3.5 percent NaCl solution results. This indicated that the detrimental effect of the 3.5 percent NaCl solution essentially saturated at ~0.1 Hz.

In a sump-tank water, a frequency effect similar to but less severe than that noted in 3.5 percent NaCl solution was observed. The application of a trapezoidal wave with hold times from 0.5 to 5 min yielded a common curve. These hold-time results in sump-tank water were essentially the same as the 5-min hold time and the 0.1-Hz sine wave 3.5 percent solution results. The crack propagation rates in sump-tank water at a given test frequency were lower than in 3.5 percent NaCl solution, but the effect of both environments saturated at a common lower bound. The only difference was that the 3.5 percent NaCl solution effect saturated at ~0.1 Hz while hold times $\geq$0.5 min were required to saturate the effect of sump tank water.

Stress ratio effects were typical in that crack growth rate increased at higher R ratios. The $R = 0.5$ results showed a significant effect of environment.

Fractographic examination (scanning electron microscope (SEM)) and metallographic sections of specimens tested in 3.5 percent NaCl solution at 0.1 Hz showed a macroscopically smooth fracture with fine striations mixed with some ductile tear at low crack growth rates. As the rates accelerated, the surface became much rougher macroscopically with a rapid increase in the amount of cleavage and secondary cracking, some of which occurred away from the main crack. In general, the observations were similar to those observed for a Ti-6A1-6V-2Sn(STOA) [8,9] where rapid acceleration in rates was associated with cracking by cleavage in the α phase and along the α-β interface.

Acknowledgments

This report is based on part of the results of a contract, No. AF33615-71-C-1688 supported by the U.S. Air Force, Air Force Materials Laboratory, Wright-Patterson Air Force Base, Ohio.

References

[*1*] Hardrath, H. F., "Fatigue and Fracture Mechanics," AIAA Paper 70-512, American Institute of Aeronautics and Astonautics, Denver, Colo., 1970.

[*2*] Hinders, U. A., "F-111 Design Experience—Use of High Strength Steel," AIAA Paper 70-884, American Institute of Aeronautics and Astronautics, Los Angeles, Calif., 1970.

[*3*] Pettit, D. E., Ryder, J. T., Krupp, W. E., and Hoeppner, D. W., "Investigation of the Effects of Stress and Chemical Environments on the Prediction of Fracture in Aircraft Structural Materials," Technical Report AFML-TR-74-183, Air Force Materials Laboratory, Dec. 1974.

[*4*] Wessel, E. T., *Engineering Fracture Mechanics,* Vol. 1, 1968, pp. 77-101.

[*5*] Irwin, G. R., *Journal of Applied Mechanics,* Vol. 85, 1962, pp. 651-654.

[*6*] Federson, G. E., "Discussion of Calibration Factors," *Plane Strain Crack Toughness Testing of High-Strength Metallic Materials, ASTM STP 410,* American Society for Testing and Materials, 1969, pp. 77-79.

[*7*] Harrigan, M. J., "Fatigue Crack Growth Rate Testing," Specification Number LB0169-004, North American Rockwell, Los Angeles Division, 6 Dec. 1971.

[*8*] Krupp, W. E., Ryder, J. T., Pettit, D. E., and Hoeppner, D. W. in *Flaw Growth and Fracture, ASTM STP 631,* American Society for Testing and Materials, 1977, pp. 344-364.

[*9*] Pettit, D. E., Ryder, J. T., Krupp, W. E., and Hoeppner, D. W., *Proceedings,* Second International Conference on Mechanical Behavior of Materials, American Society for Metals, Boston, Mass., 16-20 Aug. 1976, pp. 680-684.

[*10*] Blackburn, M. J., Feeney, J. A., and Beck, T. R. in *Advances in Corrosion Science and Technology,* M. G. Fontana and R. W. Staehle, Eds., Vol. 2, Plenum Press, 1972.

[*11*] Hall, L. R., Finger, R. W., and Spurr, W. F., "Corrosion Fatigue Crack Growth in Aircraft Structural Materials," AFML-TR-73-204, Air Force Materials Laboratory, 1973.

[*12*] Dawson, D. B. and Pelloux, R. M., *Metallurgical Transactions,* Vol. 5, March 1974, pp. 723-731.

[*13*] Kraft, J. M., *Transactions,* American Society of Mechanical Engineers, *Journal of Engineering Materials and Technology,* Vol. 96, Series H, No. 4, Oct. 1974, pp. 275-282.

[*14*] Pettit, D. E., Krupp, W. E., Ryder, J. T., and Hoeppner, D. W., "Investigation of the Effects of Stress and Chemical Environments on the Prediction of Fracture in Aircraft Structural Materials," Report LR 26026, Lockheed-California Company, July 1973.

[*15*] Kraft, J. M., "Method for Relating Plastic Flow Properties to Fatigue Crack Propagation Including Effects of Stress Ratio," NRL Memorandum Report 2980, Naval Research Laboratory, Jan. 1975.

[*16*] Krupp, W. E., Hoeppner, D. W., and Walker, E. K. in *Corrosion Fatigue,* NACE-2, National Association of Corrosion Engineers, Houston, Tex., 1972, p. 468.

[*17*] Cowgill, D. S., Fritzen, J. S., Krystkowiak, S., and Weber, K. W., "Crack Morphology Studies in the Ti-8Al-1V-1Mo Alloy," paper presented at American Society for Testing and Materials/Advanced Research Projects Agency Symposium on Stress Corrosion and Corrosion Principles, Atlanta, Ga., 1968.

[*18*] Curtix, R. W. and Spurr, W. F., *Transactions,* American Society for Metals, Vol. 61, 1968, pp. 115-127.

[*19*] Powell, D. T. and Scully, J. C. in *The Science, Technology, and Application of Titanium,* Pergamon Press, New York, 1968, pp. 247-256.

[*20*] Faber, D. N. and Spurr, W. F. in *The Science, Technology, and Application of Titanium,* Pergamon Press, New York, 1968, pp. 259-626.

[*21*] Piper, D. E., Smith, S., and Carter, G. C., *Metals Engineering Quarterly,* Vol. 8, No. 3, Aug. 1968, p. 50.

H. P. Chu[1] *and J. G. Macco*[1]

Corrosion Fatigue of 5456-H117 Aluminum Alloy in Saltwater

REFERENCE: Chu, H. P. and Macco, J. G., "**Corrosion Fatigue of 5456-H117 Aluminum Alloy in Saltwater,**" *Corrosion-Fatigue Technology, ASTM STP 642,* H. L. Craig, Jr., T. W. Crooker, and D. W. Hoeppner, Eds., American Society for Testing and Materials, 1978, pp. 223–239.

ABSTRACT: Fatigue behavior of 5456-H117 aluminum alloy has been studied by fracture mechanics and conventional test methods in air and saltwater environments. The results show that fatigue resistance of the alloy is reduced greatly by the presence of saltwater at low stress or stress intensity levels. Test data of smooth and precracked specimens are combined and discussed with regard to failure predictions.

KEY WORDS: corrosion fatigue, crack propagation, fractures (materials), failure, fatigue tests, stress ratio, *S-N* diagrams, Goodman diagram, aluminum alloys

The 5456 aluminum alloy is a popular choice for marine applications due to its high resistance to stress corrosion and other desirable attributes. When used in building naval or commercial ships, it also should have adequate fatigue properties to sustain repeated loads. This paper summarizes the results of recent studies on fatigue behavior of the 5456-H117 alloy, including high-cycle and low-cycle fatigue as well as crack growth in air and saltwater environments.

Experimental Procedure

Material

The material studied was standard 5456 aluminum alloy in the H117 temper. This is a new temper which is included in Interim Federal Specification on Aluminum Alloy 5465, Plate and Sheet for Seawater Applications

---

[1] Metallurgist and mechanical engineer, David W. Taylor Naval Ship Research and Development Center, Annapolis, Md. 21402.

(QQ-A-00250/20). The alloy was tested in the form of rolled plates in three section thicknesses as follows.

Fatigue Test	Plate Thickness, in. (m)
High cycle	1/4 (0.635×10^{-2})
Low cycle	1 (2.54×10^{-2})
Crack growth	7/16 (1.111×10^{-2})

In a supplementary experiment, a 1/4-in.-thick plate of 5086-H116 alloy, as specified in Interim Federal Specification on Aluminum Alloy 5086, Plate and Sheet for Seawater Applications (QQ-A-00250/19), was also tested in high-cycle fatigue. The nominal chemical composition and typical mechanical properties of these alloys are listed as follows.

Alloy	Mg	Mn	Cr	Al	Tensile Strength, ksi (MPa)	0.2% Yield Strength, ksi (MPa)	% Elongation, 2 in. (5.1×10^{-2} m)
5456-H117	5.25	0.8	0.1	balance	51 (351.9)	37 (255.3)	19
5086-H116	4.00	0.45	0.1	balance	46 (317.4)	30 (207.0)	22

All the materials were obtained from commercial sources and tested in the as-received condition.

Tests

High-cycle fatigue data were developed from cantilever-beam tests. Cyclic loading was provided by Tatnall-Krouse plate-fatigue machines at a speed of 2000 cycles per minute (cpm) (33.33 Hz). The specimens were tested under constant deflection condition for three stress ratios: complete reversal ($R = -1$), zero to tension ($R = 0$), and tension to tension ($R = 1/3$). When tested for corrosion fatigue, the specimens were immersed continuously in fresh Severn River water, which has one sixth to one third the salt content of natural seawater depending on the season and the tide. A sketch of the specimens is given in Fig. 1. The tapered section is uniformly stressed under cantilever bending.

Low-cycle fatigue tests were conducted on two types of specimens under constant load condition. Figure 1 gives the dimensions of the beam specimens which were loaded in a bending fatigue machine from zero to maximum flexure ($R = 0$) at a rate of approximately 14 cpm (0.233 Hz). This machine was specially built at the authors' laboratory with the capacity for testing large-scale fatigue specimens. (The operation and construction of this machine requires a lengthy description which is omitted in this

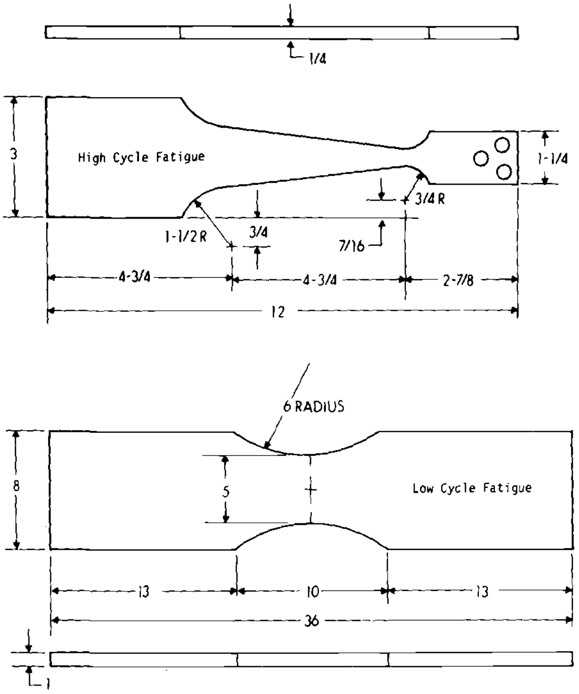

FIG. 1—*Beam-type fatigue specimens (all dimensions in inches, 1 in. = 2.54 × 10^{-2} m).*

paper.) The other specimens are 1-in.-thick square plates, 22 by 22 in. (0.56 by 0.56 m) in size. These plates were also tested in a special machine. In this machine, the specimen is simply supported along two edges and is uniformly loaded over the surface by compressed air from zero to maximum flexure at about 12 cpm (0.2 Hz). A similar machine has been described previously by Cordiano [*1*].[2] For testing in saltwater, the specimens were constantly soaked with natural seawater taken from Wrightsville Beach, N.C.

In the fatigue crack growth study, both compact tension (CT) and contoured double-cantilever-beam (DCB) specimens were tested in a Sonntag machine, which provided fatigue loading by the rotation of an unbalanced mass at 1800 cpm (30 Hz). Crack length was measured by means of a ×10 traveling microscope. Natural seawater was used to wet the specimens for testing in a saltwater environment. Details of specimen size and testing procedure were given in an earlier paper [*2*].

Failure Criteria

Failure in high-cycle fatigue consisted of complete fracture of the specimens.

[2] The italic numbers in brackets refer to the list of references appended to this paper.

In low-cycle fatigue, the deflection of each specimen was continuously monitored. Typical curves for plate and beam specimens, showing the progressive increase in deflection as cracks propagated through the specimens during cyclical loading, are shown in Fig. 2. The slope of the curves changed slowly in the early stages of the test, and then more rapidly as the crack propagated into the specimen. To provide a rational basis for comparison, an increase in deflection of 10 percent beyond the initial deflection was selected as the criterion of fatigue failure. This was chosen because it represents substantial damage to the specimens at the start of rapid increase in deflection, a warning of impending rupture. A failure criterion is not necessary for the fatigue crack growth study.

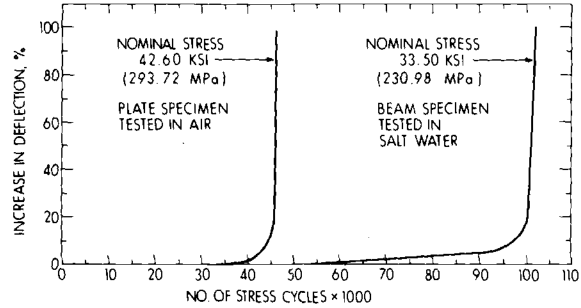

FIG. 2—*Percent increase in deflection of low-cycle fatigue specimens during testing.*

Results and Discussion

Use of Data

Both high-cycle and low-cycle fatigue results are presented as conventional *S-N* curves. The results of CT and DCB specimens are reduced to fatigue crack growth rate, *da/dN*, with the load parameter expressed in terms of stress intensity factor range, ΔK.

High-Cycle Fatigue

The high-cycle *S-N* curves are shown in Fig. 3. These curves do not exhibit a sharply defined endurance limit. Therefore, it is more realistic to define fatigue strength as the stress at a specific cycle life.

Test data on 5086-H116 are incorporated with those on 5456-H117 for stress ratio $R = 0$. Either in air or in saltwater, a single curve can be drawn through the two sets of data. Thus, in spite of their difference in yield or tensile strength, the two alloys seem to have similar fatigue behavior in both environments.

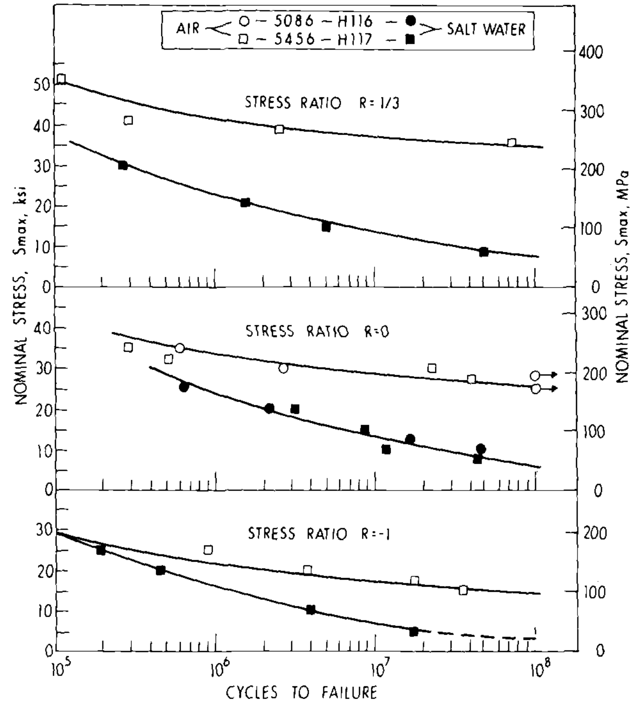

FIG. 3—*High-cycle fatigue results.*

Figure 3 also provides a direct comparison of the air and saltwater data; it shows that, in the high cycle region over one million cycles, the presence of saltwater drastically reduces the fatigue life of the alloy. However, this effect is less pronounced in the life regions below one million cycles and diminishes with decreasing fatigue life.

Based on the *S-N* curves, a modified Goodman diagram representing alloy 5456-H117 was constructed (Fig. 4). This diagram demonstrates the effect on fatigue life of variation in stress ratios at a given number of cycles to failure. Constant-life curves have been drawn for arbitrarily selected lives of one million, ten million, and one hundred million cycles. It may be seen from the diagram that the fatigue strength of the alloy for various stress ratios, based on a life of one hundred million cycles, is as follows.

	Fatigue Strength, ksi (MPa)	
Stress Ratio, *R*	Air	Saltwater
−1	14 (96.6)	4 (27.6)
0	24 (165.6)	5 (34.5)
1/3	34 (234.6)	7 (48.3)

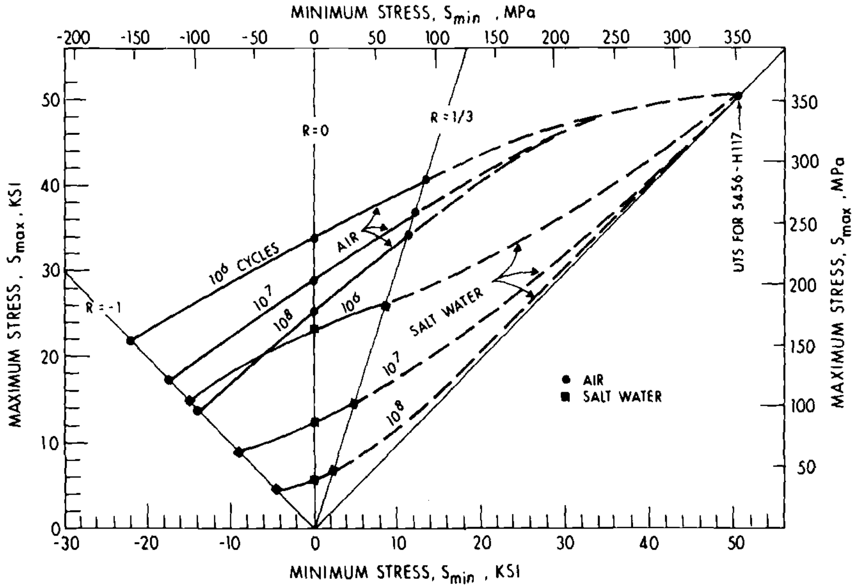

FIG. 4—*Modified Goodman diagram.*

The large reduction in fatigue strength attributable to the presence of saltwater is readily seen from these data.

Low-Cycle Fatigue

The fatigue lives on low-cycle specimens, based on 10 percent increase in deflection over the initial deflection, are plotted in Fig. 5. All the data fall in a narrow scatter band. In fact, the air and saltwater data are so close

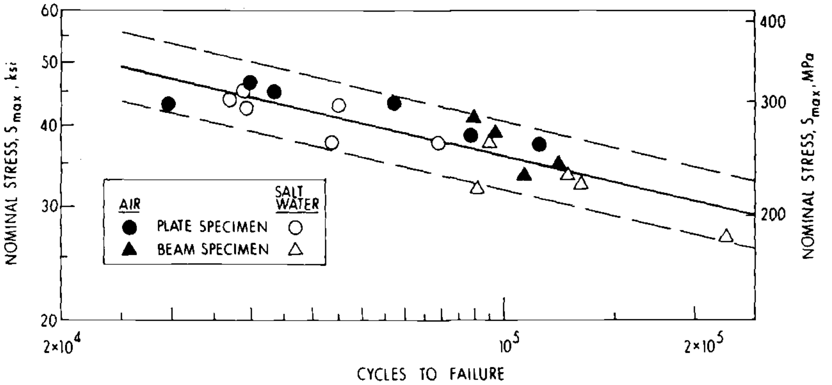

FIG. 5—*Low-cycle fatigue results.*

to each other that the effect of corrosive environment on the fatigue strength of the alloy has become negligible in low-cycle tests. Also, the beam and plate type specimens show the same fatigue behavior of the tested alloy.

In low-cycle fatigue studies, the experimental data are often analyzed in terms of plastic strain or total strain versus cycles to failure [*3*]. However, as pointed out by Langer [*4*], the fatigue curve needed by the designers is one which shows stress versus cycles. Figure 5 shows that fatigue life of alloy 5456-H117 is simply related to nominal stress in the life region investigated. The use of stress as a variable makes it possible to present the fatigue data on the conventional *S-N* curves.

Broad Life Fatigue Curves

Although fatigue tests are usually divided into high-cycle and low-cycle regions, the point of division is not quite clear. When data in Figs. 3 and 5 are plotted together, they should form smooth broad-life fatigue curves. These curves (Fig. 6) offer a complete description of both high-cycle and low-cycle fatigue behavior of the alloy. Of particular interest is that when the high-cycle saltwater data are considered separately (Fig. 3), they indicate a trend of leveling off gradually. But after being combined with the low-cycle data, they can be faired into a linear curve in the log-log graph (Fig. 6). Thus, the presence of saltwater has eliminated the possible existance of an endurance limit as discussed by Schwab and Czyryca [*5*]. In contrast, the endurance limit of the alloy in air may be approximated as 25 ksi (172.5 MPa) at one hundred million cycles.

The broad life fatigue curve in air conforms to Langer's type of equation [*4*]

$$S_{\max} = mN^{-n} + S_e \qquad (1)$$

where

S_e = endurance limit,
N = number of cycles, and
m, n = constants.

For the fatigue curve in saltwater without an endurance limit, the equation reduces to

$$S_{\max} = mN^{-n} \qquad (2)$$

The data in Fig. 6 are faired according to these equations.

Fatigue Crack Growth

The fatigue crack growth data[3] are summarized in Fig. 7. For all five

---

[3] The *da/dN* data were reduced from crack growth measurements by graphical differentiation.

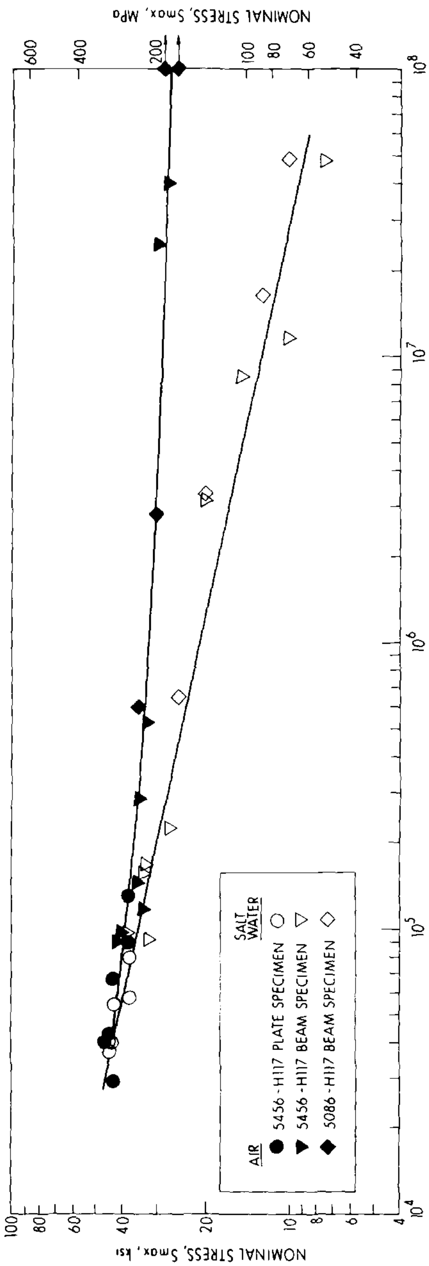

FIG. 6—*Broad life fatigue curves* (R = 0).

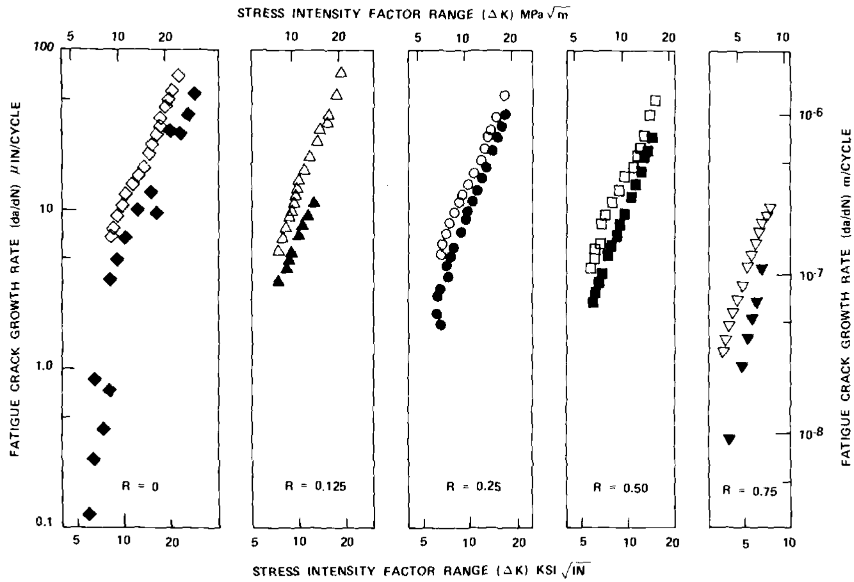

FIG. 7—*Fatigue crack growth rate versus stress intensity factor range for five* R *values (solid and open points represent data in air and saltwater, respectively).*

R values, the data in saltwater are situated above those in air, indicating an increase in fatigue crack growth rate due to the effect of saltwater. In general, the fatigue rate in saltwater is about twice as great as that in air for the same stress intensity range. Figure 7 also shows that the effect of saltwater diminishes when the stress intensity is high. This is indicated by the two sets of data for $R \geq 0.25$ as they converge over high ΔK values.

The crack growth behavior of the alloy is illustrated in Fig. 8 with regard to the effect of mean stress. As expected, an increase in mean stress brings about a corresponding increase in crack growth rates. However, for tests in saltwater, the data for $R \geq 0.125$ merge into a narrow band, which is practically parallel with that for $R = 0$. it indicates that the alloy becomes insensitive to increases in mean stress after it has reached a certain level. The same is true for tests in air, except that it occurs at $R \geq 0.25$ [*6*]. It turns out that data for $R \geq 0.25$ in air (which is omitted in Fig. 8 for clarity) coincide with those for $R = 0$ in saltwater. A curve representing the air data for $R = 0$ is incorporated in the graph to demonstrate further the difference in the two environments. Evidently, the presence of saltwater has lowered the threshold stress intensity, under which a fatigue crack will cease to propagate.

Either of the following equations may be used to represent the crack growth data on the 5456-H117 alloy.

$$\frac{da}{dN} = \frac{c(\Delta K - \Delta K_{th})^n}{[(1 - R)K_c - \Delta K]^m} \tag{3}$$

$$\frac{da}{dN} = \frac{c(\Delta K^n - \Delta K_{th}^n)}{[(1 - R)K_c - \Delta K]^m} \tag{4}$$

The constants used to fit the data with da/dN expressed in μin/cycle (2.54×10^{-8} m/cycle) are as follows.

For Eq 3

	c	m	n
Air	25.10	1	1.23
Saltwater	35.33	1	1.23

For Eq 4

	c	m	n
Air	6	1.30	2
Saltwater	9	1.30	2

The values of fracture toughness, K_c, and threshold stress intensity, ΔK_{th}, of the alloy have been estimated in previous work [2].

	K_c, ksi (MPa)	ΔK_{th} ($R = 0$)	ΔK_{th} ($R > 0$)
Air	44.9 (49.4)	6.0 (6.6)	3.6 (4.0)
Saltwater	41.7 (45.9)	3.6 (4.0)	2.6 (2.9)

Equations 3 and 4 can adequately describe the crack growth behavior from fatigue threshold to unstable crack propagation. The curves computed by Eq 3 are drawn in Fig. 8 as examples of the accuracy of these equations. The overall accuracy is satisfactory except that a part of the data for $R = 0.125$ falls on the curve for $R = 0$. It is interesting to note that the constants m and n are the same for air and saltwater tests, and the material sensitivity to environment is reflected by the value of c.

Fracture Surfaces

The overall fracture appearance of fatigue crack growth specimens tested in air and saltwater was about the same. The surfaces could be roughly divided into two regions corresponding to slow and fast crack growth (Fig. 9).

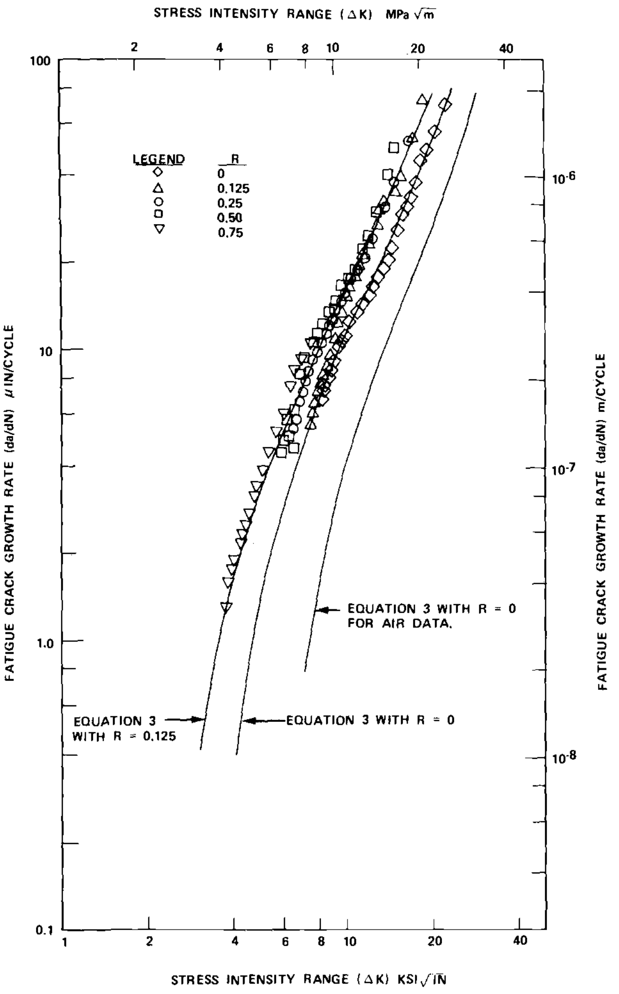

FIG. 8—*Effect of* R *on fatigue crack growth rate in saltwater.*

In Region I, where the fatigue rates were slow at comparatively low stress intensity levels, the surfaces in air were composed of striations and secondary cracks due to a fracture mechanism involving fatigue and tearing (Fig. 10). However, the fracture surfaces in saltwater had very little tearing and secondary cracks since they showed mainly fatigue striations which were coarse and rumpled. An outstanding feature is that the elongated grains were separated by cracks at the grain boundaries. The cracks ran in the direction perpendicular to that of fatigue crack propagation. This phenomenon was similar to the stress corrosion characteristics of other aluminum alloys observed by Chu and Wacker [*7,8*].

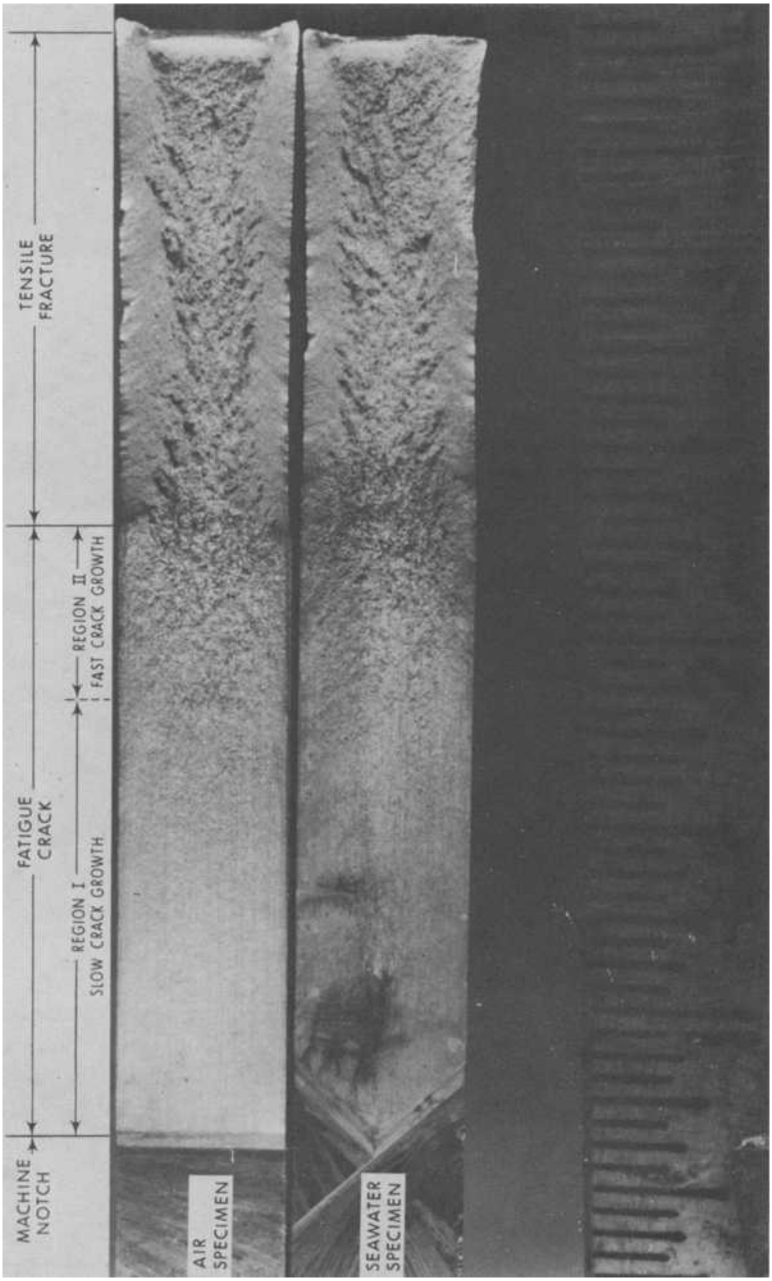

FIG. 9—*Macrophotograph of specimen surfaces.*

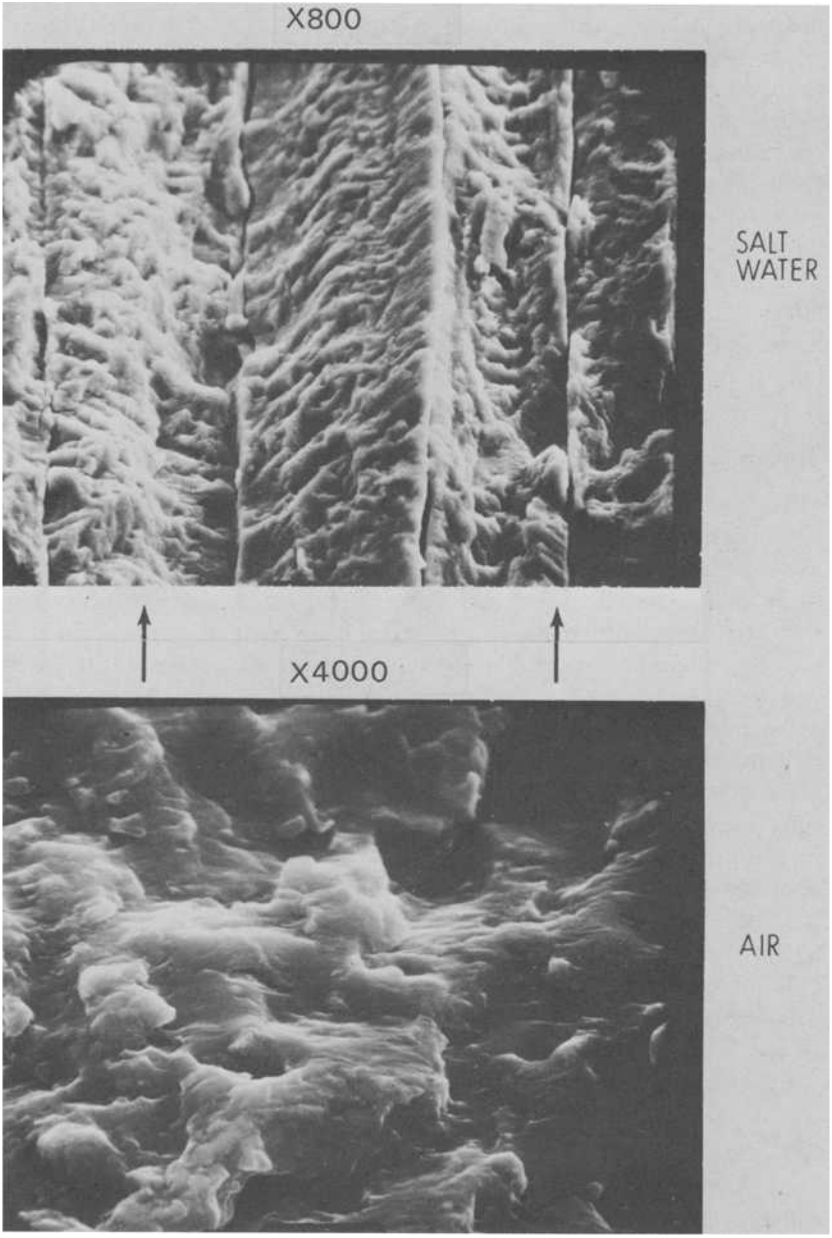

FIG. 10—*Micrographs of fatigue crack surface in Region I. (Arrows show direction of fatigue crack propagation.)*

In Region II, the crack growth was fast at high stress intensity levels, and fatigue crack propagation in saltwater became similar to that in air involving striations plus secondary cracks (Fig. 11). The grain boundary cracking disappeared. It signifies that the effect of saltwater is diminished in this region.

It is possible to draw a parallel between fatigue crack growth tests and conventional fatigue tests with regard to the presence of saltwater, since the environmental effect is also reduced as the stress is increased in low-cycle regions. Wei [*9*] suggests that the decrease in environmental sensitivity during crack propagation is most likely associated with a plane-strain to plane-stress transition in fracture mode. However, the reduction in the effect of saltwater in conventional low-cycle experiments may be mainly because the specimens are not exposed to the corrosive environment as long as in high-cycle tests.

Applications

The 5456 aluminum alloy has performed well in marine applications. Niederberger et al [*10*] conducted seawater stress corrosion tests on the alloy in nine tempers up to five years and found no failure in H321 and three other tempers. The H116 and H117 tempers are appropriate for ship structures with material properties equivalent to those of 5456-H321 plus the resistance to exfoliation or intergranular corrosion [*11*]. For these reasons, the interlaminar cracking shown in Fig. 10 may be considered only as an indication of low-level susceptibility of the alloy to stress corrosion.

Both conventional and fracture mechanics test methods have been employed in the present investigation. It may be useful to examine all the results with a view of using them together for the prediction of failure by fracture and fatigue. Speidel [*12*] has shown a method of combining data obtained from testing smooth and precracked specimens based on the relationship between stress and flaw size. A similar approach may be applied to the present data.

As an example, the simple case of an infinite plate with a center crack will be discussed (Fig. 12). The uniform normal stress, S, is related to flaw size by [*13*]

$$S = \frac{K_c}{\sqrt{\pi a}} \qquad (5)$$

where a is half-crack length. When the flaw size is such that brittle fracture may occur, the stress varies with flaw size according to the inverse square root relation, which dictates a linear curve in log-log coordinates with a slope of $-1/2$. As the flaw becomes sufficiently small, this relationship will no longer hold. The point of deviation is shown by Feddersen [*14*]

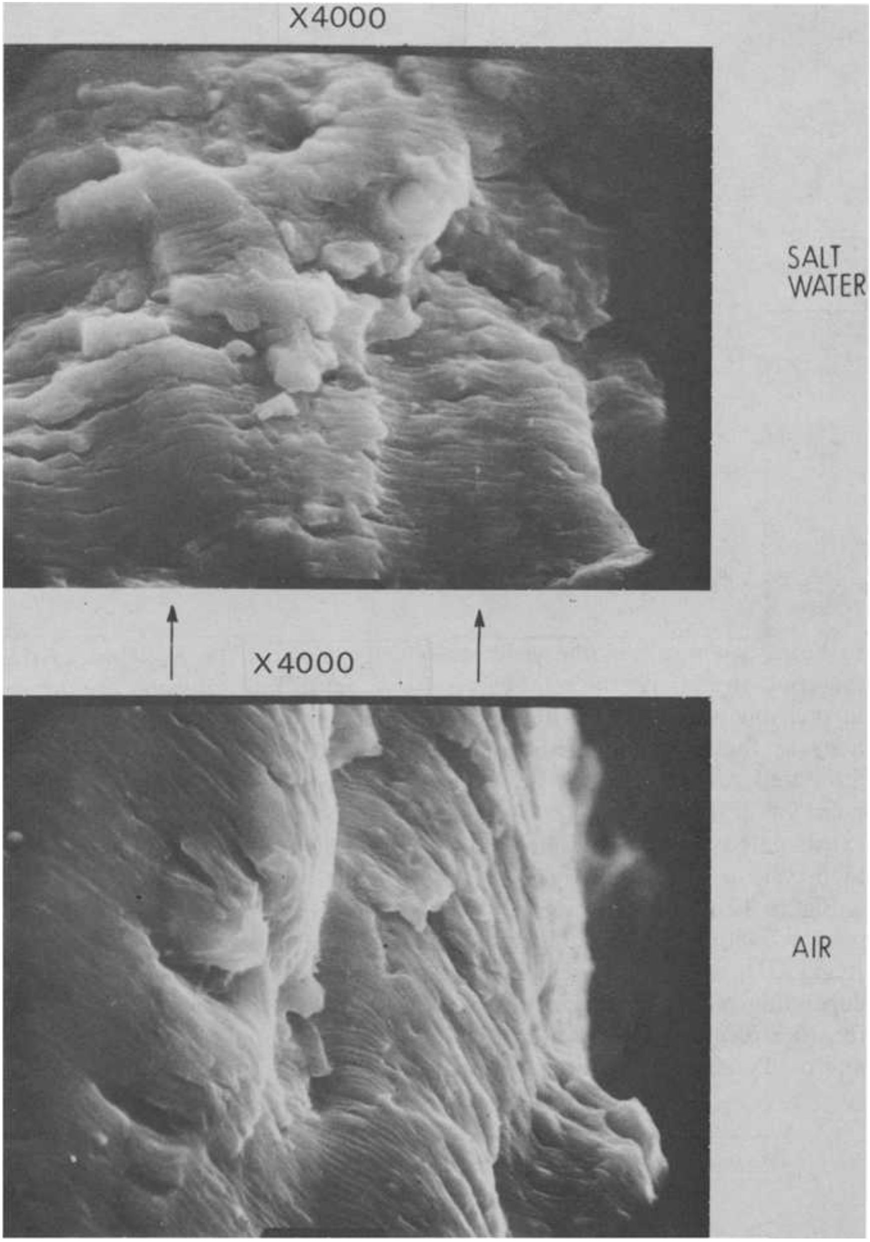

FIG. 11—*Micrographs of fatigue crack surface in Region II. (Arrows show direction of fatigue crack propagation.)*

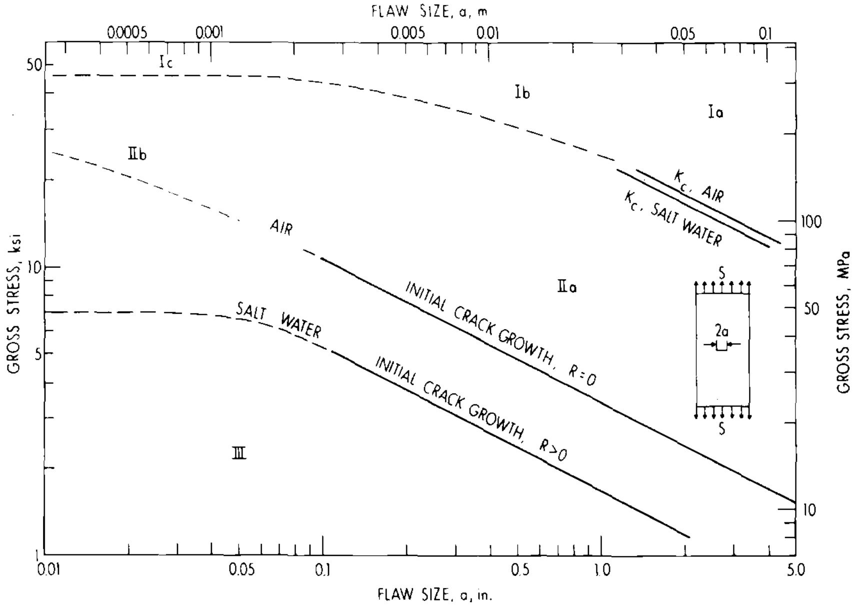

FIG. 12—*Design diagram against fracture and fatigue.*

to be at two thirds of the yield stress, regardless of the K_c value of the material. In Fig. 12, the solid curves for K_c in air and saltwater are drawn in this way with a dashed line extrapolating to the tensile strength of the alloy as the flaw diminishes to negligible size. Similar curves based on estimated ΔK_{th} values are drawn for initial crack growth. Although the point of deviation from the linear part is uncertain, the curves may be extrapolated to the endurance limit or the fatigue strength established by high-cycle or low-cycle fatigue tests.

Figure 12 maps out three regions. In Regions I and II, the material is involved with overload and fatigue failure, respectively. The safe area is Region III, where fracture and fatigue will not occur. It can be seen that, depending on the flaw size, the 5456-H117 alloy must carry low stresses in order to avoid fatigue failure in saltwater environment. Failure modes and predictions can be further classified as follows.

Region	Failure Mode	Failure Prediction
Ia	brittle fracture	Eq 5
Ib	yielding	yield strength
Ic	rupture	tensile strength
IIa	fatigue cracking	Eqs 3 and 4
IIb	fatigue fracture	Eqs 1 and 2

Summary

High-cycle fatigue curves show that aluminum alloy 5456-H117 does not have a sharply defined endurance limit and the fatigue life of the alloy is drastically reduced by the presence of saltwater. Test data for $R = 0$ indicate that alloys 5456-H117 and 5056-H116 have similar fatigue behavior in air and saltwater.

The effect of saltwater is insignificant on fatigue of the 5456-H117 alloy in low-cycle life regions. The low-cycle and high-cycle data ($R = 0$) can be combined into broad life fatigue curves.

Alloy 5456-H117 exhibits an increase in crack growth rate and a decrease in threshold stress intensity in a saltwater environment. It shows a low-level susceptibility to stress corrosion. The effect of saltwater on fatigue crack propagation in the alloy decreases at high stress intensity levels.

The results of fracture mechanics and conventional fatigue tests can be combined in terms of stress versus flaw size for predictions of failure by fracture and fatigue.

Acknowledgments

The support of this work by the Naval Sea Systems Command is gratefully acknowledged.

References

[*1*] Cordiano, H. V., *Journal of Engineering for Industry*, Feb. 1970, p. 87.

[*2*] Chu, H. P., *Journal of Engineering Materials and Technology*, Oct. 1974, p. 261.

[*3*] Coffin, L. F., Jr., *Journal of Materials*, June 1971, p. 388.

[*4*] Langer, B. F., *Journal of Basic Engineering*, Sept. 1962, p. 389.

[*5*] Schwab, R. C. and Czyryca, E. J. in *Effects of Environment and Complex Load History on Fatigue Life, ASTM STP 462*, American Society for Testing and Materials, 1970, p. 203.

[*6*] Chu, H. P. in *Fracture Toughness and Slow-Stable Cracking, ASTM STP 559*, American Society for Testing and Materials, 1974, p. 245.

[*7*] Chu, H. P. and Wacker, G. A., *Journal of Basic Engineering*, Dec. 1969, p. 565.

[*8*] Wacker, G. A. and Chu, H. P., *Corrosion*, June 1972, p. 233.

[*9*] Wei, R. P. and Landes, H. D., *International Journal of Fracture Mechanics*, March 1969, p. 69.

[*10*] Niederberger, R. B., Basil, J. L., and Bedford, G. T., *Corrosion*, March 1966, p. 68.

[*11*] Brooks, C. L., *Naval Engineers Journal*, Aug. 1970, p. 29.

[*12*] Speidel, M. O., *Proceedings*, 6th International Conference on Light Metals, Vienna, Austria, 1975, p. 67.

[*13*] Paris, P. C. and Sih, G. C. in *Symposium on Fracture Toughness Testing and Its Application, ASTM STP 381*, American Society for Testing and Materials, 1965, p. 30.

[*14*] Feddersen, C. E. in *Damage Tolerance in Aircraft Structures, ASTM STP 486*, American Society for Testing and Materials, 1971, p. 50.

Hydrogen Environments

R. P. Jewett,[1] *R. J. Walter,*[1] *and W. T. Chandler*[1]

Influence of High Pressure Hydrogen on Cyclic Load Crack Growth in Metals

---

REFERENCE: Jewett, R. P., Walter, R. J., and Chandler, W. T., "**Influence of High Pressure Hydrogen on Cyclic Load Crack Growth in Metals,**" *Corrosion-Fatigue Technology, ASTM STP 642*, H. L. Craig, Jr., T. W. Crooker, and D. W. Hoeppner, Eds., American Society for Testing and Materials, 1978, pp. 243-263.

ABSTRACT: The effect of high pressure hydrogen on the crack growth rate of various nickel-base alloys was studied at ambient temperature. Considerable enhancement of the cyclic flaw growth rate was observed for Inconel 718, wrought and cast, and Waspaloy, a nickel-base alloy similar to Inconel 718. Only slight enhancement of the flaw growth rate for Alloy 903 was observed.

KEY WORDS: corrosion fatigue, crack propagation, nickel-base alloys, hydrogen embrittlement, fractography

Currently Rocketdyne is building the space shuttle main engine (SSME), the rocket engines that will be used for the propulsion of the space shuttle vehicle. These engines are high-performance high-chamber pressure rocket engines using oxygen and hydrogen propellants, and the hydrogen pressures in the SSME are higher than those encountered in previous production engines. It has been shown that high-pressure hydrogen seriously degrades the mechanical properties of many of the commonly used engineering alloys [*1*].[2] Under the SSME program, cyclic-load crack growth rate (*da/dN*) tests are being conducted in support of fracture life verification analyses of all fracture critical parts, most of which are operating in contact with high-pressure hydrogen. The *da/dN* tests are being performed utilizing a cycle, nearly 9 min long, that simulates the SSME operating cycle.

---

[1] Members of technical staff, Rocketdyne Division, Rockwell International, Canoga Park, Calif. 91202.

[2] The italic numbers in brackets refer to the list of references appended to this paper.

This paper reports the results of *da/dN* tests for three alloys, Inconel 718, Waspaloy (a nickel-base alloy similar to Inconel 718), and Alloy 903, in high-pressure hydrogen, ambient-pressure air, at ambient and cryogenic temperatures. To understand better the effect of high-pressure hydrogen on crack behavior, the results of scanning electron fractography and light metallography examination of the *da/dN* specimens are presented. In addition, to aid in the interpretation of the results from the long SSME cycle, the results of earlier *da/dN* tests and scanning electron fractography for Inconel 718 specimens tested in hydrogen with shorter cycles are included.

Material

Forgings of Inconel 718, Waspaloy, and Alloy 903, and castings of Inconel 718 were used in this study. The size of the forgings and castings are given in Table 1. The mechanical properties and chemical composition of the various materials are given in Tables 2 and 3. The heat treatments used for each material are given in Table 4.

Experimental Procedure

The *da/dN* data presented were obtained using 5W compact specimens (CS). Cyclic load tests were also performed with part-through-crack (PTC)

TABLE 1—*Materials used.*

Material	Forging (Casting) Size, in.	Specimen Orientation
Waspaloy	1.5 by 7 by 7	TL
Alloy 903	1.25 by 7 by 7	TL
Inconel 718	2 by 7¼ by 21	TL
Inconel 718 (Cast)	(1.15 by 5.3 by 5.5)	...

NOTE: 1 in. = 25.4 mm.

TABLE 2—*Longitudinal mechanical properties.*

Material	Yield Strength 0.2% Offset, ksi	Tensile Strength, ksi	Elongation in 1 in., %	Reduction of Area, %
Waspaloy	168	215	18.5	31.0
Alloy 903	169	202	10.0	19.0
Inconel 718 Forged	171	203	21.0	35.8
Inconel 718 Cast	145	155	7.7	...

NOTE—Conversion factors: 1 ksi = 6.895 MN/m^2, and 1 in. = 25.4 mm.

TABLE 3—*Chemical Composition of alloys used (vendor analysis).*

Material	Cr	Mo	Zn	Ni	Al	Fe	Cb/Ta	Co	Ti	Cu
Inconel 718 (forged)	17.8	3.05	3.05	53.4	0.55	18.4	5.29	0.25	1.08	...
Inconel 718 (cast)	18.1	3.19	...	51.2	0.67	bal	5.02	0.50	0.91	...
Waspaloy	19.61	4.05	...	bal	1.50	0.13	...	14.04	3.10	...
Alloy 903	0.15	...	...	37.82	1.01	bal	3.00	16.04	1.77	0.16

TABLE 4—*Heat treatment of materials.*

	Solution Temperature, °F(°C)	First Age Temperature, °F(°C)	Second Age Temperature, °F(°C)
Material	Time, h	Time, h	Time, h
Inconel 718	1900 (1038)	1400 (760)	1200 (649)
	0.33	10	10
Inconel 718 (cast)	1900 (1038)	1350 (732)	1160 (621)
	2	8	8
Waspaloy	1850 (954)	1400 (760)	1200 (649)
	2	16	24
Alloy 903	1750 (954)	1325 (718)	1150 (621)
	1.25	8	8

specimens; the cross section and the precrack dimensions are given in Table 5.

Tests were conducted with the specimens either at room temperature in air or in high purity gaseous hydrogen at ambient and −300°F temperatures. The procedure for compressing and purifying the hydrogen gas has been described elsewhere [*1*]. A computer controlled 280-kip (1250-kilonewton (kN)) materials testing system (MTS) was used for loading the specimens. The load-time profile shown in Fig. 1 was used for all tests with an *R* ratio of 0.01. The complete test system has been described elsewhere [*2*].

The CS specimens were precracked in air at a stress intensity range (ΔK) of approximately 20 ksi $\sqrt{\text{in.}}$ (22 MN/m^2 $\sqrt{\text{m}}$) or less. The initial crack length (notch root + precrack) was approximately 1.1 to 1.2 in. (27.9 to 30.4 mm). Crack lengths during the *da/dN* tests were measured by the compliance technique using crack-opening displacement (COD) gages mounted at the mouth of the CS specimens. The compliance equation used for determining the crack length was developed by Thatcher [*3*]. The crack growth rate data were determined by calculating the stress intensity values over various crack growth increments, usually 0.025 in. The completed

TABLE 5—*Summary of data for Inconel 718 part-through crack specimens tested in 5000-psi (34.5-MN/m^2) hydrogen at room temperature,* R *ratio = 0.01.*

Specimen	Size of ELOX Starter Notch, in.	Size of Precrack, in.		Specimen Dimensions, in.		Maximum Load, lb	Section Stress, ksi	Number of Cycles Completed Without Failure	Time into Final Cycle of Failure, min	Initial Stress Intensity, ksi $\sqrt{\text{in.}}$
		a	2*c*	t	W					
1	0.084	0.136	0.847	0.250	2.993	57 900	77.4	0	~3	56.7
2	0.074	0.123	0.874	0.238	2.993	45 190	63.4	1	~5	44.9
3	0.765	. . .	. . .	0.252	2.982	30 140	40.1	100	. . .[a]	. . .
4	0.828	0.125	0.905	0.245	2.985	44 100	60.3	0	~5	43.2

NOTE—1 in. = 25.4 mm,
1 lb = 4.4482 N,
1 ksi = 6.8948 MN/m^2, and
1 ksi in. = 1.0988 MN/m^2 $\sqrt{\text{m}}$

[a] Did not fail after indicated number of cycles.

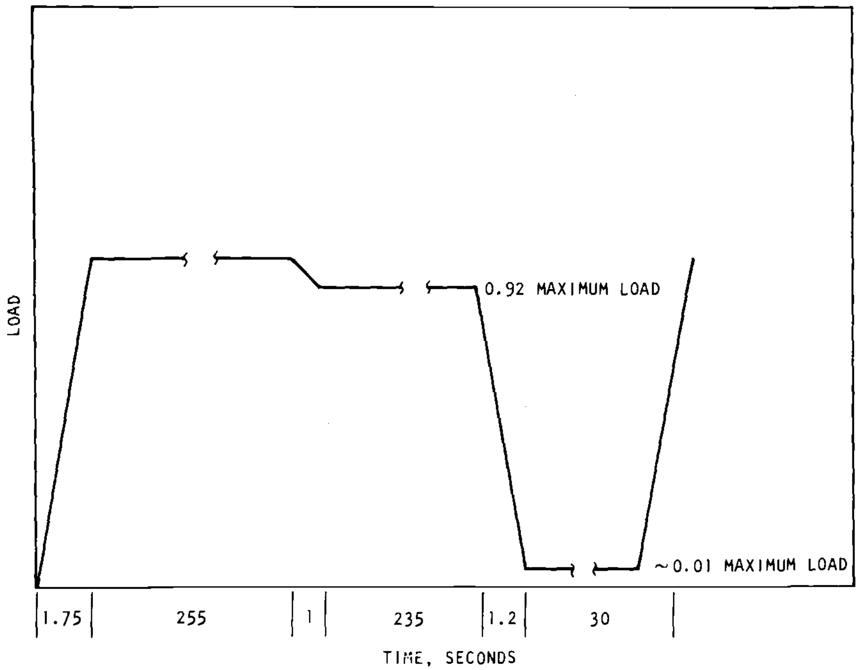

FIG. 1—*Simulated SSME load-time cycles.*

da/dN data were plotted using a third-order polynominal fit of the data.

The PTC specimens were precracked in air. The initial *K* value for cyclic tests in 5000-psi (34.5-MM/m^2) hydrogen was 40 ksi $\sqrt{\text{in.}}$ (44 MN/m^2 $\sqrt{\text{m}}$).

Results and Discussion

The results of the *da/dN* tests and the fractography and metallography examinations will be present and discussed for each of the test materials. Results are also compared with *da/dN* data and scanning electron microscope (SEM) fractography on previous tests performed utilizing tapered double cantilaver beam (TDCB) specimens [*1*].

Forged Inconel 718

The results of *da/dN* tests on forged Inconel 718 CS specimens tested with the Fig. 1 load profile are presented in Fig. 2. Each curve in this and subsequent figures represents a single specimen. The semilog presentation of the *da/dN* data is used because it better delineates the environmental effects than a log-log plot. The large effect of high-pressure hydrogen on

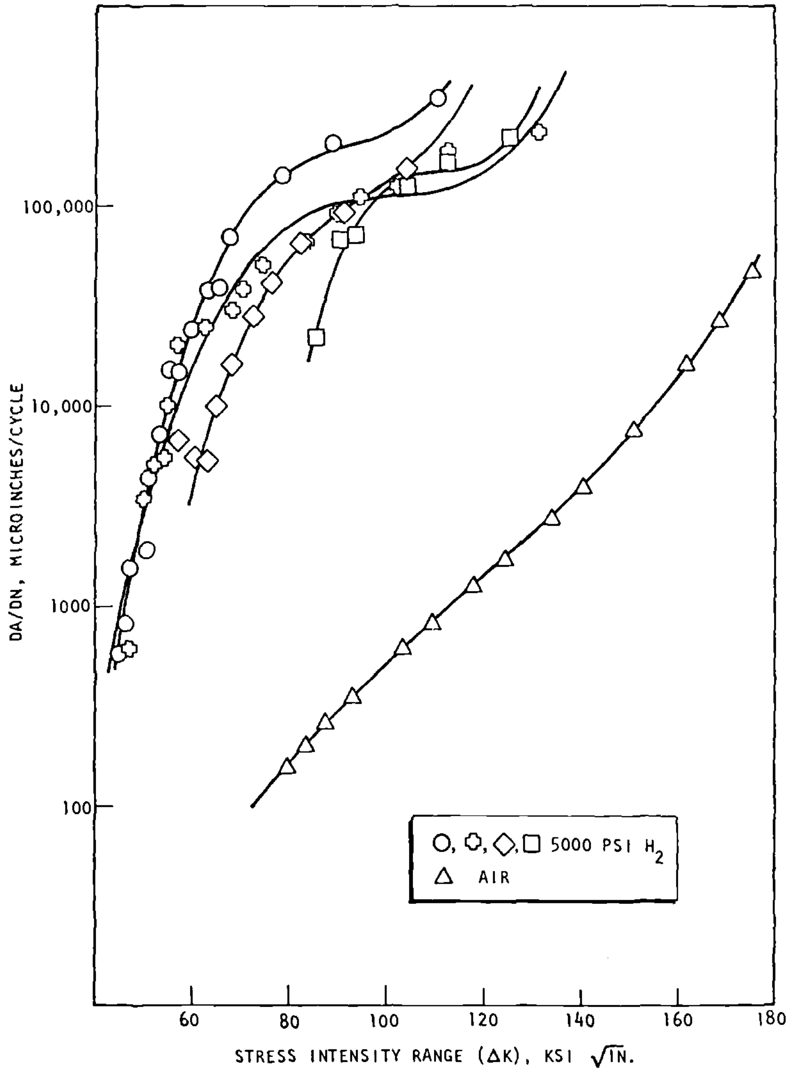

FIG. 2—da/dN *versus* ΔK *for Inconel 718 in air and 5000-psi (34.5-MN/m^2) hydrogen at ambient temperature. Specimen thickness = 1 in., and R = 0.01.*

da/dN in Inconel 718 is apparent from Fig. 2. The crack growth rates were two to three orders of magnitude faster in hydrogen than in air. Considerable scatter is evident for the four specimens tested in 5000-psi (34.5-MN/m^2) hydrogen. The majority of *da/dN* data can be extrapolated to give an apparent 40-ksi $\sqrt{\text{in.}}$ (44-MN/m^2 $\sqrt{\text{m}}$) threshold stress intensity.

The data in Fig. 2 indicate that final failure occurred at various stress intensities. These apparent differences in K_{Ic}, however, may be due to the crack growth rate not being determined in the final cycle.

Tension tests performed in 5000-psi (34.5-MN/m^2) hydrogen and 5000-psi (34.5-MN/m^2) helium on Inconel 718 in this heat treatment condition have shown approximately 50 percent reduction of notch strength (K_t = 9) due to the 5000-psi (34.5-MN/m^2) hydrogen environment [*4*]. Fractures of smooth tension specimens tested in the hydrogen environment initiated from a few surface cracks, usually one to three in number, causing almost immediate failure [*4*]. Thus after crack formation, the smooth tension test changed to a crack growth test. The failure time of the smooth tension specimens was determined then by the crack growth rate in hydrogen which was 2 to 3 orders of magnitude faster in hydrogen than in air (Fig. 2).

The SEM of specimens tested in air and hydrogen are shown in Figs. 3 through 5. Representative fractographs of specimens tested in air are shown in Figs. 3 and 4. Figure 3 shows a representative fractograph of the precrack. The fracture consists of transgranular facets with fatigue striations appearing in some of the facets. There was very little indication of ductility (dimple formation) in the precracked regions. Figure 4 contains fractography from subcritical crack growth regions of a specimen tested in air

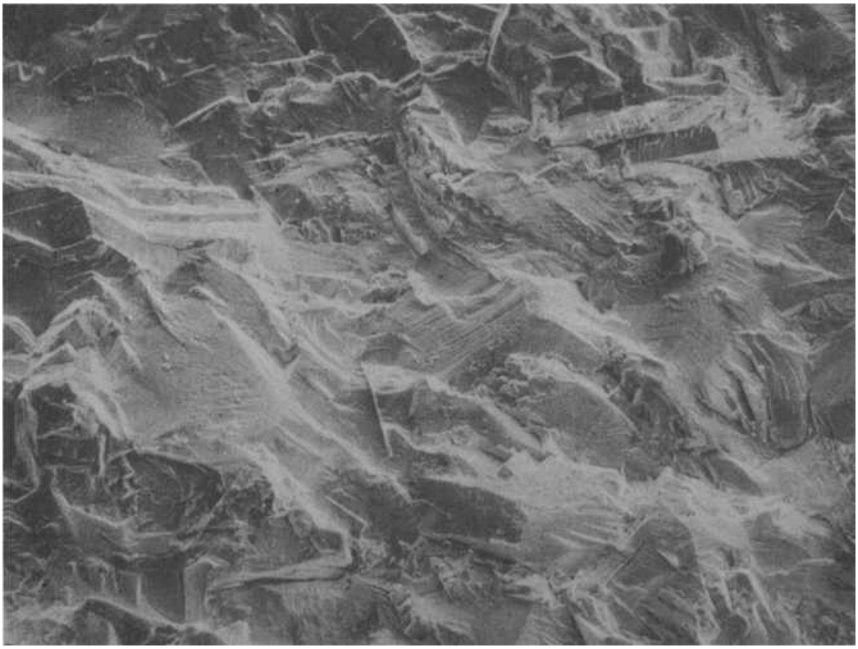

FIG. 3—*Fractograph of precrack region on wrought Inconel 718 compact specimen* (×*200*).

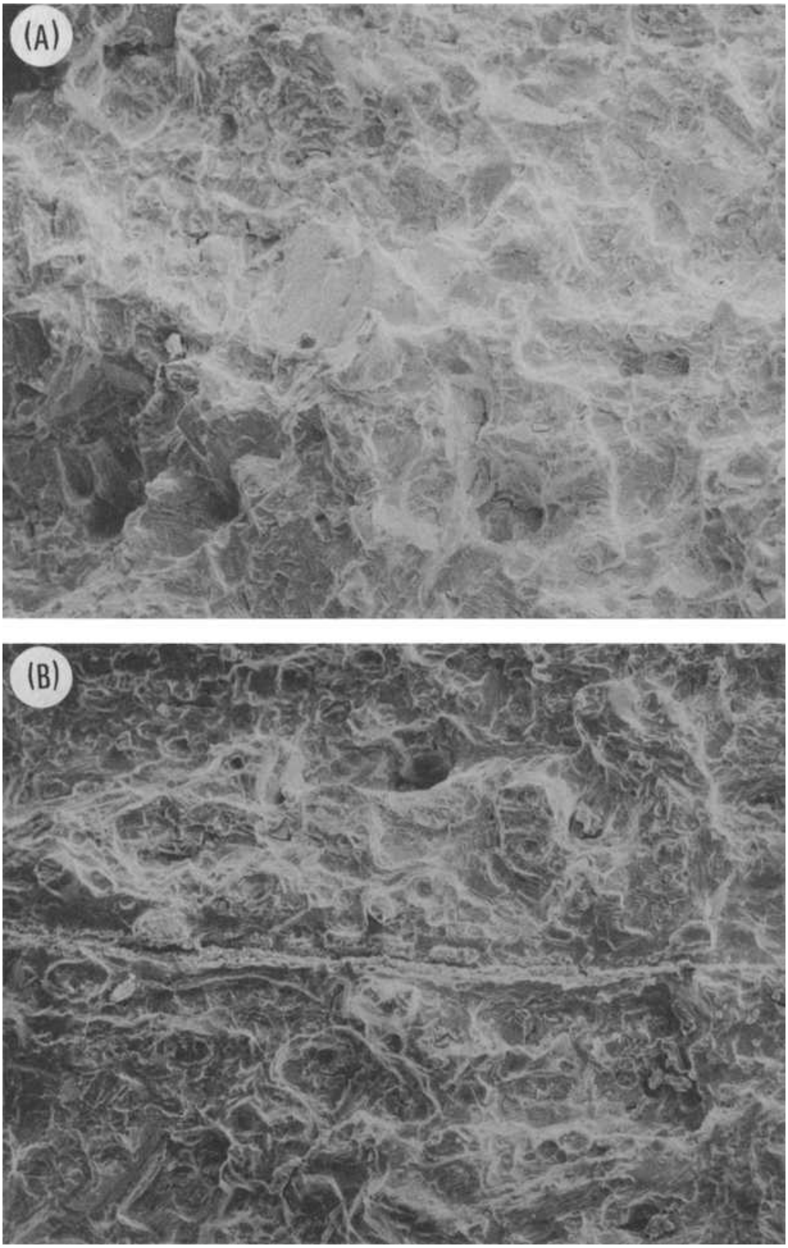

FIG. 4—*Fractographs of wrought Inconel 718 compact specimen* da/dN *tested in air at ambient temperature* ($\times 200$): (A) *9 s/cycle.* $\Delta K \times 105$ *ksi* $\sqrt{in.}$ (115.5 $MN/m^2 \sqrt{m}$), and (B) *9 min/cycle,* $\Delta K = 110$ *ksi* $\sqrt{in.}$ (121 $MN/m^2 \sqrt{m}$).

at two cyclic frequencies. Figure 4(*A*) represents a frequency intermediate between precracking and the long 9-min cycle used for the *da/dN* tests (Fig. 1). Crack growth per cycle appeared to be somewhat greater for the longer cycle duration. The fractographs consist of transgranular fracture with incomplete void formation superimposed on the transgranular facets. The fractography examinations indicated greater ductility (more complete dimple development) associated with the longer cycle and greater crack growth per cycle, which suggests that the added crack extension during the hold period occurred by a time dependent ductile tearing fracture mode.

All four CS specimens tested in hydrogen were examined by electron fractography. Figure 5 is a typical fractograph and shows mainly intergranular failure. There were essentially no differences observed between the initial subcritical crack growth (low *K* regions) and final crack growth (high *K* region). It appeared, however, that the fracture in the center of the specimen (plane strain) had a higher proportion of intergranular regions than the fracture near the sides (plane stress).

FIG. 5—*Fractograph of wrought Inconel 718 compact specimen* da/dN *tested in 5000-psi (34.5-MN/m^2) hydrogen at ambient temperature.* ΔK = *115 ksi* $\sqrt{\text{in.}}$ *(126.5 MN/m^2* $\sqrt{m}$*) (×200).*

Comparison between specimens also suggested that the percent intergranular fracture was greater in the specimens with faster crack growth rates. Metallography examination in the region of the fracture also indicated that the grain sizes were somewhat larger (approximate ASTM 4 or 5) in the specimens having the faster crack growth rates than in specimens with the slower crack growth rates (approximate ASTM 6). These results infer that large grain size and high percent intergranular fracture were associated with the specimens having the fastest crack growth rates in hydrogen.

Walter and Chandler [*4*] have shown that the threshold stress intensity for sustained load crack growth in 3 000 through 10 000-psi (20.7 to 69.0-MN/m^2) hydrogen is approximately 38 ksi $\sqrt{\text{in.}}$ (41.8 MN/m^2 $\sqrt{\text{m}}$). This is in agreement with the apparent threshold value of 40 ksi $\sqrt{\text{in.}}$ (44 MN/m^2 $\sqrt{\text{m}}$) from Fig. 2. The cyclic load crack growth above this stress intensity was shown to be proportional to the cycle duration. At fast frequencies (1.0 Hz), there was a small influence of hydrogen on crack growth, and the fracture was transgranular with ductility easily observable in the transgranular facets, but there were no discernable fatigue striations. The fracture at 0.1 Hz was mainly intergranular. The change from the transgranular at 1.0 Hz to intergranular fracture at 0.1 Hz was associated with a factor of 10 increase of *da/dN*. The increase of crack growth (which was linear with cycle duration) and change of fracture mode to intergranular fracture at longer cycle durations indicate that the effect of cycle duration on cyclic crack growth is due to a superimposed sustained load crack growth.

The *da/dN* measurements performed on the CS specimens using the SSME cycle (Fig. 1) showed that the threshold stress intensity for significant crack growth was about 40 ksi $\sqrt{\text{in.}}$ (44 MN/m^2 $\sqrt{\text{m}}$) which corresponds to the previously reported K_{TH} [*4*] for sustained load crack growth. The intergranular fracture observed in these specimens corresponds with the intergranular fracture observed in the TDCB specimens tested under sustained load [*4*]. The transgranular fracture areas in these predominately intergranular fractures corresponds to the cyclic loading crack growth component.

Several PTC specimens were tested in 5000 psi (34.5 MN/m^2) hydrogen utilizing the load time cycle shown in Fig. 1. Failures occurred within a few cycles at the initial stress intensities shown in Table 5. The inferred crack growth rate is approximately 100 000 μin./cycle at an initial K of between 40 and 60 ksi $\sqrt{\text{in.}}$ (44 and 66 MN/m^2 $\sqrt{\text{m}}$). This crack growth rate is considerably higher than the data shown in Fig. 2 at comparable stress intensities. The difference may be due to a combination of the plane strain conditions at the end of the crack and to the high *dK/da* associated with PTC specimens.

The SEM examination of the PTC specimens tested in hydrogen showed the fracture to be totally intergranular with secondary intergranular cracking. Figure 6 is representative of the fractures in the PTC specimens from

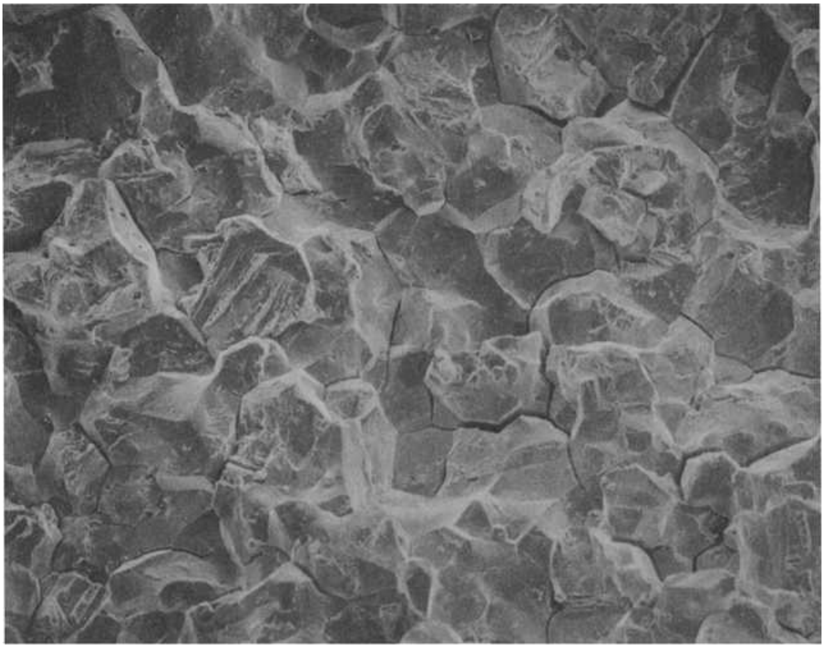

FIG. 6—*Fractograph of wrought Inconel 718 PTC specimen (No. 1, Table 5)* da/dN *tested in 5000-psi (34.5-MN/m^2) hydrogen at ambient temperature (×200).*

the region in front of the precrack to the back side of the specimens. The lack of transgranular fracture may be due to the few cycles that occurred prior to failure. Thus the intergranular fracture associated with sustained load crack growth was virtually not interrupted by cyclic loading. It is also possible, however, that the lack of transgranular fracture was due to the plane-strain stress state that exists in front of the precrack in PTC specimens.

Cast Inconel 718

The room temperature crack growth data for cast Inconel 718 are given in Fig. 7. The effect of 5000-psi hydrogen (H_2) (34.5 MN/m^2) was not as dramatic as in the forged Inconel 718 but considerable enhancement of the crack growth rate in hydrogen is evident. Tensile properties of smooth and notched tension specimens show slightly less embrittlement in 5000-psi (34.5-MN/m^2) hydrogen than wrought Inconel 718.

Typical fractographs of cast Inconel 718 *da/dN* tested in 5000-psi (34.5-

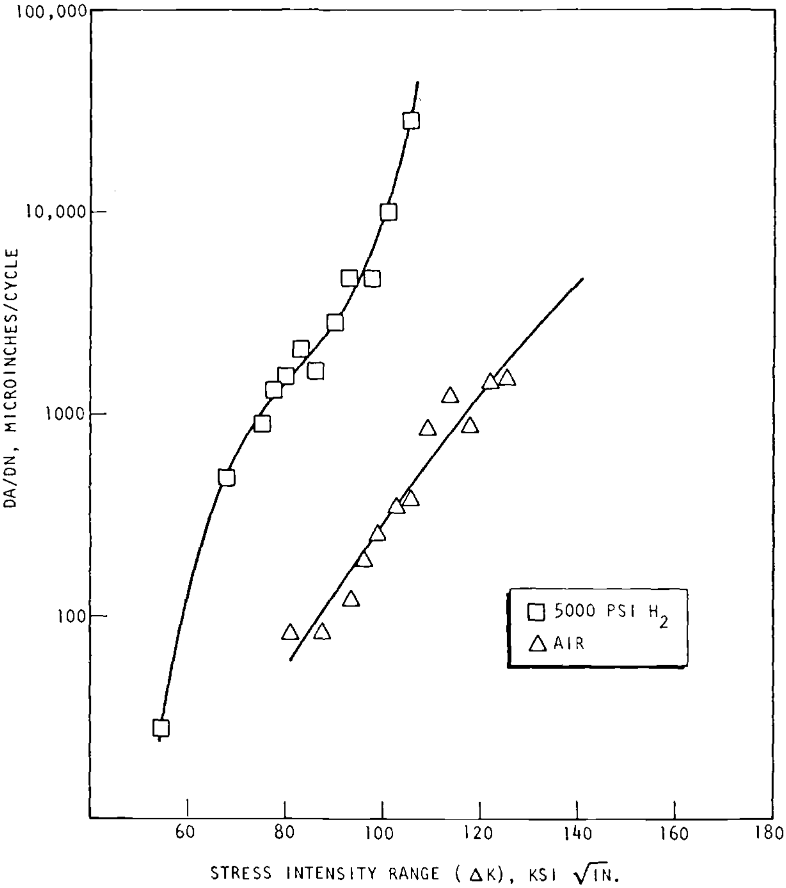

FIG. 7—da/dN *versus* ΔK *for cast Inconel 718 in air and in 5000-psi (34.5-MN/m²) hydrogen at ambient temperature. Specimen thickness = 1 in., and* R = *0.01.*

MN/m²) hydrogen are shown in Fig. 8. The fracture was transgranular and consisted of combinations of flat regions virtually free of microvoids and regions containing very small microvoids.

To relate these fracture modes to the microstructure, a specimen tested in hydrogen was sectioned, nickel plated to preserve the fracture edge, and the metallographic mount examined by SEM. Figure 9 shows the discontinuous subgrain carbide network comprising the microstructure, and the light shading around these carbide rows is the result of coring. The carbide evidently precipitated in the interdendritic spaces. It is reasonably evident from Fig. 9(*A*) that the fracture path followed the subgrain carbide network. Higher magnification (Fig. 9(*B*)) showed that the fracture proceeded around and through the carbide particles. It was quite evident that the

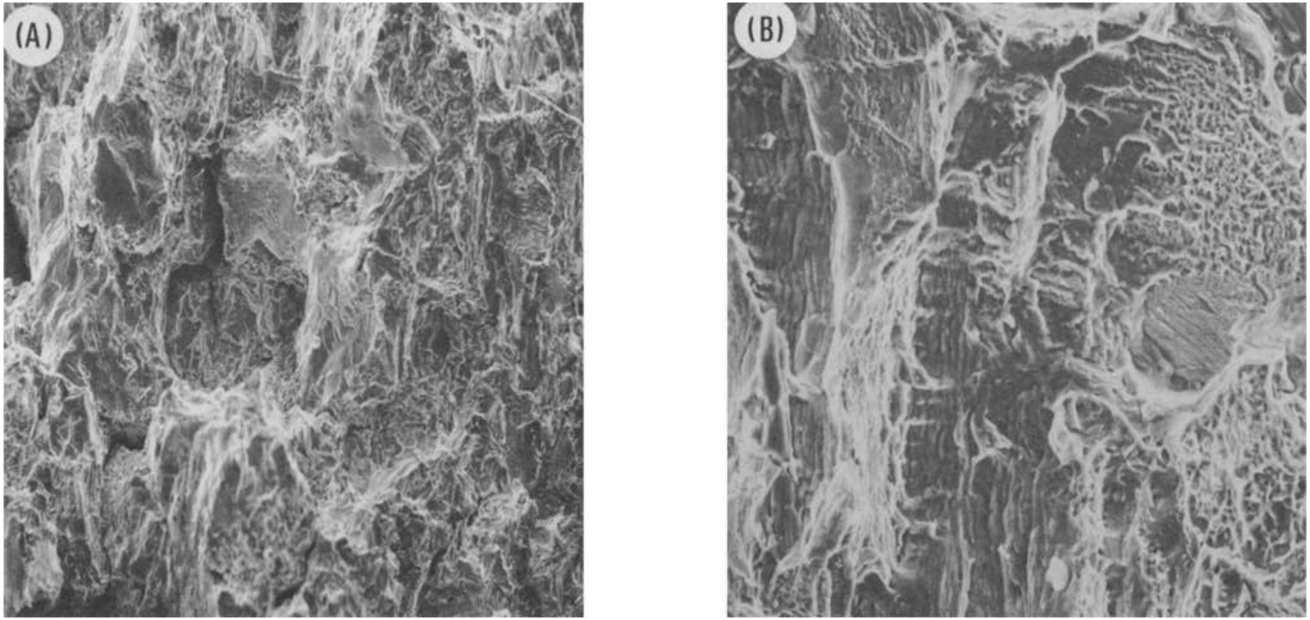

FIG. 8—*Fractographs of cast Inconel 718 specimen* da/dN *tested in 5000-psi hydrogen at ambient temperature.* (B) (×*1000) is a high magnification fractograph of the right middle of* (A) (×*100).*

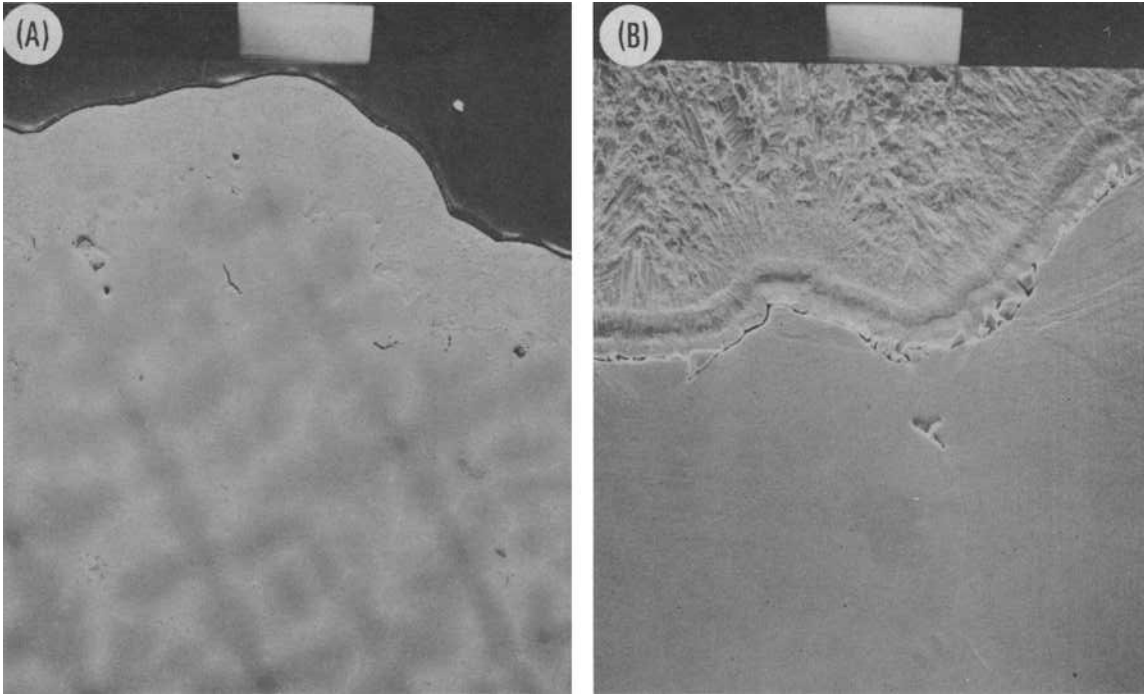

FIG. 9—*Scanning electron metallography at the fracture surface of cast Inconel 718* da/dN *tested in 5000-psi hydrogen at ambient temperature. Etchant: 50 percent hydrochloric acid (HCl) = 50 percent water (H_2O) plus hydrogen peroxide (H_2O_2).* (A) ×*50,* and (B) ×*500.*

carbide particles fractured easily as most of the larger particles present in the microstructure were cracked.

Interpretation of the fractography in terms of crack growth along the subgrain carbide network suggests that the flat brittle areas were associated with propagation around or through the larger carbides. The fine microvoid areas ajacent to the flat areas would likely be associated with very small carbides which acted as microvoid initiation sites.

Waspaloy

Waspaloy is another high-strength nickel-base alloy that is similarly embrittled by hydrogen. The tensile properties of Waspaloy are reduced in high-pressure hydrogen to a similar degree as those of Inconel 718.

Figure 10 presents the crack growth rate data for Waspaloy. The effect of 5000-psi (34.5-MN/m^2) hydrogen at room temperature on the crack growth rate at room temperature is quite similar to that observed for Inconel 718. The enhancement of the crack growth rate at −300°F (−149°C) in 4000-psi (27.6-MN/m^2) hydrogen was quite unexpected. Previous tensile property data had shown that hydrogen environment effects are not expected at cryogenic temperatures.

Figures 11 and 12 show the microstructure and a typical fractograph of Waspaloy *da/dN* tested in hydrogen at ambient temperature. The microstructure is duplex with second-phase particles present between the elongated grains. The fracture consisted mainly of transgranular brittle appearing fracture facets. The regions between these facets are associated with the intergranular microconstituents. High magnification (Fig. 12) shows that this fine featured region appears as intergranular fracture around these particles rather than small microvoids.

Alloy 903

Alloy 903 is another high-strength nickel-base alloy designed for low thermal expansion with the sacrifice of oxidation resistance. Tension tests have shown that this material is not affected by high pressure hydrogen at room temperature [5].

Figure 13 presents the data for Alloy 903 in air and in 5000-psi (34.5-MN/m^2) hydrogen at room temperature. The high-pressure hydrogen also has some effect on the crack growth rate but not to the extent that it has on the crack growth rate of Inconel 718 and Waspaloy.

The fracture surface of the Alloy 903 specimens tested in hydrogen was less brittle than corresponding Inconel 718 and Waspaloy fracture surfaces as would be expected from the relatively small increase of crack growth rate due to the hydrogen environment. Fractographic examination however did reveal the presence of brittle regions not observed on a similar speci-

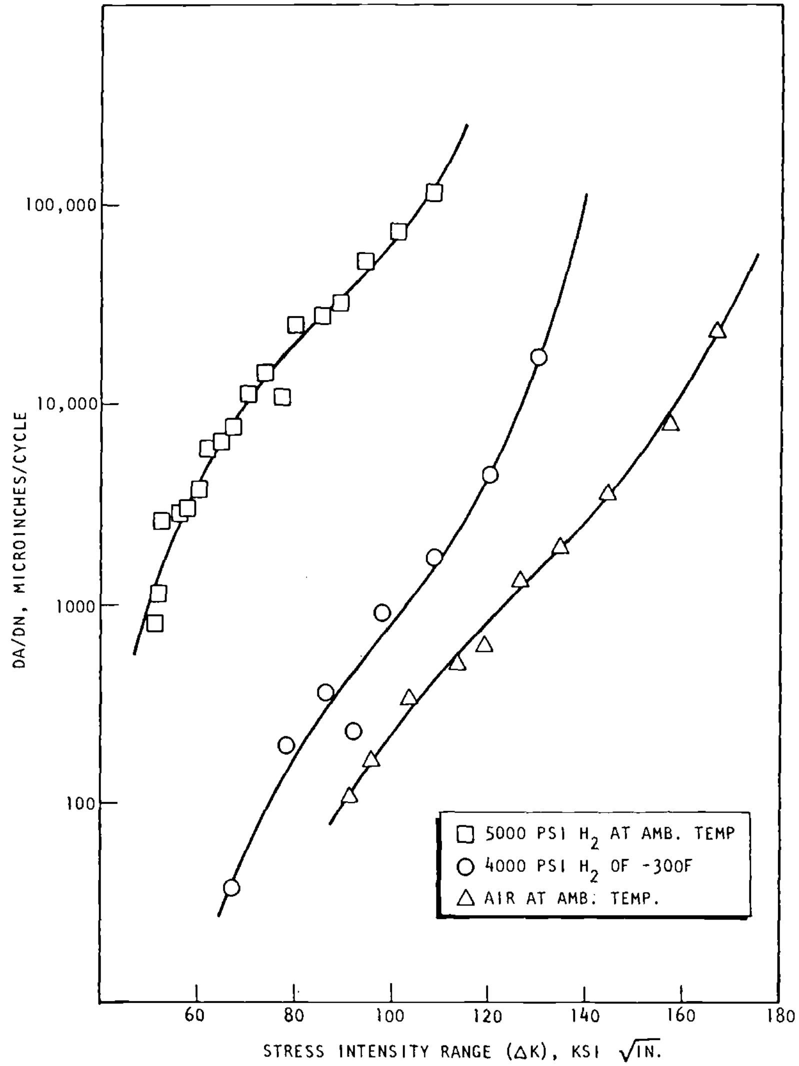

FIG. 10—da/dN *versus* ΔK *for Waspaloy in high-pressure hydrogen at various temperatures. Specimen thickness = 1 in., and* R = 0.01.

men tested in air. Figure 14 contains fractography of one of these brittle regions. The fracture consists of transgranular facets separated by colonies of very small microvoids. Energy dispersive analysis of X-rays (EDAX) revealed the brittle facets to be high in titanium, aluminum and columbium indicating that they were intermetallic compounds. It therefore appears that the hydrogen environment promoted fracture of the relatively large second-phase particles present in the microstructure.

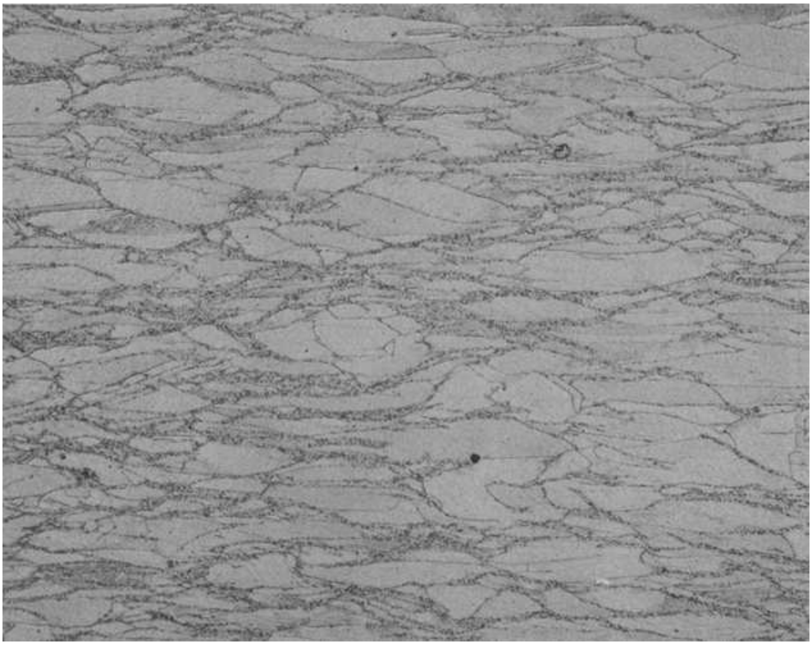

FIG. 11—*Photomicrograph of Waspaloy. Etchant: ammonium per sulfate* (×*100*).

The subcritical crack growth regions of specimens tested in air and in 5000-psi (34.5-MN/m^2) hydrogen were compared to determine whether the hydrogen promoted void nucleation and resulting decrease of dimple size as discussed by Thompson [*6*]. Qualitative comparisons indicated that the dimple sizes obtained in hydrogen were smaller than those obtained in air at approximately the same stress intensity levels. The size differences however were not as great as the ratio of 0.4 obtained by Thompson on precharged specimens.

Thus, the fractography examination of the Alloy 903 specimen suggests that hydrogen promoted (*a*) fracture of the relatively large second-phase particles in the microstructure, and (*b*) void nucleation either by affecting decohesion of small microconstituent particles from the matrix or by promoting fracturing of these particles.

Summary

The 9-min cycle crack growth rate of wrought Inconel 718 and Waspaloy was 2 to 4 orders of magnitude greater in high-pressure hydrogen than in air. The threshold stress intensity needed for a substantial increase in crack

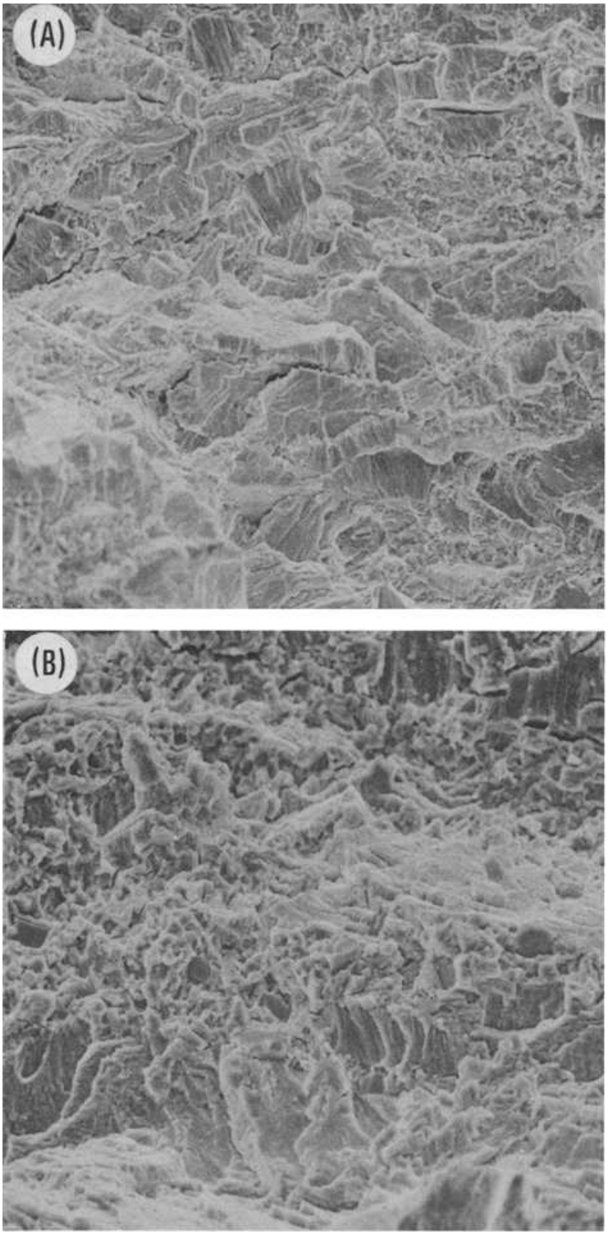

FIG. 12—*Fractographs of Waspaloy compact specimen* da/dN *tested in 4000-psi (27.6-MN/N*^{2}*) hydrogen at ambient temperature.* (B) *×1000 is a fractograph of a fine featured region between the transgranular facets in* (A) *×500.*

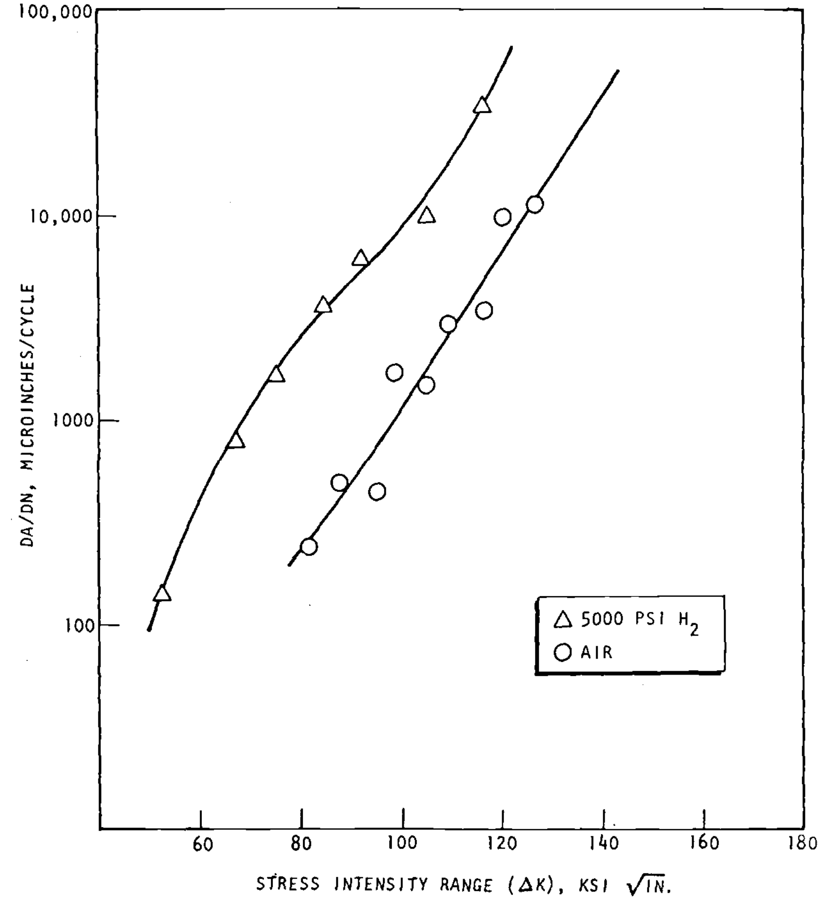

FIG. 13—da/dN *versus* ΔK *for Alloy 903 in air and in 5000-psi (34.5-MN/m*^{2}*) hydrogen at ambient temperature. Specimen thickness = 1 in., and* R = *0.01.*

growth rate appears to be about 40 ksi $\sqrt{\text{in.}}$ (44 MN/m^2 $\sqrt{\text{m}}$) which corresponds to a reported threshold stress intensity of 38 ksi $\sqrt{\text{in.}}$ (41.8 MN/m^2 $\sqrt{\text{m}}$) for sustained load crack growth in Inconel 718. Associated with the increased crack growth rate when tested in hydrogen was a change from a ductile fracture mode in air to a brittle transgranular or intergranular fracture mode in hydrogen.

The crack growth rate in cast Inconel 718 and Alloy 903 also was increased by exposure to high-pressure hydrogen but the increase was substantially less than occurred in wrought Inconel 718 and Waspaloy. The fracture of these alloys contained brittle facets separated by regions containing small microvoids. These fractography variations were related to second-phase particles in the microstructures.

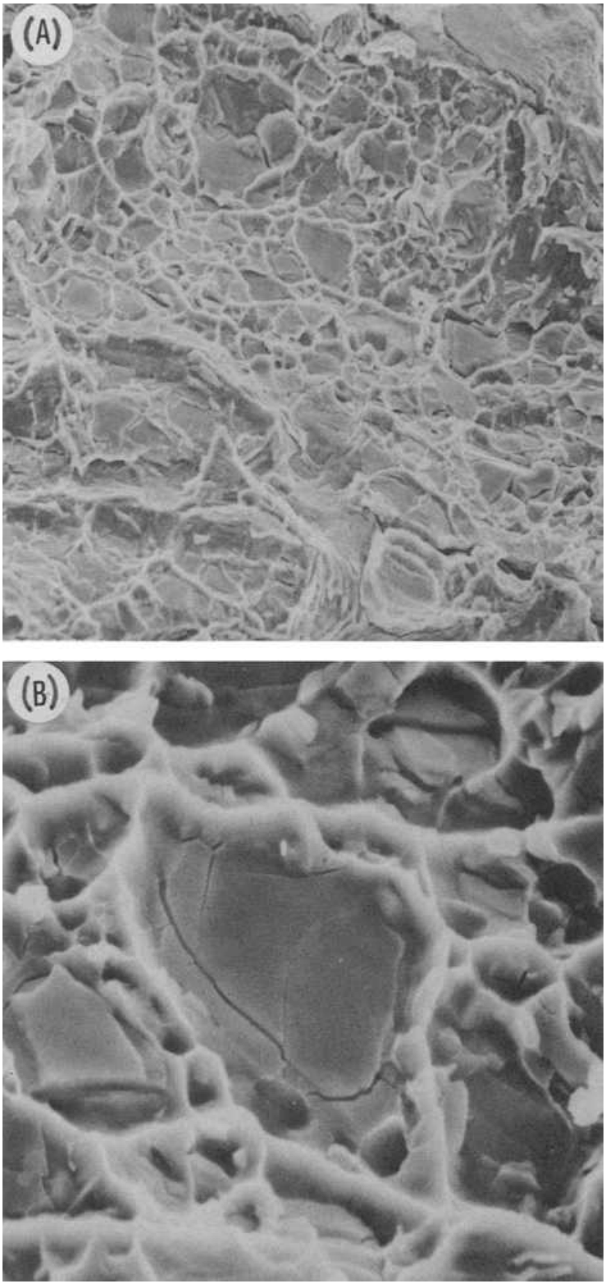

FIG. 14—*Fractographs of Alloy 903 TDCB specimen* da/dN *tested in 5000-psi (34.5-MN/m^2) hydrogen at ambient temperature.* $\Delta K = 55$ *ksi* $\sqrt{in.}$ *(60.5* $MN/m^2\sqrt{m}$). (B) (×*5000) is a higher magnification fractograph of the middle of* (A) (×*100).*

Acknowledgments

This work was supported by the National Aeronautics and Space Administration (NASA) as part of the Space Shuttle Main Engine Program, NASA Contract NAS8-27980. The *da/dN* tests were performed by R. W. Parker, D. A. Bowman, and R. F. Rothring. Metallography was performed by J. D. Frandsen and L. J. Havemann at Rockwell Science Center and Rocketdyne, respectively.

References

[*1*] Chandler, W. T. and Walter, R. J. in *Hydrogen Embrittlement Testing, ASTM STP 543,* American Society for Testing and Materials, 1974, pp. 170-197.

[*2*] Jewett, R. P., *Closed Loop,* Vol. 4, No. 3, 1974, pp. 2-9.

[*3*] Thatcher, C. S., "Fracture of Aluminum Alloy 2219-T87," Report SD72-SH-0129, Space Division, Rockwell International, Downey, Calif., 1972.

[*4*] Walter, R. J. and Chander, W. T., "Influence of Gaseous Hydrogen on Metals—Final Report," CR-124410, Rocketdyne Division, Rockwell International, National Aeronautics and Space Administration, Oct. 1973.

[*5*] Carpenter, H. W., *Metals Progress,* Aug. 1976.

[*6*] Thompson, A. W. in *Effect of Hydrogen on Behavior of Materials,* A. W. Thompson and I. M. Bernstein, Eds. American Institute of Mining, Metallurgical, and Petroleum Engineers, Inc., New York, 1976, pp. 467-477.

B. Mukherjee[1]

Effect of Hydrogen Gas on High Strength Steels

REFERENCE: Mukherjee, B., "**Effect of Hydrogen Gas on High Strength Steels,**" *Corrosion-Fatigue Technology, ASTM STP 642,* H. L. Craig, Jr., T. W. Crooker, and D. W. Hoeppner, Eds., American Society for Testing and Materials, 1978, pp. 264-285.

ABSTRACT: A possible failure mode of high strength steels that are used in hydrogen gas-cooled turbine generators can be described by a combination of environment-assisted crack initiation, crack propagation by fatigue, and sustained load and final fracture. Therefore, a project was initiated to study the fracture properties in hydrogen and hydrogen sulfide (H_2S) gas of two high strength steels, 3.5 nickel-chromium-molybdenum-vanadium ferritic and 18Mn-4Cr austenitic, which are commonly used for generator end rings. Two specimen types were employed, blunt notch specimens for crack initiation studies and precracked specimens for crack propagation and stress corrosion cracking studies. Tests were conducted to determine crack initiation due to incrementally rising load in H_2S, crack propagation due to fatigue loading in hydrogen (H_2), and K_{Iscc} in H_2. This paper presents experimental data and provides metallurgical evidence to show that the failure mechanism in the specimens is environment assisted.

KEY WORDS: corrosion fatigue, crack propagation, nickel-base alloys, hydrogen embrittlement, fractography

High strength steels are embrittled when they are exposed to hydrogen gas or a hydrogen-bearing environment at ambient temperature and are subjected to tensile load [*1*].[2] This limitation must be taken into account in materials selection and design of systems where hydrogen gas is used as fuel, propellant, or coolant. Turbine generators usually are cooled by hydrogen (H_2) gas, therefore, an experimental program was initiated to determine the effect of H_2 on the fracture properties of two high strength steels commonly used for turbine generator end rings, which are commonly

---

[1] Engineer, Fracture Mechanics, Ontario Hydro Research Laboratories, Toronto, Ontario, Canada. M8Z 5S4.

[2] The italic numbers in brackets refer to the list of references appended to this paper.

known as retaining rings in the United States. In this smoothly polished component, crack initiation will be the first and perhaps the most important stage in its resistance to failure. Such a failure, emanating from a stress concentration, has been reported by Jolly et al [*2*]. However, if crack initiation takes place, it can propagate then by a stress corrosion cracking mechanism under sustained load or by cyclic fatigue load. This experimental program, therefore, concentrated on crack initiation due to rising load, crack initiation due to sustained load, and crack propagation due to cyclic fatigue load.

In 1972, McIntyre and Priest [*3*] reported that K_{Iscc} values determined for a series of high strength steels exceeding 1380-MPa (200-ksi) yield strength exposed to sea water, H_2 gas and hydrogen sulfide (H_2S) gas environment were essentially independent of the test environment. In addition, they noted that the crack growth rates in H_2S were faster than those experienced in either sea water or H_2 gas. On the basis of these observations McIntyre and Priest proposed that K_{Iscc} testing in H_2S can be used as an accelerated test procedure for evaluating a material's stress corrosion threshold in other H_2 bearing environments. In view of the potential advantages associated with the accelerated K_{Iscc} tests, Clark and Landes [*4*] initiated an extensive program to evaluate further the technique and its limitation using fatigue precracked specimens. The accelerating H_2S environment was used in this program to assess the possibility of H_2 assisted crack initiation at stress concentrations using techniques similar to those established by Deans et al [*5*].

Test Materials

Two basic compositions, which are used practically for all end rings, were selected for this test program. A ferritic alloy steel forging of ASTM Specification for Carbon and Alloy Steel Forgings for Magnetic Retaining Rings for Turbine Generators (A 288) (hereafter referred to as 3.5 nickel-chromium-molybdenum-vanadium) (3.5-Ni-Cr-Mo-V) and an austenitic alloy steel forging of ASTM Specification for Alloy Steel Forgings for Nonmagnetic Retaining Rings for Generators (A 289) (18Mn-4Cr) are used for magnetic and nonmagnetic end rings, respectively. Both materials were taken from actual end rings and their chemical analyses and mechanical properties are shown in Tables 1 and 2. The stress-strain curves for these materials are shown in Fig. 1. For several experiments the ferritic material was retempered to obtain variations in strength levels. Because of the anisotropy of these materials, specimen orientation is an important variable. The orientation designation of the specimens used is shown in Fig. 2, and for the compact-tension and the wedge-opening-load (WOL) specimens, these correspond to ASTM Test for Plane-Strain Fracture Toughness of Metallic Materials (E 399).

TABLE 1—*Chemical composition and mechanical properties of ASTM Specification A 288 steel, ferritic material, Nanticoke unit 2 generator end ring.*

	Elemental Analysis, %									Mechanical Properties					
										0.2% Yield Stress		Ultimate Tensile Strength		Elongation,	Reduction in
Reference	C	Si	Mn	S	P	Ni	Cr	Mo	V	N/mm^2	tonf/in^2	N/mm^2	tonf/in^2	%	Area, %
KEW	0.39	0.30	0.60	0.006	0.004	3.20	0.82	0.63	0.19	1250	81.0	1340	87.0	15	42

TABLE 2—*Chemical composition and mechanical properties of ASTM Specification A 289 steel, austenitic material, taken from end rings.*

	Elemental Analysis, %										Mechanical Properties					
											0.2% Yield Stress		Ultimate Tensile Strength			Reduction in
Reference	C	Si	Mn	S	P	Cr	Ni	N_2	V	Mo	N/mm^2	tonf/in^2	N/mm^2	tonf/in^2	Elongation, %	Area, %
HVB[a]	0.45	0.33	18.3	0.004	0.05	4.08	...	...	...	0.09	990	64.0	1270	84.0	24	

[a] This ring was part explosively formed.

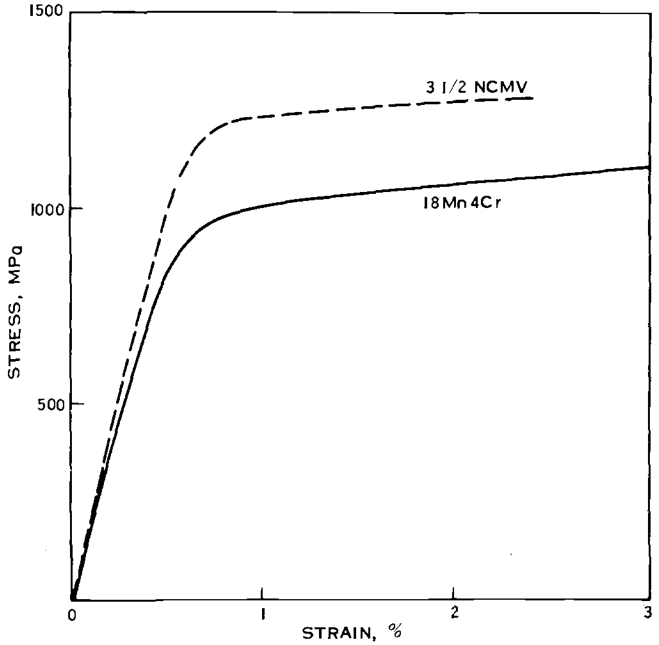

FIG. 1—*Stress-strain curves for the 3.5-Ni-Cr-Mo-V and the 18Mn-4Cr steels.*

Incrementally Rising Load Test

Round notched tension specimens, Fig. 3(*a*), and modified WOL specimens, Fig. 3(*b*), were used in this test program. The specimens were tested in a specially constructed plexiglass chamber at room temperature and atmospheric pressure in flowing H_2S gas (99.0 volume percent, liquid phase, H_2S, typically 31-ppm water) or in flowing H_2 (99.95 percent pure industrial grade H_2, 22-ppm water, 10-ppm (O_2), and <25-ppm hydrocarbon). Each specimen was degreased before insertion into the chamber. The chamber was flushed with argon gas before H_2S was introduced.

The notched tension specimens were loaded initially to 20 kN. The load was increased incrementally by 5-kN steps with a 5-min hold between steps. In general, the 3.5Ni-Cr-Mo-V specimens failed immediately upon reaching a higher load. In most of the 18Mn-4Cr specimens, failure occurred during the load holding period. Because of the extremely rapid rate of crack growth associated with the material environment system involved here, the load associated with the initiation of a crack was essentially identical to the load required to cause failure of the specimen.

The results of crack initiation testing involved in this investigation are expressed in terms of elastically calculated maximum notch stress, σ_{max}, and maximum elastic notch strain, ϵ_{max}.

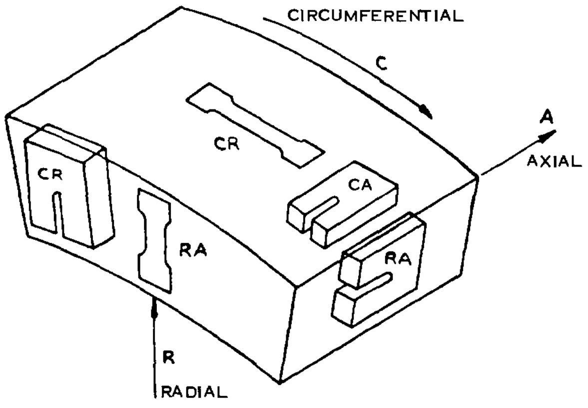

WOL SPECIMENS

FIRST LETTER DESIGNATES THE DIRECTION NORMAL TO THE CRACK PLANE AND THE SECOND LETTER, THE EXPECTED DIRECTION OF CRACK PROPAGATION.

NOTCHED TENSILE SPECIMENS

FIRST LETTER DESIGNATES DIRECTION NORMAL TO THE FRACTURE PLANE.

FIG. 2—*Specimen orientation of notched tension and WOL specimens.*

The nominal stress in the notched specimen is given by

$$\sigma_N = \frac{4P}{\pi d^2}$$

where P is the load at failure, and d is the diameter of the reduced section. The stress concentration factor, K_T, which is 2.5 for this specimen is determined from Peterson [*6*]. Maximum elastic stress and strain can then be calculated by

$$\sigma_{\max} = K_T \cdot \sigma_N$$

and

$$\epsilon_{\max} = \sigma_{\max}/E$$

The WOL specimens were loaded initially to 5 kN and incremental loading of 5 kN with a 5-min hold period was continued until failure. Each specimen surface was observed visually, but the first "sight" of initiation to fracture was virtually instantaneous. Using the geometry shown in Fig. 3(*b*), the nominal stress at the notch root is given by

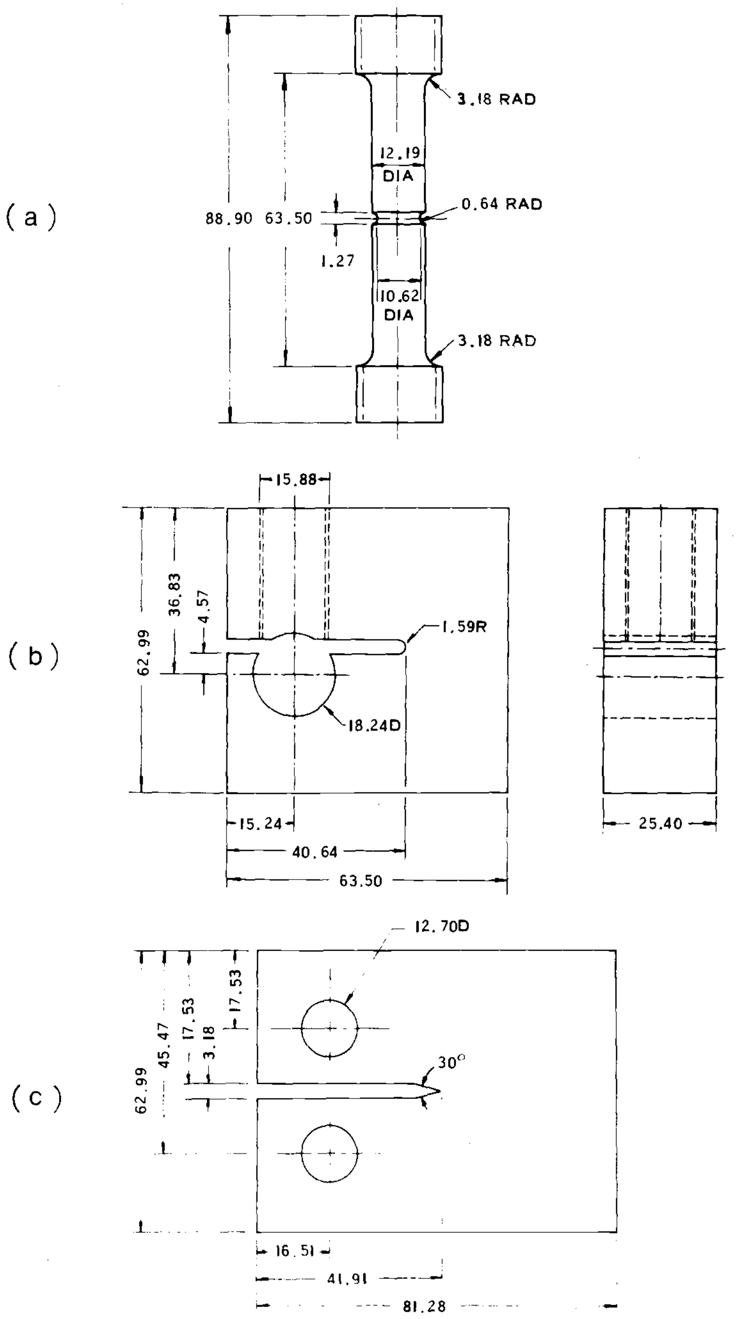

FIG. 3—*Specimens* (a) *round notched tension specimen,* (b) *modified WOL type specimen, and* (c) *WOL specimen for crack propagation tests.*

$$\sigma_N = \left[\frac{3(W + a)}{(W - a)} + 1 \right] \frac{P}{(W - a)}$$

σ_{max} is again given by $\sigma_{max} = K_T. N$ where $K_T = 3.2$ is the stress concentration factor for this geometry [*7*]. Maximum elastic stress, ϵ_{max}, is again given by $\epsilon_{max} = \sigma_{max}/E$.

Recent investigations have shown that crack initiation is primarily a strain dependent phenomenon [*8*]. Wilson [*9*] has also shown analytically that total notch strain is a unique, but not a linear, function of the elastically calculated notch stress or strain for the material of interest, provided plastic flow in the vicinity of the notch base is constrained. In order to varify Wilson's conclusion experimentally, the total strains at the root of several blunt-notched WOL specimens were measured using strain gages and the total notch root strains are plotted against applied load in Figs. 4 and 5. Calculated elastic strains also are shown in these figures. The stress-strain curves for 3.5-Ni-Cr-Mo-V and 18Mn-4Cr steels plotted in Fig. 1 show that unnotched tension specimens deform plastically at approximately 0.4 percent strain. In the modified WOL specimens, plastic flow in the vicinity of the notch base is constrained by large amounts of elastic material surrounding the plastic zone. The load strain behavior at the base of the notch is linear up to 1 percent strain for both materials and can be estimated to a close degree by an elastic estimation up to 1.5 percent strain, see Figs. 4 and 5. Elastic strains at failure, therefore, are plotted for 18Mn-4Cr steel against three variables, environment, orientation, and specimen type in Fig. 6. Experiment results from 3.5-Ni-Cr-Mo-V notched

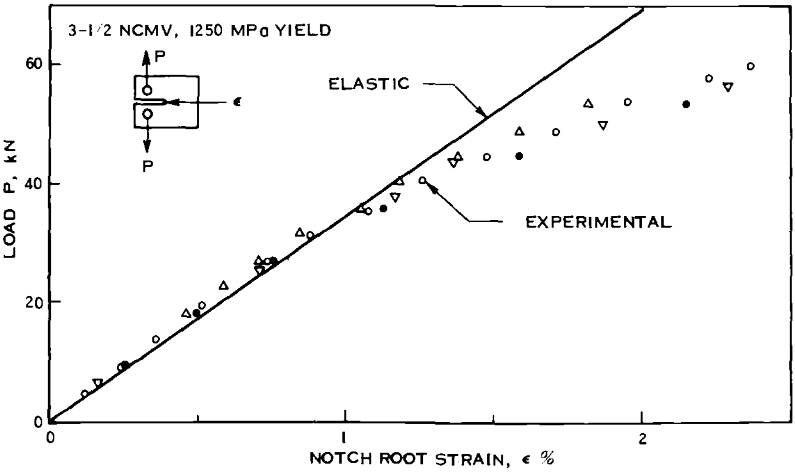

FIG. 4—*Measured notch root strain and its elastic estimation in 3.5-Ni-Cr-Mo-V modified WOL specimen.*

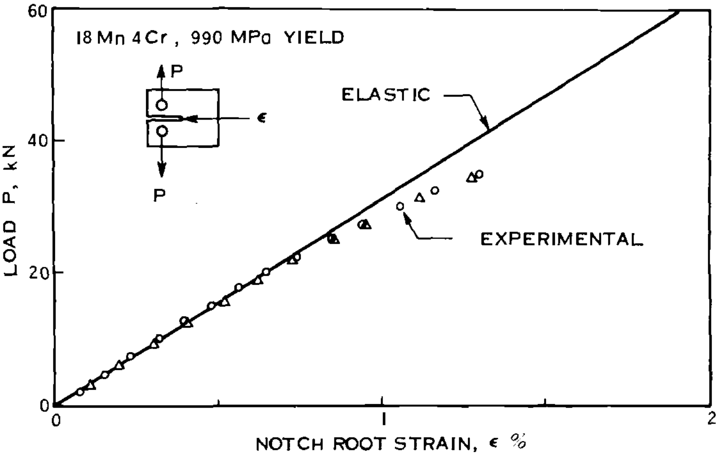

FIG. 5—*Measured notch root strain and its elastic estimation in 18Mn-4Cr modified WOL specimen.*

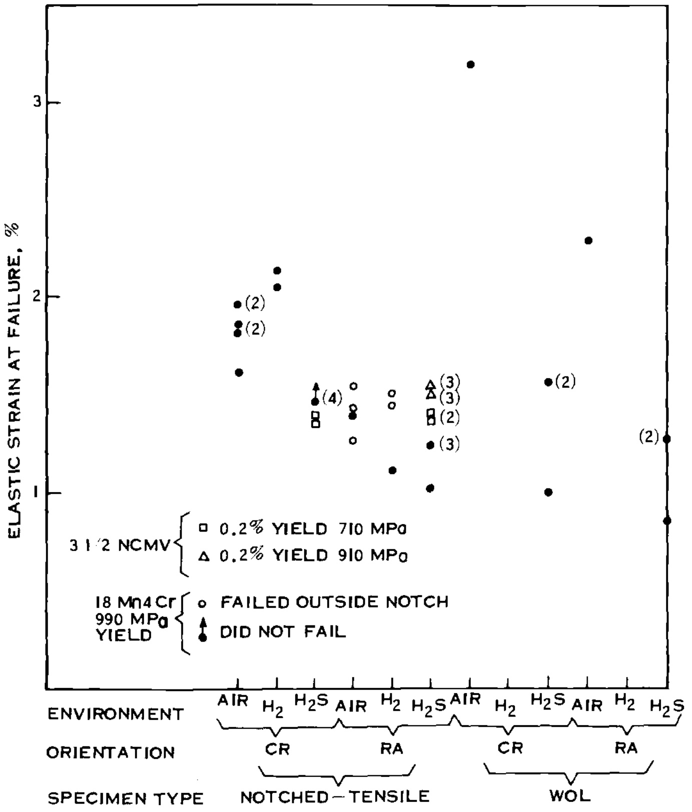

FIG. 6—*Elastic strains at failure in air, H_2, and H_2S.*

tension specimens in H_2S also are shown in Fig. 6. All H_2S test results on both end ring materials are shown in Tables 3 and 4.

Crack Initiation Under Sustained Load

Eleven modified WOL specimens (Fig. 2(*b*)) were machined from 1250-MPa yield strength 3.5-Ni-Cr-Mo-V steel and self-loaded in air to various loads between 71 and 116 kN. The elastic strain at the base of these notches ranged from 2.07 to 3.38 percent. The self-loaded specimens were transferred to a chamber containing H_2 at room temperature and 0.31 MPa (45 psi) pressure. The specimens were removed periodically and examined under an optical microscope for signs of crack initiation at root radii and specimen surfaces. The most highly stressed specimen with an initial load of 116 kN and an elastic strain of 3.38 percent failed after 330 h in H_2. The next most highly stressed specimen was loaded to 111 kN and an elastic strain of 3.23 percent. This specimen and the remaining specimens did not show any sign of crack initiation after 3000 h. These specimens then were returned in the chamber and reexamined after 7000 h, but still no signs of crack initiation were observed.

K_{Iscc} Tests

Self-loaded compact tension specimens similar to those shown in Fig. 2(*b*) were used to measure K_{Iscc} in 1250-MPa yield strength 3.5-Ni-Cr-Mo-V and 990-MPa yield strength 18Mn-4Cr steels. A sharp crack was introduced in these specimens either by fatigue precracking or by using a spark machine (electrical discharge machine (EDM)). An experimental method which has been described by Novak [*10*] was followed to self-load these specimens in air to preselected stress intensity factors. The specimens were transferred to a chamber containing hydrogen at room temperature and 0.31-MPa (45-psi) pressure. They were removed periodically and examined for signs of crack extension. In these constant displacement specimens, crack extension caused a decrease in the crack tip stress intensity factor. The reduced stress intensity factors were measured also by following the method described in Ref *10*. Results from these experiments are shown in Table 5. Two 3.5-Ni-Cr-Mo-V specimens were fatigue precracked and self-loaded to an initial stress intensity of 101 MPa $\sqrt{m}$. Both of these specimens failed after 330 h in H_2. However, the crack path turned at right angles to the anticipated propagation direction, Fig. 7, and an estimation of K_{Iscc}, therefore, was not possible. Other specimens were loaded to lower initial stress intensity factors and the cracks propagated at right angles to the applied load. In the 3.5-Ni-Cr-Mo-V steel, the stress corrosion type of crack did not incubate in the CA orientation from an EDM notch after 10 000 h in H_2; in the CR orientation its K_{Iscc} value was 67

TABLE 3—*H_2S tests of 18Mn-4Cr end ring material.*

Material Reference	0.2% Yield, Stress, N/mm^2	Specimen Type	Specimen Orientation	Notch Surface Finish	Load at Failure (kN)	σ N/mm^2	$\epsilon_{max} = \sigma_{max}/E$ % $E = 1.88 \times 10^5$ N/mm^2
HVB (this ring was part explosively formed)	990	notch tensile	CR	turned	124	3493	1.86[a]
		notch tensile	CR	turned	123	3467	1.84[a]
		notch tensile	CR	turned	123	3467	1.84[a]
		notch tensile	CR	turned	108	3053	1.62[a]
		notch tensile	RA	turned	67	1939	1.03
		notch tensile	RA	turned	83	2354	1.25
		notch tensile	RA	turned	83	2354	1.25
		notch tensile	RA	turned	83	2354	1.25
		WOL	RA	milled	27	1618	0.86
		WOL	RA	milled	40	2427	1.29
		WOL	RA	milled	27	1618	0.86
		WOL	CR	milled	31	1888	1.00
		WOL	CR	milled	49	2966	1.58
		WOL	CR	milled	49	2966	1.58

[a] Tests unbroken in H_2S at load 98 kN, $\sigma_{max} = 2769$ N/mm^2 and $\epsilon = 1.47$ percent. The specimens are taken to failure in air at values indicated by this footnote.

TABLE 4—*H_2S tests on 3.5-Ni-Cr-Mo-V end ring material.*

Material Reference	0.2% Yield Stress, N/mm^2	Specimen Type	Notch Specimen Orientation	Notch Surface Finish	Load at Failure, kN	σ_{max}, N/mm^2	$\epsilon_{max} = \sigma_{max}/E$ % $E = 2.07 \times 10^5$ N/mm^2
KEW (Nanticoke End Ring Material)	710	notch tensile	CR	turned	102	2889	1.40
		notch tensile	CR	turned	101	2865	1.38
		notch tensile	RA	turned	101	2865	1.38
		notch tensile	RA	turned	102	2877	1.39
		notch tensile	RA	turned	103	2914	1.41
	910	notch tensile	RA	turned	111	3139	1.52
		notch tensile	RA	turned	114	3228	1.56
		notch tensile	RA	turned	111	3139	1.52
		notch tensile	RA	turned	114	3228	1.56
		notch tensile	RA	turned	111	3139	1.52
		notch tensile	RA	turned	113	3203	1.54
	944	WOL	RA	milled	111	6741	3.26
		WOL	RA	milled	113	6849	3.30
	1041	WOL	CR	milled	>116	>7011	>3.38

TABLE 5—*Experimental results from* K_{Iscc} *tests in* H_2.

Material	Orientation	Notch Preparation	Initial Stress Intensity, MPa $\sqrt{m}$	Time in H_2, h	Final Stress Intensity, K_{Iscc}, MPa $\sqrt{m}$	Comments
3.5-Ni-Cr-Mo-V 0.2% yield = 1250 MPa	AR	fatigue crack	101	330		crack turned through an angle
	AR	fatigue crack	101	330		crack turned through an angle
	CA	EDM	101	10 000[a]		no growth
	CA	EDM	90	10 000[a]		no growth
	CR	EDM	80	10 000[a]	67	
18MN-4Cr 0.2% yield = 990 MPa	CR	EDM	90	7 000	85	
	CR	EDM	68	7 000	64	
	RA	EDM	79	7 000	54	

[a] First inspected after 3000 h.

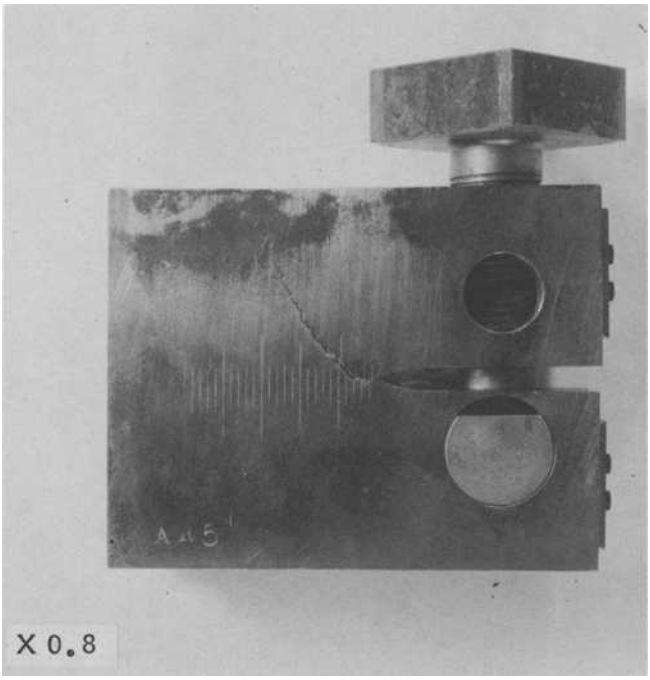

FIG. 7—*Failure in H_2 of a self-loaded 3.5-Ni-Cr-Mo-V specimen.*

MPa$\sqrt{m}$. In the 18Mn-4Cr steel, stress corrosion type of cracks initiated from EDM slots in CR and RA orientation, and its K_{Iscc} values for corresponding orientations were 64 and 54 MPa $\sqrt{m}$, respectively.

Fatigue Crack Propagation

Figure 2(*c*) shows the specimens used for studying fatigue crack propagation in the 3.5-Ni-Cr-Mo-V steel of 1250-MPa yield strength. Fatigue tests were conducted in a closed-loop servohydraulic testing machine. A chamber was designed to enclose the specimens in flowing H_2 at room temperature and 0.0344-MPa (5-psi) pressure. Fatigue crack length on the specimen surface was measured using a microscope through an observation window. Figure 8 shows crack lengths plotted against cycles to failure for two identical tests in air and H_2, and it shows that crack growth rate is faster in hydrogen than that in air. Five experiments were conducted: one specimen was tested in air at load ratio $R \approx 0$, and four specimens were tested in hydrogen, two at $R \approx 0$ and two at $R = 0.4$. Stress intensity factors at given crack lengths were determined using the following equation

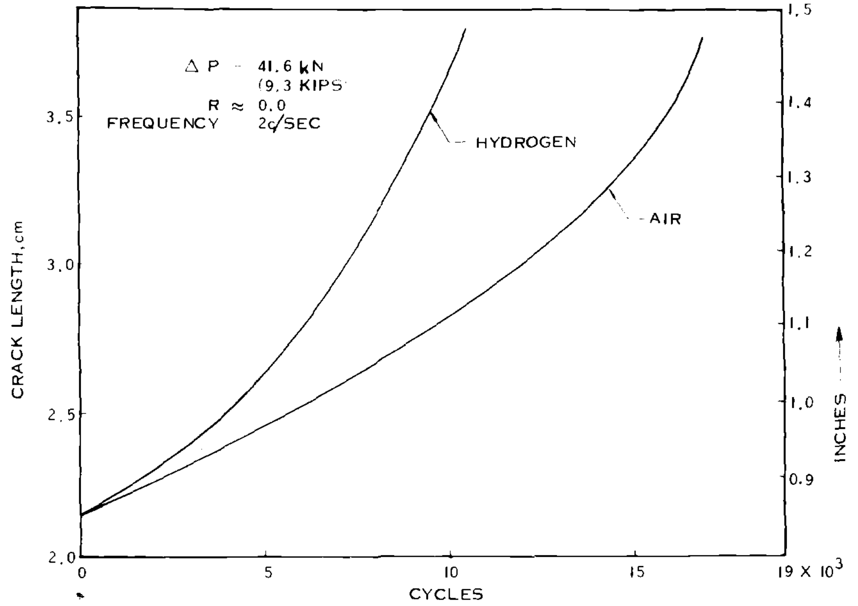

FIG. 8—*Fatigue crack growth in air and H_2 in 3.5-Ni-Cr-Mo-V steel.*

$$K_I = \frac{P\sqrt{a}}{BW}\,[30.96 - 195.8\,(a/W) + 730.6\,(a/W)^2 - 1186.3\,(a/W)^3 + 754.6\,(a/W)^4]$$

where

P = applied load,
a = total crack length (measured from load line),
B = specimen thickness, and
W = specimen width.

Crack growth rate was determined using the secant (point-to-point) method and the growth rates are plotted against ΔK, range of stress intensity factor, for five specimens in Fig. 9. Results presented in Fig. 9 show that fatigue crack growth rate is faster in H_2 than in air. At a given ΔK, an increase in load ratio, R, increases growth rate. When ΔK exceeds 100 MPa $\sqrt{m}$ (91 ksi $\sqrt{in.}$), growth rate increases very rapidly and failure occurs within a few hundred cycles. The equation of the best straight lines drawn through the experimental points using the method of least squares are given in Table 6.

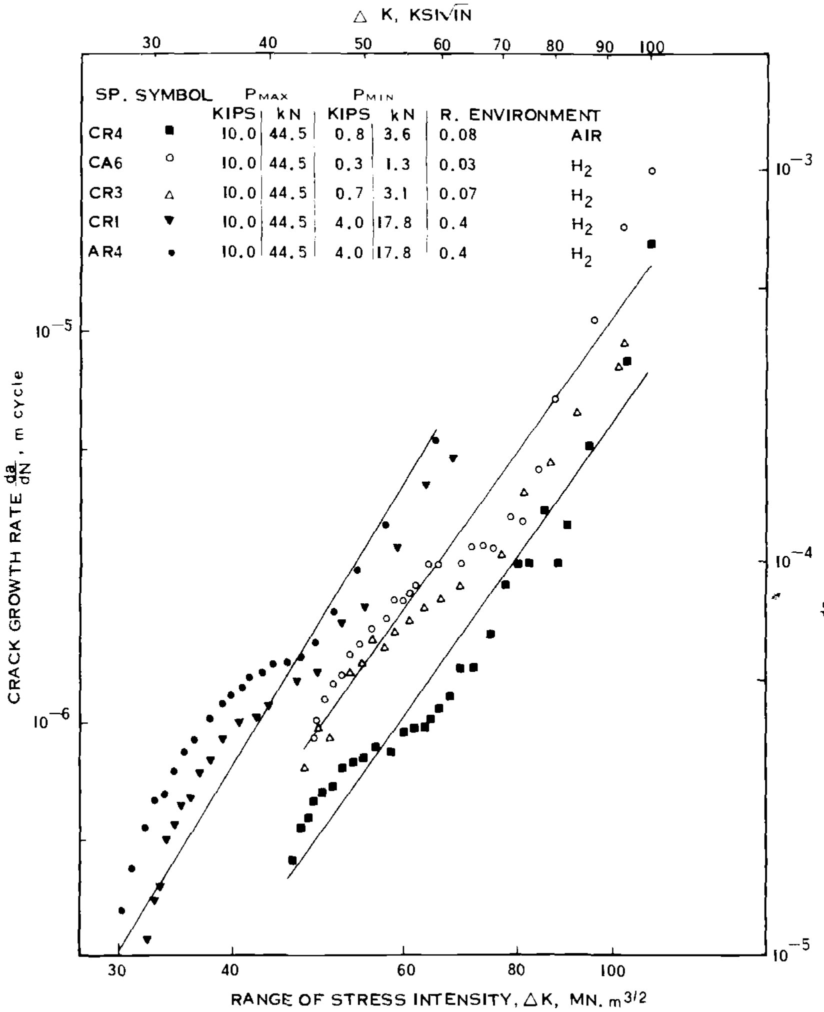

SP.	SYMBOL	PMAX KIPS	PMAX kN	PMIN KIPS	PMIN kN	R.	ENVIRONMENT
CR4	■	10.0	44.5	0.8	3.6	0.08	AIR
CA6	○	10.0	44.5	0.3	1.3	0.03	H_2
CR3	△	10.0	44.5	0.7	3.1	0.07	H_2
CR1	▼	10.0	44.5	4.0	17.8	0.4	H_2
AR4	●	10.0	44.5	4.0	17.8	0.4	H_2

FIG. 9—*Fatigue crack growth rate in air and* H_2 *in 3.5-Ni-Cr-Mo-V steel.*

Discussion of Results

The experimental data generated in this test program clearly indicate that the H_2S environment has a detrimental effect on the strain required for a crack to initiate from a blunt notch in the 18Mn-4Cr steel under incrementally rising load test. Notched tension specimens and modified WOL specimens were used in the experiments described in Fig. 6 and Table 4. These specimens exhibit different stress/strain distribution ahead of the crack tip, however, the elastic strains at failure in H_2S appear to be independent of specimen geometry. This material is highly anisotropic

TABLE 6—*Equations of crack growth rate in air and H_2.*

1. Air, load ratio, $R = 0$, frequency, $f = 2$ Hz	
$\frac{da}{dN} = 10^{-11.87}(\Delta K)^{3.31}$ m/cycle	ΔK in MPa $\sqrt{\text{m}}$
$\left[\frac{da}{dN} = 10^{-10.14}(\Delta K)^{3.31}\text{ in./cycle}\right]$	ΔK in ksi $\sqrt{\text{in.}}$
2. Hydrogen, $R = 0, f = 2$ Hz	
$\frac{da}{dN} = 10^{-11.41}(\Delta K)^{3.18}$ m/cycle	ΔK in MPa $\sqrt{\text{m}}$
$\left[\frac{da}{dN} = 10^{-9.69}(\Delta K)^{3.18}\text{ in./cycle}\right]$	ΔK in ksi $\sqrt{\text{in.}}$
3. Hydrogen, $R = 0.4, f = 2$ Hz	
$\frac{da}{dN} = 10^{-12.41}(\Delta K)^{3.94}$ m/cycle	ΔK in MPa $\sqrt{\text{m}}$
$\left[\frac{da}{dN} = 10^{-10.66}(\Delta K)^{3.94}\text{ in./cycle}\right]$	ΔK in ksi $\sqrt{\text{in.}}$

and RA is the weakest orientation. Within each orientation there is also large inherent variability of material properties. The elastic strain at failure in H_2S varied between 0.86 and 1.29 percent in RA orientation. The corresponding values in air were between 1.28 and 2.3 percent. Incremental loading test in H_2 with 5-kN load steps and 5-min hold between steps (average loading rate 1 kN/min) did not reduce significantly the strain at failure. This is consistent with the finding of Clark [*8*]. He observed that in rising load K_{Iscc} of 1240-MPa (180-ksi) yield strength 4340 steel determined in H_2S at loading rates of 0.1 to 10 kN/min is independent of loading rate, but K_{Iscc} in H_2 is strongly loading rate dependent. Loading rate of 0.1 kN/min is required to obtain K_{Iscc} value which is comparable to that in H_2S.

Elastic strains at failure in the 3.5-Ni-Cr-Mo-V steel determined from incrementally rising load in H_2S (Table 4) is somewhat difficult to interpret as the failure strains appear to be dependent on specimen geometry. The round notched tension specimens failed at elastic strains between 1.38 to 1.56 percent but the modified WOL specimens failed between 3.26 and 3.38 percent. This observation could be attributed to the difference in macroscopic failure modes of these specimens. While in H_2S, the round notched tension specimens failed in brittle manner, the modified WOL specimens showed considerable plastic deformation, see Fig. 10(*a*). It should be noted that for 18Mn-4Cr steel, both notched tension specimens and modified WOL specimens failed in a brittle manner in H_2S, see Fig. 10(*b*). However, in air, 18Mn-4Cr modified WOL specimens failed in a

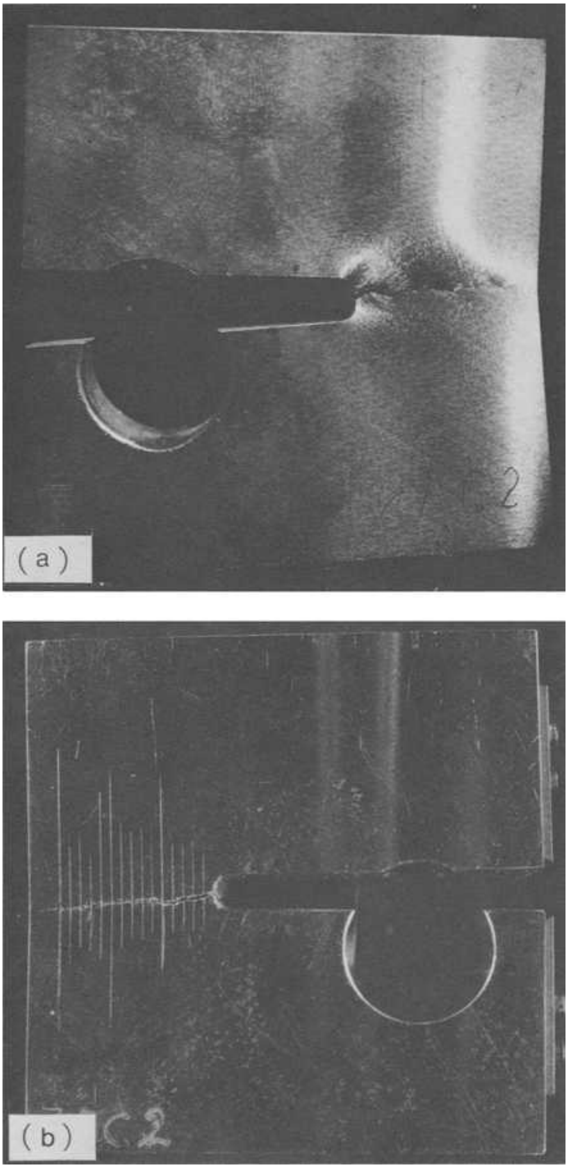

FIG. 10—*Fracture appearance of modified WOL specimens:* (a) *3.5-Ni-Cr-Mo-V 944-MPa yield strength in* H_2S, (b) *18Mn-4Cr 990-MPa yield strength in* H_2S, *and* (c) *18Mn-4Cr 990-MPa yield strength in air.*

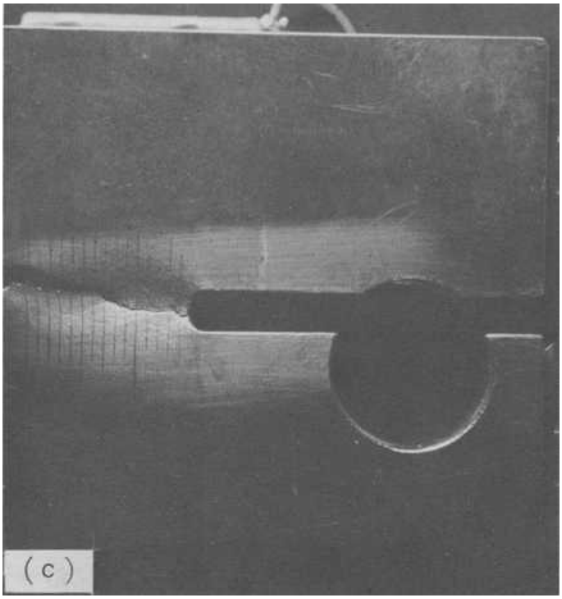

FIG. 10—*Continued.*

ductile manner, as shown in Fig. 10(*c*), with elastic strains between 2.3 and 3.2 percent.

The elastic failure strains in 3.5-Ni-Cr-Mo-V modified WOL specimens in short term incrementally rising load test in H_2S were between 3.26 and 3.38 percent. In the long term sustained load test in H_2, a WOL specimen loaded to an elastic strain of 3.38 percent failed in 330 h in H_2. Other specimens, which were loaded to strains between 3.23 and 2.07 percent, did not fail after 3000 h in H_2. Therefore, it appears that H_2S can be used to simulate the effect of H_2 in this material.

Metallurgical Examination

Fracture surfaces of all failed specimens were examined metallographically. Figures 11(*a*) and (*b*) show the fracture surface of a 3.5-Ni-Cr-Mo-V notched tension specimen tested in H_2S. Figure 11(*a*) is adjacent to the notch root where H_2S assisted crack initiation takes place. The fracture surface is entirely brittle, having been formed by cleavage mechanism. The fracture surface in the middle of the specimen, where the crack propagates very rapidly, shows by contrast much greater ductility, fracture having occurred by ductile microvoid coalescence, Fig. 11(*b*). Figures 12(*a*) and (*b*) show the fracture surface of a 18Mn-4Cr notched tension specimen tested

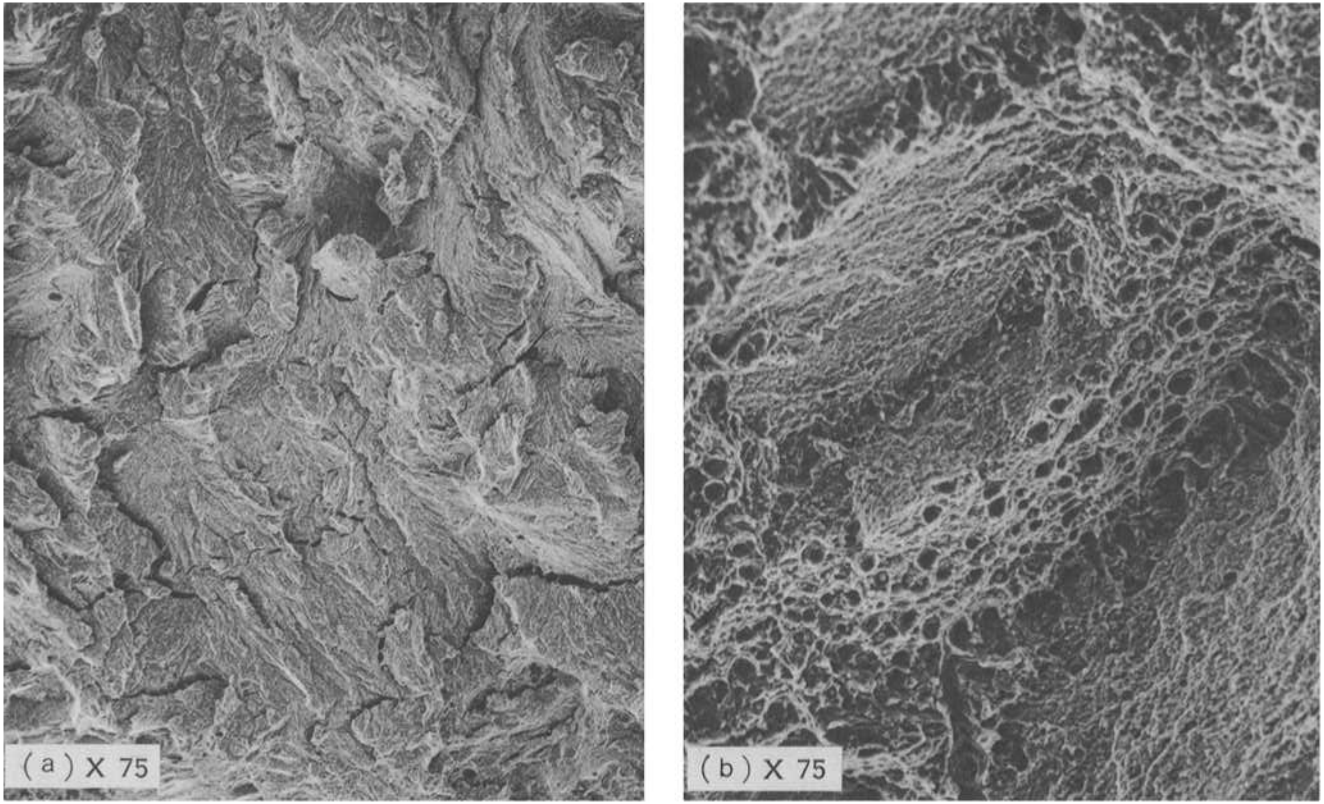

FIG. 11—*Fracture surface of a 3.5-Ni-Cr-Mo-V 710-MPa yield strength notched tension specimen:* (a) H_2S *assisted crack initiation, and* (b) *ductile fast fracture surface.*

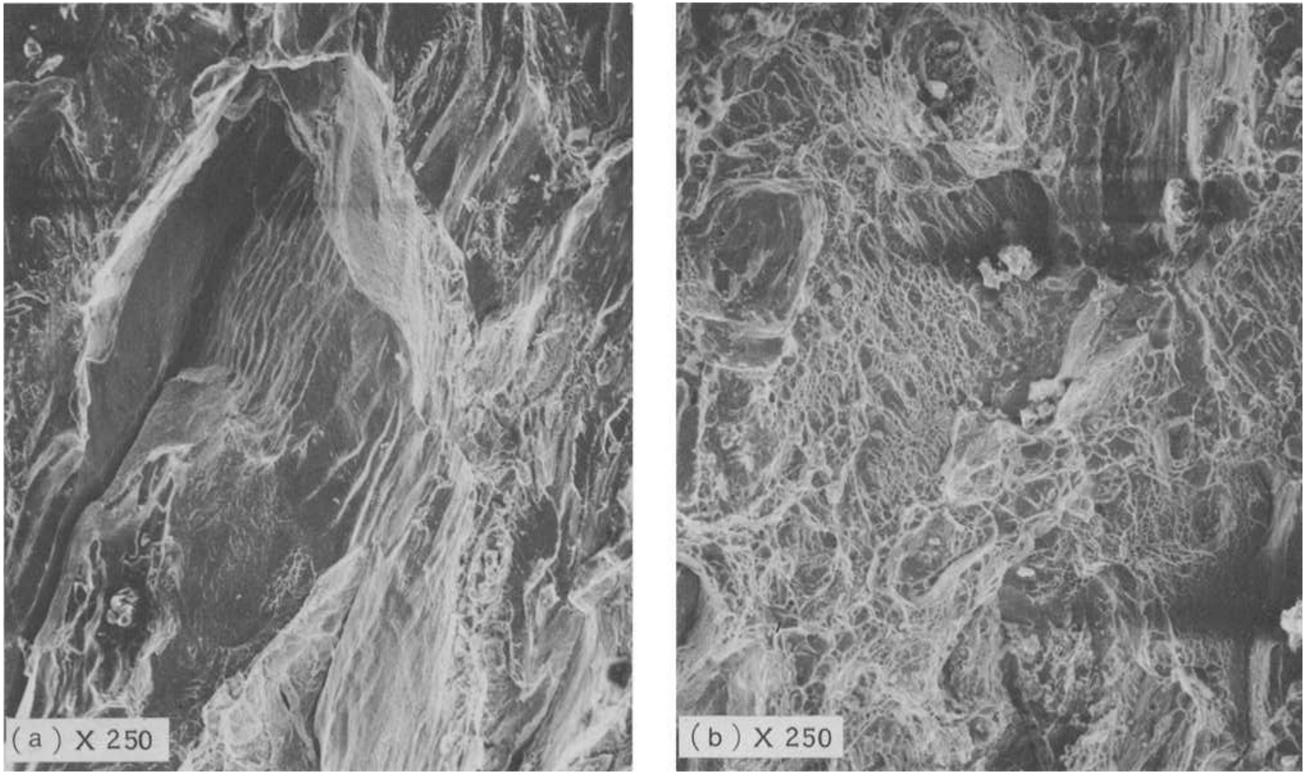

FIG. 12—*Fracture surface of a 18 Mn-4Cr 990-MPa yield strength, notched tension specimen*: (a) H_2S *assisted crack initiation, and* (b) *ductile fast fracture surface.*

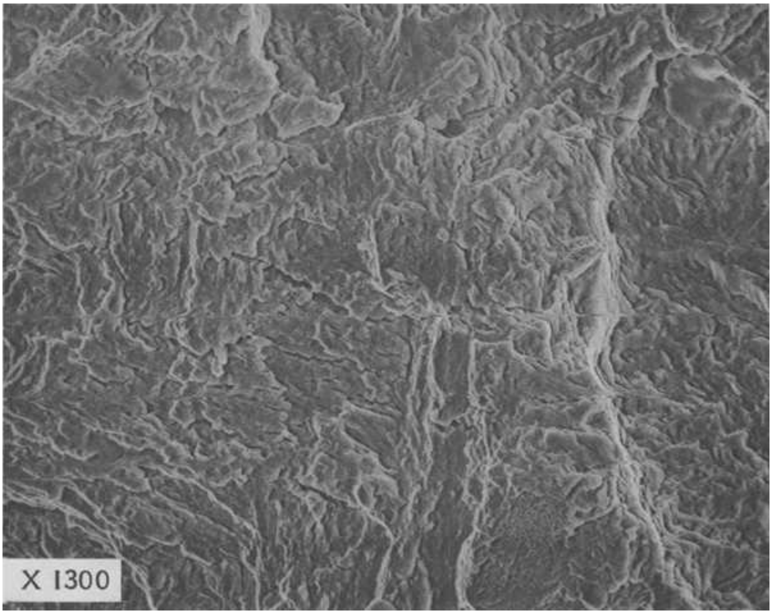

FIG. 13—*Fatigue surface of a 1250-MPa yield strength 3.5-Ni-Cr-Mo-V material in* H_2 *gas. Fracture surface is formed by brittle cleavage.*

in H_2S. Figure 12(*a*) is near the notch root where H_2S assisted crack initiation takes place and the fracture surface is entirely brittle. Regions of fast fracture at the center of the specimens, Fig. 12(*b*), are again highly ductile. Figure 13 shows the fatigue fracture surface in 3.5-Ni-Cr-Mo-V WOL specimen in H_2, and the fracture surface is formed mostly by brittle cleavage with small traces of ductile tearing.

Conclusions

1. During incrementally rising load test, H_2S gas environment significantly reduces the strain required for a crack to initiate from a blunt notch in 18Mn-4Cr and 3.5-Ni-Cr-Mo-V steels.
2. In short term tests, H_2 gas has a negligible effect on crack initiation from a blunt notch in the 18Mn-4Cr steel. If investigated, a higher strength version may behave differently.
3. Crack initiation strain in long term sustained load test in blunt notched 3.5-Ni-Cr-Mo-V steel specimens in H_2 is equivalent to that in short term rising load test in H_2S.
4. The K_{Iscc} value for the 1250-MPa yield strength 3.5-Ni-Cr-Mo-V was found to be 67 MPa $\sqrt{m}$ in 0.31-MPa H_2 gas environment.

5. The K_{Iscc} value for the 990-MPa yield strength 18Mn-4Cr steel was found to be 54 MPa $\sqrt{m}$ in 0.31-MPa H_2 gas environment.

6. The low pressure (0.0344-MPa) dry hydrogen gas environment at room temperature had a detrimental effect on the fatigue crack growth rate properties at 1250-MPa yield strength 3.5-Ni-Cr-Mo-V steel.

Acknowledgments

The experiments were conducted by D. W. Carpenter. The author would like to thank J. T. Martin, J. G. Willmot, C. E. Williams, R. G. Adderley, and J. M. Hay for their help at various stages of this work. The author would also like to thank C. A. Parsons & Co. Ltd., Newcastle-upon-Tyne, England, for the provision of test material and for many useful discussions.

References

[1] Campbell, J. E., "Effects of Hydrogen Gas on Metals at Ambient Temperature," DMIC Report S-31, Battelle Memorial Institute, April 1970.
[2] Jolly, C. B., Murphy, M. C., Paterson, A. N., and Petty, D. J., "The Failure of an End Ring of a Generator Rotor Operating in a Hydrogen Atmosphere," Technical Paper, C. A. Parsons & Company, Limited, Newcastle-upon-Tyne, England, Oct. 1975.
[3] McIntyre, P. and Priest, H., "Accelerated Test Technique for the Determination of K_{Iscc} in Steels," Report MG/31/72, British Steel Corporation, 1972.
[4] Clark, W. G. and Landes, J. D. in *Stress Corrosion—New Approaches, ASTM STP 610,* American Society for Testing and Materials, 1976, pp. 108–127.
[5] Deans, W. F. and Poynton, W. A., "The Resistance of Static Load Crack Initiation of End Ring Material in Hydrogen Atmosphere Using Accelerated Test Technique," Technical Memorandum MET 75-85, C. A. Parsons & Company, Limited, England, June 1975.
[6] Peterson, R. E., *Stress Concentration Design Factors,* Wiley, New York, 1966.
[7] Engineering Science Data, Item #69020, Elastic Stress Concentration Factors, Geometric Discontinuities in Flat Bars or Strips of Isotropic Material, Engineering Science Data Unit, 1969.
[8] Clark, W. G. in *Flaw Growth and Fracture, ASTM STP 631,* American Society for Testing and Materials, 1977, pp. 121–138.
[9] Wilson, W. K., "Elastic Plastic Analysis of Blunt Notch CT Specimens and Applications," *Journal of Pressure Vessel Technology,* 1974, pp. 293–298.
[10] Novak, S. R. and Rolfe, S. T., *Journal of Materials,* Vol. 4, No. 3, Sept. 1969.

Failure Analysis and Design Considerations

C. C. Seastrom[1]

Fatigue of Tantalum in Sulfuric Acid at 150°C

REFERENCE: Seastrom, C. C., "**Fatigue of Tantalum in Sulfuric Acid at 150°C,**" *Corrosion-Fatigue Technology, ASTM STP 642,* H. L. Craig, Jr., T. W. Crooker, and D. W. Hoeppner, Eds., American Society for Testing and Materials, 1978, pp. 289-299.

ABSTRACT: Tantalum is resistant to 80 percent sulfuric acid (H_2SO_4) at 150°C (302°F). However, data on fatigue of tantalum under these conditions were unavailable. To determine design criteria for a tantalum pump impeller, high frequency fatigue tests were conducted over a range from less than 10^6 to over 9×10^9 cycles, establishing approximate stress amplitudes which allow tantalum to achieve up to 8×10^9 cycles of loading without failure. These stresses were found to be about 11 ksi (7.7 kg/mm^2) for unalloyed tantalum and about 12.4 ksi (8.7 kg/mm^2) for Ta-2.5W. These two tantalum alloys were deliberately processed to create very soft materials with large grain sizes. Such materials may indicate behavior of these alloys in or near weld areas.

Case histories are presented on two Ta-2.5W pump impellers which failed in 80 percent H_2SO_4. The cracks were generally associated with welds. The crack surfaces show evidence of corrosion fatigue and cleavage fractures. The areas of cleavage fracture suggest an environmental effect such as hydrogen-assisted stress corrosion cracking.

KEY WORDS: tantalum, sulfuric acid, corrosion fatigue, cleavage, fracture, hydrogen-assisted stress corrosion cracking

The failure of two Ta-2.5W alloy pump impellers after several months of operation in 80 percent sulfuric acid (H_2SO_4) at 150°C (302°F) prompted this investigation into the causes of these failures. This paper deals with the examination of the fracture surfaces of the impellers and also presents a laboratory determination of the corrosion-fatigue properties of Ta-2.5W and unalloyed tantalum in 80 percent H_2SO_4 at 150°C (302°F).

---

[1] Research associate, E. I. du Pont de Nemours and Company, Inc., Jackson Laboratory, Wilmington, Del. 19898.

Examination of the Fracture Surfaces of the Impellers

Both impellers were of a semiopen design consisting of a solid Ta-2.5W hub with a Ta-2.5W plate welded to the hub as a backplate. The vanes were Ta-2.5W curved plates welded to the hub and backplate. The impellers were 13 in. in diameter.

Most of the cracks in both impellers began in the welds where the vanes were attached to the backplate and where the backplate and vanes were attached to the hub. The surface of the welds had become hardened because of contamination from air during welding. Many cracks started in this thin hardened outer layer of the Ta-2.5W alloy and continued to propagate into the softer alloy in the center of the plate. Figure 1 shows the predominantly transgranular cracking which occurred.

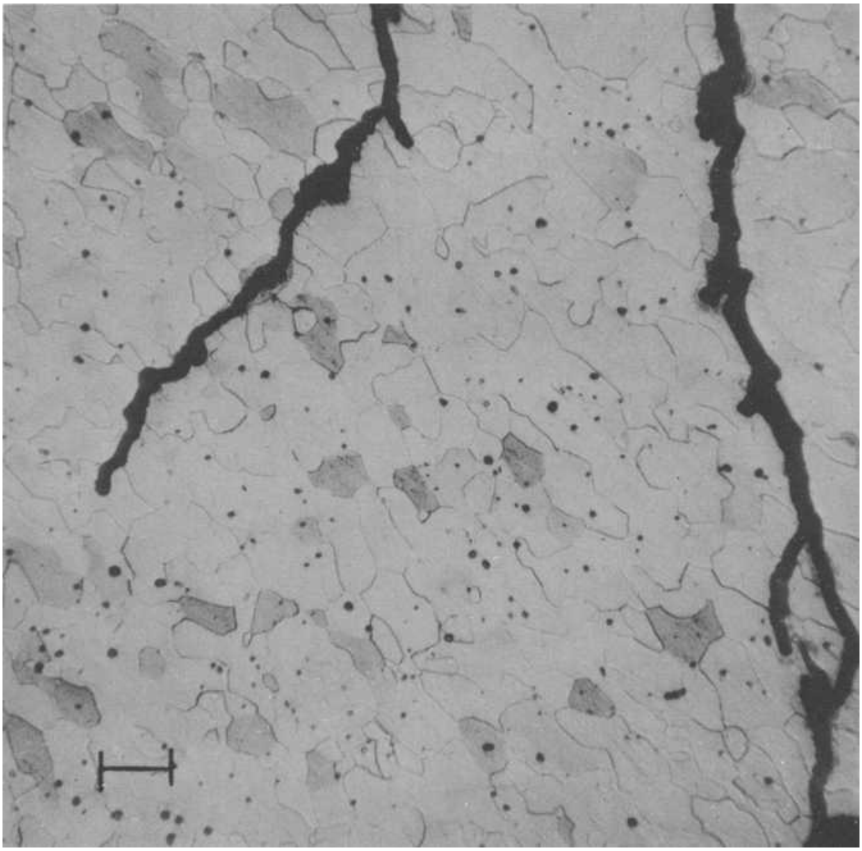

FIG. 1—*Photomicrograph of the transgranular cracking found in the second impeller to fail. Scale maker indicates 0.1 mm.*

Examination of a section that broke off the end of a vane of the first impeller showed fatigue striations along the intersection of the vane with the backplate (Fig. 2). At the time of this failure, the analysis was limited to defining that fatigue (probably corrosion fatigue) had occurred.

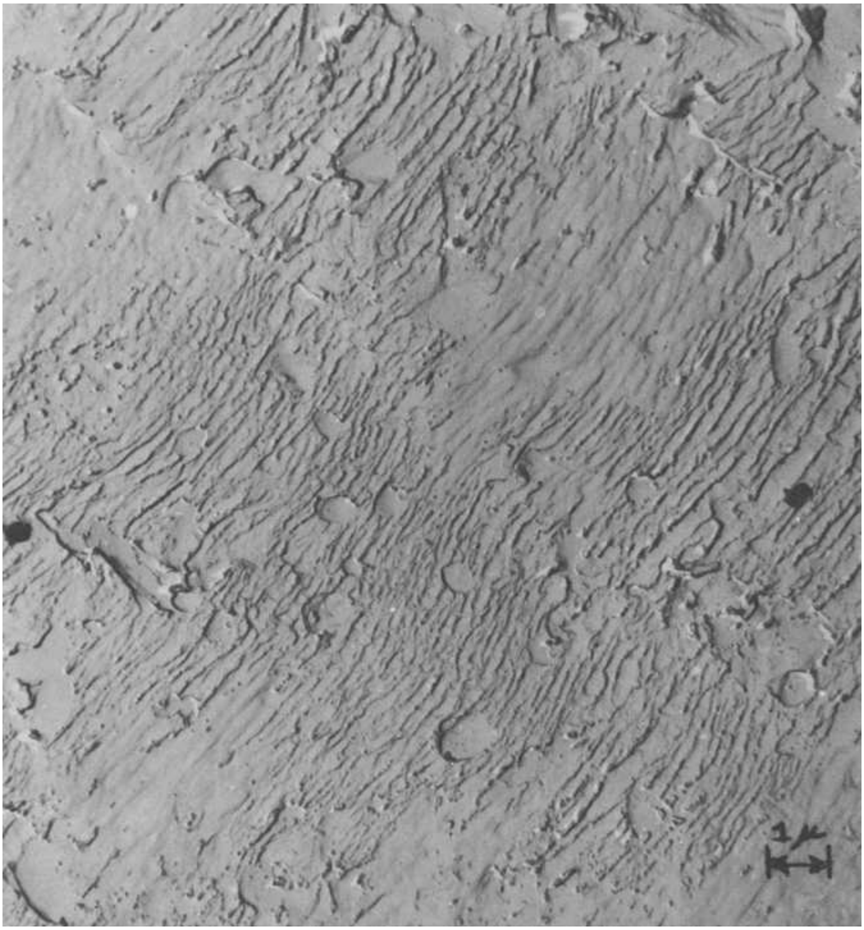

FIG. 2—*Fatigue striations on the first impeller to fail. The specimen was examined using replica technique with transmission electron microscope. Scale maker indicates 1 μm.*

The scanning electron microscope was used to examine several crack surfaces on the second impeller. Although there was evidence of fatigue (Fig. 3), much of the crack surface of the weld was found to be cleavage fracture. The appearance of the cleavage on the pump impeller is similar to that shown in Fig. 4. The cleavage fracture suggests an environmental

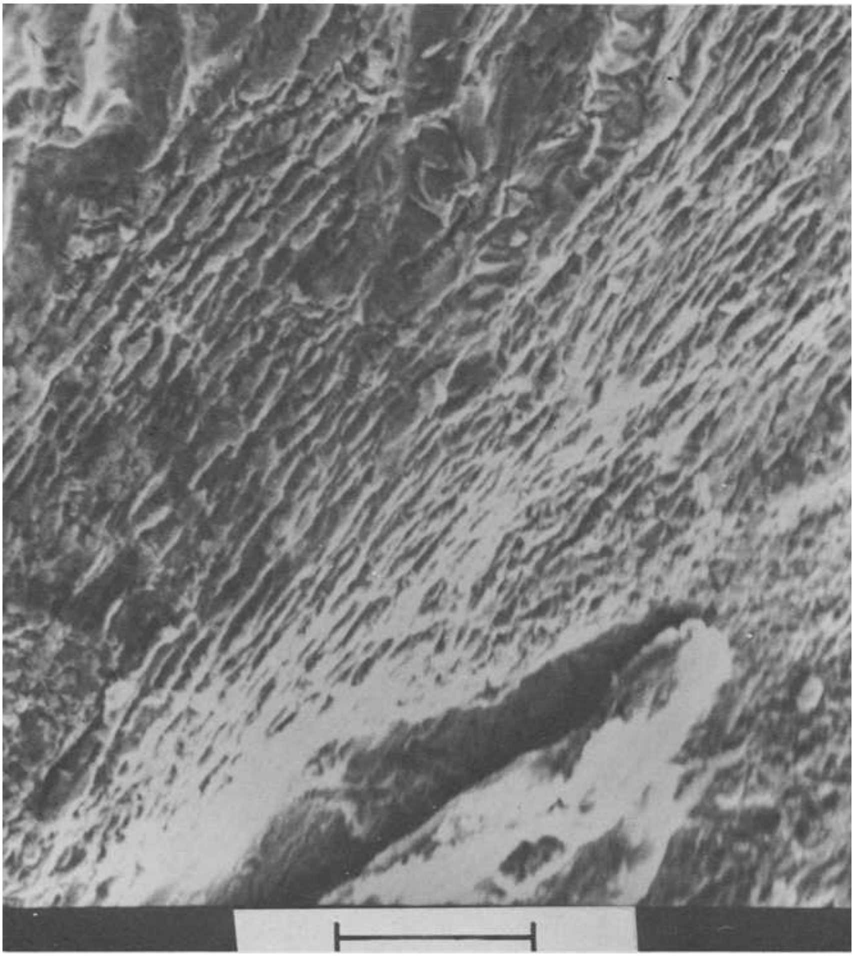

FIG. 3—*Fatigue striations along a cleavage facet on crack surface of the second impeller. The specimen was examined using the scanning electron microscope. Scale maker indicates 10 μm.*

effect such as hydrogen-assisted stress corrosion cracking, where hydrogen charging in advance of the crack causes local embrittlement. This relation between the cleavage and hydrogen charging is discussed further in the Discussion section of this paper.

A stress analysis using NASTRAN (National Aeronautics and Space Administration Structural Analysis)[2] was performed on the second impel-

---

[2] Perez, E. H. and Gamble, W. E., "Failure Analysis of Pump Impeller for 80% H_2SO_4 Service," Symposium Volume from 1977 Failure Prevention and Reliability Conference, American Society of Mechanical Engineers' Design Engineering Technical Conferences, 26 Sept. 1977, Chicago, Ill.

FIG. 4—*Area of cleavage fracture on unalloyed tantalum specimen following high frequency fatigue test in sulfuric acid. The specimen was examined using the scanning electron microscope. Scale marker indicates 10 μm.*

ler. The calculations showed that the steady-state rotational stresses exceeded the yield strength on the leading edge of the blades near the hub and in the backplate-to-hub weld when any reasonable stress concentration factor due to the lack of adequate weld penetration for these welds was included.

When the yield strength is exceeded, on a part such as an impeller, some distortion and perhaps failure would be expected in the absence of an environmental effect or fatigue. On the other hand, if the steady stress is somewhat below yield but coupled with alternating stresses and hydrogen-assisted stress corrosion cracking, failure can occur over a long time in terms of cycles of loading. In the case of these impellers the yield strength was exceeded along with alternating stresses and hydrogen-assisted stress corrosion cracking.

High Frequency Fatigue Testing

Materials Tested

This program involved the fatigue testing of two tantalum materials: (*a*) commercially pure tantalum to be referred to as unalloyed tantalum, and (*b*) a tantalum alloy containing normally 2.5W and 0.15Cb to be referred to as Ta-2.5W.

The rods of both materials were processed intentionally with only limited cold work after the next to final anneal so that a coarse grain size would be obtained from the final anneal. The large grain sizes achieved are similar to those observed in welded structures of these metals, both in the heat affected zone and in the weld metal itself.

The properties of both of the tantalum alloys tested are shown in Table 1, and the chemical analyses are shown in Table 2.

TABLE 1—*Properties of tantalum alloys tested.*

Alloy	Unalloyed Ta	Ta-2.5W
Ultimate strength, ksi	37.2	50.9
Yield strength, ksi	25.3	32.0
Elongation, 1 in.	53%	55%
ASTM grain size	0	2
Hardness, DPH	88	111
Recrystallization	100%	100%

NOTES—These properties were determined at room temperature. The mechanical properties are from tests on 3/8-in.-diameter annealed-bar stock.

Experimental Procedures

The facility[3] that conducted the high frequency fatigue tests consists of a magnetostriction transducer operating at 14.2 ±0.1 kHz. Such a frequency allows the accumulation of a large number of cycles in a comparatively short time. A description of this equipment is presented in a recent paper by Conn and Nielsen.[4] Their investigation was important in showing that environmental effects can influence the fatigue results despite the high frequency used for these tests.

[3] Test work was conducted at Hydronautics, Inc., Laurel, Md.

[4] Conn, A. F. and Nielsen, N. A. in *Fatigue at Elevated Temperatures, ASTM STP 520,* American Society for Testing and Materials, 1973, pp. 273–281.

TABLE 2—*Chemical report of tantalum alloys tested. Values in parts per million unless otherwise shown.*

	C	O	N	H	W	Cb	Zr	Mo	Ti	Fe	Si	V	Co	Mg	Ta
Unalloyed Ta	10 –	40	10 –	5 –	200	230	10 –	10 –	10 –	10 –	10 –	10 –	10 –	10 –	bal
Ta-2.5W	10	50	27	5 –	2.4%	2600	20 –	100 –	20 –	20 –	. . .	20 –	20 –	. . .	bal

NOTE—The chemical compositions are from ingot analyses.

The basis for this high frequency fatigue technique is the creation of longitudinal oscillations in a fatigue specimen at its resonant frequency producing uniaxial alternating strains. The specimen shape and dimensions are shown in Fig. 5. The maximum alternating strains are produced at the node or center of the reduced section. The original strain amplitude calculations were confirmed using strain gages mounted on the specimen. The alternating strain amplitude (one half of the total strain range) is calculated and converted to the alternating stress amplitude by multiplying by E.

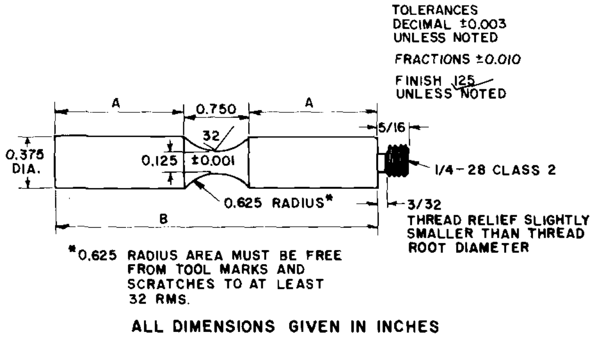

MATERIAL	A	B	RESONANT FREQUENCY kHz
UNALLOYED TANTALUM	1.005	2.760	14.2
Ta-2.5 W ALLOY	0.989	2.729	14.2

FIG. 5—*Dumb-bell shaped high frequency fatigue specimens for tantalum alloys at 150°C (302°F).*

The time to failure for each specimen is defined to be the time when a crack in the specimen causes an increase in power level required to maintain a constant displacement amplitude. In these high frequency fatigue tests the crack typically has grown to one half of the cross section when the increase in power is observed. The specimens then are easily bent open by hand if crack observation is desired.

The liquid in which the specimen was directly immersed during the fatigue testing consisted of 80 percent by weight solution of H_2SO_4 at 150°C (302°F). The acid bath was provided with a cover plate to minimize water losses.

Results of Fatigue Testing

The data for all of the fatigue specimens are plotted in Figs. 6 and 7. The curves show an approximate fatigue stress amplitude below which failure is unlikely. At 8 × 10^9 cycles, these stresses were found to be about 11 ksi (7.7 kg/mm^2) for the unalloyed tantalum and about 12.4 ksi (8.7 kg/mm^2) for Ta-2.5W.

The data show considerable scatter in the number of cycles to failure at the various cyclic stress levels imposed. Some difficulties were encountered in providing the necessary uniform finish in the narrow region of the specimen. Although attempts were made to remove these marks by hand polishing with a fine grade of emery cloth, these fabrication problems may have contributed to some of the scatter observed in these fatigue results. How-

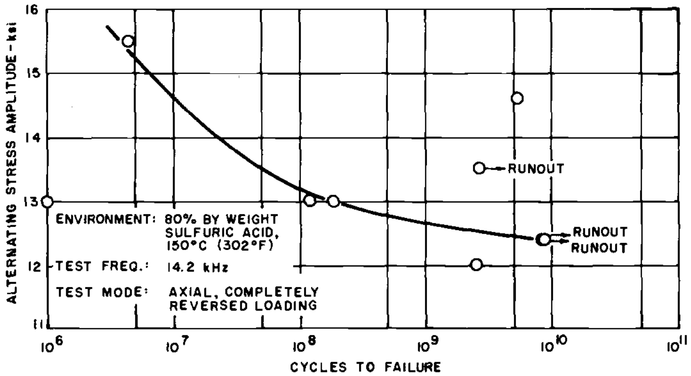

FIG. 6—*Fatigue curve for Ta-2.5W alloy in hot sulfuric acid.*

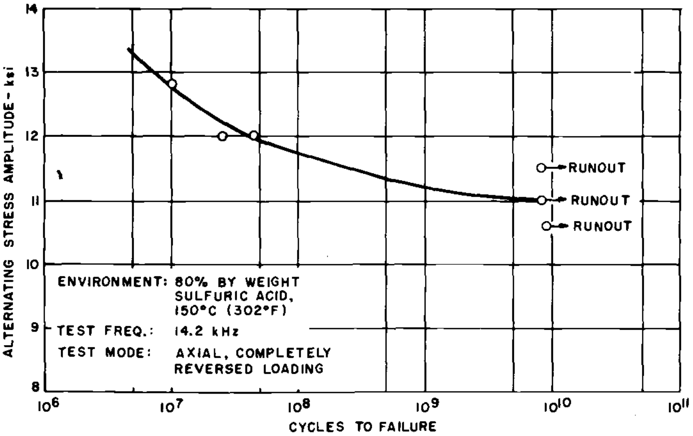

FIG. 7—*Fatigue curve for unalloyed tantalum in hot sulfuric acid.*

ever, the surface finish was as fine as it would be practical to attain on a part such as a pump impeller.

Examination of Fracture Surfaces of Unalloyed Tantalum

Specimen Using the Scanning Electron Microscope—One of the unalloyed tantalum specimens (12.8 ksi (9 kg/mm^2) alternating stress amplitude, 1.04×10^7 cycles) was examined with the scanning electron microscope. The crack had progressed approximately two thirds through the cross section when the fatigue test was stopped. The specimen was ductile when broken open by hand to expose the crack after the test. Fatigue striations were in evidence on one fourth of the surface of the crack in the area around what was thought to be the origin. The remaining crack surface showed brittle cleavage. Figure 8 shows the fatigue striations just before the junction with the cleavage (shown in Fig. 4). Similar cleavage fracture was previously found on the pump impeller.

Discussion

Areas of corrosion fatigue and cleavage were present on the fracture surfaces of both the impellers and the fatigue specimen. The fatigue striations represent the effect of corrosion fatigue, and the cleavage fracture represents hydrogen-assisted stress corrosion cracking.

An indication that hydrogen embrittlement of tantalum and Ta-2.5W alloy will cause this type of cleavage fracture comes from an unstressed coupon of unalloyed tantalum containing 854-ppm hydrogen. This specimen had become embrittled during corrosion in a nonsulfuric acid environment. The specimen showed practically no ductility when bent. The entire fracture surface was similar to the areas of cleavage fracture observed on the pump impellers and high frequency fatigue specimen. This observation is important in establishing the appearance of the fracture surface of hydrogen embrittled tantalum.

Without applied or residual stress unalloyed tantalum and Ta-2.5W in 80 percent H_2SO_4 at 150°C (302°F) are not susceptible to hydrogen charging, and the corrosion rate is very low.

The impellers operated at 3600 rpm and contained six vanes. Therefore, it is assumed that six cycles will occur each revolution. The impellers operated with a high steady state rotational stress and an unknown magnitude of alternating stress. By comparison, the high frequency fatigue tests were conducted with alternating stress applied at a frequency of 14.2 kHz and no steady state mean stress.

The high frequency fatigue data presented in Figs. 6 and 7 allow an estimate of an approximate endurance limit (for $\approx 10^{10}$ cycles) in the absence of a steady state mean stress. The higher the mean stress, the lower must be the allowable alternating stress to ensure against failure.

FIG. 8—*Fatigue striations just before the junction with cleavage area on unalloyed tantalum specimen tested in high frequency fatigue. The specimen was examined using the scanning electron microscope. Scale marker indicates 1 μm.*

Acknowledgments

The author wishes to thank Donald Warren, E. I. du Pont de Nemours and Co., Inc., for the scanning electron microscope study of the fracture surfaces of the high frequency fatigue specimens and the second impeller, and N. A. Nielsen for the transmission electron microscope study of the failure of the first impeller.

The author also gratefully acknowledges the tantalum specimens supplied by Fansteel, Inc. for the high frequency fatigue tests.

Milton Levy[1] *and J. L. Morrossi*[1]

Corrosion-Fatigue Behavior of Coated 4340 Steel for Blade Retention Bolts of the AH-1 Helicopter

REFERENCE: Levy, Milton and Morrossi, J. L., "**Corrosion-Fatigue Behavior of Coated 4340 Steel for Blade Retention Bolts of the AH-1 Helicopter,**" *Corrosion-Fatigue Technology, ASTM STP 642,* H. L. Craig, Jr., T. W. Crooker, and D. W. Hoeppner, Eds., American Society for Testing and Materials, 1978, pp. 300–312.

ABSTRACT: The main rotor blade bolt for the 540 helicopter rotor system of the AH-1G, UH-1C, and UH-1M helicopters is proposed to be improved by substituting a plasma-sprayed tungsten carbide coating on the outer shank of the 4340 steel bolt for the present cadmium or chromium plate. This study was undertaken to determine the effects of these coating systems on the fatigue behavior of 4340 steel in environments likely to be encountered in service. Both axial tension-tension and rotating bending fatigue testing of coated specimens were carried out in air and in 3.5 percent sodium chloride (NaCl) solution. The NaCl environment causes reductions in fatigue strength of bare and coated 4340 steel. The severity of the degradation depends on the coating applied and the type of fatigue test utilized.

KEY WORDS: corrosion fatigue, steels, protective coatings, tungsten carbides, environmental tests

The main rotor blade bolt for the 540 rotor system (AH-1G, UH-1C, UH-1M helicopter) is proposed to be improved by the substitution of plasma-sprayed tungsten carbide (WC) coating on the outer shank for the present cadmium (Cd) or chromium (Cr) plate. The WC coating was suggested originally to reduce the costly machining and plating operations required to recondition blade retention bolts for the AH-1G helicopter. Fretting-induced corrosion resulted in significant surface pitting on the bolts after less than 500 h of service. Based on prior results with a similar

---

[1] Corrosion research group leader and chemical engineer, respectively, Department of the Army, Army Materials and Mechanics Research Center, Watertown, Mass. 02172.

configuration bolt for the 240 rotor system, a WC-coated bolt is expected to last over 3000 h (the approximate design life of the airframe) as compared to about 300 h for current cadmium-plated new production bolts and about 500 h for chromium-plated reworked bolts. Thus a significant cost savings has been projected if bolt reconditioning and replacement were eliminated.

Although WC-coated bolts for the 240 rotor system have not experienced any fatigue problems, the Army Aviation Systems Command decided that coating effects on fatigue life should be investigated prior to approval of the WC coating for the following reasons: (*a*) the blade retention mechanism is subjected to fatigue conditions due to steady centrifugal loading; (*b*) stress analysis of the blade retention bolt provided no assurance that the part was not fatigue critical; (*c*) available data on the effect of the WC coating on the fatigue strength of 4340 steel were inadequate;[2,3] and (*d*) the need for utilizing the organic sealer in conjunction with the WC coating for enhanced corrosion resistance had not been confirmed. This study was undertaken to determine the effects of these coating systems (WC, cadmium, chromium) on the fatigue behavior of 4340 steel in environments likely to be encountered in service. In addition, the efficacy of organic 1700 sealant (an organic film for enhanced corrosion resistance) in combination with the WC and the solid film lubricant was also determined. Full-scale axial fatigue tests of the coated blade retention bolts were carried out by the Army Air Mobility Research and Development Laboratory (AMRDL)-Langley Research Center, Va. Details of the test program and the data obtained are reported elsewhere.[4]

Materials

The substrate alloy (bolt material) was VAR 4340 steel. Axial tension-tension and rotating-beam fatigue specimens were rough machined (turned) and heat treated according to the following schedule: normalized at 1650°F (899°C) for 1 h; air cooled; austenitized at 1525°F (829°C) for 1 h; oil quenched (130 to 170°F, 54 to 77°C); tempered at 900°F (482°C) for 4 h directly from the oil quench before reaching room temperature. The ultimate tensile strength of the alloy was 194 ksi (1338 MN/m^2). The fatigue specimens were subsequently finish machined (turned and polished to 8 to 16 rms finish), shot peened, and the following coating systems were ap-

---

[2] Viglione, J., Jankowsky, E. J., and Ketcham, S. J., *Materials Protection and Performance*, Vol. 11, March 1972, pp. 31-36.

[3] Levy, M. and Morrossi, J., "Erosion and Fatigue Behavior of Coated Titanium Alloys for Gas Turbine Engine Compressor Applications," AMMRC TR 76-4, Army Materials and Mechanics Research Center, Feb. 1976.

[4] Swindlehurst, C. E., Jr., "Evaluation of Tungsten Carbide Coated Blade Retention Bolts for the AH-1G Helicopter," NASA TM, National Aeronautics and Space Administration, in process.

plied: (*a*) cadmium plating plus chromate treatment, (*b*) chromium plating plus solid film lubricant (SFL), (*c*) plasma-sprayed WC plus solid film lubricant with organic sealant, and (*d*) (*c*) without organic sealant.

Detailed coating procedures are shown in Table 1. Coating thickness requirements are given in Table 2. The coated specimens were fatigue tested (both axial tension-tension and rotating bending) in air and 3.5 percent sodium chloride (NaCl) solution (to simulate marine atmosphere).

TABLE 1—*Coating procedures.*

Cadmium plating	1. degrease and rinse in flowing water
	2. cyanide dip 30 to 60 s at room temperature
	3. Cd plate at 20 A/ft^2 (215 A/m^2)
	4. rinse in water
	5. bake at 385°F (196°C), minimum 23 h (within 1 h of plating)
	6. degrease
	7. cyanide reactivation, 5 to 10 s at room temperature
	8. rinse in water
	9. 15 to 20 s in chromate conversion bath
	10. rinse in water and dry
Chromium plating	1. degrease and rinse in flowing water
	2. reverse etch in chromium plating bath (131°F, 55°C)
	3. Cr plate (131°F, 55°C)
	4. rinse
	5. bake at 375 ± 25°F (191 ± 4°C) for minimum of 3 h
	6. dip plated samples into solid film lubricant (MIL-L-46010[a])
	7. air dry for 30 min at room temperature
	8. cure at 400°F (204°C) for minimum of 1 h
Plasma-sprayed tungsten carbide	1. grit blast fatigue specimens according to MIL-A-21380B[b]
	2. plasma spray WC-Co (METCO 72F-NS) 7 to 9 mil per side (178 to 229 μm)
	3. surface grind to 3.25 to 4.0 mil per side (82.6 to 116 μm)
	4. apply Coricone 1700 sealant by spraying (specimens were prepared with and without Coricone)
	5. dry at room temperature
	6. cure at 350°F for at least 20 min
	7. dip specimens into SFL
	8. air dry for 30 min at room temperature
	9. cure at 400°F (204°C) for minimum of 1 h

[a] Military Standard for Lubricant; Solid Film, Heat Cured, Corrosion Inhibiting (MIL-L-46010).

[b] Military Standard for Abrasive Materials for Blasting (MIL-A-21380B).

TABLE 2—*Thickness of coatings.*

Cadmium	0.3 to 0.5 mil/side (7.62 to 12.7 μm)
Chromium	2.0 to 2.5 mil/side (50.8 to 63.5 μm)
Tungsten carbide (after finish grind)	3.25 to 4.0 mil/side (82.6 to 101.6 μm)
Organic sealer	0.2 mil/side (5.1 μm)
Dry film lubricant	0.35 mil/side (8.9 μm)

Fatigue testing of the bare 4340 alloy was also carried out to obtain baseline data.

Experimental Procedures

Fatigue Tests

Rotating Bending Fatigue (Intended as a Screening Test)—Stress versus cycles-to-failure studies of smooth fatigue specimens were carried out using a rotating-bending fatigue machine which applied a cyclic stress at a frequency of 50 Hz and a stress ratio of $R = -1$. The standard fatigue machine was modified by the addition of a lucite environmental chamber for corrosion fatigue studies, as shown schematically in Fig. 1. A constant displacement tubing pump delivered the test fluid through polyvinyl chloride tubing from a 2-litre reservoir at the rate of 15 litres/h. The pulsations of the pumping system were removed in a settling chamber, so that a steady stream of fluid was then returned to the reservoir by gravity flow. At

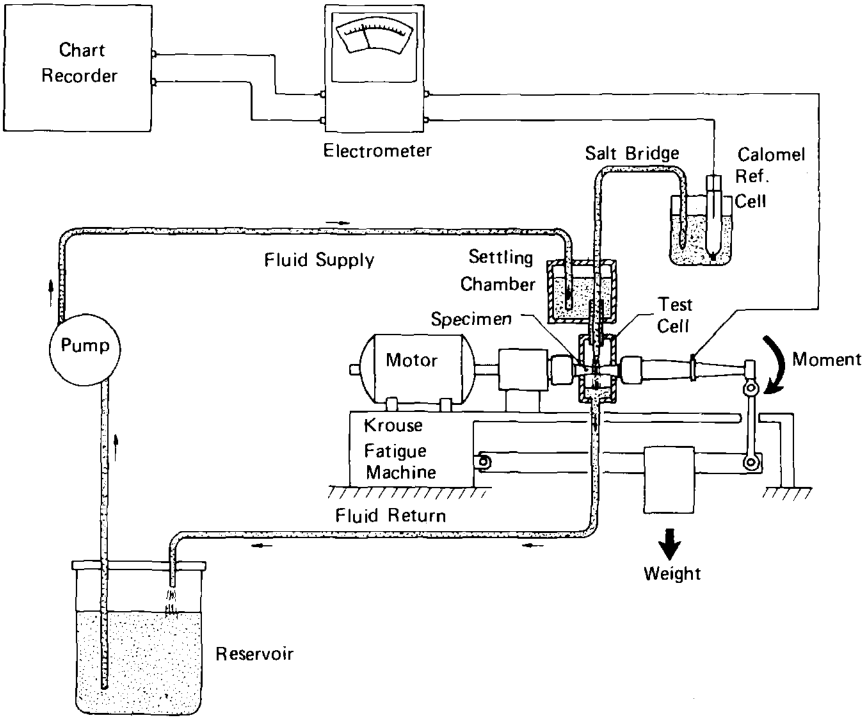

FIG. 1—*Schematic for corrosion-fatigue apparatus.*

speeds up to 3000 rpm, the fluid maintained good contact with the rotating specimen as it flowed over and around the test section.

Rotating-bending fatigue specimens measured ½ in. (12.7 mm) diameter by 4 in. long (101.6 mm), with a 2¼ in. (63.5 mm) radius reduced section giving a minimum cross section of ¼ in. (6.5 mm) diameter at the specimen center as shown in Fig. 2(*a*).

Axial Tension-Tension Fatigue Test (Intended to Simulate the High Mean Centrifugal Loads on the Blade Retention Bolt)—Fatigue testing of axial tension-tension smooth fatigue specimens was carried out using the Instron dynamic cycler model 1211 system and sinusoidal loading. The apparatus was operated at a cyclic frequency of 33 Hz and a stress ratio of $R = 0.8$. For tests in 3.5 percent NaCl solution, a plastic cell containing this environment was attached to surround completely the gage length of the specimen. Unlike the corrosion cell of the rotating bending fatigue apparatus, the solution was quiescent. Axial tension fatigue specimens are described in Fig. 2(*b*).

Results

Rotating-Bending Fatigue

Figure 3(*a*) shows the deleterious effect of NaCl solution on the fatigue life of bare 4340 steel. The fatigue strength (value at 10^7 cycles) of the bare specimen decreases from 105 to 20 ksi (724 to 138 MN/m^2), a reduction of 81 percent. Figure 3(*b*) contains *S-N* curves for the 4340 steel coated with electroplated cadmium plus chromate treatment. The air value of the bare material is identical to that of the coated material (105 ksi, 724 MN/m^2). Parallel to data for steels in general, the fatigue limit of the bare alloy in air is approximately one half the tensile strength. The NaCl solution reduced the fatigue strength of the coated alloy by 24 percent (from 105 to 80 ksi, 724 to 552 MN/m^2). If we compare the fatigue strength of the coated alloy in NaCl solution with that of the bare alloy in the same environment, it is apparent that the cadmium plus chromate treatment significantly improves the fatigue strength of the alloy in NaCl solution (from 20 to 80 ksi, 138 to 552 MN/m^2). Figure 3(*c*) shows that 3.5 percent NaCl solution caused a 5.3 percent reduction in the fatigue strength of 4340 steel coated with electroplated chromium plus solid film lubricant (from 95 to 90 ksi, 655 to 621 MN/m^2). This coating system produced a 9.5 percent degradation in the fatigue life of the bare steel (Figs. 3(*a*) and (*c*), Table 3) in air. The fatigue strength of the alloy coated with plasma-sprayed WC plus solid film lubricant with or without the organic sealant was 90 ksi (621 MN/m^2) regardless of the environment (Fig. 3(*d*), Table 3), that is, there was neither a deleterious effect of environment nor a beneficial effect of the organic sealant. A fatigue reduction of 14.3 percent was attributed to the coating system.

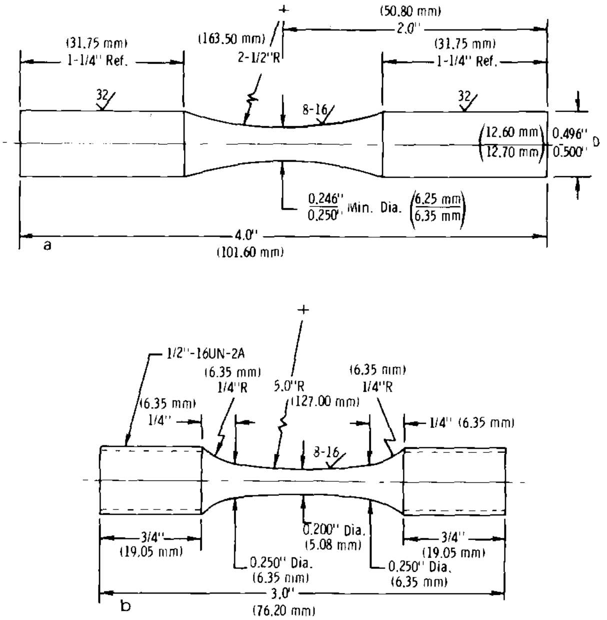

FIG. 2—*Fatigue specimen geometry.*

Axial Tension-Tension Fatigue

Figure 4, in conjunction with Table 3, contains *S-N* curves and data obtained in air for the alloy, bare and coated. Fatigue data at 10^7 cycles showed that the cadmium and chromium electroplates, particularly the chromium, improved the fatigue strength of the bare alloy. The WC coating reduced fatigue strength from 160 to 140 ksi (1103 to 965 MN/m^2) which represented a fatigue reduction of 12.5 percent. The organic sealant had no effect on fatigue strength of the alloy in air. Table 3 contains fatigue data at 10^7 cycles for the uncoated and coated alloy in 3.5 percent NaCl solution. This environment caused a 31.2 percent reduction in the fatigue strength of the bare alloy and a 45 to 60 percent reduction in the fatigue strength of the WC-coated alloy and the chromium-plated alloy. The organic sealant again provided no beneficial effect on the corrosion-fatigue resistance of the WC-coated alloy. The cadmium-plated alloy was unaffected by the NaCl solution. It is evident that the axial tension fatigue data differ from the rotating bending fatigue data in the following manner: (*a*) degradation of fatigue strength of the bare alloy due to NaCl solution is considerably less in axial tension. Gould[5] found that the attack of steel subjected to fatigue tests in seawater was more severe in bending than in direct tension due to a stretching of all the anodic areas in bending

---

[5] Gould, A. J., *Journal of the Iron and Steel Institute,* Vol. 161, No. 11, 1949.

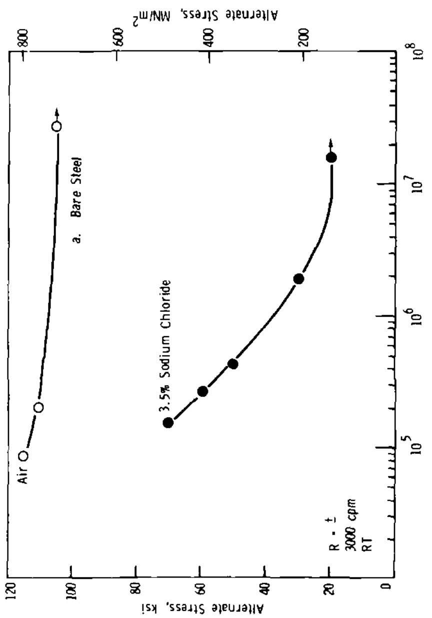

SAE 4340 FATIGUE LIFE (UNCOATED)

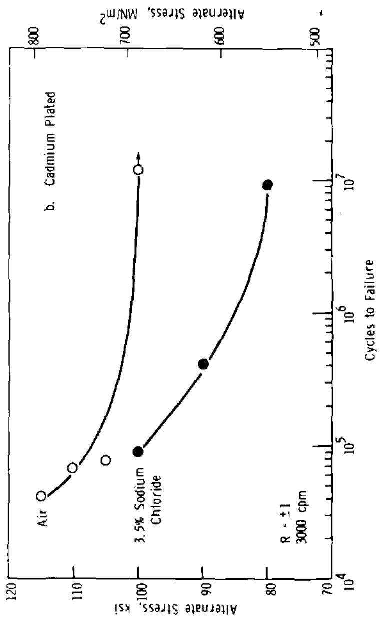

SAE 4340 FATIGUE LIFE (COATED) CADMIUM + CHROMATE

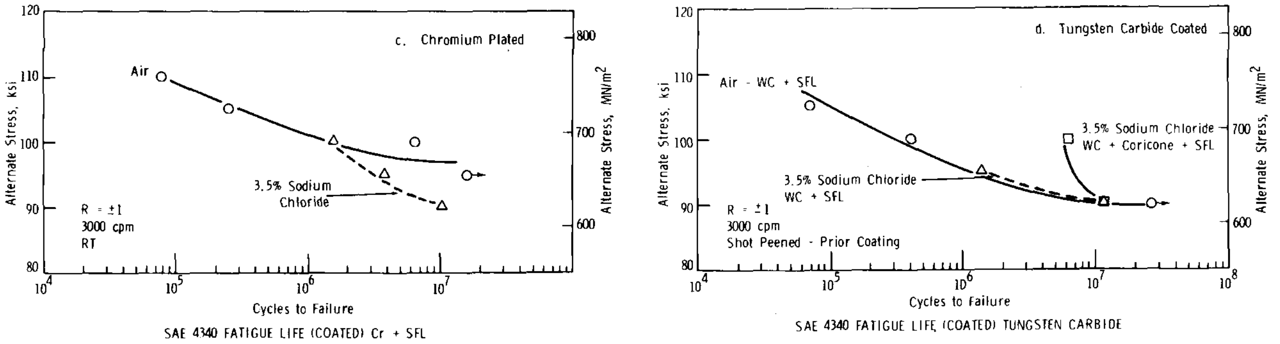

FIG. 3—S-N *curves (rotating-bending) of bare and coated 4340 steel showing effect of environment.*

TABLE 3—*Effects of coatings and environment on the fatigue strength of 4340 steel.*

		Air			3.5% NaCl		
Test	Condition	Stress, ksi	MN/m^2	Change, %	Stress, ksi	MN/m^2	Change, %
Rotating Bending[a]	bare	105	724	. . .	20	138	−81
	Cd + chromate	105	724	0	80	552	−24
	Cr + dry film[b]	95	655	−9.5	90	621	−14.3
	WC + dry film[b]	90	621	−14.3	90	621	−14.3
	WC + Coricone + dry film[b]	90	621	−14.3	90	621	−14.3
Axial Tension[c]	bare	160	1103	. . .	110	758	−31.2
	Cd + chromate	165	1138	+3.1	165	1138	0
	Cr + SFL[b]	175	1207	+9.4	90	621	−43.8[d] −48.6[e]
	WC + SFL[b]	140	965	−12.5	60	414	−62.5[d] −57[e]
	WC + Coricone + SFL[b]	140	965	−12.5	60	414	−62.5[d] −57[e]

[a] $R = -1$.
[b] Shot peened.
[c] $R = 0.8$.
[d] Compared to bare alloy air value.
[e] Compared to coated alloy air value.

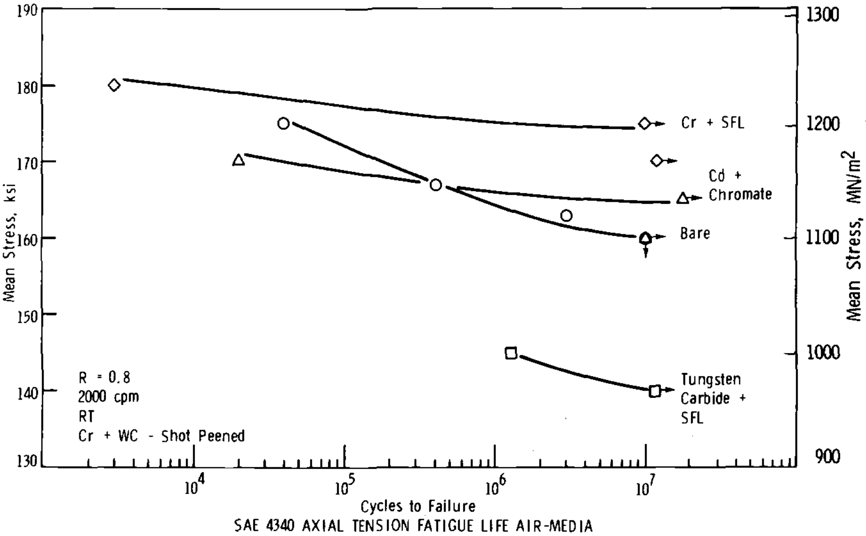

FIG. 4—S-N *curves (axial tension) of bare and coated 4340 steel in air environment.*

tests, whereas only some of these areas were stretched in direct tension tests; (*b*) based on air values only, fatigue strength reductions due to the WC and chromium coatings were quite similar in both rotating bending and axial tension fatigue tests. But in NaCl solution, significantly greater reductions in axial fatigue strength of the coated alloys were observed due to environmental effects which remain to be elucidated. Since the chromium and WC hard (brittle) coatings have a relatively low intrinsic fatigue strength in comparison with the steel, they will become discontinuous at a relatively low stress level owing to the development of fatigue cracks. (The chromium normally contains internal cracks.) These cracks will permit access of the corrosive NaCl solution to the steel base at the root of the fatigue crack. In the case of the axial tension test (high steady tensile load), it may be easier for the environment to reach the crack tip.

In full scale blade retention bolt fatigue tests carried out at AMRDL-Langley, none of the coated retention bolts (cadmium, chromium, or WC), which were subjected to cyclic load levels in excess of operational flight load levels, failed during testing in air. They sustained the equivalent of four lifetimes of fatigue loading or ~14 000 simulated hours of flight. All test conditions included ground-air-ground cycles, which for helicopter rotor components represent the centrifugal loading which occurs once per flight. Accelerated flight loads were superimposed on the centrifugal load to simulate flight-by-flight loading conditions on a rotor. A marine environment (NaCl) was not simulated in the test program.

Metallography

The WC-coated specimens were examined metallographically for an assessment of coating integrity, bonding, and the sealing capability of the SFL and organic sealant. Figure 5 contains micrographs of the cross-sectional area of the coated specimens. Figure 5(*a*) demonstrates the good bonding between plasma-sprayed WC and the substrate 4340 steel. Note

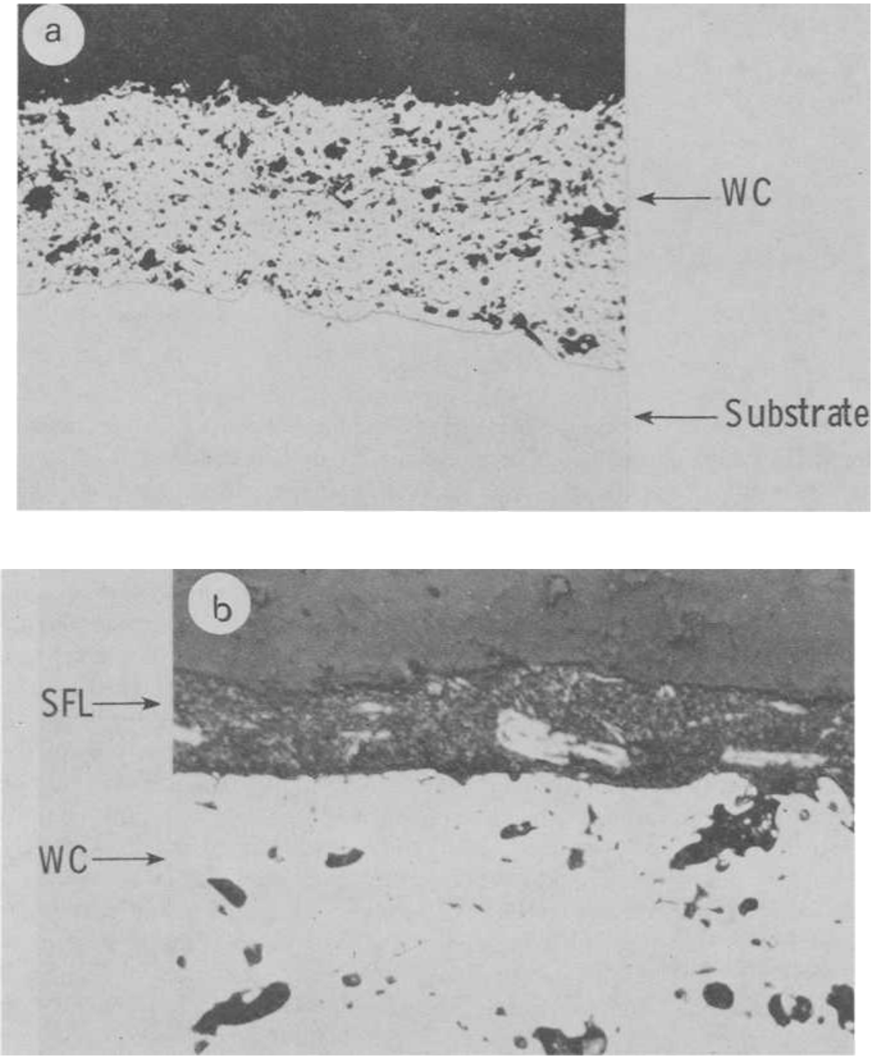

FIG. 5—*Micrographs of cross-sectional area of plasma-sprayed tungsten carbide coating interfaces.* (a) *Tungsten-carbide coating/substrate interface,* ×*200.* (b) *Solid film lubricant/tungsten carbide coating interface,* ×*1000.*

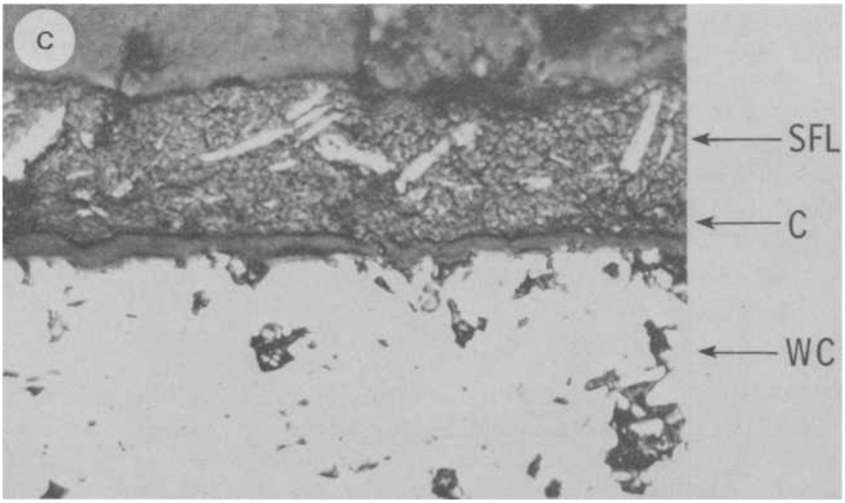

FIG. 5—*(continued)* (c) *Solid film lubricant/organic sealant/tungsten carbide interface, ×1000.*

that some porosity is present and that the pores are discontinuous. Figure 5(*b*) shows good bonding between the solid film lubricant and the WC coating. Also shown is the capability of the SFL to fill surface pores present in the WC coating. Figure 5(*c*) demonstrates the good bonding that can be obtained between SFL and organic sealant and between organic sealant and WC coating. Note that the organic sealant has filled any surface pores present in the WC coating. Since the pores in the WC coating are discontinuous, neither the SFL nor the organic sealant has infiltrated below the surface pores.

Summary

1. The NaCl solution significantly degrades fatigue strength of the bare 4340 steel. The degradation is much more severe under conditions of rotating-bending fatigue.

2. Although the fatigue strength of WC-plus-SFL coated 4340 steel is unaffected by NaCl solution in rotating bending fatigue, it is significantly reduced by this environment in axial tension fatigue testing which more closely simulated service operating conditions. Regardless of the method of testing, the organic sealant does not impart additional resistance to corrosion fatigue and the WC coating reduces the air fatigue strength of the 4340 steel by about 14 percent.

3. The NaCl solution further degrades the rotating bending fatigue strength of both cadmium and chromium-plated 4340 steel, but in axial

tension fatigue testing, further degradation is limited to the chromium-plated alloy.

4. Regardless of the method of test, the sprayed WC and the plated chromium coatings exhibit comparable fatigue behavior in NaCl solution.

5. Despite the reduced fatigue strength of the WC-coated steel specimens, full-scale fatigue tests of the blade retention bolts produced no failures through the equivalent of four lifetimes (approximately 14 000 flight hours of loading). Note that the full-scale component fatigue tests were carried out in laboratory air.

Conclusions

Prior experience in the field indicates that a 6 to 10 times improvement in life of the coated bolt can be achieved with the WC coating. Both laboratory and full-scale component fatigue tests indicate that the strength of the WC-coated bolt is adequate in a laboratory air environment. Although axial tension fatigue tests of WC coated 4340 steel showed a significant degradation of fatigue strength in NaCl solution, no service fatigue failures of WC coated retention bolts have been experienced. It appears, therefore, that the WC coating process for AH-1G blade retention bolts should be satisfactory for futher production and rework aircraft as a cost effective measure, but periodic visual inspection of the blade retention bolts should be conducted at a time interval within the 200 to 500-h range until an adequate service data base is established. Any evidence of corrosion should be sufficient grounds for replacing the bolt since field experience indicates that corrosion can be detected prior to catastrophic failure.

Acknowledgments

This work was supported by the U.S. Army Aviation Systems Command, St. Louis, Mo.

Summary

Summary

The collection of papers contained in this volume offers a broad view of current technology for characterizing, analyzing, and preventing corrosion-fatigue failure in metals. The various authors have considered aspects of corrosion fatigue in structural steels, high-alloy specialty steels, lightweight titanium and aluminum alloys, heat-resistant nickel base alloys, and corrosion-resistant tantalum. Effects of natural marine environments, laboratory salt solutions, and various industrial environments are presented. A mix of fatigue test methods have been utilized, and both crack initiation and crack propagation data are included. Although no new breakthroughs are claimed, significant progress in identifying and resolving specific problem areas is apparent among the results of these papers.

The highly diverse nature of the papers in this volume does not lend the material to precise organization nor complete summarization. Nevertheless an attempt at these tasks begins below.

Survey and Analysis

The two papers which are concerned primarily with these topics point out important deficiencies in our knowledge of both fundamental and applied aspects of corrosion fatigue. Experience with other corrosion-related failure mechanisms has demonstrated that knowledge of localized chemical and electrochemical conditions is essential to a fundamental understanding of these problems, yet we know little of the localized solution chemistry within corrosion-fatigue cracks. The model proposed by Hartt el al suggests approaches for further research on this topic and raises valid questions relating to the development of standard test methods. On a more applied level, the paper by Jaske et al reviews an extensive body of recent information relating to the problem of corrosion fatigue in common classes of weldable structural steels. The paper points out the need for further study, particularly in the areas of weldments and long-life corrosion fatigue. The latter deficiency raises a point in common with other types of corrosion-related testing, that is, the scarcity of data for long exposure times and the uncertainties of results from accelerated short-term tests.

Phenomena

The three papers in this section touch on several very important aspects of our practical understanding of corrosion fatigue. In particular, the first two papers reveal phenomena which can occur when the manner of cyclic loading departs from the simple constant-amplitude cycling most often employed in corrosion-fatigue studies. Chanani points out that under variable amplitude loading, an alloy which shows superior comparative behavior in a noncorrosive environment can exhibit inferior fatigue performance in a corrosive situation due to environmentally induced differences in crack growth retardation behavior. Endo and Komai's paper also deals with the practical problem of corrosion fatigue under complex service-related cycling. Their results emphasize the important changes which can occur in corrosion fatigue phenomena when interaction with stress-corrosion cracking occurs. The final paper in this section by Kitagawa et al presents a useful analysis of microcracking which has been observed and reported in corrosion fatigue. A common theme of the papers in this section is the poorly understood interactive effects which often occur in corrosion fatigue and act to frustrate efforts to transfer quantitatively or generalize upon corrosion-fatigue data.

Materials Characterization

Nearly half the papers in this volume are loosely categorized as dealing with the general topic of materials characterization. It is of interest to note that every one of these papers deals with materials which are quite rare and specialized, and therefore generally expensive to the user. Much of the research information presented here deals with developing or selecting materials which are resistant to corrosion fatigue failure mechanisms or with defining and evaluating those service-related conditions which are most detrimental to materials subjected to corrosion fatigue. Even a casual reading of this section points out very clearly that (*a*) a thorough knowledge and understanding of both the chemical and mechanical details of service conditions is vital in dealing with corrosion fatigue problems, (*b*) materials selection can play a critical role in dealing with corrosion fatigue, and (*c*) new metallurgical principles and alloys are being developed which offer the promise of greater resistance to corrosion-fatigue failure mechanisms.

In particular, the three papers dealing specifically with stainless steels touch upon the salient themes just mentioned. High-alloy stainless steels are utilized for superior corrosion resistance, yet many alloys in this category remain highly sensitive to corrosion fatigue. These three papers point out the roles of composition, microstructure, and bulk solution chemistry in influencing the severity of this problem. It is also pointed out that a fundamental understanding of these factors has only begun to emerge; however, optimism is expressed that present directions of research will yield superior alloys in the future. In the same vein, the paper by Zola on aluminum alloys speaks of metallurgically induced improvements in corrosion-fatigue resistance.

The paper by Crooker et al provides information relating to materials selection of high-strength structural alloys for marine service, as well as information on service-related electrochemical and cyclic frequency factors. This paper emphasizes the important differences in corrosion fatigue sensitivity that exist among naval alloys. The final two papers in this section by Ryder et al and Chu and Macco primarily describe the effects of various important service-related factors on aspects of corrosion fatigue in a given alloy for the purpose of providing comprehensive data on which to base failure predictions. Ryder et al noted the strong effects of cyclic frequency and stress ratio, and Chu and Macco noted the absence of an identifiable fatigue limit in corrosion fatigue.

Hydrogen Environments

Two papers were devoted to the specialized topic of crack initiation and growth in hydrogen-bearing gaseous environments. This is clearly a revelent topic for a volume on corrosion fatigue because the mechanism involved in many instances of corrosion fatigue failure is hydrogen embrittlement, thus the two seemingly separate phenomena are in fact closely related. These papers provide further evidence of hydrogen-cracking sensitivity in steels and in nickel-base alloys, although instances of apparent immunity to hydrogen-bearing environments were also noted. With regard to fatigue cracking in gaseous hydrogen, instances of extraordinarily large environmentally assisted increases in cyclic crack growth rates were shown to occur in some nickel-base alloys.

Failure Analysis and Design Considerations

The final two papers in this volume deal with corrosion-fatigue studies undertaken in response to specific instances of failure or the necessity for design improvement. Both papers are instructive with regard to industrial practices in response to evidence of corrosion-fatigue problems.

In closing, several aspects of the work presented herein do provide a basis for encouragement. First, despite the previously mentioned absence of any clearly identifiable breakthroughs, it is obvious in summarizing this collection of papers that progress indeed is occurring in corrosion-fatigue technology. The widespread use of newer experimental techniques, such as fracture mechanics and electron microscopy, are providing a basis for insight and comparability among data not previously possible. Alloys are being developed to the point where sensitivity to corrosion fatigue can be greatly minimized in many instances. Also, a much broader base of documented data has become available from which to judge the probable effects of numerous service conditions. Second, and perhaps most important, the ability to anticipate and predict the propensity for corrosion fatigue failure shows signs of improving. Several papers in this volume are aimed at new applications of corrosion-fatigue technology, such as offshore structures and high-performance ships. These applications are receiving attention from corrosion-fatigue specialists without awaiting the often relied upon impetus of widespread service failures. Corrosion-fatigue technology remains complex and many-faceted, however, its predictive capabilities are advancing as evidenced by the accomplishments described in this volume.

Nevertheless, the obvious complexity of corrosion-fatigue phenomena leaves many areas open to continued study. Prime examples can be drawn from the work contained in this volume. For instance, alloy selection based upon characterization tests is an important factor in preventing corrosion fatigue failure, yet the effects of experimental variables on characterization data are poorly defined and evaluated. Such knowledge is necessary in order to develop reliable consensus test methods. In the absence of such standard methods of testing, it remains difficult and hazardous to attempt strict comparisons among the results of various authors. A second pertinent example of areas which remain open for continued research lies with the application of characterization data to service conditions. Predictions of corrosion-fatigue behavior based upon laboratory characterization studies often remain highly dubious because of our incomplete knowledge of the effects of numerous service-related complicating factors. Little information currently exists to provide accurate determination of such factors as complex cyclic loading or long-term exposures to corrosion fatigue. The general areas of research cited here provide further opportunities for both basic and applied research.

T. W. Crooker,
co-editor

Index

Key to Abbreviations Used in Index

T = table
D = definition
F = figure
[ ] = see this subject under this listing

A

Air [Corrosion-agent-air]
Aircraft structure, 52, 202
Alloy 63 (duplex stainless steel), 135T
Alloy 903 (nickel-base alloy), 243
Aluminum alloys, 51, 189, 223
  Copper
    2024-T8, 51
  Magnesium
    5456-H116-H117, 189, 223
  Zinc-Magnesium, 75T
  Zinc-Magnesium-Copper
    7075-T6, 51
    7075-T73, 51
American Francaise de Normalisation (AFNOR), 122T, 131
American Welding Society (AWS-X), 28
Anodic Current, 79
ASTM A 245 steel, 22T
ASTM A 288 steel, 265
ASTM A 289 steel, 265
ASTM A 441 steel, 24T
ASTM A 537A steel, 22T
ASTM A 537B steel, 24T
ASTM standards
  E 8, 204
  E 399-74, 120, 173, 265

B

Bolts (blade retention-helicopter), 300
British Standards Institution (BS153F), 28

C

Calcareous scale, 25, 43
Cathodic protection, 19, 41, 198
Chemical industry, 134
Computer display, 98
Connection (of interacting, small cracks), 102D

- Corrosion
  - Agent
    - Acidic chloride solution, 133
    - Air, 51, 117, 202, 223
    - Dissolved oxygen, 26, 43
    - Distilled water, 99
    - Hydrogen (gas), 243, 264
    - Hydrogen sulfide gas, 264
    - Oxygen (in steam), 164
    - pH, 27
    - Saltwater, 51, 99, 223
    - Seawater, 19, 189, 225
    - Sodium chloride solution, 51, 78, 117, 155, 169, 202, 300
    - Steam, 155
    - Sulfuric acid, 118, 289
    - Temperature (variations), 27, 43
    - Water, 99
    - Water (Severn River), 224
    - Water (sump tank), 202
    - "White water", 141
  - Electrochemical, 117
  - Environment
    - Crack tip, 52
    - Splash zone, 29
  - Mechanisms, 20
    - Hydrogen embrittlement, 42
  - Pitting, 155
  - Potential, 41, 74, 84F, 123
  - Rate (steel), 26
- Corrosion-fatigue, 5, 51, 98, 117, 133
  - Low-cycle, 74, 189
- Crack
  - Blunting, 61, 95
  - Chemistry, 5, 129
  - Distribution (random), 98
  - Initiation, 19, 20D, 74, 98, 117, 133, 155, 264
  - Measurement, 98
  - Propagation, 5, 19, 20D, 74, 117, 133, 155, 169, 189, 202, 223, 243, 264
- Cyclic crack-growth
  - Long-life ($N > 10^6$), 20D
  - Rate (*da/dN*), 20, 76, 127, 189, 202, 243
- Cyclic load crack-growth, 243
- Cycling
  - Constant-amplitude, 21, 51

E

- Electrochemical potential [Corrosion potential], 123, 189
- Electrochemistry, 189
- Endurance ratio, 121

F

- Fatigue-crack growth, 51, 189
  - Environmental effects, 36
  - High frequency, 289
  - Rate (*da/dN*) [Cyclic crack-growth]
- Fatigue limit, 26
- Federal Test Method (Standard No. 151B), 181
- Fractography, 51, 74, 202, 243, 264
- Fracture mechanics, 98, 189, 223
- Frequency effect, 34, 37F

G

- Goodman diagram, 223

H

- Helicopter (AH-1), 170, 300
- Homogeneity function (*H*), 106
- HY-130 [High strength steel], 189
- Hydrofoil (ship), 190
- Hydrogen embrittlement, 42, 243, 264, 289
- Hydrostatic pressure, 26

I

IN744 (duplex stainless steel), 135T
Inconel 718 (nickel-base alloy), 243
Interaction factor (f), 102, 112D
Intercrystalline fractures, 155

K

K [Stress-intensity]

M

Marine alloys, 189
Mechanical damage, 117
Mechanical properties, 117
Metallographic structures [Microstructure]
Metallurgical variables
  Grain boundary carbides, 133
  Heat treatment (steel: varied), 22T, 32T
  Intermetallic precipitates, 133
  Orientation, 133, 202, 279
  Recrystallization annealed, 202
  Structure, 51, 118
  Thermal-mechanical treatments, 169
  Volume fraction, 133
Microstructure, 51, 117, 133, 169

N

Nickel-base alloys: Inconel 718, Waspaloy, alloy 903, 243
Nuclear industry, 134

O

Offshore applications, 19
Overload ratio, 51

P

Paper industry, 134
Passive film, 117
Potentiostated ("fixed electric potential"), 118, 189
Products
  Aluminum Alloy
    Forgings, 169
  Steel
    Bolts (blade retention), 300
    Rail, 99
    Wire, rod, bar, 22T
Protective coatings, 300
Pump impeller, 289

R

Random process, 41, 98
Reliability, 98
Retardation behavior, 51

S

Seawater [Corrosion-agent]
Secondary stress fluctuations, 74
Sensitization (of stainless steel), 136, 151D
Simulation program, 100
Small cracks (randomly distributed), 98
S-N diagrams, 223
Sodium chloride [Corrosion agent]
Solution chemistry, 5
Space shuttle, 243
Specimen
  Center-cracked-through, 202
  Compact (5W), 244
  Compact tension, 225, 265
  Double-cantilever-beam (contoured), 225, 247
  Geometry, 5, 21
  Notched, 27, 53, 76, 264
  Part-through-cracked, 202, 244
  Precracked, 117, 223, 264
  Single-edge-notch, 150
  Single-edge-notch cantilever, 190

  Smooth, 21, 76, 117, 223
  Wedge-opening-load, 265
  Welded, 28
Statistical distribution function, 98
Steels, 98, 189
  API X65, 32T, 38F
  ASTM A 245, A 537A, 22T
  ASTM A387B, A 517F, A 537, A 441, 32T, 34T
  Carbon (mild), 22T, 24T, 32T
  High strength, 75T, 99, 264
    HY-130, 189
    3.5 nickel-chromium-molybydenum-vanadium ferritic, 264
    18Mn-4Cr austenitic, 264
  High strength low alloy 4340, 400
  SAE 1020, 1015, 1036, 22T
  SAE 1018, 24T
  Stainless
    Austenitic, 118
    Austenitic-ferritic, 118, 133
    Duplex, 134
    Ferritic, 118
    Martensitic, 156
    Precipitation hardening, 17-4 pH, 189
    Special, 117
    Z6 CND 17.12, Z5 CNDT 17.12, Z3 CNDU 21.7, Z0 CE 26.1, 119T
    13Cr, 155
  Structural, 19
Stress
  Low, 20, 223
  Ratio, 202, 223
  Waveform, 74
Stress corrosion properties, 51, 74, 118, 133, 169, 199, 264
  Hydrogen-assisted, 289
Stress-intensity (factor) [*K*], 30, 81, 99, 173, 189, 223
Surface effect ship, 190

T

Tantalum, 289
Tantalum-2.5W/alloy, 289
Testing machine, hydraulic servo-fatigue, 103
Tests, rotating-bending, 118
Thermal-mechanical heat treatment, 169
Threshold stress, 85
Titanium alloys, 189, 202
  Ti-6A1-2Cb-1Ta-0.8Mo, 189
  Ti-6A1-4V, 202
Tungsten carbides (coating), 300
Turbine generators, 264

U

Uranus 50 (duplex stainless steel), 135T

V

VK-A171 (duplex stainless steel), 135T
VK-A271 (duplex stainless steel), 135T

W

Waspaloy (nickel base alloy), 243
Weibull distribution, 110F
Weight loss, 82, 84F
Welded joints, 19

Z

Zinc (anode), 25, 198

3RE60 (duplex stainless steel), 135T
17-4 pH [Stainless steel, precipitation hardening]
4340 steel, 300
5456-H117, -H116, 189, 223
7075-T73, 169
7475, 169